



ELSEVIER

Contents lists available at SciVerse ScienceDirect

Progress in Materials Science

journal homepage: www.elsevier.com/locate/pmatsci



Biological materials: Functional adaptations and bioinspired designs

Po-Yu Chen^{a,*}, Joanna McKittrick^{b,c}, Marc André Meyers^{b,c,d}

^aDepartment of Materials Science and Engineering, National Tsing Hua University, Hsinchu 30013, Taiwan, ROC

^bMaterials Science and Engineering Program, University of California, San Diego, La Jolla, CA 92093-0411, USA

^cDepartment of Mechanical and Aerospace Engineering, University of California, San Diego, La Jolla, CA 92093-0411, USA

^dDepartment of Nanoengineering, University of California, San Diego, La Jolla, CA 92093-0411, USA

ARTICLE INFO

Article history:

Received 11 October 2011

Received in revised form 23 February 2012

Accepted 27 February 2012

Available online 31 March 2012

ABSTRACT

Biological materials are typically multifunctional but many have evolved to optimize a chief mechanical function. These functions include impact or fracture resistance, armor and protection, sharp and cutting components, light weight for flight, or special nanomechanical/chemical extremities for reversible adhesive purposes. We illustrate these principles through examples from our own research as well as selected literature sources. We conduct this analysis connecting the structure (nano, micro, meso, and macro) to the mechanical properties important for a specific function. In particular, we address how biological systems respond and adapt to external mechanical stimuli. Biological materials can essentially be divided into mineralized and non-mineralized. In mineralized biological materials, the ceramics impart compressive strength, sharpness (cutting edges), and stiffness while the organic components impart tensile strength, toughness and ductility. Non-mineralized biological materials in general have higher tensile than compressive strength, since they are fibrous. Thus, the mineralized components operate optimally in compression and the organic components in tension. There is a trade-off between strength and toughness and the stiffness and density, with optimization. Mineralization provides load bearing capability (strength and stiffness) whereas the biopolymer constituents provide viscoelastic damping and toughness. The most important component of the nascent field of Biological Materials Science is the development of bioinspired materials and structures and understanding of the structure–property relationships across various length scales, from the macro-

* Corresponding author.

E-mail address: poyuchen@mx.nthu.edu.tw (P.-Y. Chen).

down to the molecular level. The most successful efforts at developing bioinspired materials that attempt to duplicate some of the outstanding properties are presented.

© 2012 Elsevier Ltd. All rights reserved.

Contents

1.	Introduction	1495
1.1.	Biological constituents	1499
1.1.1.	Biopolymers	1499
1.1.2.	Biominerals	1507
1.1.3.	Biological composites	1512
1.2.	Hierarchical structure	1512
1.3.	Cellular solids	1516
1.4.	Sandwich structures	1518
1.5.	Mechanical properties	1522
1.5.1.	Interpretation of mechanical property data	1532
2.	Fracture and impact resistance	1534
2.1.	Bone	1534
2.1.1.	Single-value toughness measurements	1534
2.1.2.	R-curve behavior	1536
2.2.	Antler	1539
2.2.1.	Exceptional fracture resistance in antler bone	1543
2.2.2.	Dynamic mechanical behavior	1548
2.3.	Horn	1550
2.4.	Hoof	1553
2.5.	Smasher limbs and telsons of stomatopods	1556
2.6.	Woodpecker skull	1557
3.	Defense and armor	1560
3.1.	Mollusk shells	1560
3.1.1.	Abalone	1560
3.1.2.	Clams	1572
3.2.	Sea urchins (Echinoideae) and sponge spicules	1576
3.3.	Diatoms and radiolarians	1580
3.4.	Skin	1582
3.5.	Osteoderms	1586
3.5.1.	Armadillo	1587
3.5.2.	Testudine	1592
3.5.3.	Crocodilia	1593
3.6.	Fish scales	1594
3.7.	Arthropod exoskeleton	1599
3.8.	Egg shells	1604
3.8.1.	Whelk eggs	1606
3.9.	Keratin armor	1610
3.9.1.	Pangolin scales	1610
3.9.2.	Quills	1610
4.	Cutting edges	1613
4.1.	Plants	1614
4.2.	Fish teeth	1614
4.3.	Rodent incisors	1616
4.4.	Squid beaks	1618
4.5.	Polychaete worm jaws	1620
4.6.	Chiton radula	1621
4.7.	Insect mandible and proboscis	1622
4.8.	Wood wasp ovipositor	1626

5.	Avian materials: lightweight and aerodynamic	1627
5.1.	Feathers	1627
5.2.	Bird beaks	1631
5.3.	Bird bones	1635
6.	Attachment	1639
6.1.	Sticking	1639
6.1.1.	Gecko foot	1639
6.1.2.	Beetles	1641
6.1.3.	Tree frog toe pad	1643
6.1.4.	Abalone foot – underwater adhesion	1645
6.1.5.	Spider web	1648
6.1.6.	Mussel byssal attachment	1648
6.2.	Superhydrophobic surfaces	1652
6.2.1.	Lotus leaf	1652
7.	Biomimetic and bioinspired materials	1653
7.1.	Introduction	1653
7.2.	Bioinspiration: fracture and impact resistance	1655
7.2.1.	Self-healing composites	1655
7.2.2.	Sheep horn composites	1657
7.2.3.	Shock absorbers based on the woodpecker's head	1657
7.2.4.	Natural graded and sandwich structures (osteoderms)	1658
7.3.	Bioinspiration: armor and defense	1661
7.3.1.	Abalone shell nacre	1661
7.4.	Bioinspiration: cutting edges	1664
7.4.1.	Ovipositor drill	1666
7.5.	Bioinspiration: aero and fluid dynamics	1667
7.5.1.	Birds	1667
7.5.2.	Fish	1667
7.6.	Bioinspiration: attachment	1669
7.6.1.	Gecko foot	1669
7.6.2.	Mussel byssal attachment	1671
7.7.	Bioinspiration: Sensors and optical devices	1672
7.7.1.	Structures from diatoms	1672
7.7.2.	Structures based on echinoderms	1673
7.7.3.	Sonar-enabled cane inspired by bats	1676
7.7.4.	Butterfly wings	1676
7.8.	Bioinspiration: medical applications	1677
7.8.1.	Bioglass	1677
7.8.2.	Tissue engineering scaffolds	1678
7.8.3.	Vesicles for drug delivery	1680
7.8.4.	The blue blood of the horseshoe crab	1680
7.9.	Other interesting bioinspired applications	1682
7.9.1.	Shark skin	1682
7.9.2.	Genetically derived materials	1682
7.9.3.	Origami structures	1686
7.10.	Bioinspiration from the molecular level: the bottom-up approach	1686
7.10.1.	Phage display	1687
8.	Conclusions and perspectives	1688
	Acknowledgements	1690
	References	1690

1. Introduction

The interface between biology and materials science has rapidly emerged to be at the forefront of materials research. Nevertheless, the study of biological systems as structures dates back to the early parts of the twentieth century. The classic work by Thompson [1], first published in 1917, can be considered the first major work in this field. Much earlier than this, embedded in the Greek mythology, Icarus' father Daedalus constructed wings from feathers and wax. He ignored his father's instructions not to fly too close to the sun, and the melting wax caused him to fall to his death. D'Arcy W. Thompson looked at biological systems as engineering structures and obtained mathematical relationships that described their form. Thus, he is rightly considered the father of this field. The nascent field of biological-based materials science can be divided into three broad (and overlapping) areas:

- I. *Biological materials* – the study of natural materials (e.g. bone, feathers, skin).
- II. *Biomimetics or bioinspired materials design* – synthesis of novel materials, devices, and structures inspired on biology.
- III. *Biomaterials* – the application of materials in the biomedical arena (e.g. implants).

The intersection of these three fields is demonstrated by the study of bone. Researchers have focused on understanding biomineralization and bone degradation (osteoporosis). This has led to a better understanding of the mechanical properties (bone as a biological material). Additionally, demineralized and deproteinized bone can be used as bone substitute in joints (hip, knee, and other joints), acting as a biomaterial. Finally, the self-healing property of bone has inspired a new class of composites that have this property (bioinspired material) [2]. In this article, we concentrate on I and II, always keeping in mind in part I how the information can be applied to II and III.

The prominence of this field can be assessed by the four international conferences on Mechanics and Biomaterials & Tissues (2005, 2007, 2009, 2011), organized by the Journal of Mechanical Behavior of Biomedical Materials, by the yearly Biological Materials Science Symposia held at the Annual TMS-AIME meeting (2006–2011), and by the number of sessions and symposia dedicated to this theme at the Materials Research Society (MRS) meetings starting in late 1980s. Globally, the field is gaining increasing momentum and recognition.

There are several books that provide valuable insights into a variety of biological materials. In the 1970s, Currey investigated a broad variety of mineralized biological (structural) materials and authored the well-known book *Bones: Structure and Mechanics* [3]. Other works of significance are *Cellular Materials in Nature and Medicine* [4], *Learning from Nature How to Design New Implantable Biomaterials: From Biomineralization Fundamentals to Biomimetic Materials and Processing Routes* [5], *Structural Biological Materials: Design and Structure–Property Relationships* [6], *Structural Biological Materials* [7], *Structural Materials in Animals* [8], *Mechanical Design in Organisms* [9], which is a symposium proceeding volume from the Society for Experimental Biology, *The Mechanical Properties of Biological Materials* [10], *Strength of Biological Materials* [11] and *Biological Materials of Marine Origin* [12]. Books on biomineralization include *Biomineralization* [13], *On Biomineralization* [14], *Biomineralization* [15], and *Biomineralization: Principles and Concepts in Bioinorganic Materials Chemistry* [16]. Books on the organic constituents in biological materials include *Collagen: Structure and Mechanics* [17] and *Biology of Fibrous Composites* [18]. Indispensable books on biomechanics are *Biomechanics: Mechanical Properties of Living Tissues* [19] and *Comparative Biomechanics: Life's Physical World* [20].

There have also been a number of overview articles presenting the field in a broad manner. Noteworthy among them are overviews in *Progress in Materials Science* [21,22] and in the *Journal of the Mechanical Behavior of Biomedical Materials* [23,24]. Other articles on broader aspects of biomineralization [12,25–27], structural biological materials [24,28–34] and bioinspired materials [22,35–41]. A special issue of the *Journal of the Mechanical Behavior of Biomedical Materials* devoted to biological materials has been published (Volume 4, Issue 5, July 2011). Additionally, there are many articles in the popular press and a four-part television series, *NOVA: Making Stuff*, recently aired on PBS. The present review avoids, where possible, duplication with an earlier article by our group [21].

The analysis of biological materials and bioinspired materials requires knowledge of both biological and engineering principles, disciplines that traditionally do not overlap. Understanding properties of biological materials also requires some understanding of zoology and animal behavior. The ram horn illustrates this point. It is an example of an appendage that has been optimized for impact resistance during fights – it serves no other purpose (except for dominance display). Knowledge of the location, energy and frequency of fights is necessary to evaluate the impact resistance of the horn and to design new bioinspired composites. Additionally, the nanostructural features of biological composites are of critical importance in the analysis of the mechanical response of biological composite samples.

Fig. 1 shows a plot of the Young's modulus as a function of density for natural materials, with synthetic materials (engineering ceramics, alloys, polymers, composites and porous ceramics) overlaid. Natural polymers such as wool and tendon have low densities ($<2 \text{ g/cm}^3$) and stiffnesses up to $\sim 10 \text{ GPa}$ (cellulose), while most biominerals have densities $<5 \text{ g/cm}^3$ with stiffnesses of up to $\sim 100 \text{ GPa}$ (hydroxyapatite, calcite). Minimizing the density is often a goal in the fabrication of synthetic materials, and it behoves the materials scientists to examine biological materials to glean new insights into the design for new materials.

The unique structures and characteristics of biological materials are distinguished from their synthetic counterparts. These are shown in Fig. 2, which are represented by six interrelated components:

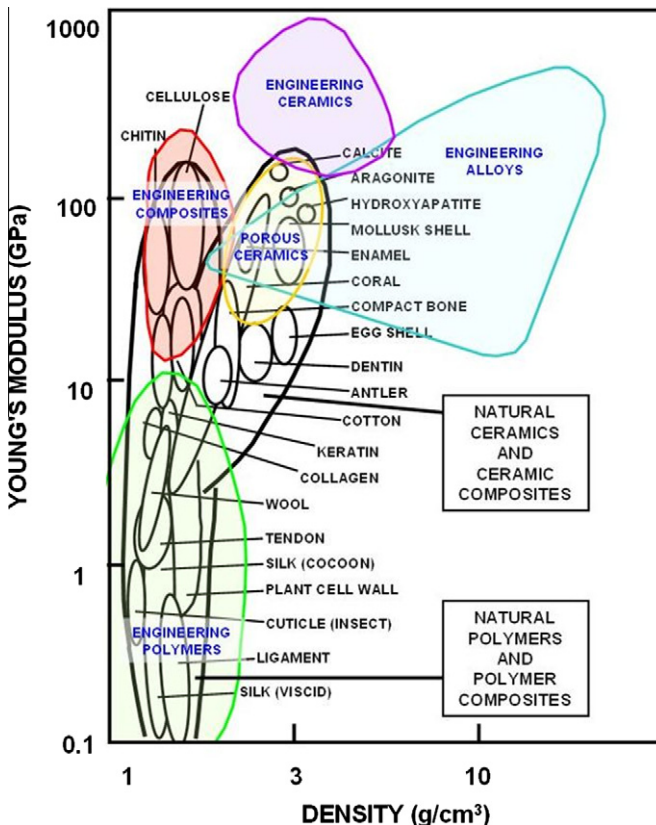


Fig. 1. Young's modulus as a function of density for various biological materials, overlaid on a map indicating regions of synthetic materials [42,43].

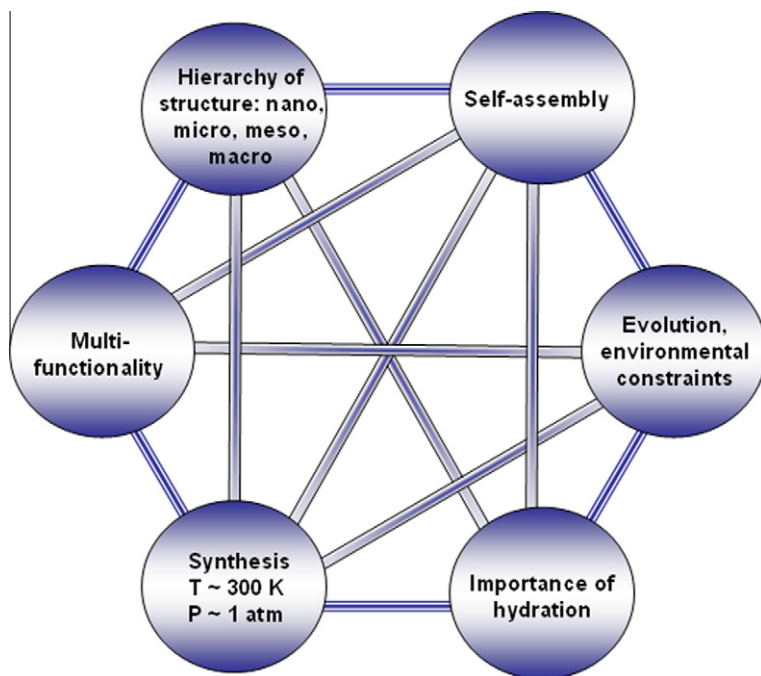


Fig. 2. Schematic representation of characteristic constraints/components in the study of biological systems. Modified from [44].

- *Self-assembly* – the structures are assembled from the bottom-up, rather than from the top-down, due to the lack of a preexisting scaffold. Genetic messages, cellular activity, and enzymatic activity plays a fundamental role.
- *Functionality* – many components serve more than one purpose; for example, feathers provide flight capability, camouflage and insulation.
- *Hierarchy* – there are different, organized scale levels (nano- to ultrascale), conferring distinct and translatable properties from one level to the next.
- *Hydration* – the properties are highly dependent on the level of water in the structure. There are some remarkable exceptions, such as enamel, but this rule applies to most biological materials and is of primary importance.
- *Mild synthesis conditions* – the majority of biological materials are fabricated at atmospheric pressure and room temperature and in an aqueous environment, a significant difference from synthetic materials fabrication.
- *Evolution, environmental constraints* – the limited availability of useful elements dictates the morphology and resultant properties.

Due to the remarkable physical and mechanical properties that biological materials exhibit, this field has attracted significant attention resulting in the research area of bioinspired design. There are many examples of bioinspired design, one of the earliest and one of the best known being Velcro[®] (based on the hooks in plant burrs). Other successful applications are: surfaces that are self-cleaning (Lotusan[®] paint, based on the hydrophobic surface of a lotus leaf), anti-slip surfaces (dog paw), anti-reflective surfaces of solar panels (insect eye), fiber-reinforced composites (wood), deployable structures (flowers), adhesive tape (gecko foot), low-drag dirigibles (penguin body) and boat hulls inspired by on the structure of shark skin [35,40].

Bioinspired materials design has gained considerable interest during the past decade, mainly due to the growth of interdisciplinary interactions between biologists, chemists, physicists and materials sci-

entists. It is a broad field that ranges from protein sequencing, chemistry, and self-assembly [45] leading to the fabrication of dental layers [46], luminescence probes [47], liquid crystals [48], and contact lenses [49] based on biological design. Hard biological materials are composites of an inorganic mineral phase with a biopolymer, created in a process called biomineralization. The potential to fabricate materials based on the unique and complex structures found in nature has produced considerable recognition from the materials community. For bioinspired structural materials, this potential has resulted in numerous publications outlining possible synthesis strategies to achieve fabrication of these hierarchical materials [38,50–57]. Biomineralized hydroxyapatite ($\text{Ca}_{10}(\text{PO}_4)_6(\text{OH})_2$), the main mineral components of bones and teeth, calcium carbonate (CaCO_3 , the main component of seashells, bird eggs, crustaceans and coral) and amorphous silica ($(\text{SiO}_2 \cdot n\text{H}_2\text{O})$), the main mineral content of sponge spicules and diatoms) have been the primary materials examined. It is remarkable that such a wide variation of shapes, structures, and functions are built with only a few, low atomic number ions. It would be significant if the superior mechanical properties of structural biological materials could be transferred to engineering materials, where the promise is enormous because of the great availability of synthesis and processing methods, extending the limited library of compositions and processes used by nature. Section 7 of this monograph is fully devoted to bioinspired materials and structures.

In terms of the hierarchical structure, there are several defining features [58]:

- The presence of *structural fibrous constituents* (e.g. collagen, keratin) that display widely varying properties, depending on the function (e.g. collagen in tendon, bone, heart muscles);
- There are *controlled orientations of the structural elements leading to anisotropy which matches the traction application directions*. For example, the minerals in bones are aligned with the collagen molecules, which are then assembled into oriented mineralized fibrils, which are in turn, oriented into lamellar sheets;
- There are *robust interfaces between the hard and soft constituents*, exemplified by high fracture resistance of nacre in mollusk shells, which is attributed to the mineral/biopolymer interface;
- Often, there is the *ability for self-repair* (bone);
- The *properties are mutable* – they can adjust due to changes in ambient conditions (e.g. chemical and mechanical signals);
- The *capacity for resiliency* (energy absorbed during elastic deformation), *toughness* (energy absorbed during failure) and *fatigue resistance*, which are important properties for structural integrity.
- *A controlled and complex shape formation*.

Most biological structural biological materials are multifunctional – bone is a noteworthy example. Skeletal bones support and shape bodies, serve as calcium and phosphorous stores, produce bone marrow and protect soft, critical organs (e.g. ribs, skull, vertebrae). However, there are some structural biological materials that have been optimized for one primary function, for example, the deer antler. An antler is a unique bone tissue that is deciduous, having an exceptionally high growth rate and serves as defense against predators and in mating competition – access for reproductive rights. Unlike skeletal bone, antlers do not store elements, produce marrow or support bodies. In fact, they are a high liability for the male animal. The antler growth is so large during the peak growth period in the summer that the skeleton has to dissolve to provide enough calcium.

The study of hard biological materials such as seashells, antler, teeth and bone has yielded fascinating insights into how these inorganic/organic materials adjust their microstructure and growth conditions to provide superior structural properties. In 1959 the pioneering work of John D. Currey produced the first reports how collagen and apatite interact to produce the mechanical properties of bone [59,60]. Subsequently he carried out the first studies on the structure and properties of mollusk shells, sea urchin tooth, narwhal tusk, antler and other biological mineralized materials [61–66]. More recently, our group has examined the structure and mechanical properties of the abalone [67–70], crab exoskeleton [71], the toucan beak [72–74], the armadillo carapace [75], bird feathers [76], antler [77–79], bone [80–82], horn [83,84], teeth [85,86], underwater adhesives [87], fish scales [88], and porcupine quills [89].

1.1. Biological constituents

Biological materials are composed of only a few elements. If one considers that there are approximately 100 stable elements in the periodic table, only ~10% are found as the building blocks of organic and inorganic tissues. Notable are the deficiency of metallic elements and the prevalence of the lightest elements – the first two rows of the table. The principal elements are hydrogen, carbon, nitrogen, oxygen, silicon, phosphorous, sulfur, and calcium. In addition, trace elements (e.g. iron) have been found to be crucial for phase determination in some system. For example, iron oxide is present in radular teeth of chiton (Section 4.3) [90]. There are a few notable exceptions where metal ions are present as cross-linkers which form metal complexes with specific amino acid residues, in particular imidazole from histidine and catechol (in DOPA protein, Section 6.1.6). These types of bonds are reversible and such physio-chemical design could be employed for self-healing materials [91–93]). The most common synthetic metals (iron, aluminum, copper) are virtually absent and only present in minute quantities and highly specialized applications. The reason is that the processing of these elements requires high temperatures that are not available in natural organisms.

1.1.1. Biopolymers

The structural organic constituents of biological tissues are either protein-forming polypeptides (primarily, in biological materials: collagen, keratin, elastin, resilin, fibroin, abductin) or polysaccharides (chitin, cellulose) as shown in Table 1. Structural proteins can be further divided into those that are dominated by stiff secondary structure regions (such as triple-helix in collagen or β -sheet strands in silk or β -keratin) and those that mostly contain amorphous, random-coil domains (as found in elastin, resilin, abductin). The crystalline fibers are molecular aggregates that align in a preferred direction. The stiffness of these crystalline biopolymers is generally orders of magnitude greater than the amorphous ones, but they have strains to failure orders of magnitude lower (Table 2) – the elastic energy is stored in the atomic bonds in the crystalline biopolymers whereas it is stored as entropy changes in the elastomeric biopolymers (see Section 1.5 for mechanical property discussion). Collagen and keratin have similar properties to cross-linked polymers whereas elastin, resilin and abductin have rubber-like properties.

1.1.1.1. Proteins. Crystalline protein molecules have a few well-defined secondary structures such as the α -helix, the β -sheet, the β -turn, and the coiled-coil (supercoil bundle of at least two α -helices). Proteins are long-chain of amino acids whose side-chains have various sizes (and hence steric constraints), charges, and hydrophobic/hydrophilic characteristics. All of these residues have specific roles

Table 1

Fibrous structural biopolymers found in living organisms with predominant amino acid residues and sugar chains. Gly = glycine, Pro = proline, Hyp = hydroxyproline, Cys = cysteine, Ser = serine, Ala = alanine, Asp = asparagines.

	Dominant amino acids	Distribution
<i>Proteins</i>		
Collagen	35% Gly, 12% Pro, 10% Ala, 9 Hyp ^a	Bone, teeth, vasculature, organs
Keratin	22% Cys, 13% Pro, 13% Ser ^b	Hair, nails, claws, horn, hooves, feathers
Elastin	32% Gly, 21% Ala, 13% Pro ^c	Skin, ligaments, vasculature, lungs
Resilin	37% Gly, 10% Asp, 11% Ala ^d	Insect wing hinges
Abductin	68% Gly, 6% Ser ^f	Hinged parts of bivalve mollusks
Fibroin	45% Gly, 30% Ala, 12% Ser ^e	Silkworm silk
Polysaccharides		
Chitin	(C ₈ H ₁₃ O ₅ N) _n	Exoskeletons of crustaceans, insects, squid and octopus beaks
Cellulose	(C ₆ H ₁₀ O ₅) _n	Plants

^a Rat tail tendon [8].

^b Sheep wool [94].

^c Rat smooth muscle [95].

^d Wing hinge, *Schistocera gregaria* [96].

^e *Bombyx mori* silk [96].

^f Sea scallop [97].

Table 2

Stiffness, tensile strength and strain to failure for selected biological and synthetic materials.

	E (MPa)	σ_f (MPa)	ϵ_f	Reference
<i>Biopolymers</i>				
Abductin	1–4			[98,99]
Cellulose	150,000		0.024	[99]
Collagen (along fibers)	1000	50–100	0.09	[19,99]
Elastin	0.3–1.5		>2	[8,99,100]
Fibroin	10,000	70	0.09	[99]
Keratin (wool)	5000	200	0.5	[101]
Kevlar 49 fiber	130,000	3600	0.03	[102]
PMMA	1600	15	0.013	[103]
Resilin	0.6–1.8	3	>3	[19,104]
Rubber	0.01–0.1	15	8.5	
<i>Silk</i>				
• Cocoon silk (<i>Bombyx mori</i>)	7	600		[102]
• Spider silk (webframe and dragline, major ampullate, <i>Araneus diadematus</i>)	10,000	1100	.18	[101]
• Spider silk (viscid, catching spiral, <i>Araneus diadematus</i>)	3	500	0.27	[101]
Tendon	2000–9000	50–100	0.09	[19,105]
<i>Biominerals</i>				
Aragonite (CaCO_3)	72000			[67,106,107]
Hydroxyapatite ($\text{Ca}_{10}(\text{PO}_4)_6(\text{OH})_2$)	112,000	115		[108]
Hydroxyapatite (from enamel)	83,000	60		[109–111]
Magnetite (Fe_3O_4)	72,000			[106]
Radular teeth (Fe_3O_4 from chiton)	90,000–125,000			[106]
Silica ($\text{SiO}_2 \cdot n\text{H}_2\text{O}$)	600–2,000			[112]
Silicon carbide (SiC)	450,000	3500		
Zirconia (ZrO_2)	200,000	250		
<i>Biocomposites</i>				
<i>Bone</i>				
• Trabecular bone	800–14,000	1–100		[3]
• Cortical bone (longitudinal)	6000–20,000	30–150	0.03	[3]
Nacre (abalone)	40,000–70,000	160		[61]
Wood (oak)	10,000	100		

in stabilizing the overall protein and in providing to the proteins their specific secondary structures and folding. The side-chains can also be chemically modified by post-translation modifications, and this is specifically important in structural proteins such as collagen (proline hydroxylation for instance) shown in Fig. 3a. In mammals, the most abundant protein is collagen, which is found in the bones, teeth, cartilage and blood vessels, among others. Fish scales also contain collagen, as does the musculature of vertebrates. Plants, mollusks and crustaceans have polysaccharides as the structural organic part.

Although there are 29 types of collagen, 90% of the collagen in the human body is of five types. Type I is found in the skin and bone, type II is the chief component in cartilage, type III is usually found along with type I, type IV is found in the cell basement membrane and type V is found in hair and the placenta. A defining feature of collagen is the frequently occurring amino acid sequence of Gly-Pro-X or Gly-X-Hyp (Gly = glycine, Pro = proline, Hyp = hydroxyproline, X = other amino acids).

Many of the protein-based fibers, except keratin, have glycine as the majority residue – the smallest amino acid – which is the only residue small enough to tuck into the twists along the triple helix (Fig. 3a). Three α -helix strands of the collagen molecule twist together to form the tropocollagen molecule (Fig. 3b), which is stabilized and held together by hydrogen bonding. The tropocollagen assembles into strands of ~ 300 nm in length separated by ~ 40 nm (Fig. 3c). These strands are organized into a staggered array to form collagen fibrils that are ~ 1 μm in diameter and are micrometers to tens of

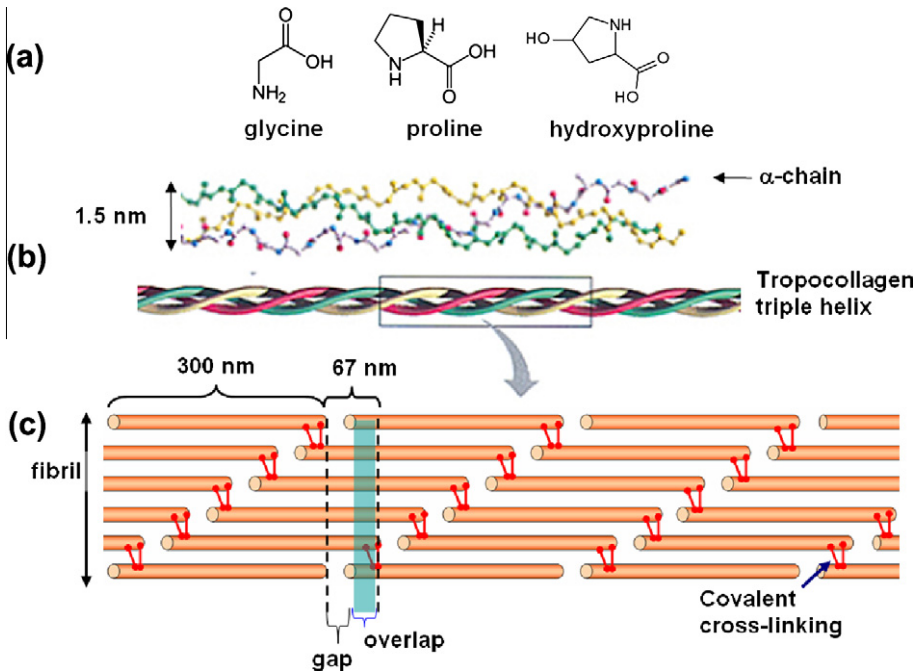


Fig. 3. Structure of collagen: (a) major amino acid residues; (b) tropocollagen forms from a triple helix of collagen strands; (c) tropocollagen assembles to form collagen fibrils – a staggered arrangement of 300 nm long molecules form gap and overlap regions in the fibril ($\sim 1 \mu\text{m}$ diameter).

micrometers long. The interruption between the tropocollagen molecules gives rise to two important dimensions – the gap and the overlap regions that combine to form the characteristic banded structure of 67 nm spacing, observed in the TEM micrograph in Fig. 4a. In Fig. 4b, a micrograph from TEM tomography (maximum intensity projection) illustrates the three-dimensional structure of the collagen fibrils in demineralized cortical antler bone. The fibril bundles have a preferred orientation, which is aligned along the long axis of the antler. These results are very similar to the TEM observation on the demineralized human compact bone studied by Giraud-Guille [113,114], who verified the twisted plywood architecture of collagen fibrils in bone.

Keratins are composed of two α -helices bundling into a superhelix coiled-coil. In mammals, this coiled-coil structure is the primary constituent of hair, nails, hooves, horns and the epidermal layer of the skin [115]. In reptiles and birds, the claws, scales, feathers and beaks are β -keratin, tougher than the α -form, and are usually configured into a β -pleated sheet arrangement. An important amino acid of keratin is cysteine ($\sim 22\%$), which has a thiol side-group that forms covalent disulfide bonds with another cysteine residue. In both type of keratins, the disulfide bond provides cross-linking thereby stabilizing the network, adding to strength, and providing insolubility in water. Fig. 5 shows the molecular and filamentary structure of α -keratin. Isolated α -helix chains form a dimer (coiled-coil, 45 nm in length, 1 nm in diameter) with sulfur cross-links, assemble to form protofilaments and then bimerize to form intermediate filaments (IFs), 17 nm in diameter. The IFs are embedded in a sulfur-rich amorphous keratin matrix [116]. The amorphous keratin matrix consists of two types of proteins, one containing a high amount of Cys residues and the other containing biased amounts of Gly and Tyr residues [117]. The matrix has been modeled as an elastomer [118]. Thus, keratin is a polymer/polymer composite of short crystalline IFs embedded in an amorphous matrix. A TEM micrograph of ram horn keratin is shown in Fig. 6 – the dark strand is the crystalline IF, which is surrounded by the lighter amorphous matrix. The tensile strength of human hair ($\sim 200 \text{ MPa}$) is an order of magnitude greater than that of human nail [11], which is due to the lower order alignment of the keratin molecules in

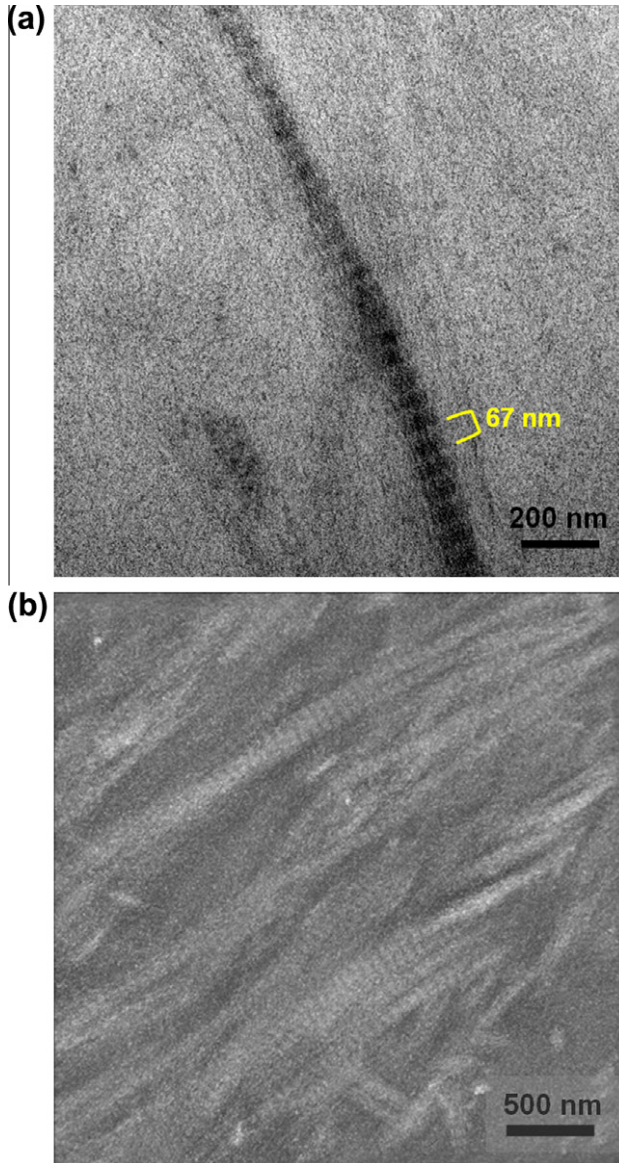


Fig. 4. (a) TEM micrographs showing a collagen fibril with characteristic 67 nm periodicity (b) the maximum intensity projection showing the three dimensional structure of collagen fibrils in cortical antler bone.

naïl. The molecular structure of β -keratin with a pleated structure is illustrated in Fig. 7. Positioned side-by-side, two or more protein strands (β -strand) link through hydrogen bonding. The linked β -strands form small rigid planar surfaces that are slightly bent with respect to each other, composing a pleated sheet arrangement.

Elastic proteins are an important class of materials that can store and release energy quickly and efficiently. These elastomers have several underlying requirements: they must be flexible and free to react to stress and they must have a degree of cross-linking to form a network thereby distributing the stress uniformly throughout the system. The cross-links can be either covalent or non-covalent.

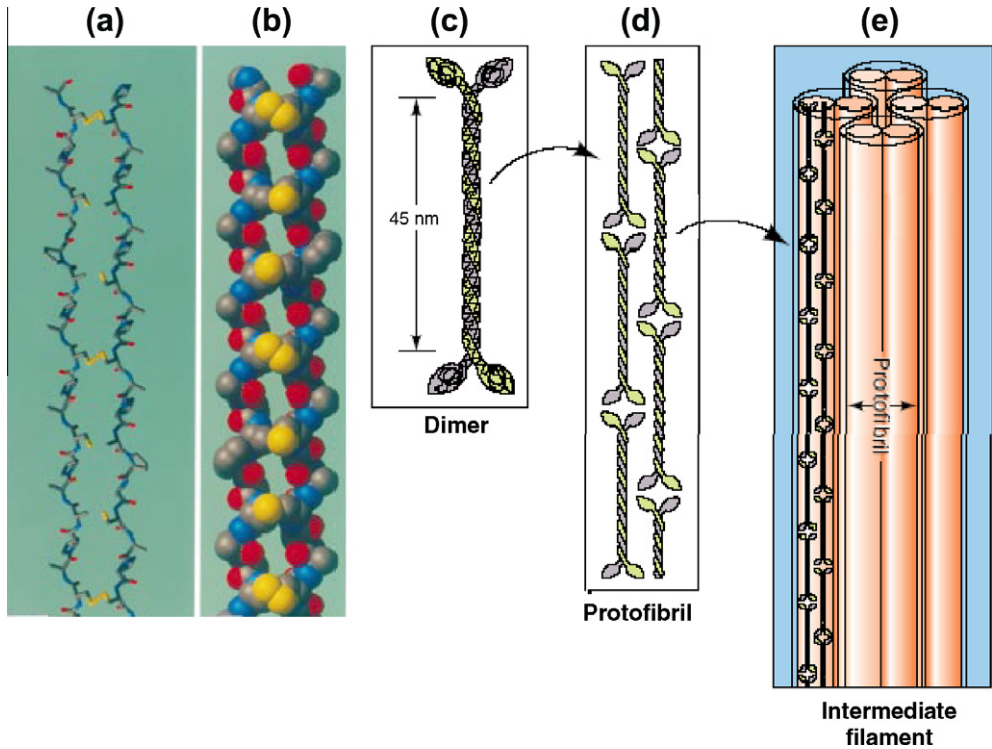


Fig. 5. Molecular structure of α -keratin: (a) ball and stick and (b) space filling model of two isolated α -helix chains of the dimer with sulfur cross-linking bonds. Yellow = cysteine residue. Taken from [116]. (c) Two keratin polypeptides form a dimeric coiled coil, (d) protofilaments form from two staggered rows of tail-to-head associated coiled coils, (e) protofilaments bimerize to form a protofibril, four of which form an intermediate filament. Taken from [119].

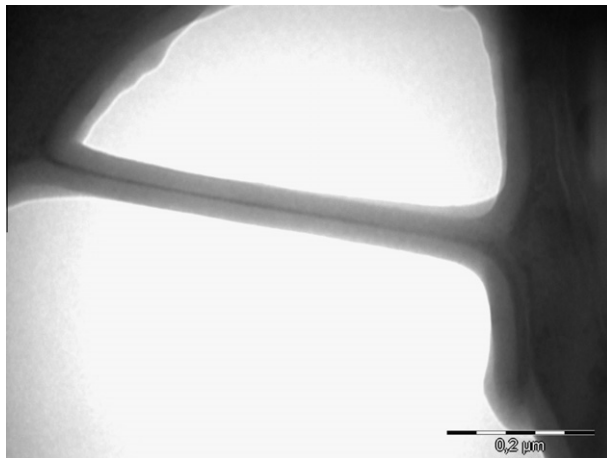


Fig. 6. TEM micrograph of α -keratin intermediate filament from a sheep horn. The strongly diffracting core of crystalline keratin is surrounded by an amorphous matrix. Scale marker = 200 nm. Taken from [32].

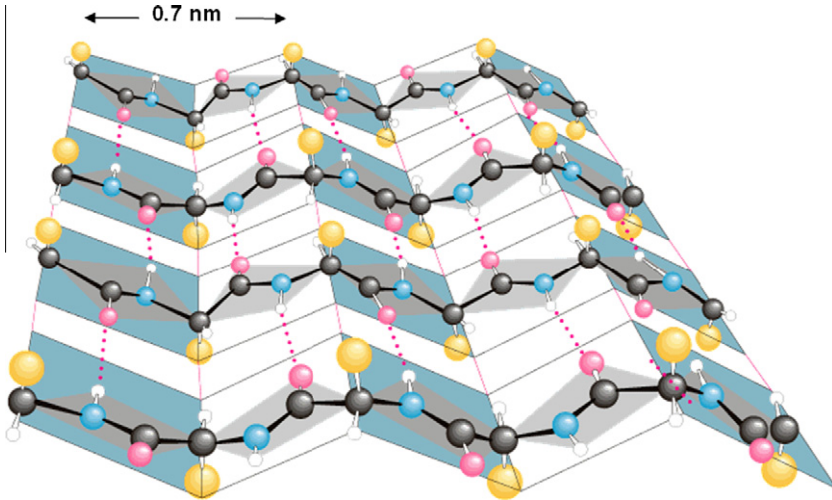


Fig. 7. β -pleated sheet configuration. Hydrogen bonding (dotted red line) holds the protein chains together (Irving Geis).

Elastin is found in vertebrates (skin, arterial walls, *ligamentum nuchae* in the neck of ungulates), resilin is found in insect flight systems, abductin is found in the hinges of bivalve mollusks, and fibroin is found in spider and silkworm silk. These fibers provide extensive elasticity and resilience in tissues that undergo reversible, repetitive deformation. For elastin, there are several distinct morphologies: in the skin and lungs as rope-like networks; in blood vessels as thin concentric sheets; and in cartilage as three-dimensional cellular structures [120,121]. Most of the work on elastic proteins has been performed on elastin due to the biomechanical significance in the body. Fibroin has captured much interest lately due to its exceptionally high specific strength and extensibility. Spider silk producing genes have been successfully transferred to goats [122,123] and silkworms so that large scale manufacturing of the material may be possible. Unlike silkworms that can be colonized to produce silk, spiders in close proximity will kill each other. Abductin was isolated from swimming scallops [96] and its sequence was obtained by Cao et al. [124]. Abductin is the only known natural elastomer that functions in compression and its elastomeric properties have been investigated by Denny and Miller [125]. It forms a pad at the junction (hinge) of the two valves in bivalves. Despite the excellent elastic resilience and extensibility, the material has not been widely studied.

Elastin is typically thought of as a gel with randomly coiled peptide chains that are cross-linked. There is a strong interaction of water with the protein, resulting in an inability to produce a good diffraction pattern [126]. The deformation characteristics of elastin are compared with collagen in Fig. 8. Elastin can undergo over 200% strain before the protein strands have completely straightened out [127]. The elastin backbone is highly mobile. On stretching the configurational entropy is reduced, which provides the restoring force upon unloading [128]. Elastin does not creep under an applied load. In contrast, the collagen molecule is much more rigid.

Resilin has been hard to be examined, since only small portions are available from insects. It is extremely resilient and also has excellent fatigue properties and successful recombinant expression in bacterial cultures has been obtained [129]. In 1960s, Weis-Fogh [130,131] first described the chemical and mechanical properties of resilin. He found that it could be stretched up to 300% and when unloaded, regained the original shape. Additionally, it can maintain a load without relaxation. It has a low stiffness (0.6–4 MPa) but a high energy storage capability with a coefficient of resilience of up to 98%. Besides wing joints, it can be found in cuticular structures such as the abdominal wall of a termite queen, the thorax of flying insects, the material responsible for flea jumping, the element in the sound-producing tymbal mechanism in cicadas and tendons in dragonflies [132,133]. A locust can beat its wings over 20 million times during its lifetime, a flea can release stored energy in 1 ms and

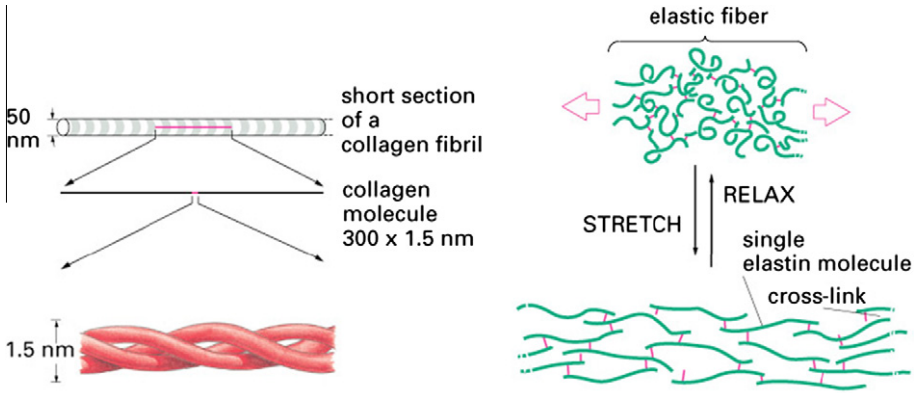


Fig. 8. Comparison of collagen and elastin. The low stiffness of elastin is due to the tangled nature of the protein strands in elastin that are embedded in a gel-like matrix. Applying a force to elastin results in the tangled chains straightening out but remaining cross-linked which returns to the tangled state when the force is released. Taken from [134].

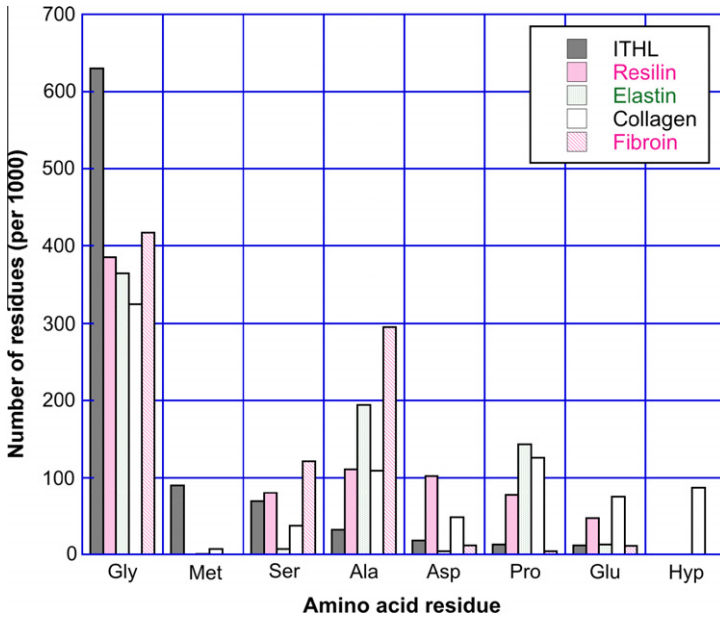


Fig. 9. Amino acid residues per 1000 residues for the internal triangular hinge ligament (ITHL) for *Aequipecten irradians* (a scallop), resilin from a desert locust wing hinge (*Schisocera gregaria*), elastin from an ox neck ligament, collagen from a calf skin and fibroin silk from a silkworm (*Bombyx mori*). Abbreviations: Asp, aspartic acid; Glu, glutamic acid; Pro, proline; Gly, glycine; Ala, alanine; Met, methionine; Hyp, hydroxyproline. Data from [96].

a cicada can emit sound pulses over 400 million times during a lifetime. This remarkable protein is unique among the elastic proteins and demonstrates a wide functional diversity.

Abductin is another low stiffness, resilient elastic fiber that is found in the propulsion systems of swimming bivalve mollusks. A scallop propels its body through water by opening and closing the shell halves (valves) through constriction and release of the internal triangular hinge ligament (ITHL), in response to contractions of the abductor muscle in the animal. Kelley and Rice [96] found the ITHL has properties similar to elastin and resilin. Alexander [98] measured the Young’s modulus to be 4 MPa,

compared with 0.6–1.8 MPa for elastin and resilin. Unusual for the other elastic proteins, there was ~ 3 wt.% mineral phase, presumably calcium carbonate that provides the additional stiffness. Comparison of amino acid residues for various proteins is shown in Fig. 9.

Fibroin is found exclusively in spider and silkworm silk. The distinguishing amino acid sequence is $(\text{Gly-Ser-Gly-Ala-Gly-Ala})_n$ that is in antiparallel β -sheet arrangements. The Gly residue (45%) allows for tight packing and thus makes silk a high strength fiber. There are two types of spider silk – the radiating dragline web frame (major ampullate, MA) and the catching spiral (viscid) of the web. Fig. 10 shows a hierarchical diagram of spider silk. The silk fibrils consist of stiff β -sheet configured nanocrystalline regions surrounded by an amorphous matrix. The crystalline regions add to the strength while the amorphous regions are responsible for the high toughness and extensibility. As shown in Table 2 and Fig. 11, the mechanical properties are quite different. The dragline silk has a high stiffness and failure strength, in contrast to the catching spiral with a much lower stiffness and strength. To capture prey in the web, a combination of silks is necessary – strong web frame coupled with a highly elastic, energy-absorbing spiral. Fig. 12 shows the effect of strain rate on the Young's modulus, tensile strength and ultimate strain of the MA silk of *Araneus sericatus*. The modulus, strength and the, surprisingly, extensibility trend with increasing strain rate – a phenomenon that does not occur in synthetic materials. Normally, with an increase in strain rate, a metal becomes stronger but the strain to failure decreases. For spiders, this combination of properties results in a truly remarkable material. According to Gosline et al. [102], the toughness of both MA and viscid spider silk is higher than that of Kevlar[®] fibers.

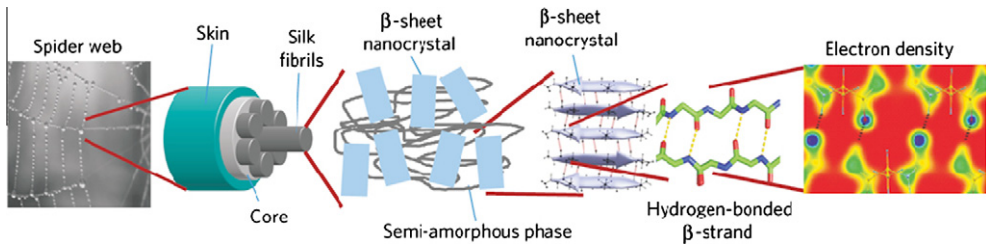


Fig. 10. Hierarchical spider silk structure, displaying key structural features, including the electron density at the nanometer scale, hydrogen bonded β -strands, β -sheet nanocrystals, a hetero-nanocomposite of stiff nanocrystals embedded in a softer semi-amorphous phase and silk fibrils, which assembles into macroscopic silk fibers. Adapted from [135].

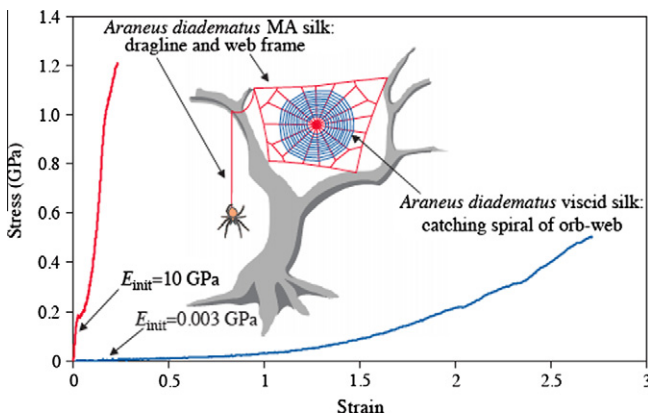


Fig. 11. Stress–strain curves for major ampullate (MA) gland (red) and viscid silk (blue) from the spider *Araneus diadematus*. E_{init} = initial stiffness. Taken from [102].

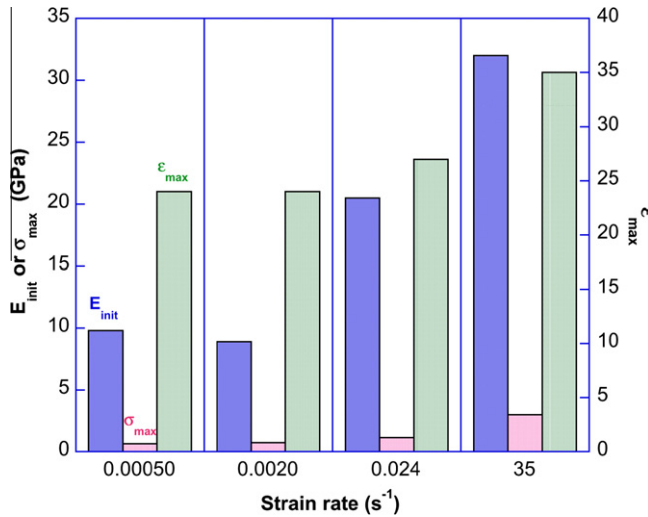


Fig. 12. Strain rate effect on the Young's modulus (E_{init}), tensile strength (σ_{max}) and strain (%) of MA spider silk (*Araneus sericatus*). Data from [136].

1.1.1.2. Polysaccharides. Polysaccharides are long chain molecules with the general formula, $(C_6H_{10}O_5)_n$ where $40 \leq n \leq 3000$. Cellulose and chitin are the two most abundant natural polysaccharides and of interest as fibrous building blocks in plants (cellulose) and animals (chitin). Chitin is a polymer of *N*-acetyl glucosamine $((C_8H_{13}O_5N)_n)$ and is found in the exoskeletons of insects and crustaceans, the beaks of cephalopods (squid, octopus) and in the organic matrix in mollusk shells. The molecular structures of chitin, chitosan, and cellulose are shown in Fig. 13. Chitin differs from cellulose by the substitution of an acetyl amine group for a hydroxyl group resulting in a higher strength for chitin. It is considered to be functionally equivalent to the structural protein keratin. Chitosan does not exist in nature and is produced by the deacetylation of chitin at ~60–100%. It has been widely applied as a biomaterial and for tissue engineering [137]. Cellulose is the structural component of plant cell walls. Like chitin, pure cellulose is not found in nature. It is usually associated with lignin and hemicellulose. Depending on the species, wood contains 40–55% cellulose, 15–35% lignin and 25–40% hemicelluloses on a dry basis. Cotton is the purest natural source, containing over 90% of cellulose.

1.1.2. Biominerals

There are three principal groups of biominerals: carbonates, phosphates, and silica. They seem to have appeared at about the same time, in the pre-Cambrian ~550 million years ago. The tubular fossil *Cloudina* is often considered one of the first examples of a biomineralized skeleton. It consists of half rings that were apparently constructed by the secreting gland of a worm. These half rings were made of calcium carbonate. Fig. 14 shows the evolution in the number of clades (a clade is a group consisting of a species and all its descendants) of the three groups. During the Cambrian (550–500 MY) there was a large increase in the number of species. For calcium carbonate, the earliest morphology of aragonite was the spherulitic/prismatic one that does not need to be mediated by proteins. This morphology is seen in abalone nacre after a mesolayer is formed and prior to the onset of the tiled configuration of nacre (Section 3.1). This morphology evolved during the mid Cambrian to produce:

- Aragonite fibers in a tangential arrangement (such as that observed in limpets).
- Cross-lamellar aragonite (such as that in conch).
- Foliated calcite (oysters).
- Brick-and-mortar structure (abalone nacre).

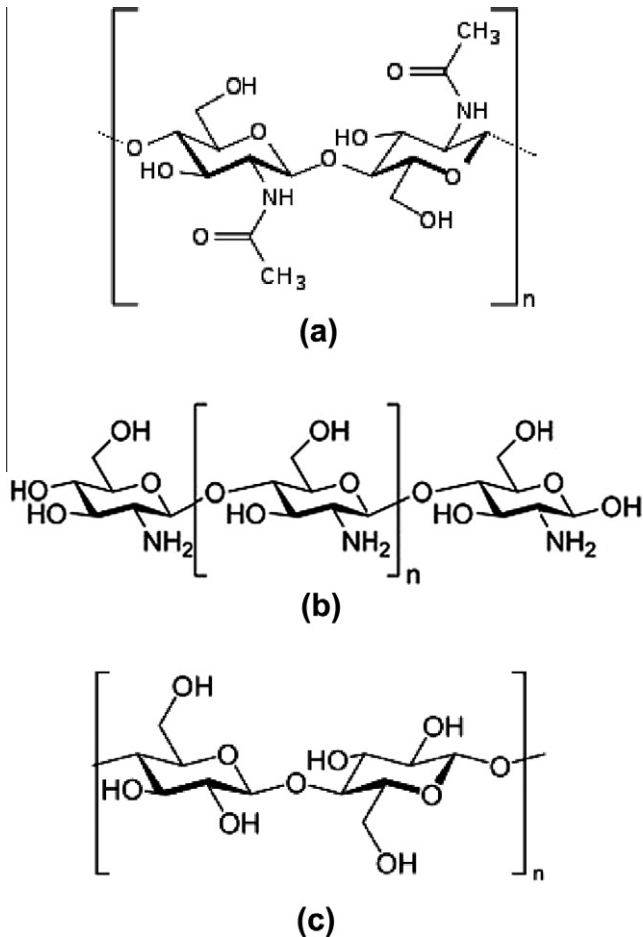


Fig. 13. Molecular structure of (a) chitin, (b) cellulose and (c) chitosan. Taken from [137].

In Table 3, common biominerals are shown (out of ~60 total). The terrestrial animals have calcium carbonate or calcium phosphate minerals whereas marine species can possess either calcium- or silicon-containing minerals. The calcium-containing minerals are crystalline, with some amorphous calcium carbonate found in the exoskeletons of crustaceans. Crystalline SiO_2 is not biogenetically synthesized; it occurs only in the amorphous, hydrated form ($\text{SiO}_2 \cdot n\text{H}_2\text{O}$). Diatoms (phytoplankton) are the most ubiquitous animal found in the oceans and form beautiful and intricate $\text{SiO}_2 \cdot n\text{H}_2\text{O}$ exoskeletons. Sea water contains ~3 ppm Si and ~400 ppm Ca and it may be puzzling as to why calcium-containing minerals are not formed in diatoms. Using finite element modeling, Hamm et al. [138] calculated the tensile fracture stress of a diatom frustule to be 540 MPa, much higher than that of aragonite (CaCO_3) at 100 MPa. Since the densities are similar, this implies that the thin, delicate cages of the diatoms are more structurally robust if fabricated from $\text{SiO}_2 \cdot n\text{H}_2\text{O}$ than CaCO_3 . In addition, the key energetic issue is that silica autopolymerizes (no energy input), which can be catalyzed with a minimum amount of organics. To nucleate CaCO_3 , a supersaturated solution is needed, which requires a much higher concentration of calcium than silicon. Additionally, the cells have to exclude calcium from the cytoplasm because it is used as a second messenger in trace amounts, so there is likely to be high energy involved in transporting the calcium to the correct location. Silicic acid is generally

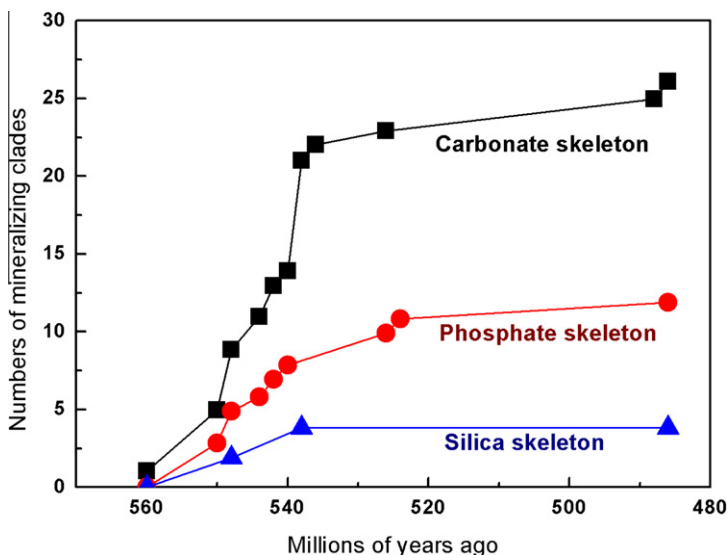


Fig. 14. Evolution in the number of clades (groups of taxa that appear to derive their biomineralization from a common ancestor) for the three principal biominerals: carbonates, phosphates, and silica. Adapted from [139].

Table 3

Biominerals found in living organisms. Adapted from [140].

	Chemical formula	Distribution
Atacamite	$\text{Cu}_2\text{Cl}(\text{OH})_3$	<i>Glycera dibrianchiata</i> (blood worm) jaw
Barium sulfate	BaSO_4	Algae (gravity sensor)
Calcium carbonate	CaCO_3	
Calcite (rhombohedral)		Mollusk shells, bird eggs, sponge spicules, sea urchin spines
Aragonite (orthorhombic)		Mollusk shells, corals
Amorphous		Arthropod exoskeletons, mollusk shells, plants
Calcium oxalate	CaC_2O_4	Kidney stones, plants
Calcium sulfate	CaSO_4	Jellyfish larvae (gravity sensor)
Dolomite	$\text{CaMg}(\text{CO}_3)_2$	Sea urchin spicules and teeth
Ferrihydrate	$5\text{Fe}_2\text{O}_3 \cdot 9\text{H}_2\text{O}$	Ferritin (animals), plants
Greigite	Fe_3S_4	<i>Cryosmallon squamiferum</i> foot
		(gastropod living near hot vents in Indian Ocean)
Hydroxyapatite	$\text{Ca}_5(\text{PO}_4)_3(\text{OH})$	Bones, teeth, osteoderms
Iron (III) oxide/hydroxide	FeOOH	Chitin and limpet teeth
Magnetite	Fe_3O_4	Mollusk radula, bacteria
Pyrite	FeS_2	<i>Cryosmallon squamiferum</i> foot
Silica (hydrated)	$\text{SiO}_2 \cdot n\text{H}_2\text{O}$	Diatom exoskeleton, sponge spicules

non-toxic and actually can diffuse across membranes so less energy is required for transport [141]. Glass sponge spicules are also $\text{SiO}_2 \cdot n\text{H}_2\text{O}$.

Calcium carbonate (CaCO_3) is found as crystalline calcite (rhombohedral, $R\bar{3}c$), aragonite (orthorhombic, $Pmcn$), and vaterite (hexagonal, $P63/mmc$) structures as well as in the amorphous form. Calcite is the more stable polymorph. Fig. 15 compares the crystal structures of the primary polymorphs, illustrating both a side and top view. Bird eggs, some sponge spicules and sea urchin spines are composed of calcite. Mollusk shells and corals are aragonitic; the former, or parts thereof, can also be calcitic. Magnesium additions to calcite forms a modified dolomite, $\text{Ca}_{1-x}\text{Mg}_x\text{CO}_3$, which is stronger and harder than pure calcite and is precipitated in sea urchin teeth and spicules. Amorphous calcium carbonate is also found in some plants, sponges, sea urchins, mollusks and sea worms [142].

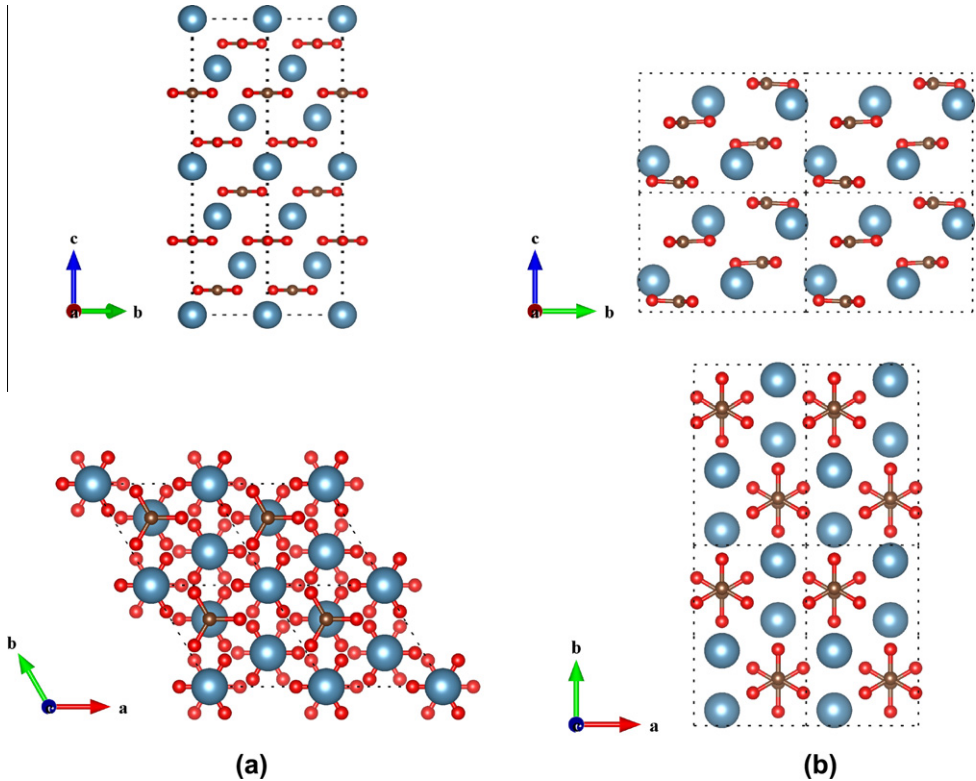


Fig. 15. Comparison the crystal structures of CaCO_3 : (a) calcite, side and top views, $a = b = 0.4989$, $c = 1.7062$ nm; (b) aragonite (orthorhombic), side and top views, $a = 0.49614$, $b = 0.79671$, $c = 0.57404$ nm. (Ca = blue, C = brown, O = red). Lattice parameters taken from [143] and [144].

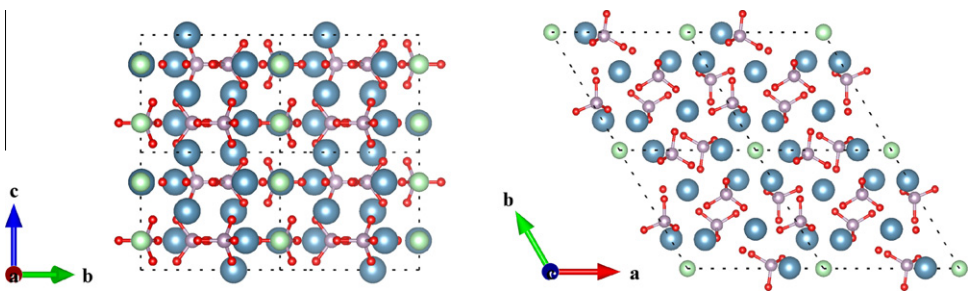


Fig. 16. Crystal structure of hydroxyapatite: side and top views, $a = b = 0.9432$, $c = 0.6881$ nm. (Ca = blue, P = purple, O = red, OH = green). Lattice parameters taken from [145].

In mammals, derivatives of hydroxyapatite ($\text{Ca}_{10}(\text{PO}_4)_6(\text{OH})_2$) are the predominant minerals found in bone, teeth and the osteoderms of turtles, crocodiles and armadillos. Hydroxyapatite has a hexagonal structure ($P6_3/m$) with lattice parameters $a = 0.9432$ nm and $c = 0.6881$ nm (Fig. 16). In bone, the minerals are non-stoichiometric, with 4–6% of the phosphate groups replaced by carbonate groups, making the structure more similar to that of dahllite. The bone crystals are in the form of platelets approximately 40–60 nm in length and 20–30 nm in width. The thickness of bone crystals measured

from TEM [146–149] and small angle X-ray scattering (SAXS) [150,151] varies from 1.5 nm for mineralized tendon to 4 nm for some mature bones. Recent atomic force microscopy (AFM) studies found that the bone crystals are longer than those observed by TEM, with widths and lengths ranging from 30 to 200 nm [152–154]. This discrepancy may be due to breakage of the fragile crystallites during TEM sample preparation. Fig. 17a and b shows X-ray diffraction patterns from the minerals from cortical elk antler and bovine femur bone. The broadness of the peaks indicates the crystals are nanocrystalline, which is confirmed by the TEM micrographs (Fig. 17c and d). The minerals have a plate-like morphology with a thickness of 4 nm and a lateral dimension of 40–150 nm. In teeth, a portion of the hydroxyapatite is converted to fluorapatite ($\text{Ca}_{10}(\text{PO}_4)_6\text{F}_2$), with fluorine replacing the hydroxyl groups, resulting in a harder mineral.

Magnetite (Fe_3O_4 , $Fd\bar{3}m$, $a = 0.8391$ nm) has two functional uses. It acts as a navigation sensor in the skulls of tuna and pigeons, for example, but it also has a high hardness and forms teeth of some

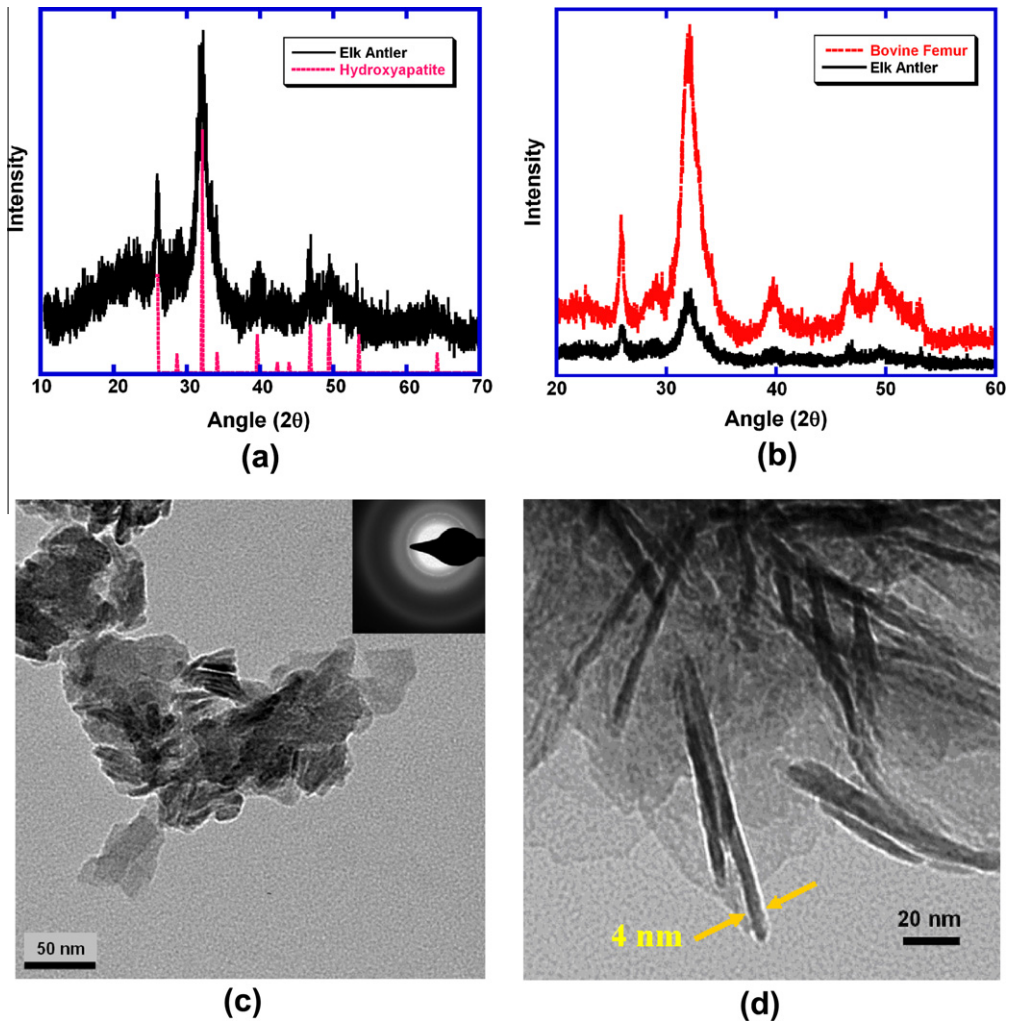


Fig. 17. XRD patterns of elk antler compared to (a) pure hydroxyapatite and (b) bovine femur. (c) TEM micrograph of mineral crystallites derived from elk antler (Insert: selected area electron diffraction pattern). (d) High magnification TEM micrograph showing the platelet-like crystallites with thickness ~ 4 nm. Adapted from [77].

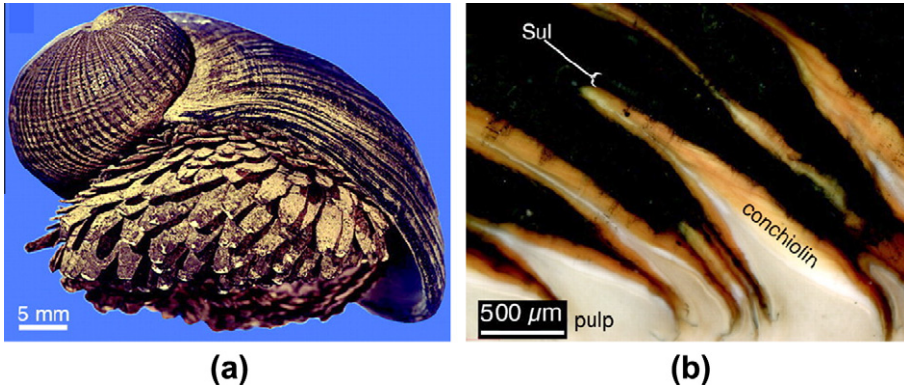


Fig. 18. The gastropod, *Crysmallon squamiferum* (a) retracted in shell; scales and shell are rusty from storage in low grade ethanol and (b) longitudinal sections of scales, viewed with light microscopy. Sul, sulfide layers (black in (b)). Taken from [155].

mollusks. The hardness of magnetite is found to be 3X higher than that of either enamel or calcium carbonate, which is a useful property for chitons, who use their teeth to scrape off nutrients from rocks [106]. There is also magnetite in the chiton radula, described in Section 4.5. Another transition metal mineral, atacamite (copper-based), is found in the jaw of the blood worm, *Glycera dibrianchiata* [156]. It forms short fibers that are parallel to the jaw surface and improve their bending stiffness [157].

A newly discovered gastropod, *Crysmallon squamiferum*, has been found near hot black-smoker chimney vents in the Indian Ocean. Tube worms, shrimp and crabs also live there. Animals that live there must survive in extreme environments – complete darkness, temperature variations of 2–400 °C, high pressures and high concentrations of sulfides that are emitted by the vents. As a consequence, the foot is covered with hundreds of scale-shaped sclerites consisting of proteins (conchiolin) and minerals – pyrite, FeS_2 , and greigite, Fe_3S_4 , both of which appear to be mediated by proteobacteria present on the surface [155,158]. Fig. 18 shows a photograph of the gastropod. The outermost layer of the shell is composed of greigite, similar to the sclerites [159].

1.1.3. Biological composites

In biological composites the minerals provide strength and stiffness while the biopolymers impart toughness and ductility. Fig. 19 shows a Wegst–Ashby map of toughness and stiffness for biological materials [42]. The structural biopolymers (collagen, keratin) show high toughness but low stiffness whereas the minerals have a high stiffness but low toughness, given their brittleness. Composites of the biopolymers and minerals yield materials that exhibit both high toughness and stiffness, such as the mollusk shells, coral, bones, and teeth, for example, yet are lightweight. Thus, these materials are truly composite materials that materials scientists are familiar with – the combination of two dissimilar materials yields a better material that transfers the sought-after property from each constituent into the composite.

1.2. Hierarchical structure

Hierarchical structures can be described as a group of molecular units/aggregates that are in contact with other phases, which in turn are similarly assembled at increasing length scales. Biological materials exhibit hierarchy at several to many length scales, depending on the complexity of the structure. For example, the diatom, a single celled marine organism that builds a hydrated, amorphous silica cage ($\text{SiO}_2 \cdot n\text{H}_2\text{O}$) around itself may, at first glance, involve two levels of hierarchy: the inorganic shell and the internal cell. However, at the microscopic scale, the cage structure can take on a surprising number of configurations. About 60,000 different diatoms have been identified, which marine scientists speculate is only about 10% of the total number. The silica cage is constructed of nanosized ribs,

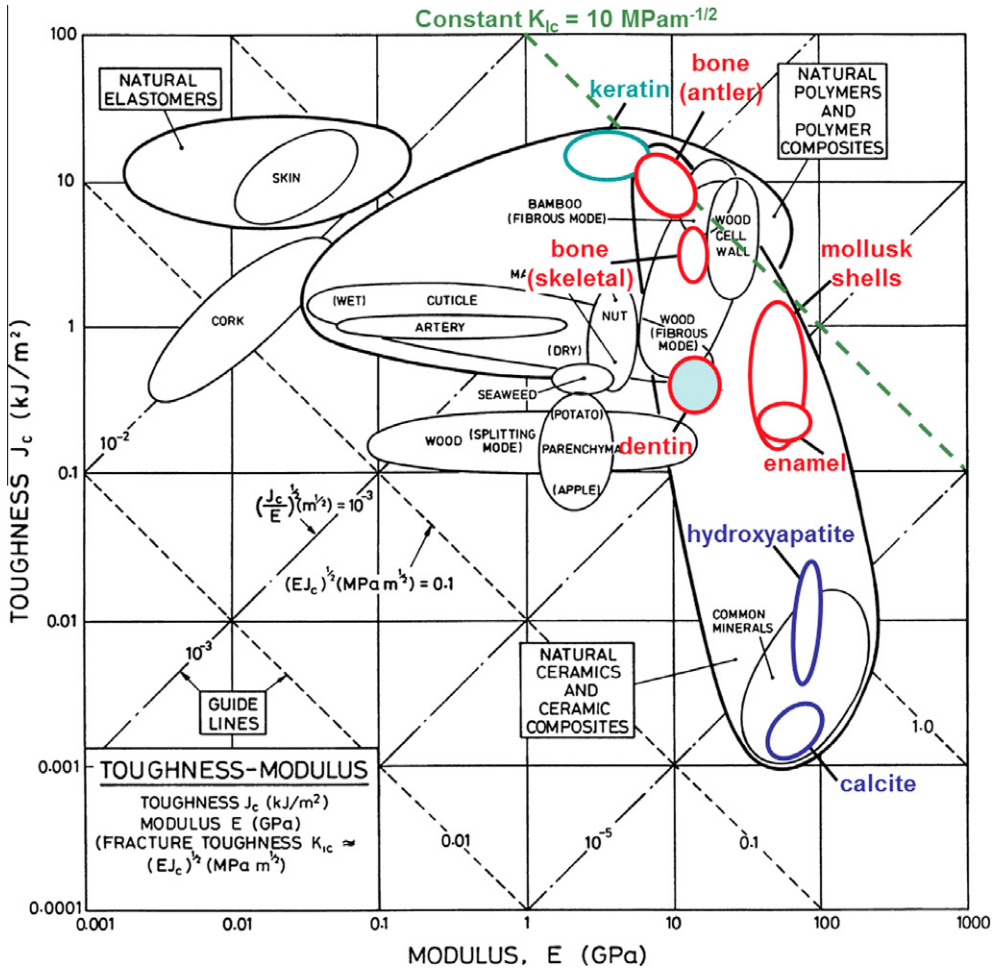


Fig. 19. Property map of biological materials, showing location of the biominerals (blue) and mineralized composites (red) along with keratin as a typical structural protein. Modified from [42].

which are composed of 50 nm diameter particles and the cell itself is a complex arrangement of sub-cellular elements. Further probing reveals ordered assemblies of proteins, lipids and polysaccharides that form the subcellular constituents and nanoporous regions in the $\text{SiO}_2 \cdot n\text{H}_2\text{O}$ cage [160]. Thus, one must indicate the smallest length scale that will be used to define the number of hierarchical levels. Materials scientists can routinely probe down to the molecular level, which is used in this article as the smallest scale. The lengths include nano-, nano/micro-, micro-, micro/meso-, meso-, meso/macro- and macro-scale.

Using bone as a biological composite example for a biological composite, the hierarchical structure is shown in Fig. 20, which is broken down into seven levels [161]. Level 1 is basic constituent: the tropocollagen molecules (300 nm in length, 1.5 nm in diameter) and non-stoichiometric hydroxyapatite platelets (tens of nm in length and width, 2–4 nm in thickness). Level 2 is the mineralized collagen fibrils, ~100 nm in diameter. The minerals are formed within and outside collagen fibrils, which are held together by non-collagenous proteins [162].

In level 3, the mineralized fibrils are aligned and form fibril array. Level 4 is various fibril array patterns. At this level, bone can be classified into two distinct forms: woven bone and lamellar bone.

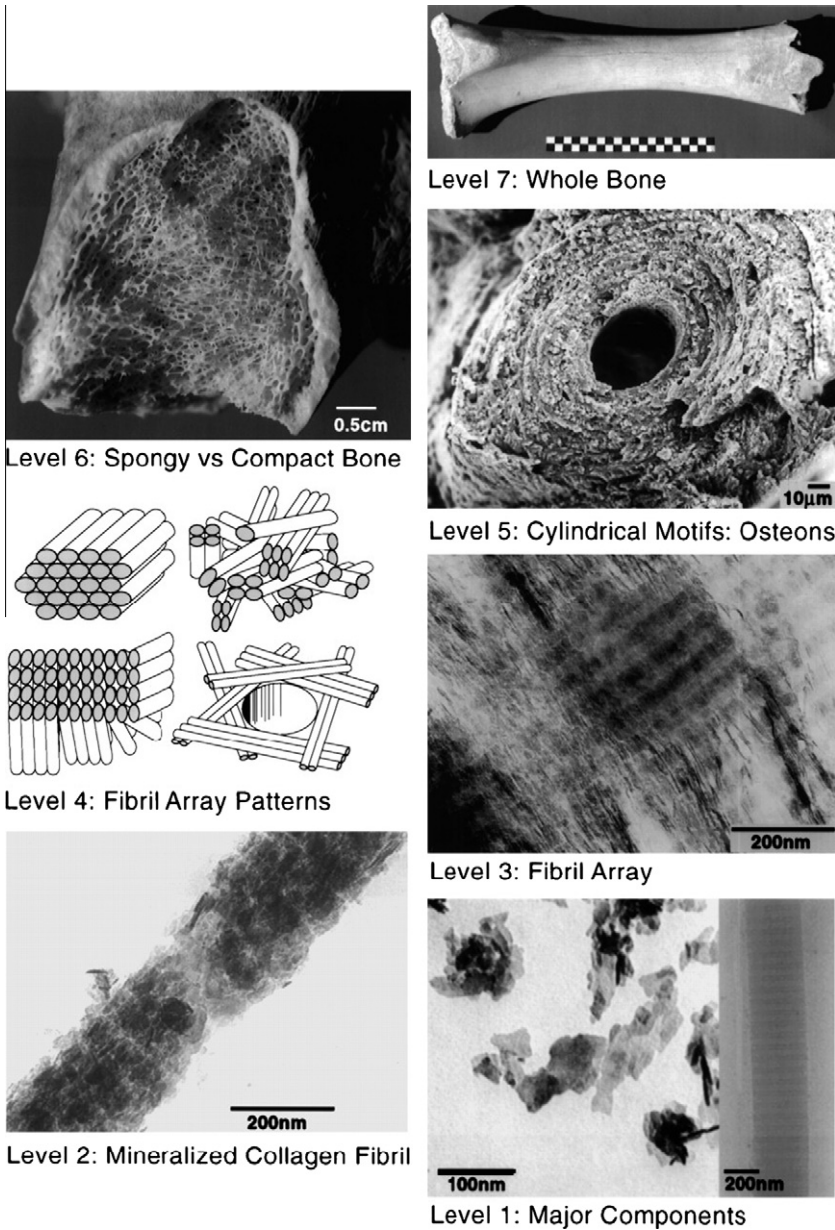


Fig. 20. Hierarchical structure of bone. Level 1: TEM micrographs of mineral crystallites and collagen fibrils. Level 2: Mineralized collagen fibrils. Level 3: Mineral fibril array. Level 4: Fibril array patterns. Level 5: Osteon consist of concentric lamellae. Level 6: Spongy and compact bone. Level 7: Whole bovine femur bone (scale bar: 10 cm). Taken from [161].

Woven bone is quickly formed (more than $4 \mu\text{m}$ per day), poorly organized bone where collagen fibrils and mineral crystals are loosely packed and randomly oriented. Lamellar bone is slowly formed (less than $1 \mu\text{m}$ per day), highly organized bone in which collagen fibrils and associated minerals align parallel to each other and assemble into lamellae $\sim 3\text{--}7 \mu\text{m}$ in thickness.

In level 5, several sequential layers of lamellae arranged in concentric rings around the vascular channels and form an osteon in compact (or cortical) bone. Osteons have a cylinder shape

200–250 μm in diameter aligning roughly parallel to the long axis of the bone. The flat lamellae can also form trabeculae 50–300 μm thick, which is the basic framework of cancellous (trabecular or spongy) bone. At the macro-structural level, external compact bone and internal cancellous bone (level 6) further form the whole bone (level 7).

The stiffness, strength and toughness of a structure depend on the level and number in the hierarchy, which is illustrated for bone. The simplest form of hierarchy is to consider self similarity in the different levels. This so-called Russian doll model, shown in an illustrative manner in Fig. 21a, was implemented by Ji and Gao [163]. The hierarchical levels (N) of bone are shown in Fig. 21b [163]. There is a high aspect ratio (Φ) of the mineral phase in bone that is aligned in a soft matrix. In Fig. 21c–e, the calculated stiffness, strength and toughness are shown as a function of N . The influence of N is quite strong – the stiffness decreases as the strength and toughness increases. This gain in strength and

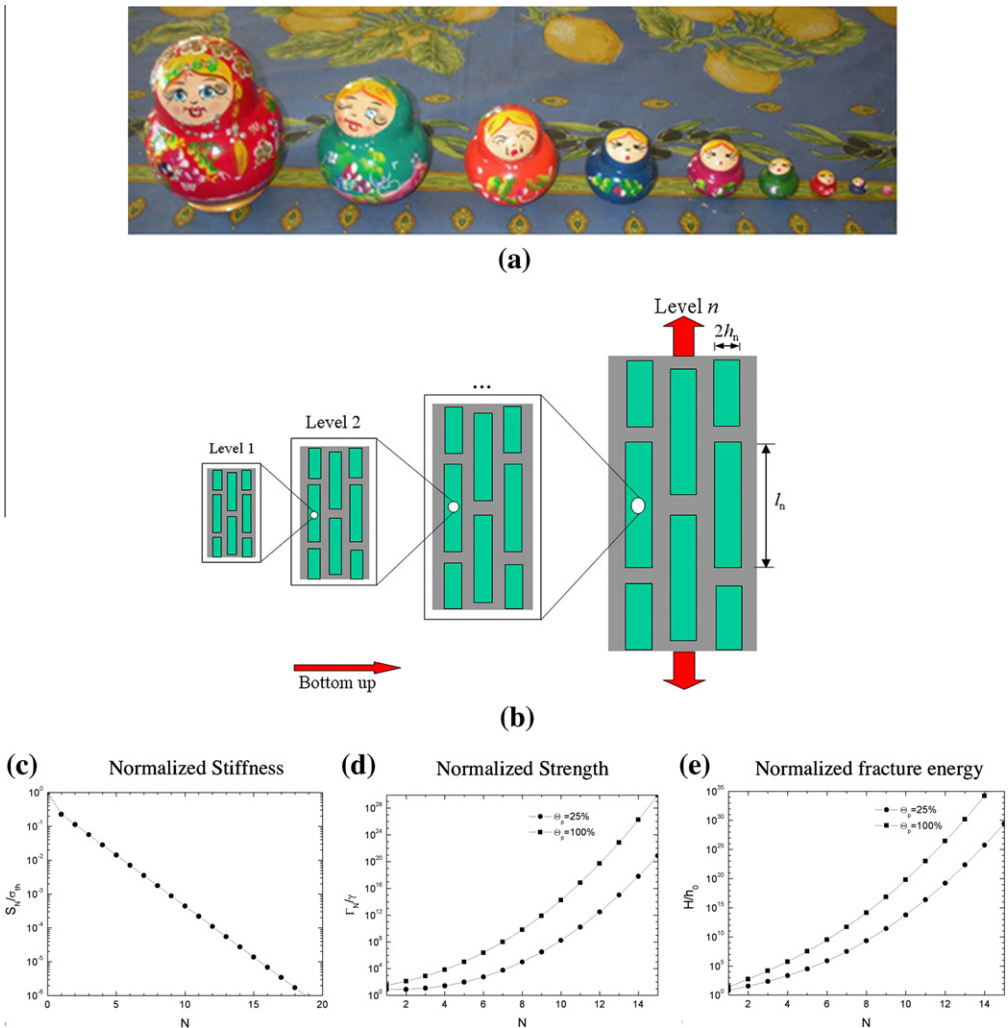


Fig. 21. Number of hierarchical levels (N) and resultant properties. (a) Russian doll analog for first approximation to hierarchical structure in which levels are identical but with different scales; (b) N levels of hierarchy in bone and resultant properties (taken from [163]); (c) normalized stiffness as a function of N , (d) normalized fracture strength as a function of N and (e) normalized fracture energy as a function of N . Taken from [164].

toughness can be attributed to an increase in the number of crack arresting mechanisms. The predicted values are based on the theory proposed by Ji and Gao [163].

Mechanical testing, if properly designed and implemented, can probe all levels (e.g. nanoindentation, microindentation, nano-tensile/compressive testing, bulk testing). Bechtle et al. [165] defined hierarchical levels for nacre, enamel, sponge spicule, dentin, conch shell, cortical and antler bone. They pointed out that there is a lack of correspondence between properties relating one level to another. This remains a major challenge to fully understand the complex behavior of biological composites and for the design of future bioinspired materials. One important issue is the interfacial strength, since it determines the linkage efficiency between different layers and hierarchical levels.

1.3. Cellular solids

A cellular solid is an interconnected network of struts or plates that form the faces of cells. Cellular solids are characterized by the shape and distribution of the cells and can be classified as open or closed cell forms. Open cell forms arise if only cell edges are present and the closed cell form develop if faces are present. Low density trabecular bone is an example of the open cell form, while cork is an example of the closed cell form. There are many examples of cellular structures in the natural world: bone, plant stems (e.g. wood), cuttlefish bones, corals, sponges, horseshoe crab exoskeletons, feathers, quills and the interior of bird beaks. Thus, a cellular solid can be composed of minerals (CaCO_3 , hydroxyapatite) or biopolymers (keratin, chitin). Many cellular solids are anisotropic, which develop from the main loading orientations. The cells tend to orientate to produce maximum mechanical efficiency. For example, for the trabecular bone in the femur head, the compressive strength is much higher in the direction of maximum load than in the transverse directions [166]. There are four levels of hierarchy of a simple cellular solid [4]:

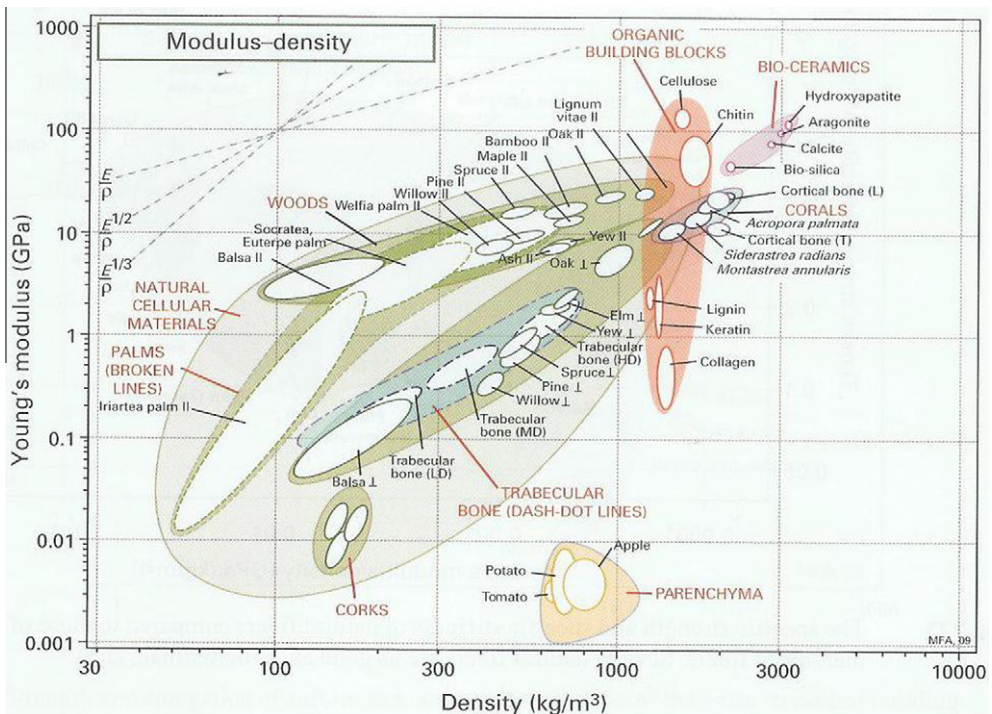


Fig. 22. Plot of the Young's modulus as a function of density for natural cellular materials. Taken from [4].

- The basic building blocks of the cell walls – the biominerals and/or biopolymers.
- The cell wall – often a composite, such as trabecular bone (collagen and hydroxyapatite).
- The morphology of the cell walls – spherical, edged (honeycomb).
- Natural structure – the cellular solid is typically embedded in a stronger, stiffer sheath (sandwich structures, filled tubes, etc.).

Fig. 22 shows a plot of the Young’s modulus as a function of density for a variety of natural cellular solids, demonstrating that there is a power law relationship between E and ρ . The most important property of a cellular solid is the relative density, ρ^*/ρ_s , where ρ^* is the measured density and ρ_s is the density of the solid making up the walls or struts. When the cell walls become thicker, the relative density increases. The transition between a cellular solid and a solid with isolated pores (porous solid) occurs at a relative density ~ 0.3 . Many of the materials properties (e.g. stiffness, strength, energy absorption) are directly related to the relative density, often with a power law dependence. Gibson and co-workers have written two excellent books on natural and synthetic cellular materials [4,167]. Fig. 23 illustrates the compression stress–strain curve for an isotropic open cell foam. The foam compresses elastically by bending of the cell walls. After the elastic limit is reached, a plateau region is sustained where non-linear plastic deformation (buckling) or cell wall fracture occurs as the load increases. Finally, when the cell walls have completely collapsed or fractured, additional stress simply densifies the remainder. In general, the relationship between the relative stiffness (E^*/E_s) and density for an open cell foam is given as [167]:

$$\left(\frac{E^*}{E_s}\right) \approx \left(\frac{\rho^*}{\rho_s}\right)^n \tag{1.1}$$

where the E^* refers to the measured property, E_s is the stiffness of the fully dense solid, and n is a power ranging from 1 and 3. For a closed cell foam, the relationship becomes [167]:

$$\left(\frac{E^*}{E_s}\right) = \phi^2 \left(\frac{\rho^*}{\rho_s}\right)^n + (1 - \phi) \frac{\rho^*}{\rho_s} + \frac{P_0(1 - 2\nu^*)}{E_s \left(1 - \frac{\rho^*}{\rho_s}\right)} \tag{1.2}$$

where ϕ = fraction of edges in the foam, ν^* = measured Poisson’s ratio and P_0 is the gas pressure in the cells.

Fig. 24 shows photographs of cancellous bone in three different states: untreated, demineralized and deproteinized [81]. The methods of demineralization and deproteinization are outlined in [82].

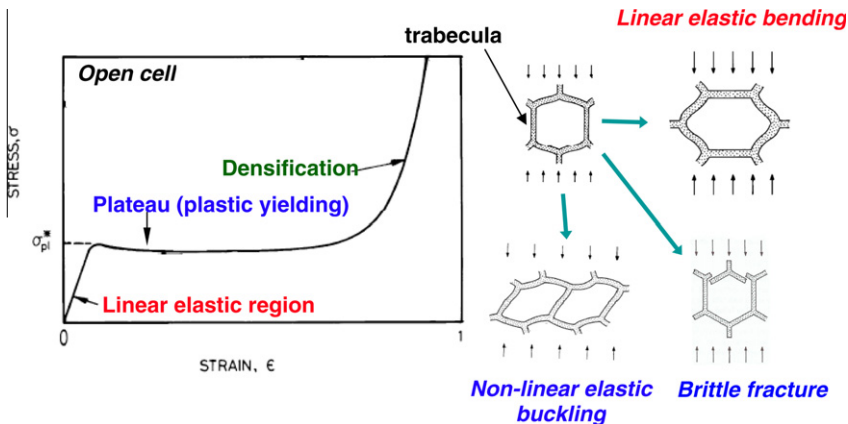


Fig. 23. Stress–strain curve and deformation modes for compression of an open cell structure. Initially, the cell walls bend elastically. Further loading produces non-linear elastic buckling and/or brittle fracture of the walls during the plateau region. After the cells have collapsed at the end of the plateau region, further loading produces densification. Adapted from [167,168].

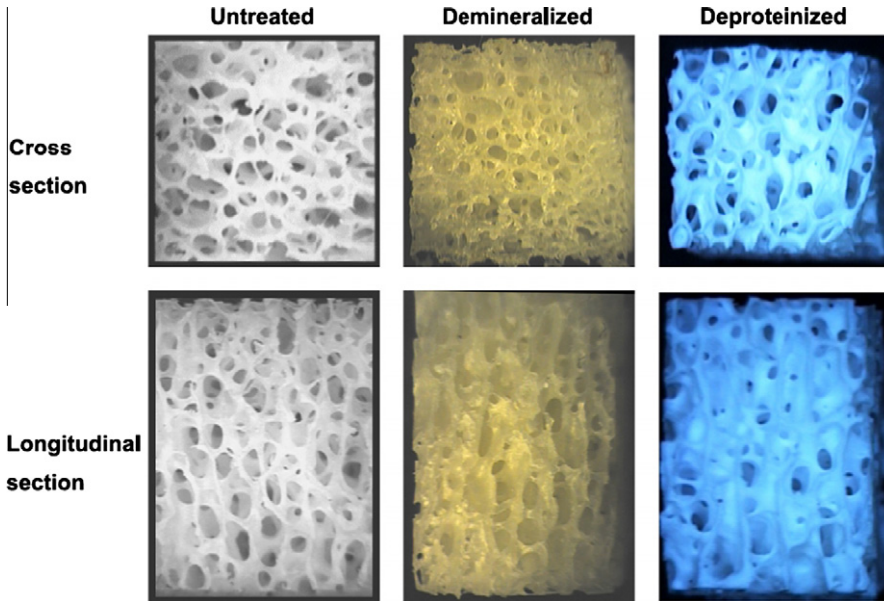


Fig. 24. Optical microscopy of untreated, demineralized and deproteinized bovine cancellous bone (femur head). Taken from [81].

In Fig. 25a, stress–strain curves are presented for untreated cancellous bovine femur and antler bone. The curves show a linear elastic region that arises to a peak stress (σ_p), then a bumpy plateau region (fracture of trabeculae) followed by densification. The antler bone is less mineralized, so σ_p is lower. Fig. 25b shows a plot of the relative elastic modulus as a function of relative density. A linear relationship is observed on the log–log plot. For the untreated bone, the slope is $n = 2$ (Eq. (1.1)). For demineralized bone, the samples are 100% biopolymers and n ranges from 1 to 2, indicating a less strong dependence on density. However, for the deproteinized case (100% mineral), the slope is higher: $n = 3$.

In the derivation of Eq. (1.1), the cell walls are considered isotropic. A higher value of n indicates there is more bending of the trabeculae corresponding to axial shortening. However, all the data fit onto a plot compiled by Gibson et al. [4] for human and bovine trabecular bone taken from various locations. The relative compressive strength (Fig. 25c) also follows a similar form to Eq. (1.1). The ratio of elastic modulus to compressive strength is approximately 100 (Fig. 25d), which is in agreement with compact bone specimens from various species previously reported by [169]. It is an interesting observation that this correlation also applies for untreated, demineralized, and deproteinized cancellous antler and bovine femur [81].

1.4. Sandwich structures

Sandwich panels are structural components consisting of a core of a low density material adhered to two denser face plates. Fig. 26a shows an example of a sandwich panel, indicating its dimensions (Fig. 26b). This configuration results in a lightweight, extremely stiff structure. The core material serves to increase the area moment of inertia, whereas the face plates carry the load. Examples abound in nature including the skull, porcupine quills, osteoderms, bird beaks and feathers. In most cases, the sandwich structures should have minimal compliance (deflection/unit load) and weight. Fig. 27 illustrates the various failure modes for a sandwich panel in three-point bending. If the applied stress exceeds the yield strength or buckling strength, the tensile face or compressive face will fail, providing there is a good bond between the face plates and the core. Given the high shear stresses across the core, it may fail in shear. Finally, debonding between the face plates and the core can occur.

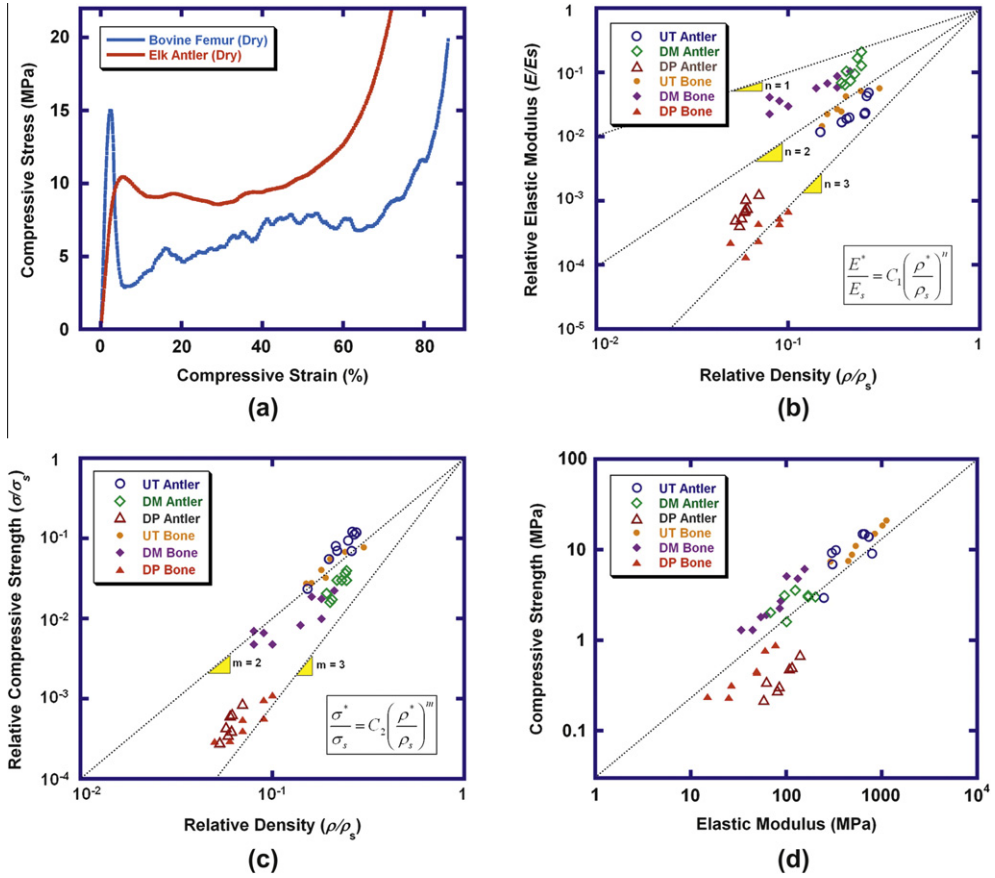


Fig. 25. (a) Stress strain curves for cancellous bovine femur and antler bone. (b) Relative elastic modulus (b) and compressive strength (c) as a function of relative density for untreated (UT), demineralized (DM) and deproteinized ((DP) bovine femur and antler bone. (d) Relationship between compressive strength and elastic modulus. $\rho_s = 1.72$ (antler), $\rho_s = 2.06$ (femur), $\rho_s = 1.35$ (DM), $\rho_s = 3.15$ (DP) g/cm³; $E_s = 7.6$ (antler), $E_s = 20$ (femur), $E_s = 1.5$ (DM), $E_s = 112$ (DP) GPa. Adapted from [81].

Gibson and Ashby [166] examined the mechanical properties of sandwich panels and give the bending compliance of a sandwich panel as:

$$\left(\frac{\delta}{P}\right) = \frac{2}{B_1 E_f b \left(\frac{t}{L}\right)^2} + \frac{1}{B_2 b \left(\frac{t}{L}\right) G_c^*} \tag{1.3}$$

where δ is the deflection of the panel under a load P , B_1 and B_2 are constants that depend on the loading geometry (Table 4), b the width of the panel, t the thickness of the face sheets, c the thickness of the core and G_c^* is the shear modulus of the core material. The first term of Eq. (1.3) is the compliance of the faces and the second term is the compliance of the core.

Considering the case of cancellous bone surrounded by cortical bone in three point bending: $\rho_f = 2 \times 10^3$ kg/m³ and $\rho_c^* = 0.4 \times 10^3$ kg/m³, $E_f = 20$ GPa, $G_c^* = 300$ MPa [170], $B_1 = 48$, and $B_2 = 4$. Eq. (1.3) can be rearranged as:

$$\left(\frac{t}{L}\right) = \frac{2}{B_1 E_f b \left(\frac{t}{L}\right) \left[\left(\frac{\delta}{P}\right) \left(\frac{t}{L}\right) b - \frac{1}{B_2 G_c^*} \right]} \tag{1.4}$$

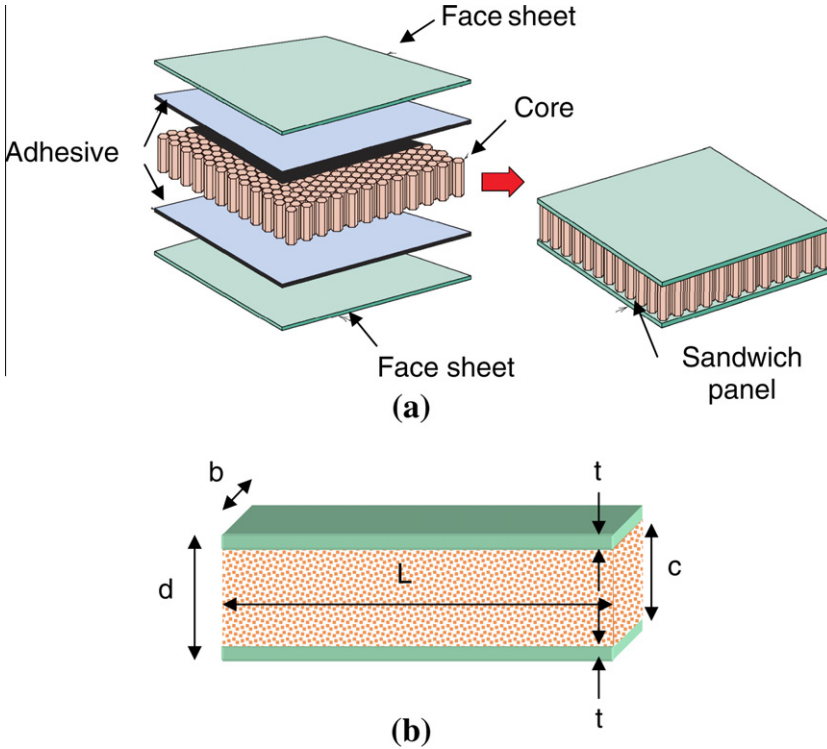


Fig. 26. (a) Synthetic sandwich composite structure consisting of a honeycomb structure inserted between dense face sheets. Adapted from [171] and (b) dimensions of sandwich panel.

The relationship between (t/L) and (c/L) is plotted in Fig. 28 for a constant compliance. As the core thickness increases, the face plate thickness first decreases sharply and then goes to zero for large values of (c/L) . There is an optimal value that minimizes both (t/L) and (c/L) , indicated on the plot. With the material properties given, this roughly corresponds to what is found in the cranial bone. The weight (W) constraint can be added to the plot as:

$$\left(\frac{t}{L}\right) = \frac{1}{2\rho_f} \left[\frac{W}{gbL^2} - \rho_c^* \left(\frac{c}{L}\right) \right] \tag{1.5}$$

This relationship will generate a straight line on the (t/L) vs. (c/L) plot with the minimal weight obtained from the optimal point.

In the case of foam-filled cylindrical tubes, which is the case for feathers, quills, and plant stems, failure is usually analyzed under compression and bending. The local buckling stress (σ_{cr}) under uniaxial compression is given as [172]:

$$\sigma_{cr} = \frac{Et}{a} \left(\frac{1}{12(1-\nu^2)} \frac{(a/t)}{(\lambda_{cr}/t)^2} + \frac{(\lambda_{cr}/t)^2}{(a/t)} + \frac{2}{(3-\nu_c)(1+\nu_c)} \frac{E_c}{E} \frac{\lambda_{cr}a}{t^2} \right) \tag{1.6}$$

where E is the stiffness of the cylindrical tube, t the thickness of the tube, a the radius of the tube, ν the Poisson's ratio of the tube, λ_{cr} the half buckled wavelength/ π , E_c the stiffness of the core and ν_c is the

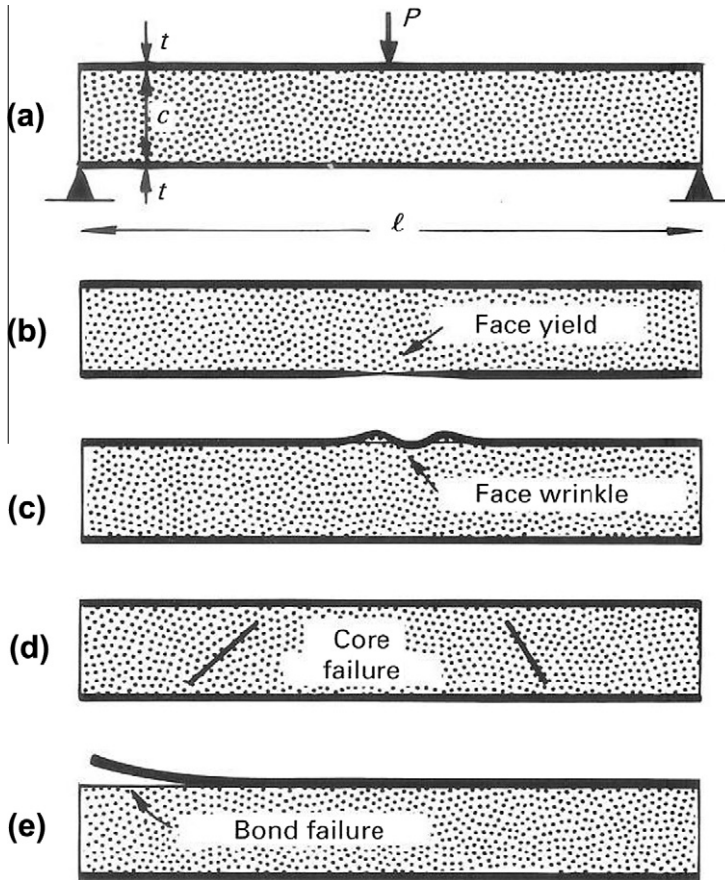


Fig. 27. Failure modes for sandwich structures: (a) three-point bend configuration, (b) face yield, (c) face wrinkle, (d) core failure and (e) bond failure. Taken from [4].

Table 4
 Constants for bending and failure of sandwich panels [168].

Mode of loading	B ₁	B ₂	B ₃	B ₄
Cantilever, end load (<i>P</i>)	3	1	1	1
Cantilever, uniformly distributed load (<i>P/l</i>)	8	2	2	1
Three point Bend, central load (<i>P</i>)	48	4	4	2
Three point Bend, uniformly distributed load (<i>P/l</i>)	384/5	8	8	2
Ends built in, central load (<i>P</i>)	192	4	8	2
Ends built in, uniformly distributed load (<i>P/l</i>)	384	8	12	2

Poisson's ratio of the core. The solution for λ_{cr}/t is given in Fig. 29. In the case of feathers and quills, the foam serves as an elastic foundation for the sheath (tube):

$$\frac{\lambda_{cr}}{t} \approx 0.69 \left(\frac{E}{E_c} \right)^{1/3} \tag{1.7}$$

Section 3.9.2 describes tubular sandwich structures (quills) in more detail.

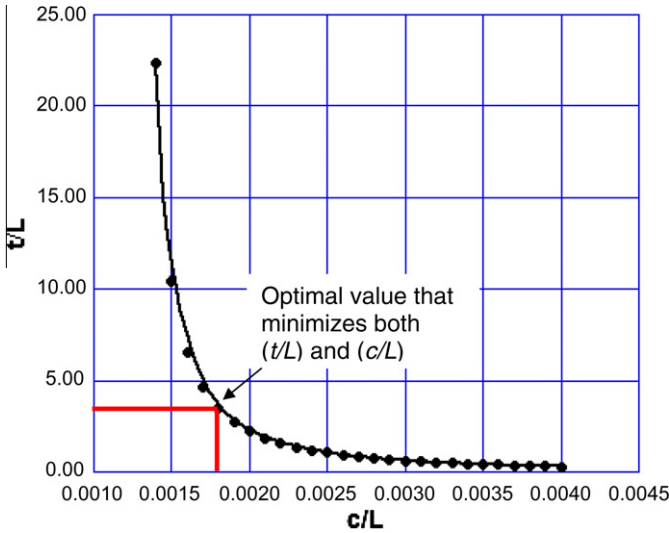


Fig. 28. Plot normalized face plate (cortical) thickness as a function of the core (cancellous) thickness for a sandwich panel construction (Eq. (1.4)). A constant stiffness $(P/\delta) = 7.5 \times 10^4 \text{ N/m}$ was used, estimated from the data in [173], $L = 1 \text{ m}$, $b = 50 \text{ mm}$.

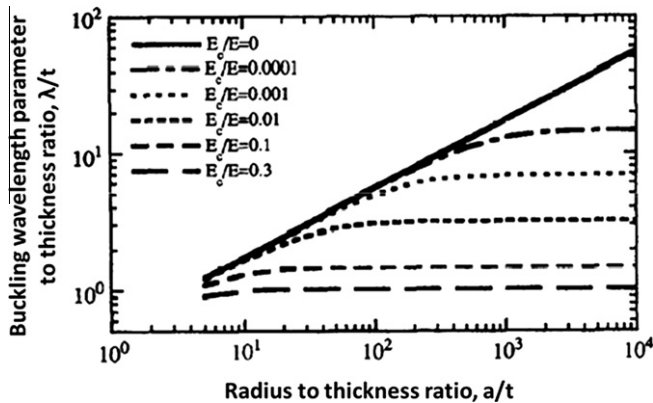


Fig. 29. Buckling wavelength parameter (Eq. (1.8)) as a function of the radius to thickness ratio of a foam filled cylinder. E = stiffness of the cylinder, E_c = stiffness of the foam. Taken from [172].

1.5. Mechanical properties

Fig. 30 shows different stress–strain (σ – ε) curves that can be applied to biological systems. The mineral constituents in biological composites (e.g. hydroxyapatite and calcium carbonate) have linear stress–strain curves with the slope defined as the stiffness or Young’s modulus, $E = \Delta\sigma/\Delta\varepsilon$ (Fig. 30a). The material fails at the fracture strength, σ_f . The resilience is given as the area under the stress–strain curve and represents the amount of elastic energy that can be stored in the material. Another linear elastic solid, such as a biological composite (e.g. bone) has an initial linear region – at the yield strength, σ_y , the curve deviates from linearity as the material starts to undergo permanent deformation. This permanent deformation involves damage by microcracking, fiber pull-out, organic/inorganic

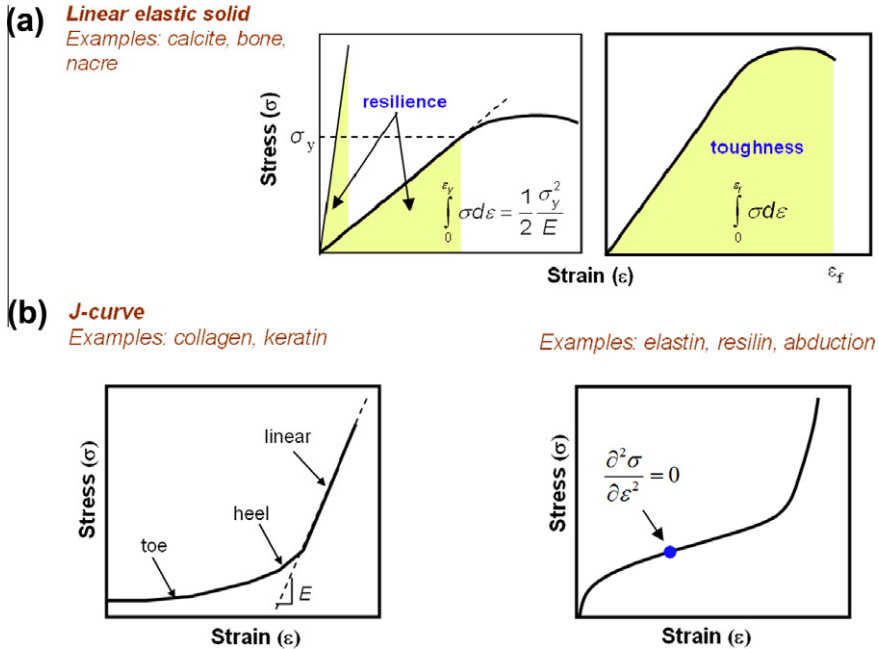


Fig. 30. Stress–strain curves for various materials. (a) Linear elastic solid. The stress–strain relationship on the left is typical for a biomineral (e.g. calcite) that is linear (slope = stiffness or Young’s modulus) until the fracture stress. The area under the curve is the resilience, which is the amount of elastic energy that can be stored in the material. The curve on the right shows significant plastic (permanent) deformation where the stress–strain curve deviates from linearity at the yield stress (σ_y). For example, in bone, plastic deformation is accompanied by such damage modes as microcracks, fiber pullout, and mineral/collagen debonding. The resilience is amount of elastic energy that can be stored in the material (area under the stress–strain curve up to σ_y) and toughness is given as the total area under the stress–strain curve (b) most biopolymers have a *J-curve* (left). The *J-curve* is found in the stiffer fibrous proteins such as collagen and keratin. In these materials, at small strains, a configurational change of the molecules occurs until they have straightened in the loading direction. After they are fully aligned, the molecules begin to slide past each other, which requires much more force. Rubber-like elastic polymers have been modeled as hyperelastic solids [174–178]. They may exhibit an inflection point: $d^2\sigma/d\varepsilon^2 = 0$. Some biopolymers such as elastin, resilin and abductin, have similar responses. (c) Pronounced viscoelastic behavior and an inflection point ($d^2\sigma/d\varepsilon^2 = 0$) are present in biological polymers undergoing phase transition induced elasticity, such as whelk eggs, spider silk, wool, and hagfish thread. Viscoelastic materials show a lag between the applied stress and displacement, which can be modeled with springs and dashpots. The elastic modulus storage and loss components that correspond to the stored elastic energy and the energy lost (heat). The stress–strain curve for a fully recoverable material shows that the loading and unloading curves do not follow the same path (hysteresis) – the energy lost is represented by the area inside of the hysteresis loop.

debonding. The toughness is given as the total area under the stress–strain curve up to the fracture stress.

Biopolymers (e.g. collagen and keratin) typically exhibit a ‘*J-curve*’ (Fig. 30b). It is characterized by a gradual increase in the slope $d\sigma/d\varepsilon$ with increasing strain, ε ($d^2\sigma/d\varepsilon^2 > 0$). At low stress levels, the material can extend by molecular rearrangement through uncoiling or straightening. This portion of the stress–strain curve is commonly referred to as the ‘toe’ region. As the stress increases to the point where there is an upswing (following the ‘heel’ region), the material supports increasing loads and it takes more stress to extend the material. The deformation in the ‘toe’ and ‘heel’ regions is entirely through reconfiguration of the molecules – no bonds are broken. Most physiological stresses occur in the low stress region where the compliance is high. In the high stress portion of the curve, two processes occur, either separately or concurrently: (a) the molecules stretch elastically and reversibly or they (b) slide past each other, breaking crosslinking bonds and overcoming van der Waals bonds. In the latter case, the deformation is irreversible. The tracking of bond length

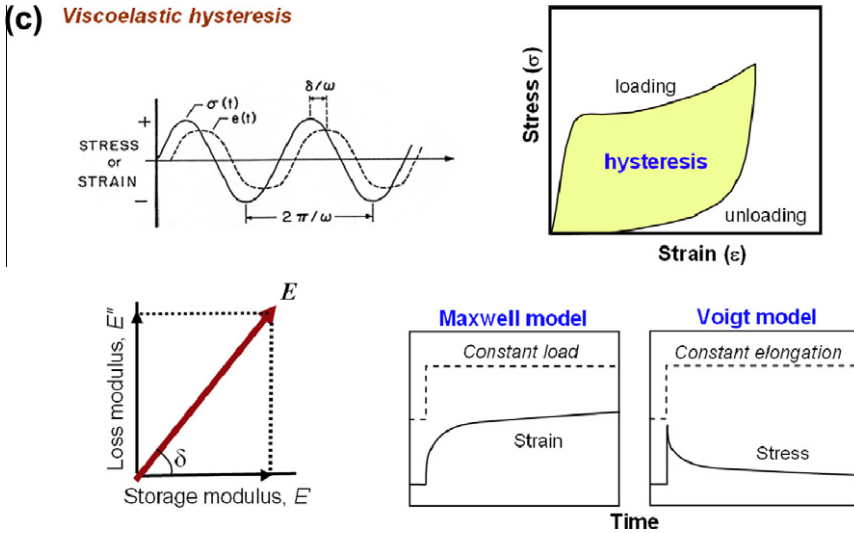


Fig. 30 (continued)

change with strain (or stretch ratio, $\lambda = \varepsilon + 1$) has been determined by synchrotron small angle X-ray scattering (SAXS) by Liao et al. [179] for bovine pericardium (collagen) and by Fratzl et al. [180] for rat tail collagen.

Loading and unloading follow the same curve if the material is elastically reversible. This property is important in aortal walls and in the lungs, for example, where energy loss (heat) is undesirable. Fig. 31 shows the *J-curve* for a rat tendon (collagen). The toe region corresponds to uncrimping of the collagen molecules, the heel region is where unfolding of the molecules occurs until finally, in the linear portion, the molecules have aligned and begin to slide past each other [180]. The stress required to extend the material in the linear part is high, meaning that fracture or damage would not be typically incurred under normal physiological displacements. Another important attribute is the concavity of the curve. Comparing with an equivalent Hookean solid, the energy released upon unloading is much less, thereby decreasing the amount of energy that is transferred to a damage zone, for example, which would impel crack propagation.

Another example of a biopolymer is an inflected curve (having a strain at which $d^2\sigma/d\varepsilon^2 = 0$). This stress–strain curve is shown in Fig. 30b. In biological polymers, elastin, resilin, abductin are akin to rubber. The inflected curve is characteristic of biopolymers undergoing phase transitions and has been observed for egg whelk [181], spider dragline [6], Merino wool [182,183], and hagfish thread [184]. The decrease in slope during the phase transition is caused by an intermediate disorder phase before nucleation of the second, stiffer phase. These transformations are characterized by the formation of a plateau in the tensile stress–strain curve, as shown in Fig. 30b, and by considerable hysteresis on unloading. The decrease in slope during the phase transition is caused by the increased length of the product phase. This is analogous to the shape memory effect in metals (in particular, the stress strain response of shape memory alloy, NiTiNol). Upon unloading, the reverse transformation may occur, in which case the overall strain is zero.

The initial portion of the curve where the slope (stiffness) decreases with extension has been modeled by considering entropic terms for rubber [174,185]. The basic assumptions are that the extension is solely due to configurational changes of the randomly oriented chains (no chemical bond stretching, no change in enthalpy) and that there is a Gaussian distribution of the randomly oriented protein chains. As opposed to *J-curve* materials, elastomers with $d^2\sigma/d\varepsilon^2 < 0$ are prone to tensile instabilities – a process that can induce a bubble (e.g. aneurysm in a vein or artery). The instability can be obtained from Considère as: $d\sigma/d\varepsilon = \sigma_i$.

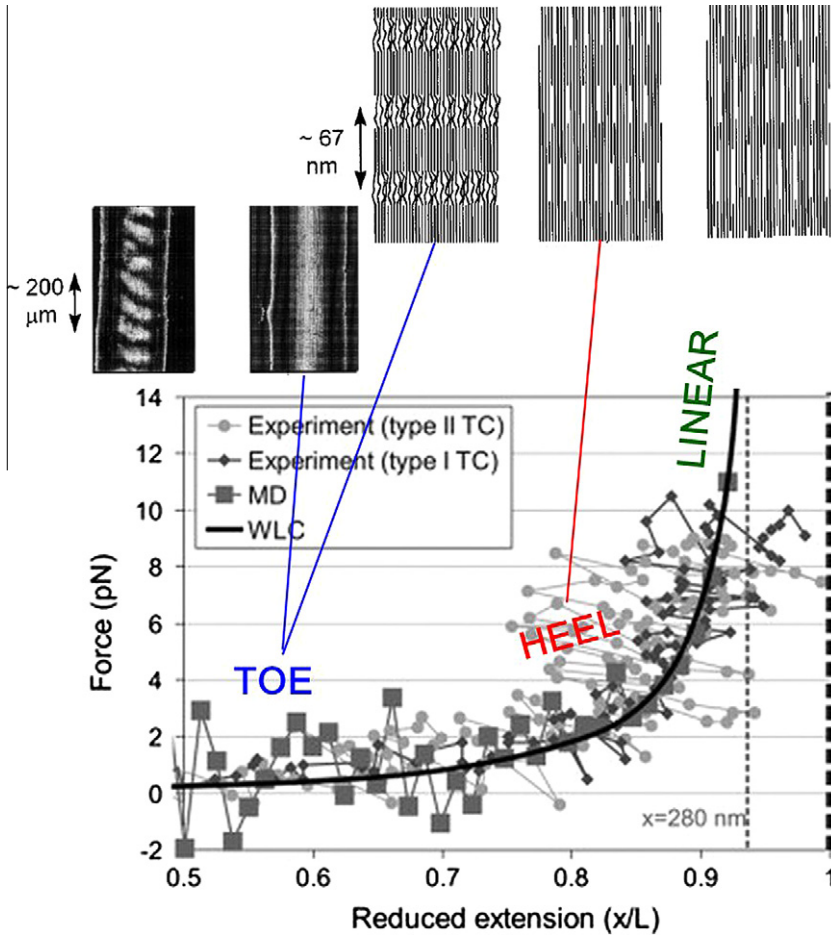


Fig. 31. Solid line: Molecular dynamics predicted stress–strain curve for collagen (rat tendon) showing J-curve behavior. The low stress region (toe) the tendon can be extended with a small stress by uncrimping the collagen molecule. The heel region corresponds to straightening out kinks and the linear region represents sliding of the molecules past each other. Taken from [180]. The points represent experimental data. Adapted from [30,32,180].

The configurational entropy is expressed by the Boltzmann equation: $S = k \ln \Omega$ (S = entropy, k = Boltzmann’s constant, Ω = number of ways to arrange a chain) and defining the force, $F = (d\Delta G/dx)$ where ΔG is the change in the Gibbs free energy and x is the displacement. Considering a cubic solid (ϵ_0^3) that is stretched uniaxially in tension maintaining a square cross-section, the true stress can be derived as [174]:

$$\sigma = nkt \left(\lambda - \frac{1}{\lambda^2} \right) \tag{1.8}$$

where n is the number of chain segments and $\lambda = l_1/l_0$ is the stretch ratio in the loading direction ($\epsilon = \lambda - 1$). This is known as the Treloar equation also assumes an isotropic material with no change in pressure, volume or temperature [174]. This expression has been shown to fairly well predict the stress–strain behavior of rubbers for $\lambda < \sim 4$ ($\epsilon < \sim 3$) [174]. At higher stretch ratios, the experimental stress rises faster than the theoretical predictions due to a much larger material stiffness (Fig. 32). At large extensions, some of the starting assumptions are no longer valid, due to the chains becoming

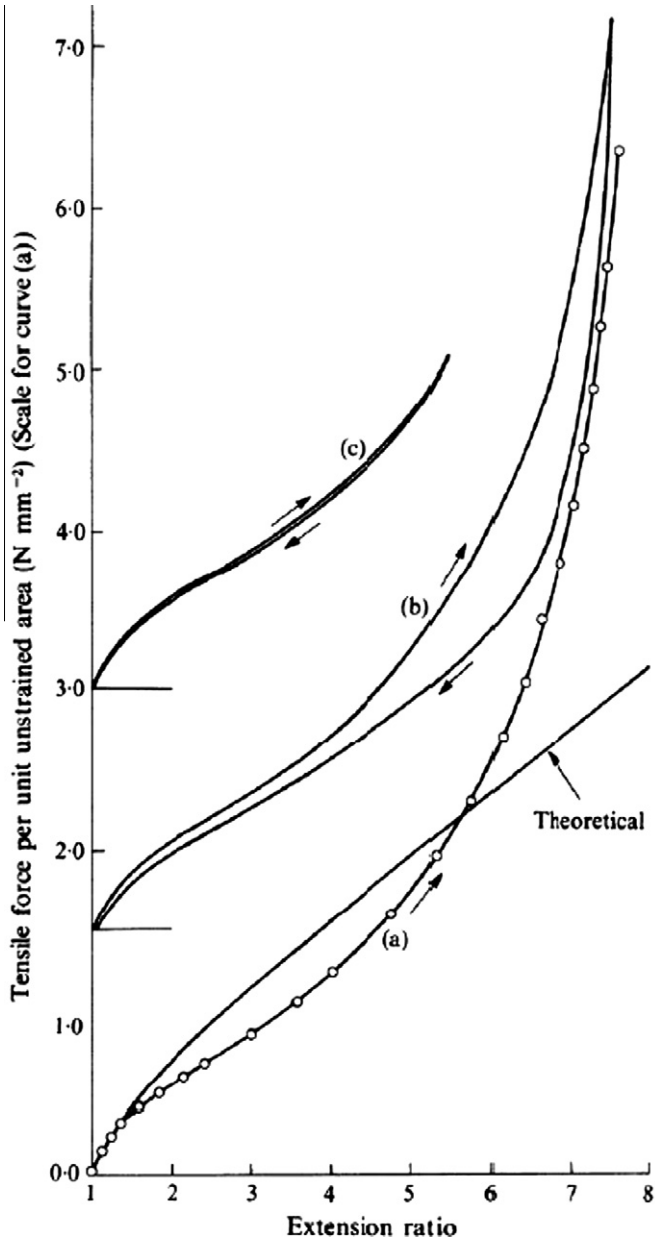


Fig. 32. Stress as a function of extension ratio for simple extension. For rubber, up to $\lambda \sim 5.5$ the curve is reversible (curve *c*). At larger elongations, hysteresis occurs (curve *b*). Curve *a* represents a sample that broke in tension and is compared to a theoretical prediction (Treloar equation – Eq. (1.8) with $nkT = 0.39$ MPa). Taken from [174].

aligned. Additionally, the stretching induces intermolecular bond deformation. Mooney arrived at an expression assuming an isotropic, constant volume solid using a strain energy function [175] (which was later modified by Rivlin and Saunders [176]) to give the Mooney–Rivlin equation for the true stress:

$$\sigma = \left(2C_1 + \frac{2C_2}{\lambda}\right) \left(\lambda^2 - \frac{1}{\lambda}\right) \tag{1.9}$$

where C_1 and C_2 are materials constants. The model is valid for strains up to ~ 2 (e.g. auto tires, where C_1 and $C_2 \sim 0.2$ MPa). A measurement of the looseness of the network is given by $2C_1/C_2$.

A phenomenological model that is widely used is the Ogden equation, developed initially for elastomeric materials such as rubber. It is based on the following one-term strain-energy density per unit volume:

$$\Phi = \frac{2\mu}{\alpha^2} (\lambda_1^\alpha + \lambda_2^\alpha + \lambda_3^\alpha - 3) \tag{1.10}$$

where $\lambda_1, \lambda_2,$ and λ_3 are the principal stretch ratios, α is a strain-hardening exponent, and μ can be interpreted as a shear modulus. The physical interpretation of this equation is simple: the deformation energy is a power function of the stretch ratios. The change in strain energy under a uniaxial stress ($\sigma_1 \neq 0$ and $\sigma_2 = \sigma_3 = 0$) is density is defined as:

$$d\Phi = \sigma_1 d\lambda_1 \text{ or } \sigma_1 = \frac{d\Phi}{d\lambda_1} \tag{1.11}$$

Assuming a constant volume (a reasonable approximation for biological materials at ambient pressure), the deformed volume V_1 is equal to the initial volume V_0 . Letting $V_0 = V_1 = 1$, we have:

$$V_0 = V_1 = (1 + \varepsilon_1)(1 + \varepsilon_2)(1 + \varepsilon_3) = \lambda_1 \lambda_2 \lambda_3 = 1 \tag{1.12}$$

Thus, strain energy density, for uniaxial compression or extension with k being the ratio between the two stretch ratios orthogonal to the longitudinal one ($\lambda_2/\lambda_3 = k$):

$$\Phi = \frac{2\mu}{\alpha^2} \left(\lambda_1^\alpha + k^{\alpha/2} \lambda_1^{-\alpha/2} + k^{-\alpha/2} \lambda_1^{-\alpha/2} - 3\right) \tag{1.13}$$

$$\sigma = \frac{2\mu}{\alpha} \left(\lambda_1^{\alpha-1} - \frac{1}{2}(k^{\alpha/2} + k^{-\alpha/2})\lambda_1^{-1-\frac{\alpha}{2}}\right) \tag{1.14}$$

For the case of isotropy, we assume that $k = 1$ and have, for uniaxial tension or compression:

$$\sigma = 2\mu \left(\lambda_1^{\alpha-1} - \lambda_1^{-1-\frac{\alpha}{2}}\right) \tag{1.15}$$

when $\alpha = 2$, the equation reduces to the form of the Treloar equation (Eq. (1.8)). The Ogden equation provides a good representation of the J curve behavior. [177]: This model fits well to any incompressible rubbery solid for strains up to ~ 7 . Another model is the Arruda–Boyce model [178], which has been shown to work well with silicone and neoprene for strains up to ~ 3 . All the above models were developed for synthetic elastomers and later used in biological materials. Fig. 33 plots the theoretical curves for the Treloar, Mooney–Rivlin, Ogden and Arrunda–Boyce models.

Although these constitutive equations have not often been applied often to biopolymers, they have applications. The best known equation is by Fung [186] who applied it successfully to blood vessels and other soft biological tissues. This is the first model developed specifically for biological materials and predicts the classic J -curve response. The increase in slope is due to the extension of the collagen and elastin fibers. If they are stretched beyond a critical strain (or stretch ratio), failure takes place. It is instructive to plot the slope, $d\sigma/d\varepsilon = E$, as a function of stress. This is done in Fig. 34 for the aorta of a dog (circumferential strip). The slope first increases by a relationship that can be described by a power function. Then, it reaches a linear range, in which the increase is more gradual. This non-linear elastic behavior is a characteristic feature of many soft tissues in the human body. The Fung equation [186] has the form:

$$\sigma = (\sigma^* + \beta)e^{\alpha(\varepsilon - \varepsilon^*)} - \beta \tag{1.16}$$

where $\sigma^*, \varepsilon^*, \alpha, \beta$ are material parameters The parameters α and β are defined in Fig. 34. α is the slope of the linear portion and β is related to the intercept. σ^* and ε^* correspond to the onset of the linear

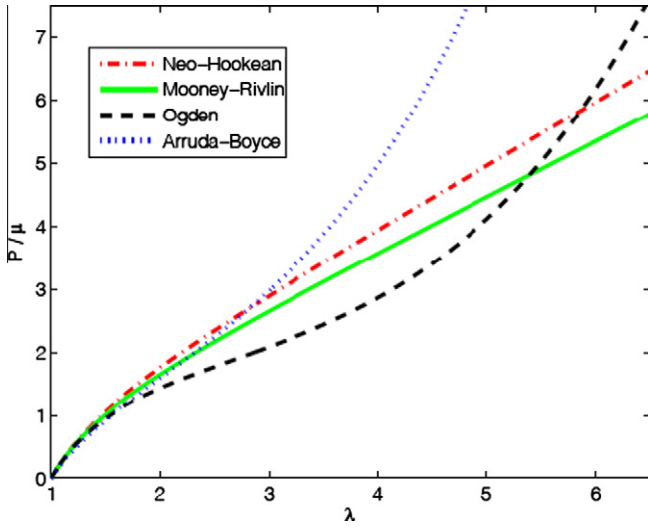


Fig. 33. Plot of the theoretical curves for different models of rubber elasticity: neo-Hookean (Treloar, (Eq. (1.8)), Mooney-Rivlin (Eq. (1.9)), Ogden (Eq. (1.15)) and Arruda-Boyce. Taken from [187].

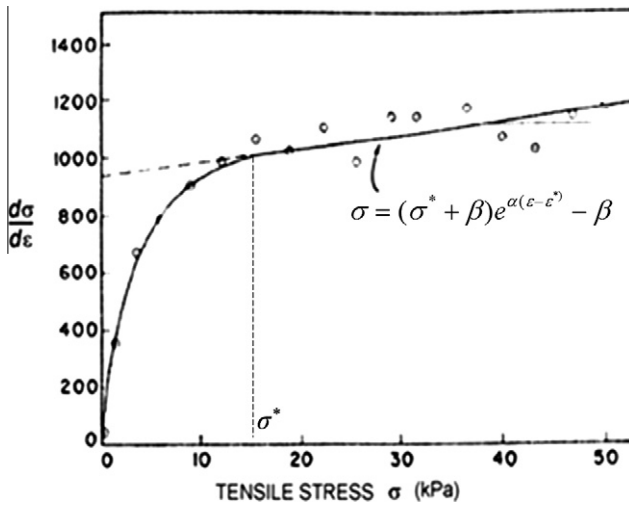


Fig. 34. Representation of mechanical response of a dog aorta (circumferential strip) in terms of tangent modulus (slope of stress-strain curve) vs. tensile stress; slope and intercept provide parameters for Fung equation. Adapted from ([19] p. 329).

portion. The Fung equation represents the linear portion of the plot shown in Fig. 34 (stresses and strains beyond σ^* and ϵ^* , respectively).

The non-linear elasticity of protein-based fibers, cells and gels has recently been studied using statistical mechanics or the Worm-like chain (WLC) model in combination with finite element analysis and other simulation techniques, which provide more realistic mechanical response of these non-linear elastic constituents [188–191].

Biological materials often undergo time-dependent, repeated loading. A viscoelastic solid will undergo creep (time dependent deformation under a constant load) or stress relaxation (time dependent

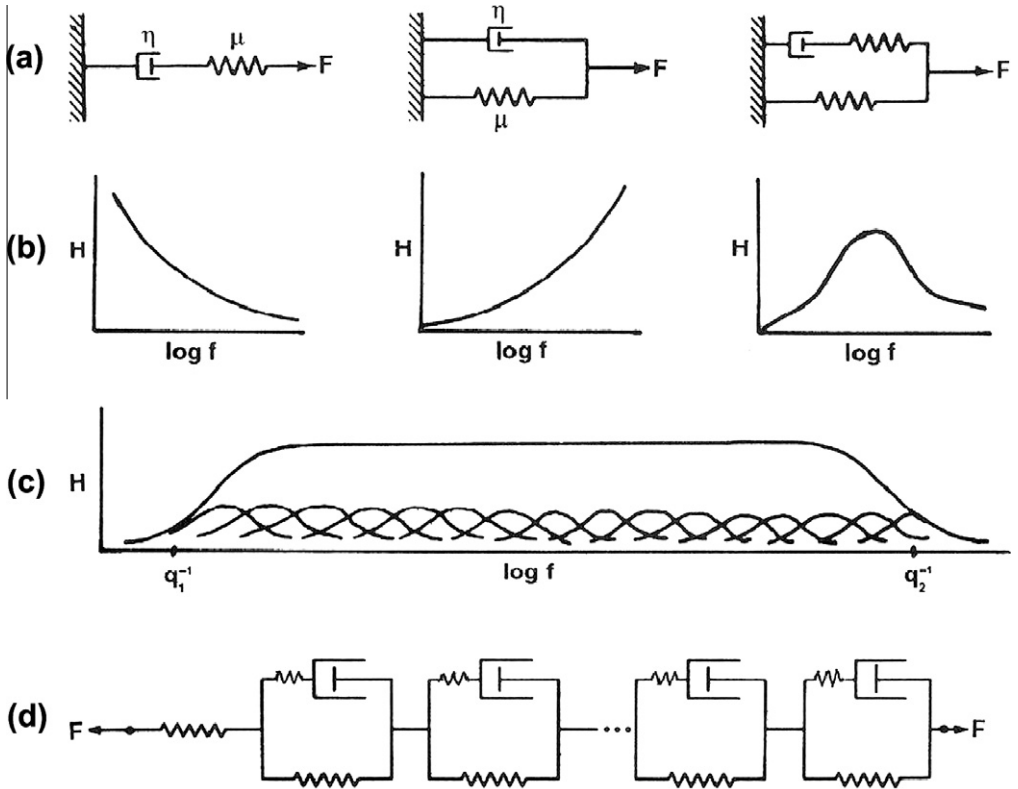


Fig. 35. Viscoelastic models: (a) spring (μ) and dashpot (η) Maxwell, Voigt and Kelvin models, (b) the hysteresis (H) as a function of the log frequency (f) for each model, (c) most biopolymers show this behavior, with the spring and dashpot model shown in (d). The hysteresis is a constant over a wide range of frequencies. Taken from [19].

stress reduction under a constant displacement), as illustrated in Figs. 34 and 35c. When a load is held fixed, the material will start to creep ($d\epsilon/dt \neq 0$, $d\sigma/dt = 0$) as molecules reconfigure to lower energy states. If instead, a material is at a fixed displacement ($d\epsilon/dt = 0$, $d\sigma/dt \neq 0$), the applied load relaxes over time. The viscoelastic material has components of an elastic solid (spring model) and a viscous solid (dashpot model) with a lag between the applied strain and stress (or applied stress and strain), as shown in Fig. 35c. The strain is fully recoverable, unless the material has undergone material damage. This results in a storage modulus, E' , that represents the stored elastic energy and a loss modulus (E'') that represents the energy that is dissipated. Tendons, which have aligned collagen fibrils, have very low hysteresis, which makes them very efficient in storing and releasing energy. The area in the hysteresis loop is the amount of energy (heat) that is dissipated during one cycle. Fig. 35a illustrates various viscoelastic models: Maxwell (spring and dashpot in series), Voigt (spring and dashpot in parallel) and Kelvin (spring and dashpot in parallel with a spring). The hysteresis is plotted as a function of the logarithm of the frequency, showing that the amount of hysteresis is a strong function of the frequency (Fig. 35b). However, most viscoelastic biopolymers show a response that shows a constant hysteresis over a wide range of frequencies (Fig. 35c). This can be modeled by a series of Kelvin units that have variable spring and dashpot parameters (Fig. 35d).

Fracture resistance is of primary importance to a biological material. Crack branching and deflection from the preferred propagation direction are two intrinsic mechanisms to increase the fracture energy. A hierarchically structured material has an optimal configuration in providing barriers to crack propagation. One prominent process is the Cook–Gordon mechanism of crack blunting [192]. Fig. 36

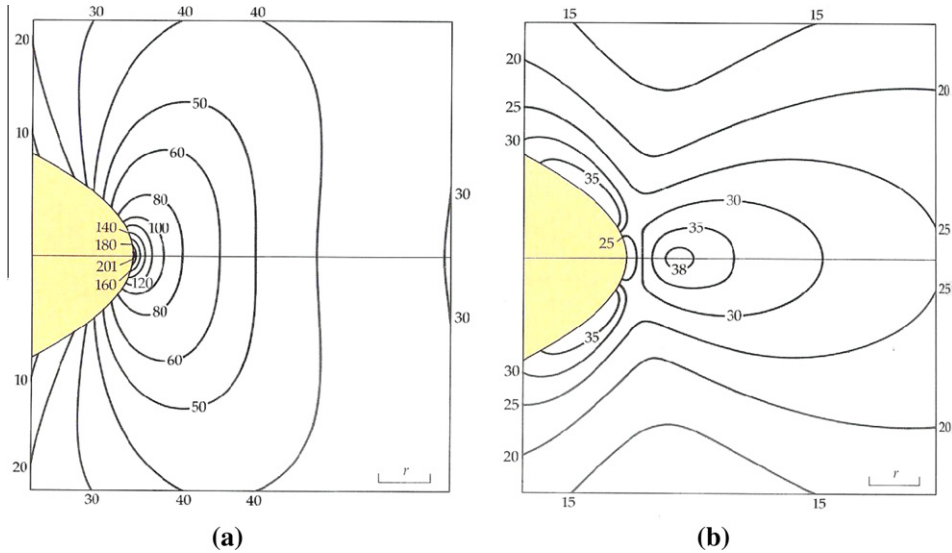


Fig. 36. Stress contours around an elliptically shaped crack for a material placed in tension: (a) in the plane of the crack – the maximum stress σ_{11} is at the crack tip and (b) perpendicular to the crack – the maximum stress σ_{22} is slightly ahead of the crack tip. Taken from [193].

illustrates this with stress contour diagrams for an elliptically shaped edge crack in a material that is under a tensile load. In Fig. 36a, the stress contours show a maximum at the crack tip, which will drive the crack further into the material. In Fig. 36b, the stress contours for the plane perpendicular to the crack show a maximum tensile stress σ_{22} just ahead of the crack. The stress can operate to open a weak interface in this region and thus provide a surface that will blunt crack. This is a well-known mechanism of toughening composites.

Fig. 37 demonstrates this, for a tensile force applied to a semi-elliptically shaped edge crack, crack tip stress is given by the Inglis equation, $\sigma_{11} = \sigma_a(1 + 2\sqrt{a/\rho})$, where σ_a is the applied stress, a = length of the crack and ρ = crack tip radius. This equation predicts a very large stress at the crack tip, which diminishes to σ_a far from the crack tip. However, the stress (σ_{22}) in the plane perpendicular to σ_{11} has a maximum slightly ahead of the crack tip. This stress may be large enough to separate an interface and thus to form a secondary crack (perpendicular to the main crack) if its interfacial strength is low. Then, as the crack propagates and impinges on the weak interface, it becomes blunted, which then requires a higher stress in order to propagate. Indeed, synthetic composites are designed in such a manner that the interfaces have tailored strength to enable the Cook–Gordon mechanism to operate.

Another consideration for biomineralized materials is the aspect ratio of the mineral. The inorganic constituents in bone and nacre are in the shape of long, thin plates. For nacre the length:thickness ratio is ~ 20 and for bone is ~ 10 . Gao et al. [194] pointed out that the elastic modulus, E_c , of a composite with a volume fraction α of the mineral phase has a functional dependence on the aspect ratio (Φ) of:

$$\frac{1}{E_c} = \frac{4(1 - \alpha)}{G_p \alpha^2 \Phi^2} + \frac{1}{\alpha E_m} \quad (1.17)$$

where G_p is shear modulus of the protein phase, E_m is the elastic modulus of the mineral phase, α is the volume fraction and Φ is the aspect ratio of the mineral. This equation shows that increasing the aspect ratio of the mineral significantly increases the elastic modulus of the composite. This could be an underlying reason why biological composites do not contain spherically shaped crystalline inorganic reinforcement.

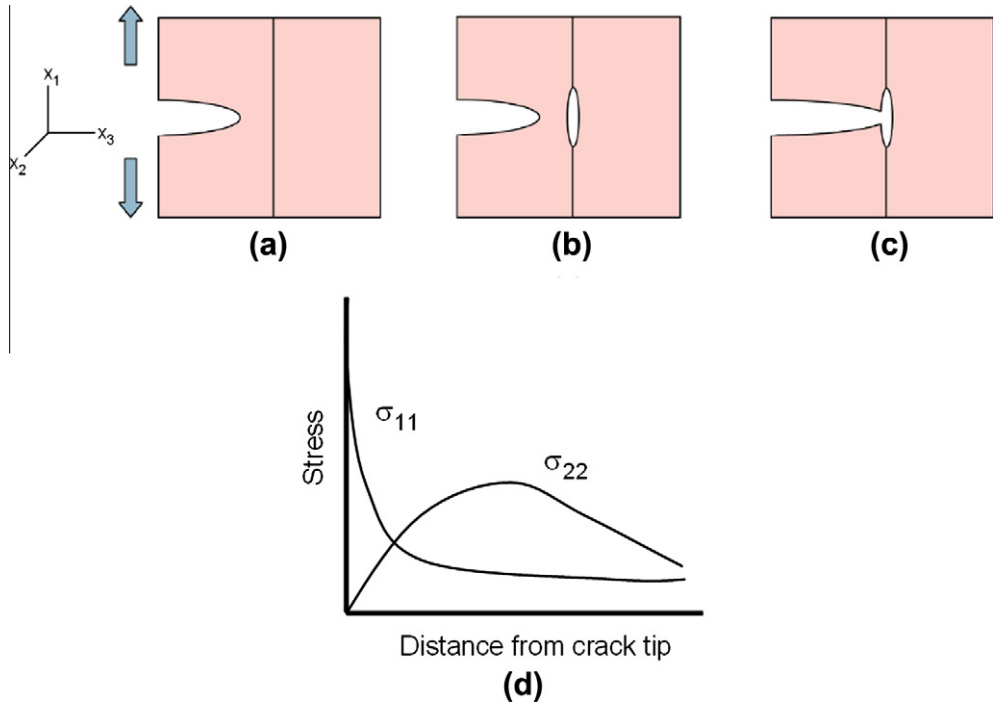


Fig. 37. Illustration of the Cook–Gordon crack blunting mechanism: (a) elliptically shaped crack in a solid under an applied tensile stress (in the x_1 direction) with a plane of weakness (interface or barrier) ahead of the crack, (b) the stress perpendicular to the crack tip (σ_{22}) is enough to open a gap in the material ahead of the crack along the weak interface, (c) when the crack impinges on the opening, the tip is blunted and requires additional stress to propagate, which can also widen the gap region, (d) stress as a function of distance from the crack tip for σ_{11} and the σ_{22} .

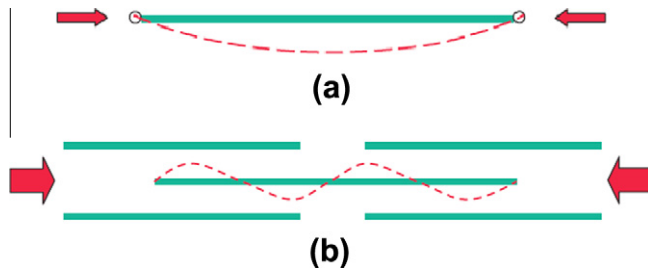


Fig. 38. (a) Classic Euler buckling of a long, slender rod. (b) Buckling of minerals confined by a biopolymer matrix in a composite, such as bone or nacre. Taken from [195].

Because the minerals have a large aspect ratio, one consideration is the stability against buckling. Fig. 38a shows an illustration of classic Euler buckling: when a load on a long, slender rod exceeds the Euler buckling limit, the rod will initially bend elastically and then eventually fracture. Given that minerals in biological composites are surrounded and supported by a much more compliant matrix, the buckling behavior will be distinct from the case of a simple rod, as illustrated in Fig. 38b. Ji et al. [195] examined this condition and discovered that for sufficiently large aspect ratios (as in nacre and bone), the critical buckling stress is independent of the aspect ratio but strongly dependent on the volume fraction of the mineral. This is a surprising result, given that the classic critical Euler buckling

load for a rod with a rectangular cross-section is highly dependent on the aspect ratio ($\sigma_{cr} = \pi^2 E / 12 \Phi^2$). In biological materials, although the minerals have a variation in size, the result is a constant buckling stress throughout the biocomposite. This suggests that the mineral shape has evolved to maximize stiffness by having a large aspect ratio, which in turn leads to a uniform buckling stress when the minerals are embedded in a biopolymer matrix.

1.5.1. Interpretation of mechanical property data

The mechanical properties (e.g. strength, stiffness, toughness) of biological materials often exhibit a wide variability. This is due, in part, to the heterogeneous nature of the materials. Even the most careful preparation of specimens (precise cutting and polishing) from the same organism yields scattered data. For example, the strength and stiffness of a wing feather depend on the location along the shaft [76]. Cancellous bone has variable porosity, even with specimens sampled adjacent to each other. Depending on the location of the cancellous bone, the predominance of plates (stiffer) or struts (less stiff) will yield different values of the Young's modulus. Another factor is the level of hydration which has a significant influence on the properties of biological samples. Wet samples have a lower stiffness and strength but a higher toughness. Ambient-dried bone samples measured in an arid climate will show different mechanical property values than the same bone tested in a humid climate. Thus, reporting the mean and including the standard deviation and exact preparation and storage procedures are essential in biological materials.

If there is a population of N samples and have measured a property, x , (strength, stiffness, etc.), the data often conforms to a Gaussian (normal) distribution. This distribution is symmetric about the most frequent value and indicates how many samples have a particular value. If the sample distribution is not normal and there is skewedness to the data, Weibull suggested another method to interpret data, based on a three-parameter model. If $F(x)$ is the cumulative distribution function of variable x_i , the probability of finding samples having a value $x_i \leq x$ is:

$$P(x_i \leq x) = F(x) \quad (1.18)$$

The Weibull distribution is written as:

$$f(x) = \frac{m}{\theta} \left(\frac{x - x_u}{\theta} \right)^{m-1} \exp \left[- \left(\frac{x - x_u}{\theta} \right)^m \right] \quad (1.19)$$

where m is the shape parameter, θ is the scale parameter and x_u is the location parameter. If $m = 1$, Eq. (1.19) reduces to the exponential distribution. Taking $x_u = 0$, integration of Eq. (1.19) yields the cumulative probability distribution function ($x_i \geq 0$), and taking into account the volume of the sample, V_i :

$$F_v(x_i, V_i : \theta, m) = 1 - \exp \left[- \left(\frac{x_i}{\theta} \right)^m \right] \quad (1.20)$$

where $F_v(x_i, V_i : \theta, m)$ is the probability that x has a value less than x_i . The variable x_i can be the measured Young's modulus or fracture strength (or any other variable), and θ is the scale or statistical dispersion parameter for either the set of values for Young's modulus or for fracture strength, respectively. Eq. (1.21) can be arranged to (after taking the logarithm twice):

$$M[\ln x - \ln \theta] = \ln \ln \left(\frac{1}{1 - F(x)} \right) \quad (1.21)$$

Plotting $\ln \ln (1/(1 - F(x)))$ as a function of $\ln x$ will yield a straight line of slope m (Weibull modulus) and intercept $m \ln \theta$. When $x = \theta$, $F(x) = 0.632$, and θ is often called the characteristic value – when $x_i = \theta$, 63.2% of the samples have $x_i \leq \theta$. The mean or expected value is:

$$\bar{\sigma} = E(x) = \pi \Gamma \left(\frac{1}{m} + 1 \right) \quad (1.22)$$

with standard deviation:

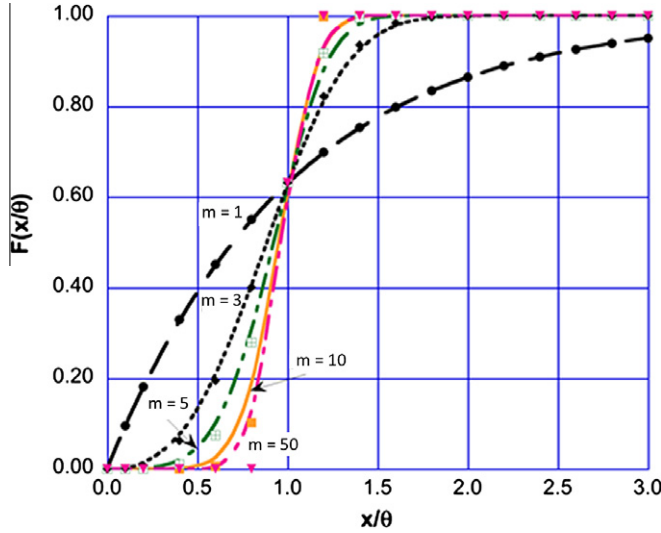


Fig. 39. Weibull cumulative distribution showing the effect of different values of β , the fitting parameter. $\beta = 1$ is an exponential function. As β increases, the scatter in the data decreases.

$$\sigma_{SD} = \theta \left(\Gamma \left(\frac{2}{m} + 1 \right) - \Gamma^2 \left(\frac{1}{m} + 1 \right) \right)^{1/2} \tag{1.23}$$

where Γ is the gamma function, values of which can be found in statistical tables. Fig. 39 shows a plot of Eq. (1.23) for various values of m . Several interesting features can be identified – all curves intersect at $x = \theta$ at $F(x/\theta) = 0.632$ and as m increases, there is less scatter in the data. When plotting strength data, $x = \sigma_f$ (fracture strength), $\theta = \sigma_o$, the characteristic strength and m is the Weibull modulus. For plotting the Young’s modulus, $x = E$, $\theta = E_o$. Some report the average strength (modulus, etc.) is at $F(x) = 0.5$.

The effect of the volume of the sample is a significant parameter on the probability of failure. Leonardo da Vinci first noticed that the strength of a pianoforte wire increased as the length decreased. Weibull considered a volume, V_o , that has a statistical distribution of non-interacting flaws. Fig. 40 illustrates this concept with a volume, V consisting of n volume elements of V_o . The failure probability is zero at σ_u and increases as the applied load increases. The probability of survival, $P(V)$, is given as:

$$P(V) = P(V_o)^n \tag{1.24}$$

Then, the failure probability is written as:

$$F(V) = 1 - \exp \left[- \frac{V}{V_o} \left(\frac{\sigma}{\sigma_o} \right)^m \right] \tag{1.25}$$

Furthermore, comparing two materials with the same failure probability but with different volumes, the relationship between the two strengths is given as [99]:

$$\frac{\sigma_1}{\sigma_2} = \left(\frac{V_2}{V_1} \right)^{1/m} \tag{1.26}$$

Some caveats as to the applicability of the Weibull analysis for the fracture strength are [196]:

- The sample size effect has a power law dependence on the fracture, which indicates there is no characteristic length. If the material has large inhomogeneities, this does not apply. Fig. 40a shows a hypothetical chain in which each link as a specific probability of failure, given by the generic

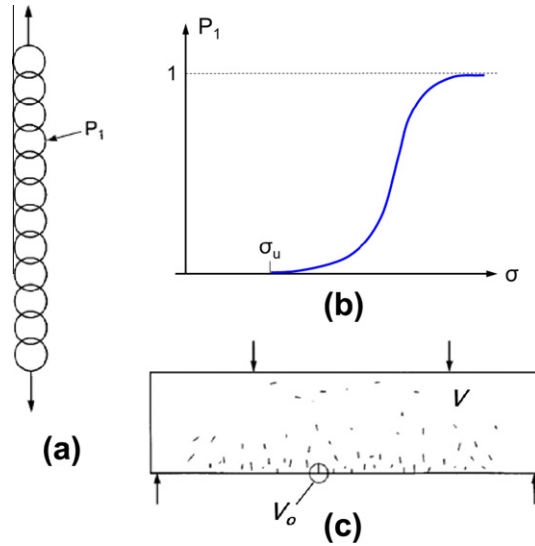


Fig. 40. (a) Chain with many links of random strength, (b) failure probability of a small element, (c) structure with many microcracks of different probabilities to become critical. Taken from [196].

function shown in Fig. 40b. A specimen containing an array of cracks with different sizes and orientations is shown in Fig. 40c. The flaw that will be first activated under the four-point loading is shown circled.

- The material is mathematically equivalent to a sample placed in uniaxial tension. Thus, the structural geometry and failure mechanisms are not taken into account.
- There is evidence that the size effect in quasi-brittle materials is more pronounced than what Eq. (1.26) predicts.
- The theory predicts that the material fractures as soon as a microscopic crack becomes a macro-crack. This ignores the contribution of stable crack growth (Section 2.1.2).

2. Fracture and impact resistance

2.1. Bone

Bone is a composite material of a protein (mainly type-I collagen), a mineral phase (carbonated hydroxyapatite), and water assembled into a complex, hierarchical structure. On a volumetric basis, bone consists of about 33–43 vol.% minerals, 32–44 vol.% organic, and 15–25 vol.% water [197]. The hierarchical structure of bone has been reviewed by several groups [3,31,161,198–200] and is shown schematically in Fig. 20. The skeletal system has multifunctionality. In general, it supports the body, protects the organs, produces blood cells, and stores mineral ions. There are some less familiar bony tissues in the animal kingdom that have unique functionalities, which have been recently reviewed by Curry [201]. For example, bird bones are designed for flying and have to be light weight and flexible; bones are used as protective armor, such as the turtle shell [202–204], armadillo carapace [205,75], and fish scales [88], must be stiff and impact resistant; mammalian ear bone (whale bulla) is extremely dense and highly mineralized in order to transmit acoustic signals [52,206]. In this chapter, we focus on one of the most important functions of bone, which is the ability to resist fracture.

2.1.1. Single-value toughness measurements

The fracture mechanics in bone is of great interest and important. Although there have been extensive studies at this point, the fracture mechanics of bone are complicated and still remains to be better

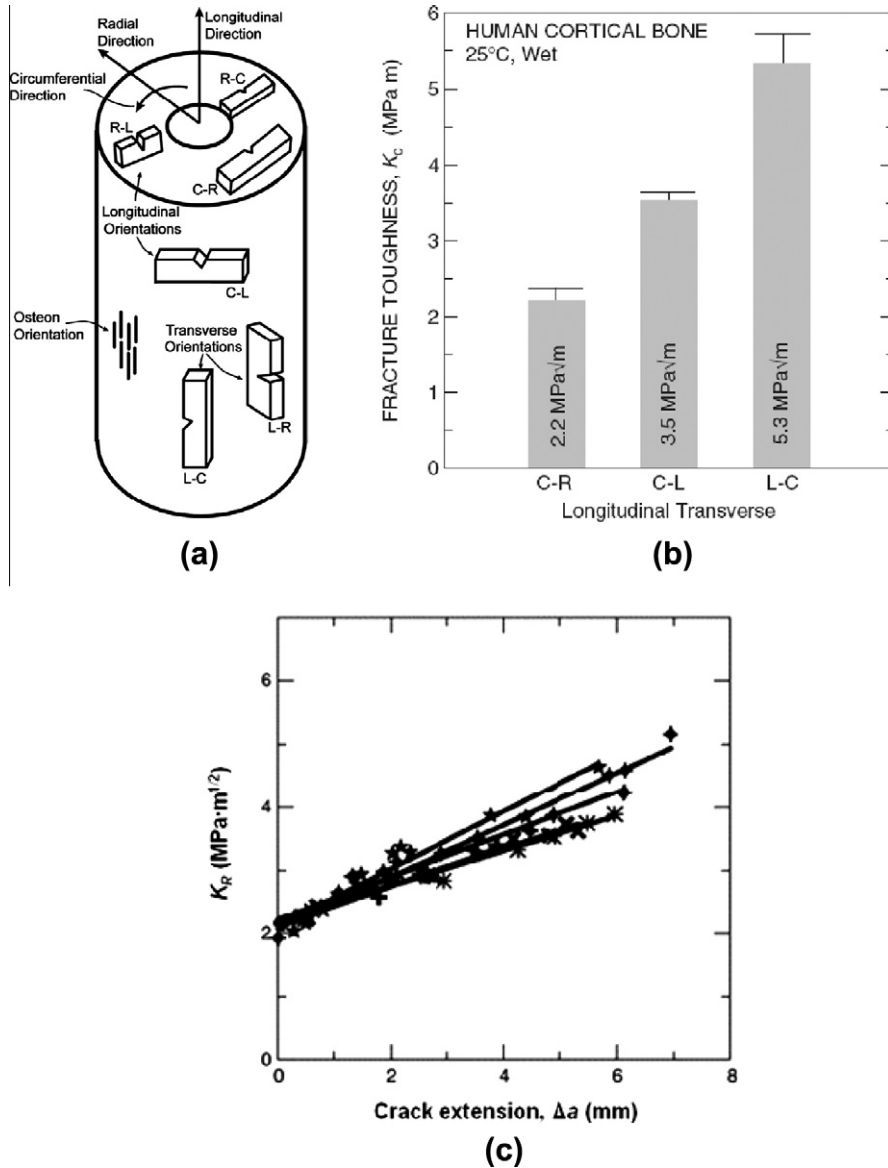


Fig. 41. (a) Schematic illustration showing the orientation codes used by standard fracture toughness measurements (ASTM E399); (b) variation in fracture toughness with orientation in human humeral cortical bone [207]; (c) typical rising R-curve behavior observed in human cortical bone [208].

understood due to its highly hierarchical structure. Most quantitative studies have focused primarily on “single-value” approaches, such as the work of fracture (W_f), the fracture toughness (K_c), the crack extension force (G_c), and its extension to elasto-plastic materials, the J integral (J_c).

The fracture toughness (K_{Ic}) varies in the range of 1.7–6.6 MPa m^{1/2} depending on species, bone types, orientation, and test geometry [209]. Fig. 41a is a schematic illustration showing the orientations used by standard fracture toughness measurements [210]. The first symbol designates the frac-

ture plane orientation and the second the crack propagation direction. For example, L–C (Longitudinal–Circumferential) and L–R (Longitudinal–Radial) represent transverse cracking (across osteons) and C–L (Circumferential–Longitudinal) and R–L (Radial–Longitudinal) represent longitudinal cracking (splitting osteons) directions. The fracture toughness in the L–C orientation is significantly higher than that in the C–R and C–L orientations. Fig. 41b shows experimental fracture toughness results in human cortical bone with three different orientations [207]. The fracture toughness in the L–C orientation is significantly higher than that in the C–R and C–L orientations. It has been reported that fracture toughness decreases with increasing mineral content [206,211–214] or porosity [215–219]. The cement line, the boundary between secondary osteons and the surrounding interstitial bone, plays a key role in the fracture of bone [214,220,221]. Cracks have been observed to deflect and propagate along the cement lines, which are considered as a weak path for fracture. The weak path provided by cement lines lead to the strong orientation dependency in bone fracture .

2.1.2. R-curve behavior

The single-value approach, although useful, provides limited insights into fracture behavior of bone because bone and other biological materials have fracture toughness enhancement during crack propagation. The resistance-curve or “R-curve” fracture-mechanics approach is more appropriate to explain the toughening mechanisms [208]. The R-curve graphically represents the resistance to crack propagation of the material as a function of crack growth and is widely used in fiber-reinforced composites. It can be experimentally determined by growing a crack of controlled size and measuring the stress necessary to propagate it. The rising R-curve behavior in bone has recently been studied in several groups [222–229]. R-curve behavior is the result of extrinsic toughening mechanisms (described below), and the crack resistance is determined in terms of the driving force required for crack extension (Δa). The toughness (K_R) starts at a crack-initiation toughness, $K_0 \sim 2 \text{ MPa m}^{1/2}$, increases with crack extension (Δa), and finally reaches a value of $\sim 5 \text{ MPa m}^{1/2}$, as shown in Fig. 41c. The slope of the R-curve is considered as a measure of crack-growth toughness.

Crack toughening mechanisms in bone are shown in Fig. 42 [230]. For composite materials, there are intrinsic (operating ahead of the crack, $<1 \mu\text{m}$) and extrinsic (operating behind the crack, $>1 \mu\text{m}$) toughening domains. In the extrinsic domain, Vashishth et al. [222] established R-curve behavior in cortical bone in which the fracture toughness (K_{Ic}) increases with increasing crack length, resulting from microcracks (extrinsic mechanism) that develop in the process zone wake around the crack tip. Collagen fiber bridging (extrinsic) facilitates crack closure thereby shielding the crack tip from additional stress. Uncracked ligaments bridge the main crack, helping to support the load decreasing the energy needed to propagate the main crack. Finally, crack deflection occurs and where the Cook–Gordon crack deflection mechanism operates.

Extrinsic toughening mechanisms act to shield the crack from applied load [231,232]. Four types of extrinsic toughening mechanisms are present: crack deflection, uncracked ligament bridging, collagen fibril crack bridging, and microcracking (Fig. 42). Intrinsic mechanisms, on the other hand, typically act ahead of the crack tip and reduce stresses and strains through localized yielding and redistribution [222,223], or may even promote crack growth. The intrinsic toughening arises from, first, the energy required for the collagen molecules to uncrimp and then when extended, slide past each other. Secondly, nano/microcracks can develop within the collagen fibrils. Thirdly, it has been demonstrated that there are sacrificial bonds within or between the collagen molecules that dissipate energy when stretched and are reformed after the load is released [172,233].

An analysis of crack bridging fibers has been conducted by Li [234]. The fiber bridging stress, σ_{fb} is related to the normalized crack opening displacement, $\beta \equiv 2\delta/L_f$ (L_f = fiber length):

$$\sigma_{fb}(\beta) = C\beta \left[2 \left(\frac{C'\tau\alpha}{\beta} \right)^{1/2} - 1 \right] \quad (2.1)$$

where C is a constant that incorporates the geometry of the crack and the volume fraction of the fibers, C' is a materials constant, α = aspect ratio of the fibers (L_f/d_f) and τ is the interfacial shear strength between the fibers and the protein matrix. Eq. (2.1) indicates that the fiber bridging stress increases with

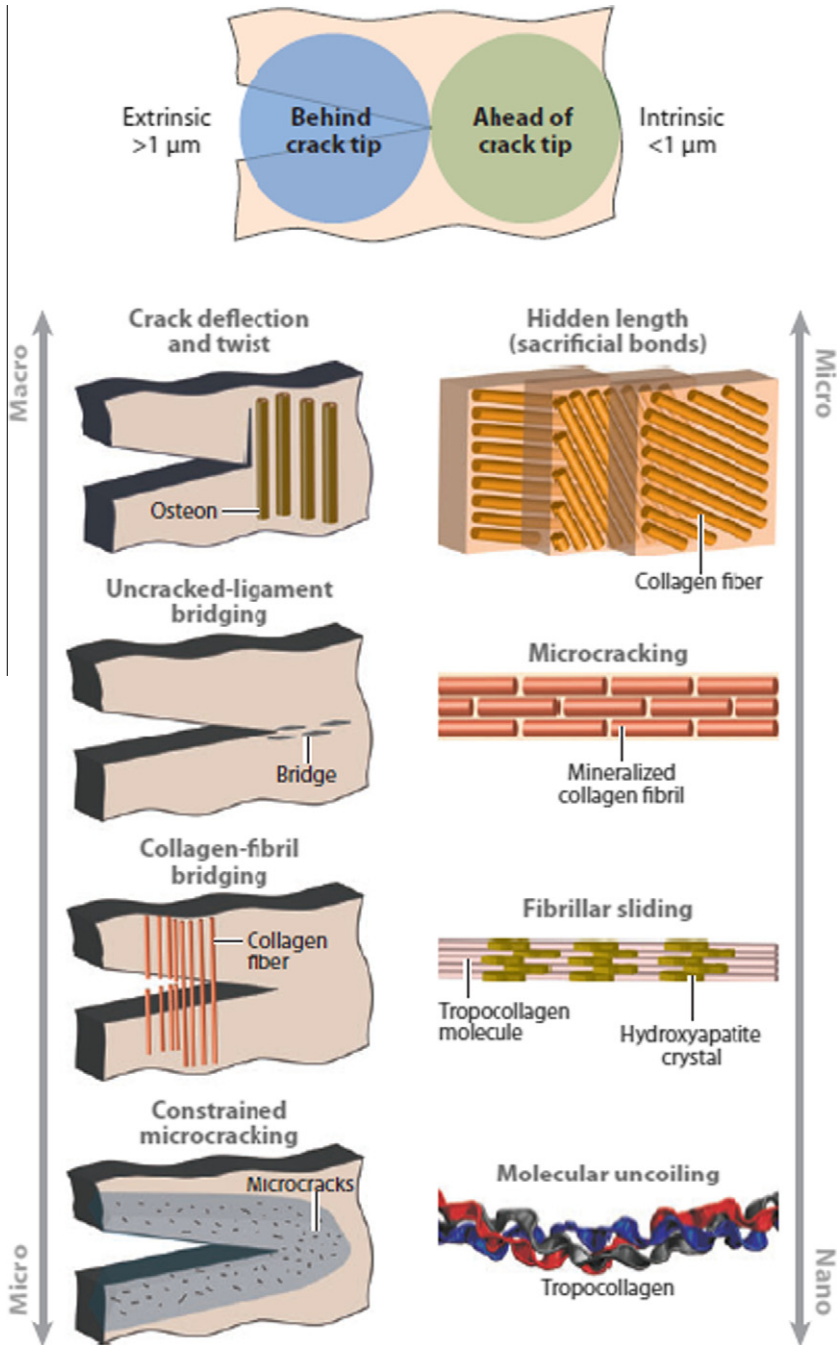


Fig. 42. Fracture toughening mechanisms in bone are found at all hierarchical levels: (a) collagen molecular uncrimping/uncoiling, (b) collagen fibers sliding past each other, (c) microcracking, (d) separation of sacrificial bonds, (e) microcracking around crack tip, (f) collagen fiber bridging (g) uncracked ligament bridging and (h) crack deflection. There are two prevailing domains – extrinsic (crack tip shielding, length scale >1 μm) and intrinsic (plastic deformation, length scale <1 μm). Taken from [230].

an increase in the aspect ratio of the fibers. However, there is a limit to the length of the collagen fibrils, as minerals must be accommodated at the ends.

In bone, crack deflection is caused by osteons which change the crack propagation with certain angle from the original direction (optimum condition = 90°). Crack bridging is provided by collagen fibers, which also contributes crack-tip shielding. The uncracked ligament bridging is another extrinsic toughening mechanism that provides crack-tip shielding. Microcracking is an intrinsic toughening mechanism that is initiated ahead of the crack and forms a process zone with dilatation with tends to “close” the crack. Nalla and co-workers [235] evaluated the contributions of the mechanisms to the fracture toughness of human cortical bone. The most important toughening mechanism for bone is crack deflection which contributes over 50% ($\sim 3 \text{ MPa m}^{1/2}$) to the fracture toughness. The second most important mechanism is the uncracked ligament bridging which contributes 1–1.5 $\text{MPa m}^{1/2}$.

Although the R -curves provide a means to characterize crack propagation, the underlying assumptions for such K_R calculations are based on linear-elastic fracture mechanics (LEFM), which cannot account for the energy associated with permanent deformation during bone fracture. The fracture toughness of materials with considerable permanent deformation, such as bone and antler, is usually underestimated. Koester et al. [236] first applied a non-linear fracture mechanics approach based on the J -integral to determine the R -curve for human cortical bone. This approach accounts for the contribution from plasticity to the toughness, and provides a sound means to determine the R -curve fracture toughness in a material that undergoes multiple large-scale crack deflections. The effective stress intensity (K_{eff}) is calculated from the elastic modulus (E) and J -integral (J_c) as follows:

$$K_{eff} = (E \cdot J_c)^{1/2} \quad (2.2)$$

They also used *in situ* mechanical testing on small bending samples under environmental SEM to examine how physiologically pertinent short cracks (<600 μm) propagate in both the transverse (L–C) and longitudinal (C–L) orientations in human cortical bone. The R -curves (Fig. 43) showed that the effective stress intensity in the transverse orientation was much higher than that in the longitudinal orientation, reaching a value of $\sim 25 \text{ MPa m}^{1/2}$, much higher than the fracture toughness of bone previously reported in the literature. Synchrotron X-ray computed tomography images showed the dominant toughening mechanisms were crack deflection (in-plane) and twisting (out-of-plane) in the transverse orientation, predominantly at the cement lines, as shown in Fig. 44.

The mechanistic origins of toughness in bone at varying hierarchical length scales have recently been reviewed by Ritchie et al. [199] and Launey et al. [230]. The toughening mechanisms of bone at the molecular and nanometer regimes were studied by Buehler and Wong [237] using molecular dynamics simulations and theoretical analysis. Fig. 45 shows a typical J -shaped stress–strain curve. At low strains, molecular rearrangement occurs (toe region), in the heel region, hydrogen bonds break (which are reformed after the load is released) and finally the polymer backbone undergoes deformation with a substantial increase in stiffness. Fig. 46a shows computationally generated stress–strain curves under tensile stress for a pure and mineralized collagen fibrils. The mineralized collagen fibrils exhibit a higher strength and greater energy dissipation under deformation. Furthermore, the mineralized collagen fibrils show higher stiffness and significant softening at larger strains, with a sawtooth-shaped stress–strain curve due to repeated slip between the collagen and mineral. Deformation mechanisms of pure and mineralized collagen fibrils under increasing tensile stress are shown in Fig. 46b and c, respectively. The mineralized collagen fibrils assemble into fibers or arrays, which are “glued” together by non-collagenous proteins, as shown in Fig. 47a. At this structural level, the toughness of bone has been attributed to the additional energy required to break sacrificial bonds in the “glue” [162,238]. AFM pull-off force measurements (Fig. 47b) indicate that the bonds break at a fraction (0.1–0.5) of the force required to break the backbone of the macromolecules and sawtooth force–displacement curves are observed. Fig. 47c shows a possible toughening mechanism which involves breaking the sacrificial bonds in non-collagenous glue between mineralized collagen fibrils. At the largest length scales, the primary toughening mechanisms are constrained microcrack formation, collagen fibril bridging, uncracked ligament bridging as well as crack deflection and twist previously discussed in Fig. 42.

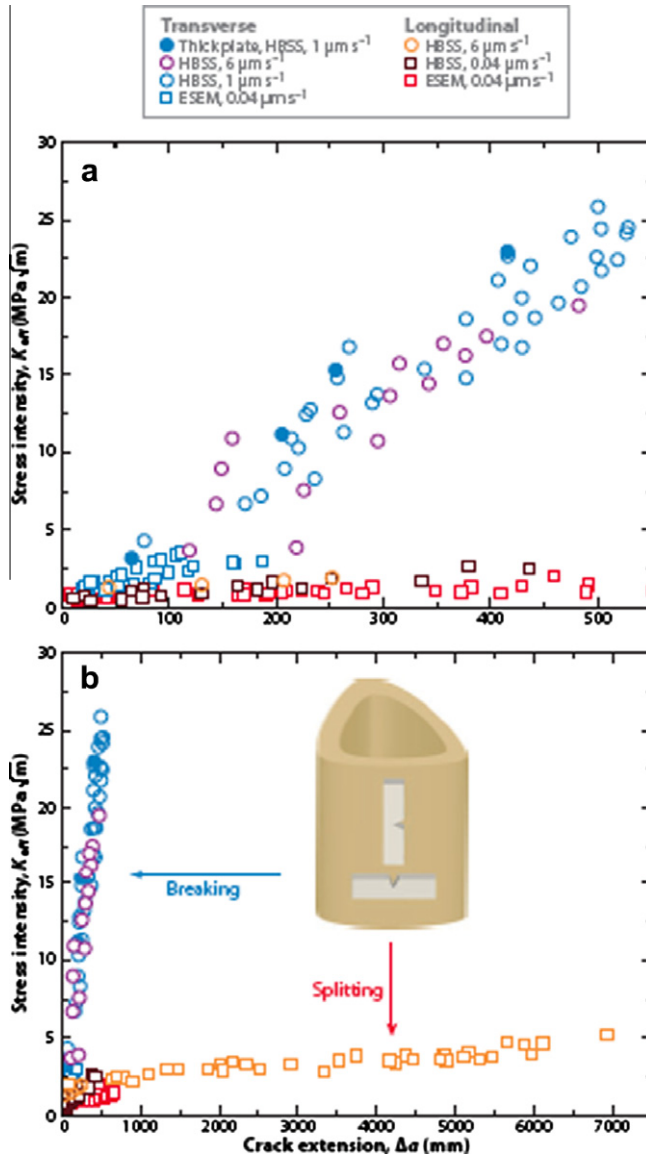


Fig. 43. Fracture toughness resistance curve data for the transverse and longitudinal orientations in hydrated human cortical bone. Non-linear-elastic fracture mechanics measurements of the fracture toughness of bone show that resistance to crack propagation increases much more rapidly in the transverse (breaking) direction than in the longitudinal (splitting) direction. Adapted from [236].

2.2. Antler

Antlers are bony protuberances that form on the heads of the male deer species. The comparisons between elk antler and bovine femur bone are summarized in Table 5. Both antler and bone utilize the same basic building blocks, namely type-I collagen fibrils and carbonated hydroxyapatite crystallites, which is verified by amino acid analysis, X-ray diffraction, and TEM observation [77]. However, there

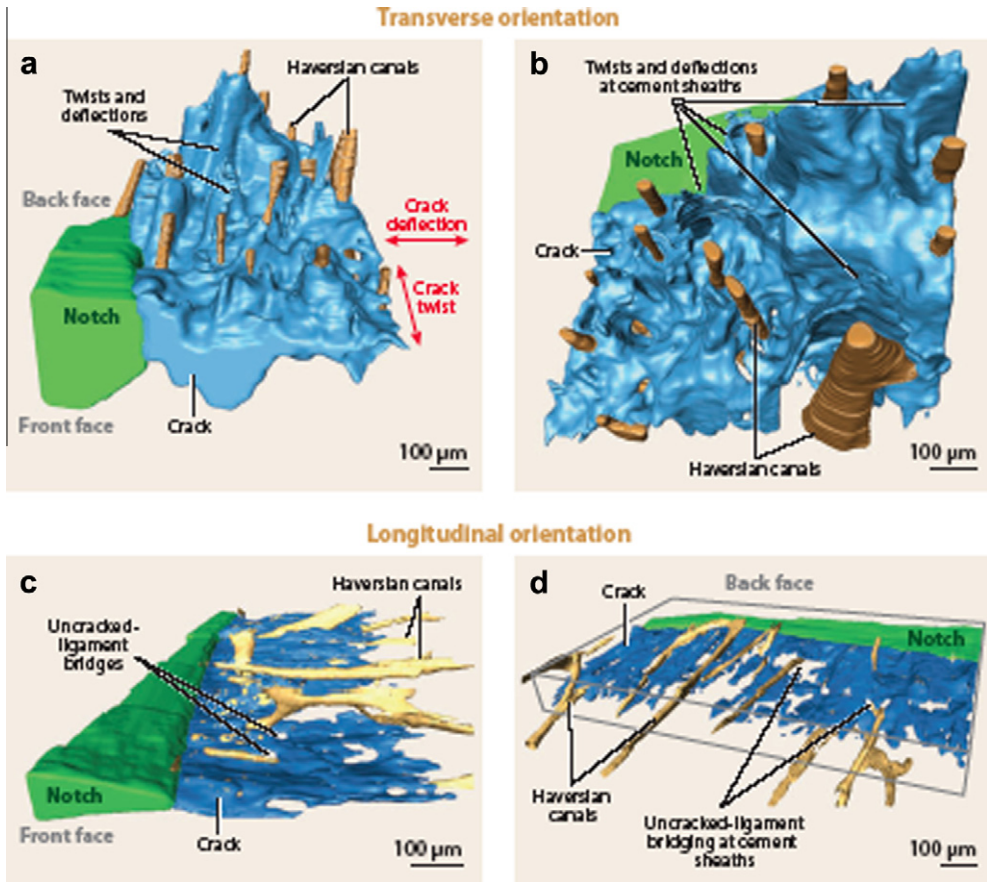


Fig. 44. Three-dimensional reconstructions in the transverse and longitudinal orientations from synchrotron X-ray computed tomography. Panels *a* and *c* show an edge on view of the notch and crack to show the shape of the crack paths. Panels *b* and *d* are oriented to highlight the dominant toughening mechanisms in the two orientations. Adapted from [230].

are several distinct differences between the two. Antlers and skeletal bones have different functions. The primary functions of antlers are defense, social display and combat between male species [239–242]. Skeletal bones contain bone marrow while antlers have no marrow. There exists a transition zone between cortical and cancellous bones in antlers, whereas there is no such transition zone in skeletal bone. The cancellous bone is well aligned and uniformly distributed through the entire antler while that in bovine femur is located in the femur head. The mineral content in antler (36 vol.%) is lower than that in bovine femur (43 vol.%) and is the lowest among bony tissues [3].

Antlers consist mainly of primary osteons due to limited growth time (1–2 months) required for secondary osteon remodeling [243]. Cross-sectional micrographs of cortical antler (Fig. 48a and c) are compared with that of bovine femur (Fig. 48b and d). In Fig. 48a, osteons (100–225 μm diameter), Volkmann canals, vascular channels (15–25 μm diameter) and lacunae spaces (~10 μm diameter) are observed, as indicated in the micrograph. The osteons are irregular in shape and appear situated in a matrix (dark gray region in the micrograph). A high density of vascular channels which may be related to the fast growth rate can be observed. The void space is estimated to be ~9.1% by area in the antler, counting the vascular channels and lacunae. In Fig. 48b, the more uniformly shaped secondary osteons in the bovine femur are more sparsely distributed compared with those in the antler. In the femur, secondary osteons occupy ~41% by area. The void space is estimated to be 5.1%, in agreement with

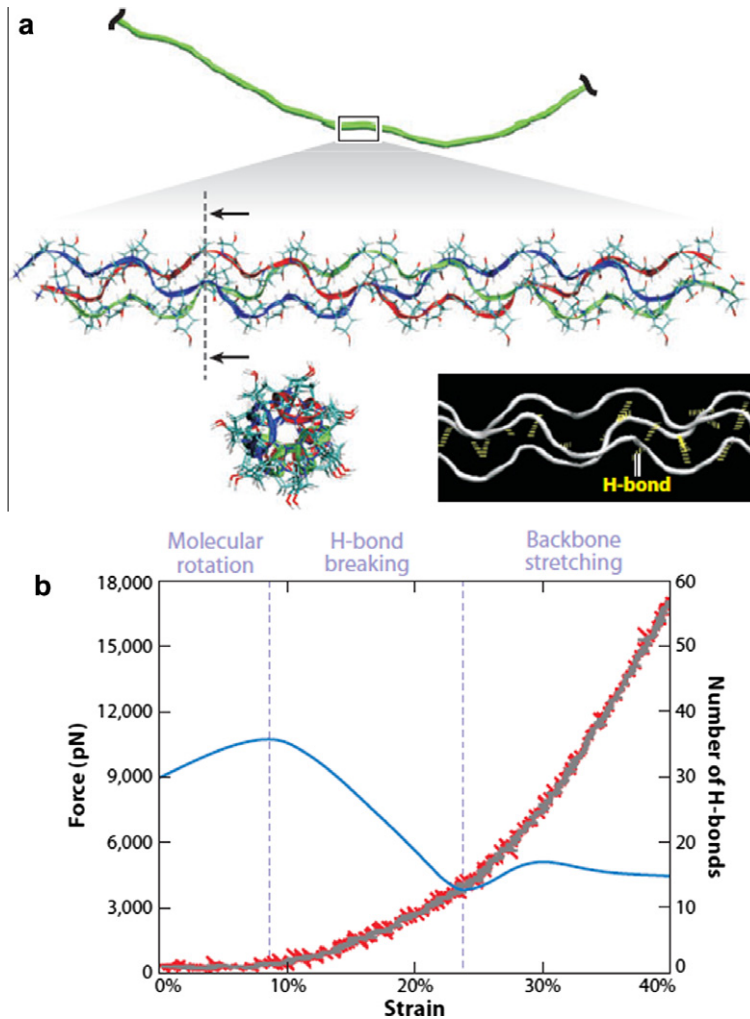


Fig. 45. Structure and nanomechanics of a triple-helical tropocollagen molecule (a) the structure of tropocollagen molecule and hydrogen-bond (H-bond) structure (b) the force-extension behavior and the corresponding number of H-bonds during tensile deformation. Three deformation stages are molecular rotation, H-bond breaking, and finally backbone stretching. Adapted from [230].

a porosity of 5.8% measured in other bovine femur [244,245]. Fig 48c shows the back-scattered electron (BSE) images of cortical antler. A prominent hyper-mineralized region which is 10–20 μm in width surrounding primary osteons is present in antler. This hyper-mineralized region forms irregular and complex interfaces between osteons and corresponds to the matrix previously shown in the optical micrograph (Fig. 48a). A BSE image of cortical bovine femur taken at the same magnification is shown in Fig. 48d. Secondary osteons appear darker compared to the surrounding interstitial bone. The interstitial bone was found to have a higher mineral content which leads to higher elastic modulus and strength than the secondary osteons [246–248]. Using quantitative BSE imaging and electron dispersive spectroscopy (EDS) analysis, Skedros et al. [249] showed that cement lines are highly mineralized, in contrast to earlier conclusions that they were poorly mineralized [221,250–252]. The hyper-mineralized cement lines are considered to be the primary path for microcrack

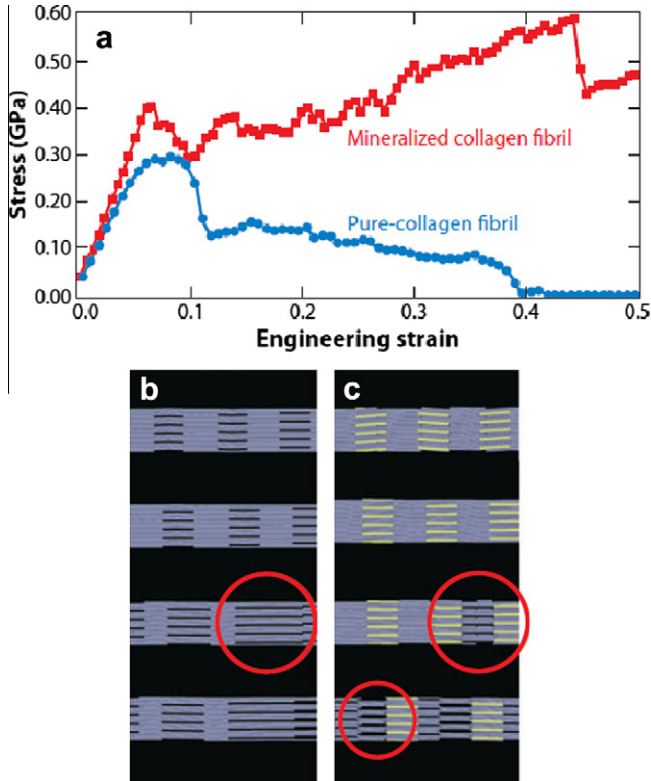


Fig. 46. (a) Computational result of the stress–strain response of a mineralized vs. an non-mineralized collagen fibril, showing the significant effect that the presence of mineral crystals in collagen fibril has on the mechanical response. Snapshots of the deformation mechanisms of (b) collagen fibrils and (c) mineralized collagen fibrils. Slip initiates at the interface between mineral particles and tropocollagen molecules. Repeated occurrence of slip (red circles denote local areas of repeated molecular slip) reduces the density, leading to the formation of nanoscale voids Adapted from [230].

propagation. Since the cement lines are preferentially aligned in the longitudinal direction of the bone, they play an important role in enhancing fracture toughness by deflecting and attenuating the propagation of microcracks and preventing bone from breaking [214,220,221]. Skedros et al. [243] hypothesized that the hyper-mineralized interface between antler primary osteons may be functionally analogous to cement lines.

Currey was the first to perform strength, fatigue, creep, hardness and high-strain rate tests on mineralized tissue from various taxa [65,206,253–259]. The general findings were that the elastic modulus and strength increased with increasing ash (mineral) content while the work of fracture decreased. Antler was found to have the lowest mineral content and consequently lowest elastic modulus among mineralized tissues with a mineral content of ~ 57 wt.% (or ~ 36 vol.%), in contrast to the highly mineralized whale rostrum at 98 wt.% (56 vol.%) [254]. Mammalian, reptilian and avian bones fall between these values. Red deer antler and bovine femur bone were found to have similar ultimate tensile strengths, which varied between 100 and 140 MPa, however the strain at failure (8–10%) and work of fracture (6.2 ± 0.6 kJ/m²) for antler was 4–5 times greater than bovine femur [206,258]. The modulus of elasticity (7.4 GPa) was roughly half of that of the femur. In antler, the post-yield region of the stress–strain curve was considerably longer and accompanied by a gradual slope to failure, compared with bone, as shown in Fig. 49 [259]. In bone, after the ultimate strength was reached, the stress dropped rapidly until failure or increased slightly by about 10% to failure [256].

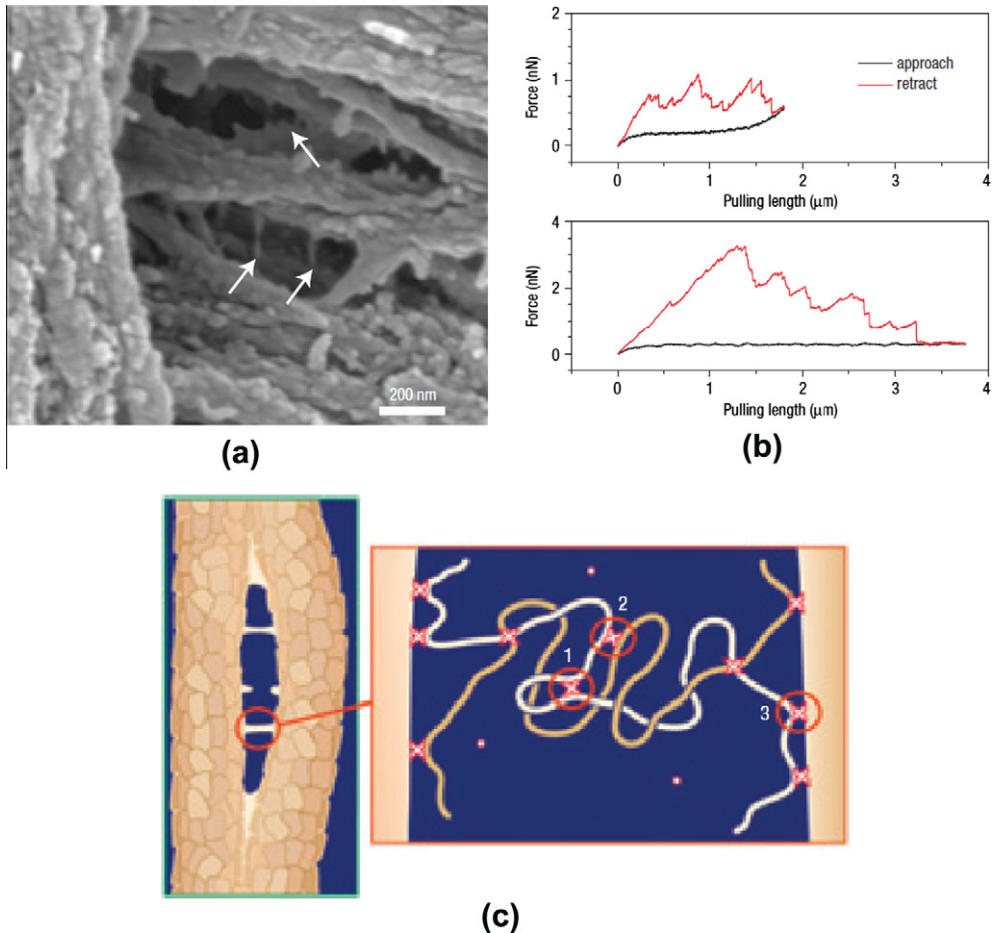


Fig. 47. (a) SEM micrograph showing individual collagen fibrils are held together by glue filaments (arrows); (b) representative force-extension pulling curves obtained from AFM measurement (upper curve: not all filaments were broken; lower curve: all filaments were broken) showing characteristic saw-tooth shape, corresponding to successive fracture of polymer chains; (c) possible deformation mechanism which involves breaking the sacrificial bonds in non-collagenous glue between mineralized collagen fibrils. Adapted from [162].

2.2.1. Exceptional fracture resistance in antler bone

Vashisht [225] studied the fracture toughness of red deer antler and bovine femur using both single-value crack initiation toughness (K_{Ic}) approach and the R -curve measurements. Results showed that bovine femur has higher initiation fracture toughness (K_{Ic}) than antler; however, the slope of R -curve (or the crack-growth toughness) obtained from antler is about twice that of bovine femur. Vashisht proposed that both bone and antler derive their toughness by forming microcracks during the process of crack propagation (extrinsic toughening). Antler (lower mineral content, lower stiffness and yield strength) forms microcracks in a frontal process zone at lower stresses. In contrast, for bovine femur, a bone of higher stiffness and yield strength, these microcracks are formed at higher stresses, yielding higher initiation toughness. Zioupos et al. [66] studied the fracture surface of antler by laser confocal microscopy and observed that microcracks were more isolated and dispersed from each other in antler than those in the bone before the formation of the fatal macrocrack. The macrocracks in antler follow a much tortuous route resulting in rougher fracture surfaces compared to bone.

Table 5

Comparisons between elk antler and bovine femur bone.

Property	Antler bone	Bovine femur bone
<i>Similarities</i>		
Basic building blocks	Protein: Type-I collagen	
Hierarchical structure	Mineral: Carbonated hydroxyapatite Collagen/mineral < mineralized collagen fibrils < lamella < osteon/trabecula < cortical/ cancellous bone < antler/bone	
<i>Differences</i>		
Function	Combat & social display	Support body, protect organs, and produce blood components, mineral storage
Bone marrow	No marrow	Bone marrow
Transition zone	Transition zone	No transition zone
Cancellous bone	Uniformly distributed	Localized in the head region
Mineral content (cortical bone)	57 wt.%	67 wt.%
	36 vol.%	43 vol.%
Osteon type	Primary	Secondary
Cement line	No cement lines Hyper-mineralized regions	Cement lines

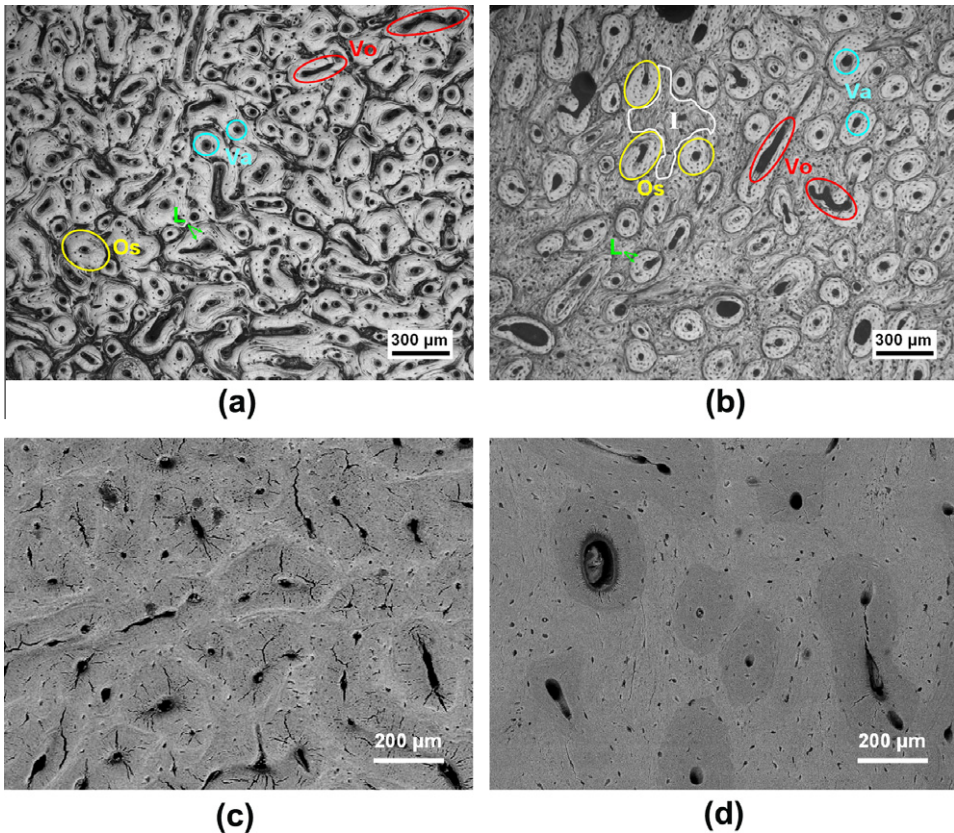


Fig. 48. Optical micrographs of cortical bone from elk antler and bovine femur: (a) cross-sectional area of (a) elk antler and (b) bovine femur (Os: Osteons, Va: Vascular canals, Vo: Volkmann canals, L: Lacuna, I: interstitial bone). Backscattered electron (BSE) images showing cross-sectional microstructure of (c) elk antler and (d) bovine femur. Taken from [78].

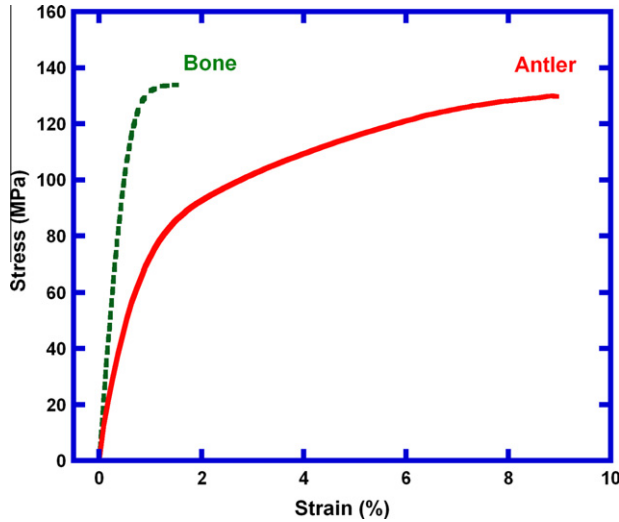


Fig. 49. Typical tensile stress–strain curves of bovine femur bone and red deer antler. Reproduced from [259].

Launey et al. [78] studied the R -curve behavior using non-linear fracture mechanics along with *in situ* environmental SEM observations. Three anatomical orientations in antler samples are shown in Fig. 50a. Representative load vs. load-line displacement curves obtained from three-point bending tests for the transverse, *in-plane* longitudinal, and *anti-plane* longitudinal orientation of antler cortical bone are shown in Fig. 50b. The maximum load for the transverse orientation reaches 105 N, approximately three times higher than those for the *in-plane* and *anti-plane* longitudinal orientations, which are ~ 30 N. The load–displacement curves show extensive plastic deformation after yielding, which indicates a non-linear elastic fracture behavior of antler. Full $J_R(\Delta a)$ resistance curves for hydrated antler cortical bone with short crack lengths ($\Delta a < 600 \mu\text{m}$) tested in transverse, *in-plane* longitudinal, and *anti-plane* longitudinal orientations are shown in Fig. 50c. The results are compared with results on human cortical humerus bone tested in both transverse and *in-plane* longitudinal orientations [236]. The R -curves on antler were terminated after about $600 \mu\text{m}$ of crack growth as none of the specimens broke in half. The significant rising R -curve behavior shown in antler indicates extensive toughening mechanisms. The results clearly show that antler, like human bone, develops most of its fracture resistance during crack growth, and not during initiation. J value in the transverse orientation reaches exceptionally high values of $\sim 60 \text{ kJ/m}^2$ over the first $600 \mu\text{m}$ of crack extension (Fig. 50d), representing the highest toughness reported for mineralized tissues to date [78], which is twice the toughness of human cortical bone ($J \sim 30 \text{ kJ/m}^2$) [236]. Antlers tested in their longitudinal orientations (*in-plane* and *anti-plane*) are far less tough yet still reach (steady-state) fracture toughness of $J_c \sim 4\text{--}5 \text{ kJ/m}^2$, i.e., more than an order of magnitude higher than in human cortical bone (to extend a crack $\sim 500 \mu\text{m}$).

The prominent toughening mechanisms in antler were identified by performing fracture toughness tests *in situ* in the ESEM on rehydrated samples [78]. Sequential series of ESEM backscattered electron images of crack growth during *in situ* R -curve testing in the *in-plane* longitudinal orientation are shown in Fig. 51a–d. The crack trajectory is somewhat parallel to the long axis of the osteons and the microcracks formed in front of the main crack can be observed. The formation of such microcracks ahead or parallel to the main growing crack leaves intact regions in between, resulting in the “uncracked-ligament” bridges [207,236]. The black arrows indicate the uncracked ligament bridges and the white arrows designate the vascular channels running along the osteons. Crack paths are consequently quite planar with little evidence of deflection around the interface of osteons, resulting in much smoother fracture surfaces. In the *anti-plane* longitudinal orientation (Fig. 51e–h), the crack path is deflected around the hypermineralized regions surrounding the primary osteons in antler. The crack

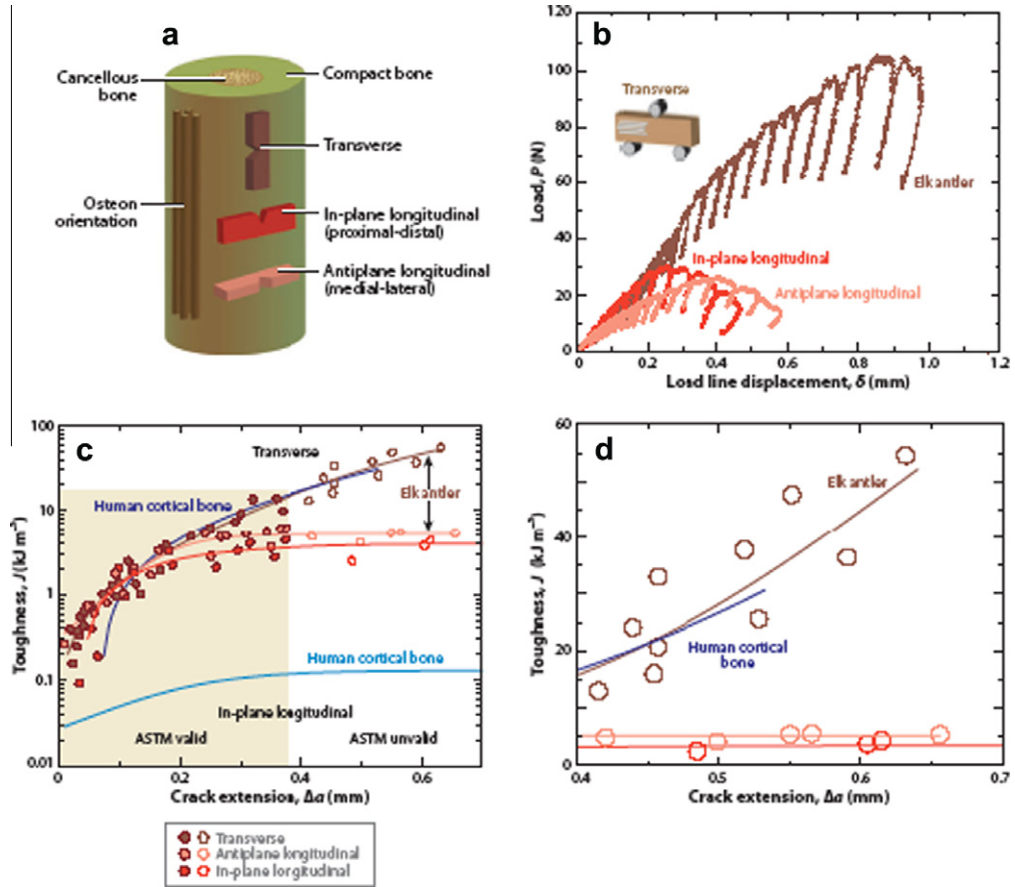


Fig. 50. (a) The structure of antler bone, as well as the three anatomical orientations of the specimens taken from the cortical bone. (b) Curve for typical load vs. load line displacement obtained during *R*-curve testing for the transverse, in-plane longitudinal, and antiplane longitudinal orientations of hydrated antler cortical bone. Each partial unloading event during the test corresponds to a data point in panel c. (c) Full $JR(\Delta a)$ resistance curves for stable ex situ crack extension in hydrated antler cortical bone tested in the transverse, in-plane longitudinal, and antiplane longitudinal orientations. (d) Expansion of panel c showing $JR(\Delta a)$ resistance curves at larger crack extension ($\Delta a > 400 \mu\text{m}$). The *R*-curves for short crack lengths ($\Delta a \approx 600 \mu\text{m}$) are compared with data taken from human cortical bone in both the transverse and the in-plane longitudinal orientations of the humerus. Adapted from [78].

trajectory is the result of two competing factors; the external load forces the crack propagating forward and the hypermineralized interface provides a preferentially weak path. The main crack in such orientation follows a much more tortuous route compared with that in the *in-plane* longitudinal orientation, which additionally contributes to the toughness. The toughness in the *anti-plane* longitudinal orientation is higher than that in the *anti-plane* longitudinal orientation. In the transverse orientation, the prominent toughening mechanisms are in-plane crack deflection and out-of-plane crack twisting. As shown in the BSE images in Fig. 51i and j), the crack deflects by as much as 90° at the interface between the osteons, resulting in a much more complicated crack path compared with those in the *in-plane* and *anti-plane* longitudinal orientations. The major crack travels through a long route in a crack extension Δa less than $500 \mu\text{m}$.

A through-thickness slice obtained from synchrotron X-ray computed micro-tomography shows a crack twisting in the transverse orientation (Fig. 52a). The arrows indicate some of the major twists at $\sim 90^\circ$. A comparison between the crack propagation in the transverse and *in-plane* longitudinal

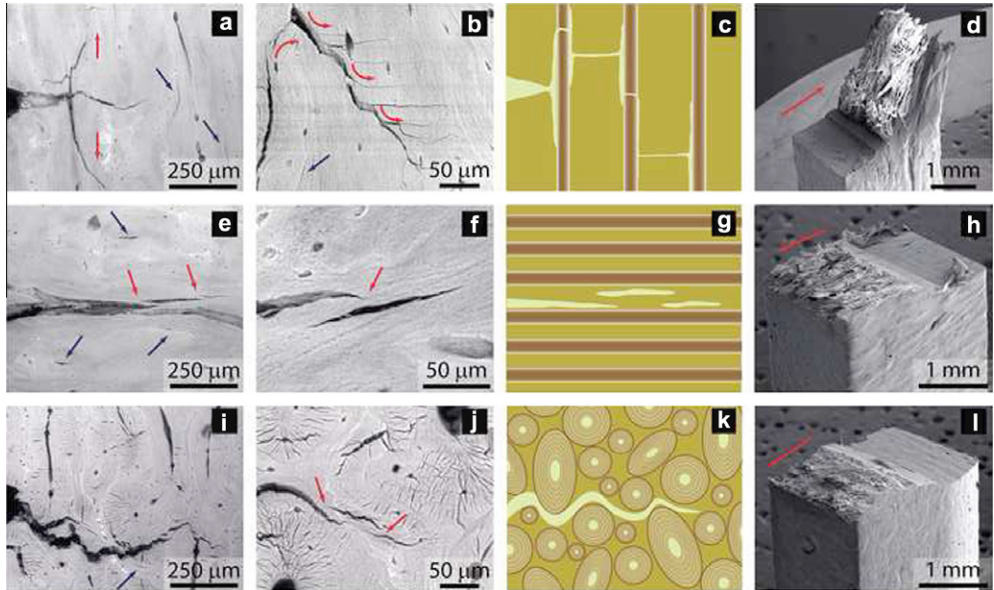


Fig. 51. Mechanisms for stable crack propagation and toughening in the transverse and longitudinal orientations of antler cortical bone. ESEM backscattered electron images of stable crack growth during *in situ* R-curve testing in the (a and b) transverse, (e and f) in-plane longitudinal, and (i and j) anti-plane longitudinal orientations. (d, h, and l) SEM fractography images and (c, g, and k) schematics of the crack trajectory for each orientations. Adapted from [78].

orientations is shown in the three-dimensional μ -CT visualizations (Fig. 52b and c, respectively). The purple planes are the major cracks and the brown lines are vascular channels. In the transverse orientation, the crack undergoes significant deflection and twisting as it interacts with the osteons and their interfaces (Fig. 52b) while in the *in-plane* longitudinal orientation, the crack is very planar and parallel to the vascular channels. As microcracking predominates along the “weaker” hyper-mineralized osteon interfaces (and lamellar boundaries), the largest microcracks form along the long axis of the antler, which is nominally orthogonal to the fracture direction in the transverse orientation. Crack paths in the transverse orientation are highly deflected and twisted, resulting in much higher toughness compared with that in the longitudinal orientation. The results show that, similar to human cortical bone, antler combines multiple of toughening mechanisms operating over a range of dimensions to develop toughness through crack deflection/twist and crack bridging processes, both mechanisms which result from the occurrence of microcracking. Such microcracking is essential for many of the toughening mechanisms in bone, notably crack bridging and crack deflection which predominate at micrometer-scales and above [199].

The other characteristic of antler bone is its lower strength and much lower stiffness than human bone, which is associated with its extensive plasticity; this further contributes to its intrinsic toughness. The low yield strength in the longitudinal direction allows crack-tip plastic zones to form at lower stresses than in human bone [65,236], which contributes to the large inelastic deformation and thereby to its intrinsic toughness. Recently, *in situ* tensile testing on cortical antler bone combined with small angle X-ray diffraction measurements [202] revealed that while both antler and bovine bone show similar nanoscale fibril shearing [260] mechanisms during elastic deformation. However, they are different during inelastic deformation with inhomogeneous fibril stretching in antler leading to defects and consequent de-bonding between adjacent fibrils. The result is that strain localization in antler is suppressed at the microscale. Moreover, this process is thought to induce the formation of microcracks, which further contributes to its extensive inelastic deformation prior to failure.

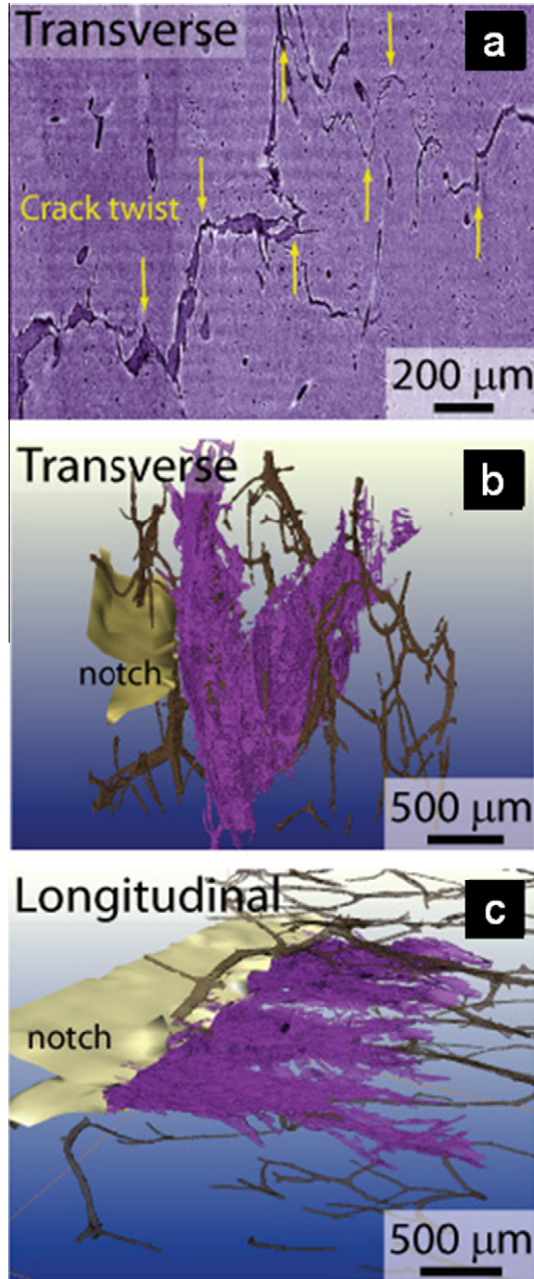


Fig. 52. Synchrotron X-ray computed micro-tomography images of cortical elk antler: (a) a through-thickness slice highlighting the twists of the crack (arrows); 3-dimensional crack path in the (b) transverse and (c) *in-plane* longitudinal orientations in antler cortical bone. Adapted from [78].

2.2.2. Dynamic mechanical behavior

The dynamic mechanical behavior of antler was investigated using the split Hopkinson pressure bar (SHPB) [79,261]. The strain rate was nearly constant ($\sim 10^3 \text{ s}^{-1}$) throughout the test with adequate

pulse shapers, which extend the incident pulse rise time in order to satisfy dynamic stress equilibrium. The dry antler shows high compressive strength and elastic modulus yet lower strain to failure compared with the rehydrated one. The toughness (area under stress–strain curve) for antler in the wet condition ($\sim 20 \text{ MJ/m}^3$) is approximately twice that in the dry condition ($\sim 11 \text{ MJ/m}^3$).

The compressive mechanical behavior of antler as a function of strain rate varying from 10^{-3} to 10^3 s^{-1} in either dry or rehydrated conditions is shown in Fig. 53a and b, respectively. The compressive stress–strain curves clearly indicate the visco-elastic behavior of antler. Both the dry and rehydrated antler samples exhibit increase in elastic modulus and compressive strength with increasing strain rate. The strong strain-rate dependency of antler is in agreement with that of human cortical bone

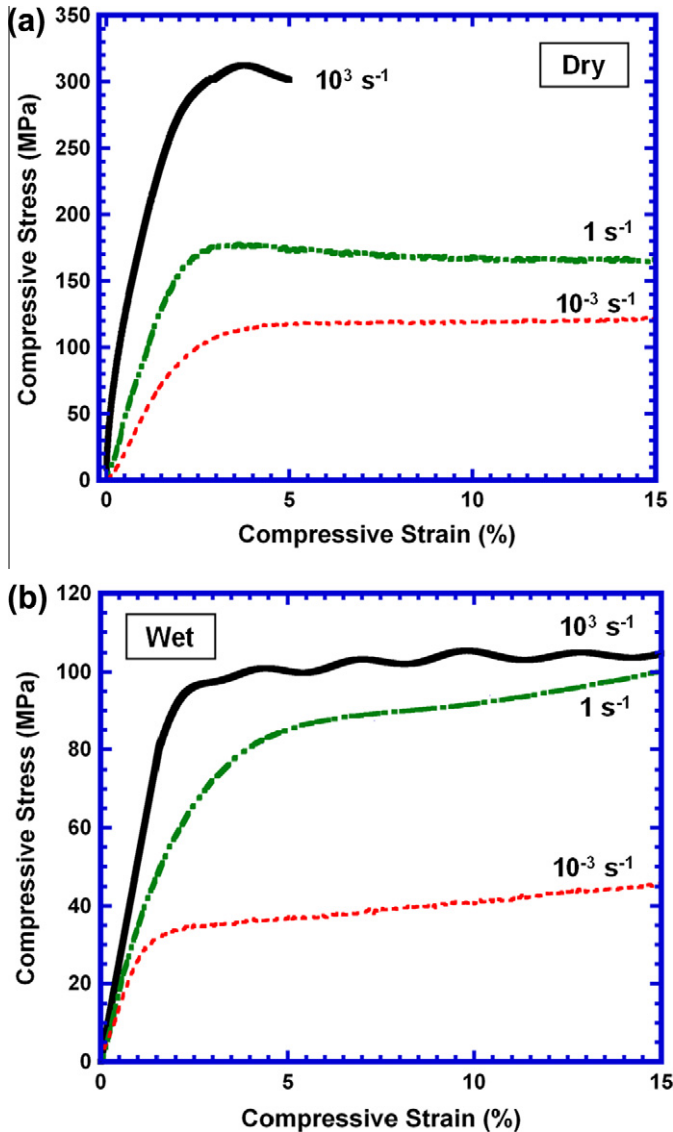


Fig. 53. Compressive stress–strain curves of antler as a function of strain rate varying from 10^{-3} to 10^3 s^{-1} in (a) dry and (b) wet conditions.

in tension previously reported by McElhane [262] and bovine femur bone in compression more recently confirmed by Adharapurapu et al. [263]. The strain-rate sensitivity of bone and antler is primarily due to the collagen, which has visco-elastic behavior. Antler has higher volume fraction of collagen than mammalian long bones and is expected to be more strain-rate sensitive.

2.3. Horn

Horns appear on animals from the bovidae family, which includes cattle, sheep, goats, antelope, oryx and waterbuck, and are tough, resilient and highly impact resistant. In the case of male big horn sheep, the horns must be strong and durable as they are subjected to extreme loading impacts during the life of the animal and, unlike antlers, will not grow back if broken. Horns are not living tissue – there are no nerves and they do not bleed when fractured. On the living animal, horns encase a short bony core (*os cornu*) composed of cancellous bone covered with skin, which projects from the back of the skull. The horn is not integrated to the skull and can pull away if the hide is removed. The skin covering the bony core is a germinative epithelium that generates new cells to grow the horn. Unlike other structural biological materials (e.g. bone, tusk, teeth, antlers, mollusk shells), horn does not have a mineralized component and is mainly composed of α -keratin. The shape of these horns, often following a logarithmic spiral/helicoidal pattern, was described in detail by Thompson [1] and modeled by Skalak et al. [264].

Fig. 54 shows hierarchical structure of horn from a desert bighorn sheep. At the lowest level, the intermediate filaments (IFs) embedded in the amorphous matrix and IFs that extend from one lamella to the other. There lamellae are flat sheets that are held together by other proteinaceous substances. Long tubules extend the length of the horn interspersed between the lamella. The resulting structure

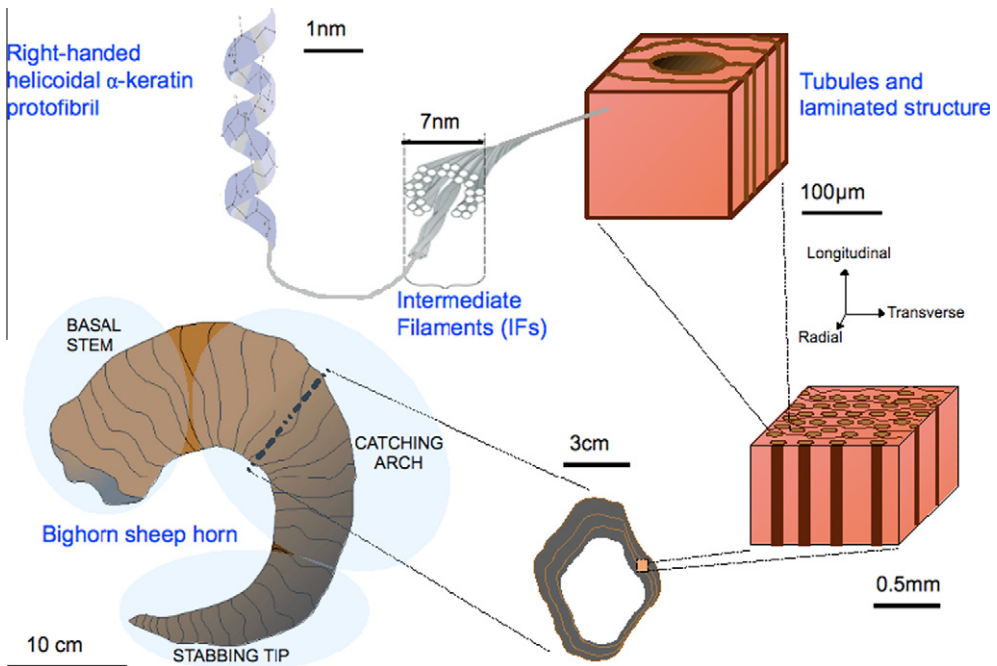


Fig. 54. Hierarchical structure of bighorn sheep horn (*Ovis canadensis*): The horns show a spiral fashion with ridges on the surface, which correspond to the seasonal growth spurts. Horns are composed of elliptical tubules, embedded in a dense laminar structure. Each lamina has oriented keratin filaments interspersed in a protein-based matrix. These filaments are two-strand coiled-coil rope polypeptide chains (intermediate filament types I and II) helically wound assemble forming 'superhelical' ropes of 7 nm in diameter. Taken from [83].

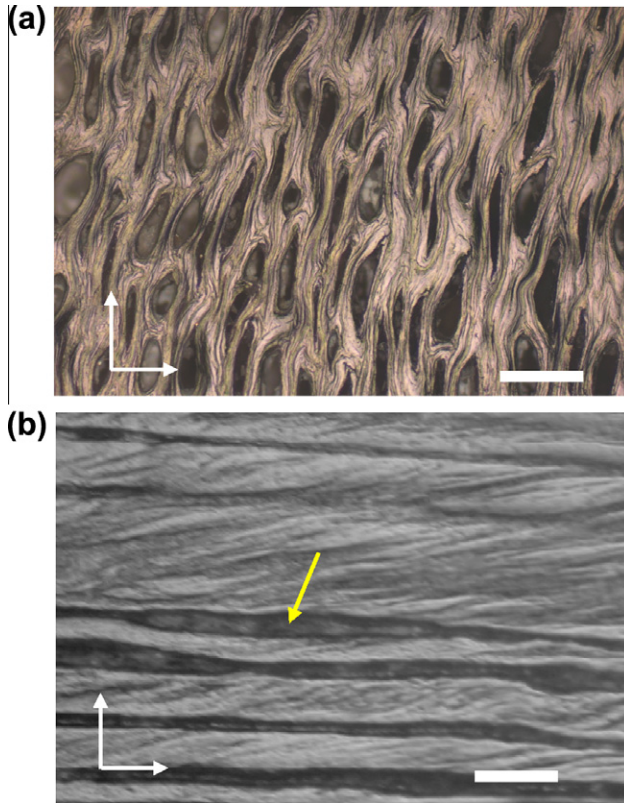


Fig. 55. Optical micrographs of the ambient dried horn: (a) cross-section showing the dark elliptical-shaped tubules and (b) longitudinal section showing the outline of the parallel tubules (Scale bars = 200 μm , yellow arrow points to a tubule). Taken from [83].

is a three-dimensional, laminated composite that consists of crystalline, fibrous keratin embedded in an amorphous keratin matrix, and has a porosity gradient across the thickness of the horn. Optical micrograph of the transverse section in Fig. 55a shows a lamellar structure with elliptically shaped porosity interspersed between the lamellae. The lamellae are $\sim 2\text{--}5\ \mu\text{m}$ thick with the pore sizes ranging from 60 to 200 μm along the long axis of the pores. This porosity results from the presence of tubules that extend along the length of the horn, as shown in the longitudinal section in Fig. 55b.

Kitchener and co-workers [265–270] were the first to provide insights into the fighting behavior of various species in the bovidae family. Mechanical property measurements (strength, stiffness, work of fracture revealed that horns are capable of high energy absorption before breaking and that hydration is important for decreasing the notch sensitivity. The maximum impact force of a big horn sheep can be calculated from the mass, velocity, and deceleration: 3400 N [268]. Kitchener further calculated the critical crack length for crack propagation to be $\sim 60\%$ of the transverse dimension of the horn, indicating the superior flaw sensitivity of the material. The specific work of fracture was found to vary along the length of the horn: for fresh waterbuck (*Kobus ellipsiprymnus*) horns they were found to range from 10 to 80 kJ/m^2 . This work of fracture is greater than most other biological and synthetic materials (antler 6.6 kJ/m^2 ; bone 1.6 kJ/m^2 ; glass 5 J/m^2 ; mild steel $>26\ \text{kJ}/\text{m}^2$) [265]. This was attributed to crack arrest and deflection mechanisms such as delamination and keratin fiber pullout. Kitchener [266] examined the effect of hydration on the elastic modulus of horns from the oryx (*Oryx gazella*). They considered the structure of the horn as a chopped fiber composite, where the crystalline α -keratin fibers (40 nm long) were embedded in an amorphous keratinous matrix. Applying the Voigt

model and using a chopped fiber composite analysis with a volume fraction of fibers of 0.61, they predicted a value of the elastic modulus close to the experimental value, indicating that a fibrous composite model of horn keratin is a reasonable assumption. The elastic and shear modulus decreased significantly with an increase in the moisture content [266,267]. The keratin fibers were not affected, rather the matrix swelled with the water, which decreased the elastic and shear moduli. Warburton [271] earlier had determined on a sheep horn that moisture severely decreased the elastic modulus, reducing it by as much as 75% with 20 wt.% water (compared with dry horn).

Tombolato et al. [83] studied microstructure, elastic properties and deformation mechanisms of desert bighorn sheep, *Ovis canadensis*. Compression and bending tests were performed in both hydrated and ambient dried conditions. The elastic modulus and yield strength are anisotropic and correlated with the orientation of tubules. Three-point bending tests showed that the elastic modulus and strength are higher in the longitudinal orientation (tubules parallel to the long dimension of the specimen) than those in the transverse orientation (tubules parallel to the long dimension of the specimen). An optical micrograph taken from the central region of the hydrated samples tested in three-point bending in the longitudinal direction is shown in Fig. 56a. Toughening mechanisms, such as delamination and crack bridging are observed. In Fig. 56b, the fracture surface from a longitudinally oriented sample shows numerous tubules surrounded by concentric lamellae. The compressive deformation mechanisms of horn in three orientations (longitudinal, transverse, and radial) are summarized in Fig. 57. Lamellar microbuckling is observed in longitudinal and transverse orientations while collapse of tubules is the main deformation mechanism in the radial orientation. Trim et al. [84] investigated the mechanical behavior of bighorn sheep horn under tension and compression in hydrated and dry conditions. They found that tensile failure occurred by matrix separation followed by fiber pull-out (Fig. 58a). The horn keratin failed in a brittle manner in the dry condition while

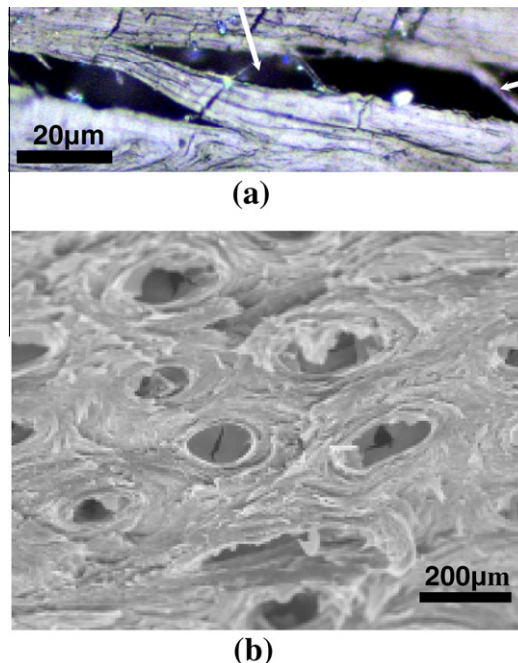


Fig. 56. Micrographs of a ram horn: (a) optical micrograph taken from the central region of the hydrated samples tested in three-point bending in the longitudinal direction. Toughening mechanisms of delamination and crack bridging are observed. (b) SEM micrographs of the three-point bending test fracture surface from a longitudinally oriented sample in ambient dried conditions. The microstructure is characterized by numerous tubules, with concentric rings surrounding them. Taken from [83].

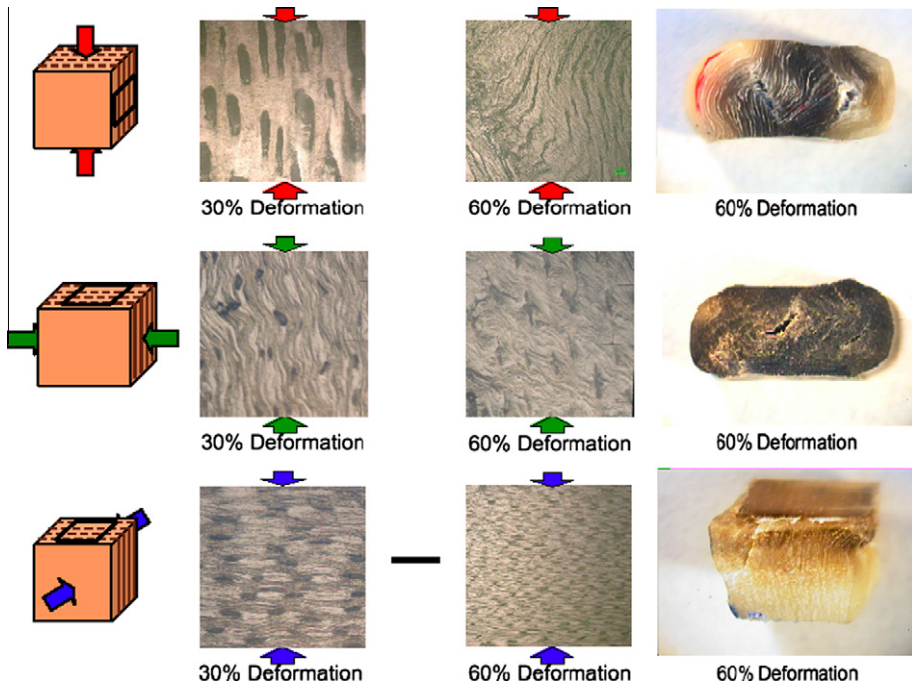


Fig. 57. Optical micrographs of the deformation of ambient dried horn (*Ovis canadensi*) at 30% and 60% strain for (a) longitudinal, (b) transverse and (c) radial directions. Pictures on the right show the accumulated damage in the samples. Taken from [83].

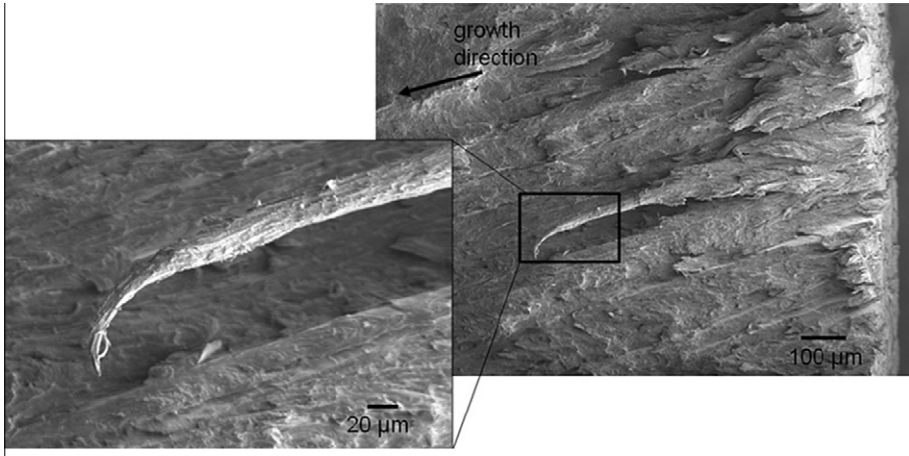
wet horn keratin was much more ductile. Compressive failure occurred by microbuckling followed by delamination (Fig. 58b), in agreement with Tombolato et al. [83].

The rhinoceros horn is another example of biological structural material composed of α -keratin. Ryder [272] observed that the tubules, 300–500 μm in diameter with a medullary cavity of $\sim 20 \mu\text{m} \times 60 \mu\text{m}$ in major and minor axis, respectively, in the horn were slightly coarser than that of equine hoof (20 $\mu\text{m} \times 40 \mu\text{m}$), and there was little intertubular material. Hieronymus et al. [273] found that, unlike the horns of other ungulates, the rhinoceros horn does not have a bony core. Thus, it can be sawed off to protect the animal against poaching. The rhinoceros horns consist of tubules embedded in the amorphous keratin matrix, as shown in Fig. 59.

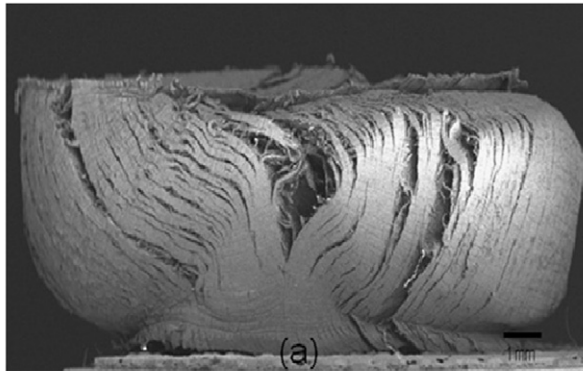
Lee et al. [274] investigated dynamic mechanical behavior of a wide range of biological materials (abalone nacre, elk antler, armadillo carapace, bovine femur, steer and ram horns) and compared them with synthetic composites using a drop weight impact testing systems. The impact strengths of horns are the highest among biological materials, as shown in Fig. 60, confirming the exceptional energy absorbing capability of horn.

2.4. Hoof

Hooves are the most similar biological material to horns and have been the subject of the largest body of scientific literature. Hooves contain tubules $\sim 220 \times 140 \mu\text{m}$ in major and minor axis, respectively, with a medullary cavity of $\sim 50 \mu\text{m}$. These tubules are oriented in the longitudinal direction (parallel to the leg). The keratin forms in circular lamellae ($\sim 5\text{--}15 \mu\text{m}$ thick) surrounding the tubules, as shown in Fig. 61 [275]. It was concluded that the tubules serve only a mechanical function – to increase crack deflection, thereby increasing the toughness, making the equine hoof a highly fracture resistant biological material [275,276]. Hooves must support large compressive and impact loads



(a)



(b)

Fig. 58. (a) SEM micrographs of fracture surface of horn keratin tested in tension showing fiber pull-out; (b) micro-buckling and delamination after compressive deformation. Adapted from [84].

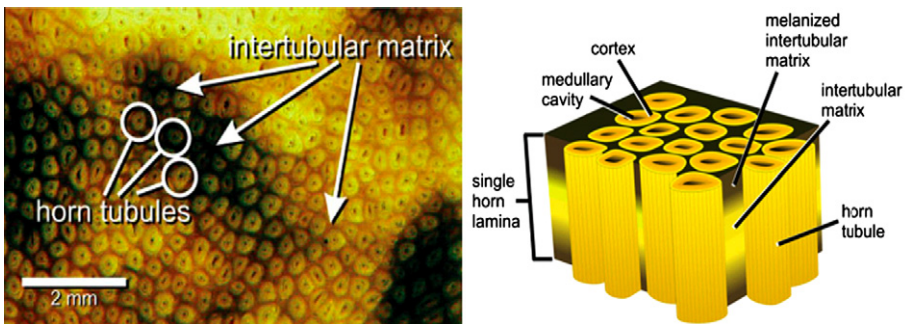


Fig. 59. Optical micrograph of the white rhinoceros horn, showing tubules and the intertubular matrix along with illustration indicating microstructural features. Adapted from [273].

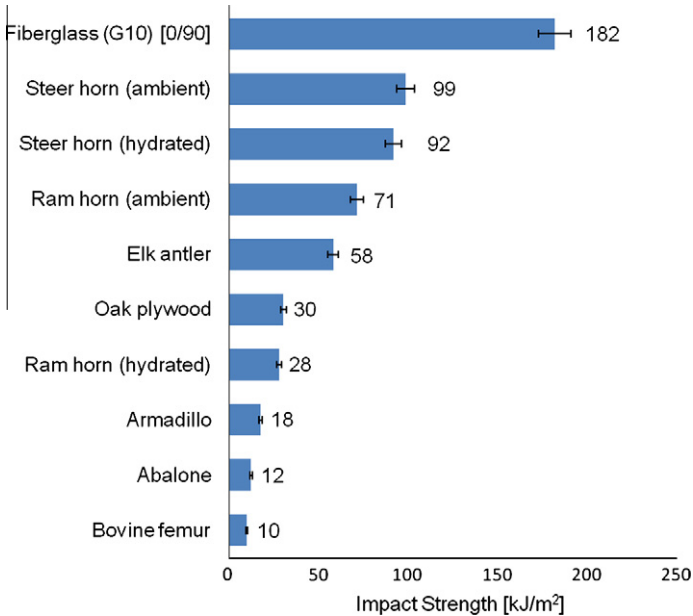


Fig. 60. Comparisons of impact strength among structural biological materials and synthetic composites from drop weight tests. Taken from [274].

and provide some shock absorption from the impact. The most thorough studies have been from Gosline and co-workers [275–279]. The hoof keratin is described as a nanoscale composite comprised of IFs as fiber oriented reinforcement of a hydrated keratin matrix, as shown in Fig. 6. Bertram and Gosline [278] measured the effect of hydration on tensile and fracture properties. They found the stiffness to decrease in the hydrated condition, ranging from 14.6 GPa (ambient) to 0.4 GPa (100% relative humidity, RH). Water penetrates the intertubular matrix as well as the amorphous polymer surrounding the keratin fibers, acting as a plasticizer thereby reducing the density and stiffness of the material [7]. This might have saved Europe from the onslaught of Mongolian hordes in the thirteenth century. The horses moved preferably over dry or frozen terrain and the soft and water soaked European soil was a deterrent for them, since the hooves were not protected by horseshoes.

The J -integral toughness was found to be maximum at 75% RH (22.8 kJ/m²). [275,276] tested stiffness, tensile strength, and work of fracture, in fully hydrated conditions, to correlate IF volume fraction and alignment with mechanical properties. They found that stiffness increased toward the outer hoof wall, ranging from 0.30 GPa at the inner region to 0.56 GPa on the outer surface of the hoof wall, despite the porosity increase in that direction. The increase in elastic modulus was attributed to an increase in the volume fraction of keratin fibers. Further studies revealed that the stiffness increase was due to IF volume fraction rather than IF orientation. In the tubular material, the IFs are aligned in the tubule direction. However, they are more aligned perpendicular to the tubule direction in the intertubular matrix. These different orientations help resist crack propagation through crack redirection, suggesting that the hoof wall structure evolved to maximize the fracture toughness [276].

Bovine hooves are similar to equine hooves, in both structure and properties [280,281], as shown in Table 6. Baillie and Fitford [282] described the bovine hoof structure as comprised of tubules embedded in intertubular material. Franck et al. [280] determined the tensile, compressive, and bending strengths and stiffness. They are similar to the ones for equine hooves, considering the slightly different moisture content. Clark and Petrie [281] found the fracture toughness for the bovine hooves (J -integral 8.5 kJ/m²) to be lower than for the equine ones (J -integral 12.0 kJ/m²) [277].

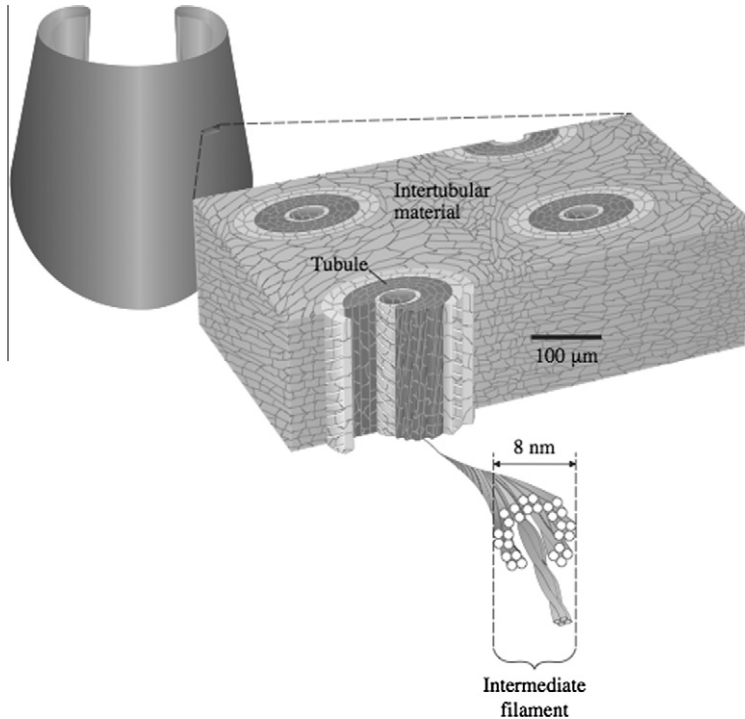


Fig. 61. Illustration of the front view of the equine hoof wall and a sketch of a hoof wall sample showing cells forming tubules and intertubular material. Intermediate filaments are drawn on the lamella of the cut-away tubule. Taken from [276].

The structural differences found between the bovine and equine hooves appear to mainly affect the toughness. The bovine tubule wall is thinner and the keratin cells in the intertubular material are more oriented parallel to the tubules than in the equine hoof. Accordingly, the intertubular IFs are more aligned in the direction of the tubules compared to those of equine hoof. Finally, in the bovine hoof the interaction between tubular and intertubular material appears to be stronger than in the equine hoof, indicating a stronger interface. These differences account for the higher fracture toughness of the equine hoof compared with the bovine hoof.

2.5. Smasher limbs and telsons of stomatopods

Stomatopods (mantis shrimps) use a modified front claw to smash or spear prey. As with other crustaceans, they are composed of chitin. The smashers have a highly developed club (dactyl heel) that can be propelled at accelerations up to 10 g's, reaching speeds up to 23 m/s and generating forces of up to 1500 N. This is reported to be the fastest appendicular striker in the animal kingdom [283]. The telson (tail fan) is another robust appendage that is battered during intraspecies fights. The telson is thumped on by smasher clubs of an opponent until one or the other backs down. Fig. 62a is an illustration of a stomatopod, *Gonodactylus chiagra* [284], showing the locations of the smashing limb and telson. Fig. 62b shows high-speed photographs of the smashing limb in action; the positions of pre-strike and strike are shown in Fig. 62c and d, respectively.

The smasher limb is so robust that it can be used to break apart mollusk shells and shatter glass aquaria, and may deliver up to 100 strikes per day. Currey et al. [284] found there was a gradient in mineralization across the thickness of the cuticle, with a high concentration of calcium phosphates at the surface, resulting in a hard surface with a tough interior. Although the surface becomes pitted due to the hard strikes, it is replaced by molting every few months. Patek et al. [283] investigated the

Table 6

Comparison of mechanical properties of keratinized structures.

Source	RH (%)	Water content (%)	E (GPa)	σ_f (MPa)	ε_f (%)	Toughness (MJ/m ³)	Reference
Claw, ostrich	0		2.7	90	5.7		[285]
	50		2	69	6.7		[285]
	100		0.1	14	50.5		[285]
Hagfish slime threads		In water	0.006	180	220		[183]
Hair, human	70		1.5				[286]
Hoof, bovine		30	0.4	16.2 14.3 (b)			[280]
Hoof, equine	41		0.2	19.4 (b)			[287]
	100		0.3–0.6	6.5–9.5			[275]
Horn, oryx	0		6.1	137			[266]
	20		4.3	122			[266]
	40		1.8	56			[266]
Horn, bighorn sheep	0		1.5				[271]
	20		2.2				[83]
	10.6		0.81	127 (b)		56	[83]
Nail, human	0		4.34				[288]
	55		2.34				[288]
	100		0.47				[288]
Quill, porcupine	100		3.5				[289]
	65		1.9–2.3	63–170 (c)			[18]
	65		2.7	146	25		[290]
	100		1	60	49		[290]
Quill, hedgehog		Dry	3.8				[291]
		Wet	2.3				[291]
Stratum corneum	26		8.9		1.9		[292]
	68		2.4		7.7		[292]
	100		0.01		140		[292]
Wool, Cotswold	0		5.6				[293]
Wool, Lincoln	65		4.5				[117]
	100		2.5				[117]
		In water	3	150	45		[183]

motion of the smashing limb and concluded that energy is stored and released in a hyperbolic-paraboloid (saddle-shaped) region (Fig. 62c), a configuration that resists local buckling. This was the first description of a biological hyperbolic-paraboloid spring.

Taylor and Patek [294] investigated the impact resistance of the telson through drop-weight impact tests with a small steel ball. The coefficient of restitution was found to be 0.56 with the ball losing most of its kinetic energy during the impact. They concluded that the telson behaves like an inelastic punching bag, dissipating 69% of the impact energy. Fig. 63 shows micro-CT scans of the telson, showing the small ridges (carinae) present on the domed surface. Using high-speed photography, Taylor and Patek [294] observed that the whole telson is compressed through deformation of the regions between the carinae, not the carina itself. The carinae were found to be highly mineralized but surrounded by lower mineralized, thinner saddle-shaped regions, which increased the flexibility of the cuticle between the carinae.

2.6. Woodpecker skull

Woodpeckers can hammer into wood at ~20 times/s with speeds of 6–7 m/s and a surprisingly large deceleration force of up to 1200 g [295,296]. The National Football League has determined that 98 g will cause concussions. Woodpeckers avoid brain injury by the incorporation of several structural features [296]:

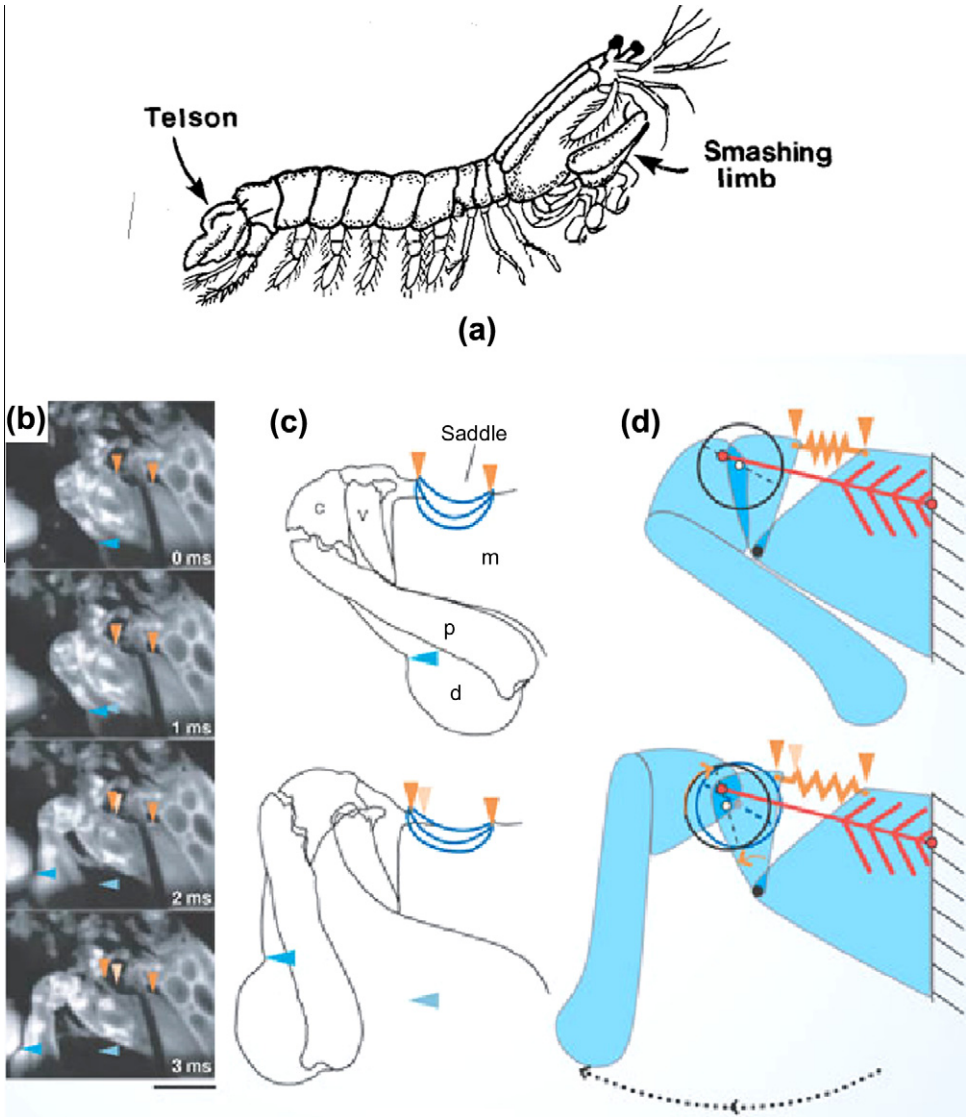


Fig. 62. (a) Illustration of a 10 cm long stomatopod, *Gonodactylus chiagra*. Adapted from [284]. (b) A high-speed image sequence illustrates the distal extension of the saddle (orange triangles) occurring simultaneously with the extension of the smashing heel of the dactyl and propodus (blue triangles) of the peacock mantis shrimp (*Odontodactylus scyllarus*). Scale bar, 1 cm. (c) The compressed (top) and released (bottom) saddle on the smashing limb (segments: m, merus; v, meral-V; c, carpus; p, propodus; d, dactyl). (d) The saddle modeled as a spring (orange) that stores elastic energy to drive the movement. Top, pre-strike phase. The lateral extensor muscle and apodeme (red) pull on the carpus to compress the saddle, while flexor muscles (not shown) engage a click mechanism to prevent extension of the appendage. Bottom, the strike occurs when the latch is released, enabling the saddle to extend and two pivot points to rotate in opposite directions. The meral-V forms a pivot point (black circle) as it rotates distal-ventrally (anticlockwise here) and pushes the second pivot point, the carpal-meral fulcrum (white circle), distally. The isometrically contracted extensor muscle maintains a constant distance between its carpal and meral attachment points (red circles), forcing the carpus to rotate (clockwise here) and driving the dactyl heel towards the prey. Adapted from [283].

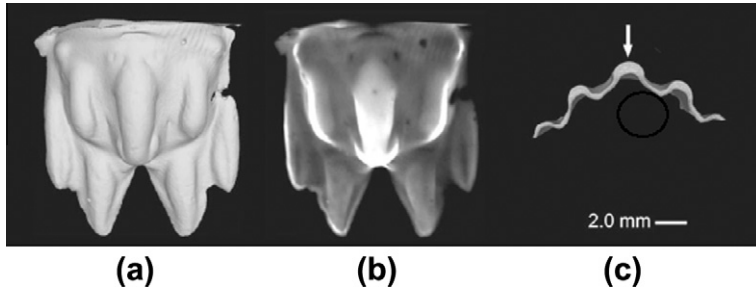


Fig. 63. Micro-computed tomography images of the telson from the stomatopod, *Neogonodactylus wennerae*: (a) surface morphology, (b) relative amounts of mineralization, indicated by the brighter regions and (c) transverse sections showing location of impact of the steel ball. Adapted from [294].

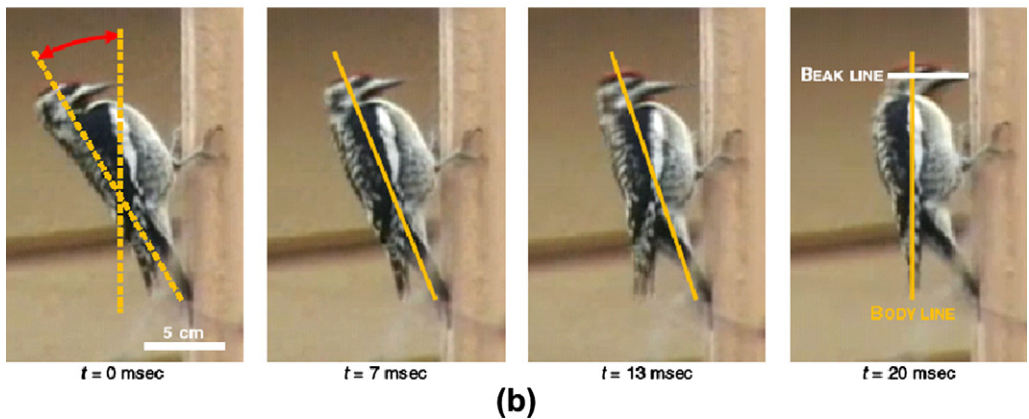
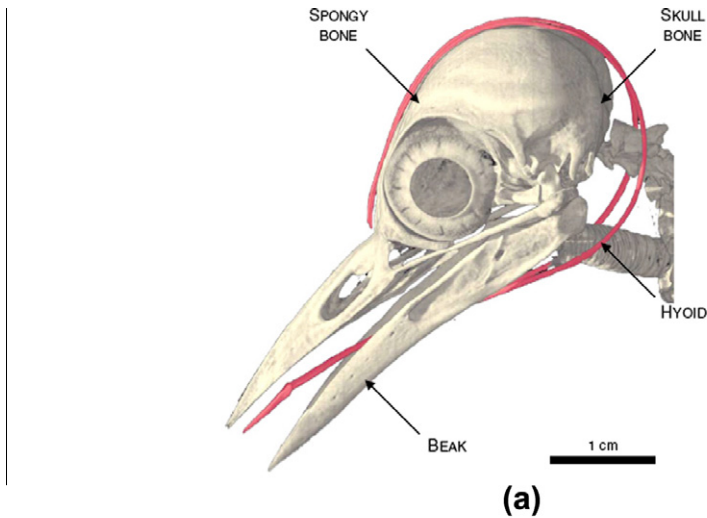


Fig. 64. (a) Head structure of a woodpecker (*Melanerpes aurifrons*) with the hyoid highlighted in red. The spongy bone is in the front of the skull. Taken from (http://www.digimorph.org/specimens/Melanerpes_aurifrons). (b) A red-bellied woodpecker (*Melanerpes carolinus*) showing the perpendicular position of the beak with respect to the wood. The tail keeps the body in balance and as parallel to the wood surface as possible. Taken from [297].

- A hard, elastic beak.
- A small amount of cerebrospinal fluid that reduces fluid transmission of shock.
- The small, smooth brain is tightly enveloped by spongy bone.
- The neck muscles are exceptionally strong, holding the bill rigidly.
- The skull is surrounded by muscles and tendons in a sling-like structure that performs as an isometric shock absorber and distributor, limiting brain movement.

Fig. 64a shows the skull of a woodpecker (*Melanerpes aurifrons*). Outlined in red is the hyoid region in the skull that supports the tongue. The forefront of the skull is composed of spongy bone whereas the remainder is denser bone. This spongy bone is thought to aid in shock absorption. The beak is not only hard, but self-sharpening [295,296,298]. Fig. 64b shows the position the beak and the body during hammering. The woodpecker manages to keep its beak perpendicular to the wood surface while maintaining its body parallel to it. This precise alignment keeps shearing forces in the beak to a minimum. It also wisely chooses soft wood.

3. Defense and armor

The ability to protect one's body from external attack is a basic requirement for animals that are typically slow moving or have no defensive weapons such as talons or teeth. Defensive shields or armors are found in marine and terrestrial species. Mollusk shells are the most common marine species protection structures. The most notable land example is the testudine (turtle and tortoise) shell, which acts as a protective 'house' for the soft animal bodies. Crocodylia (crocodiles, alligators, caymans) also have a tough protective covering embedded with bony segments (osteoderms) that is considerably more flexible than the testudinae. Many fish species have flexible dermal armor as do some mammals, such as the armadillo and pangolin.

3.1. Mollusk shells

Mollusk shells are primarily composed of calcium carbonate. In many species, they form structural arrangements that are 'glued' together by biopolymer adhesives. Mollusk shells have evolved to incorporate various design strategies in the arrangement of calcium carbonate. Fig. 65 shows a classification of the principal shell structures according to Currey and Taylor [61], who classified the microstructures of the shells into nacre (columnar and sheet), foliated, prismatic, crossed-lamellar, and homogeneous complex crossed-lamellar. Kobayashi and Samata [299] expanded this classification, identifying more than ten morphological types of bivalve shell structures. They used the names simple prismatic, nacreous, foliated, composite prismatic, crossed-lamellar structures, among others to describe them. It should be noted that there is a significant variation in this classification. Often, researchers classify the structures into different names according to their own interpretations.

We focus here on three structures: the nacreous structures in the abalone and Araguaia clam shell and the complex crossed lamellar structure of the clam *Saxidomus purpuratus*. Menig et al. [300] and Lin et al. [68] present detailed characterization of the conch. These were investigated by our group. Some shells with the crossed lamellar structure can exhibit a comparable strength to the nacreous structure. The largest flexure strengths reported are 370 MPa for *Haliotis rufescens* [218] and 360 MPa for *Pinctada maxima* [301]. The maximum compressive strengths are 540 MPa for *H. rufescens* ([67], loading perpendicular to lamellae) and 567 MPa for Araguaia river clam ([23], loading perpendicular to lamellae). In general, the strengths of the wet specimens are lower than the strengths of the dry ones, although the toughness of the wet shells is higher.

3.1.1. Abalone

The abalone belongs to a class of mollusks called gastropoda (Greek: *gaster*, stomach; *poda*, feet). The best-known gastropods are terrestrial snails. Abalone falls in the Haliotidae family in the genus *Haliotis*. Out of the 180 known species, *H. rufescens* (red abalone) is the most studied. The lustrous interior of the shell is called nacre (mother-of-pearl). Several hierarchical levels in the structure of abalone

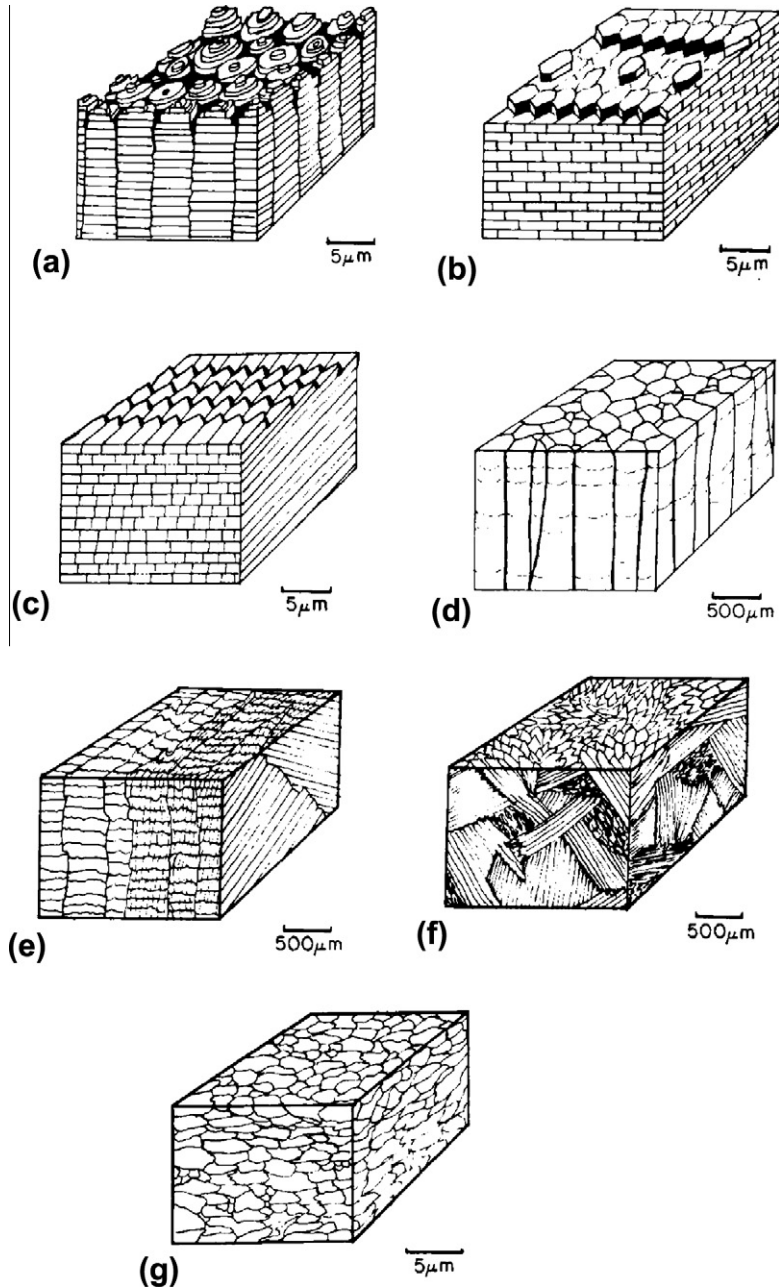


Fig. 65. Currey–Taylor classification of shell microstructures. Notice the difference in size of the structural units between types. The blocks are oriented so that their vertical faces are in the thickness of the shell. The blocks would be loaded in the direction of their longer dimension. (a) Columnar nacre–aragonite. (b) Sheet nacre–aragonite. (c) Foliated–calcite. (d) Prismatic–calcite or aragonite. (e) Crossed-lamellar–aragonite. Cross-foliated structure is similar but made of calcite. (f) Complex cross-lamellar aragonite. (g) Homogeneous (from [63]).

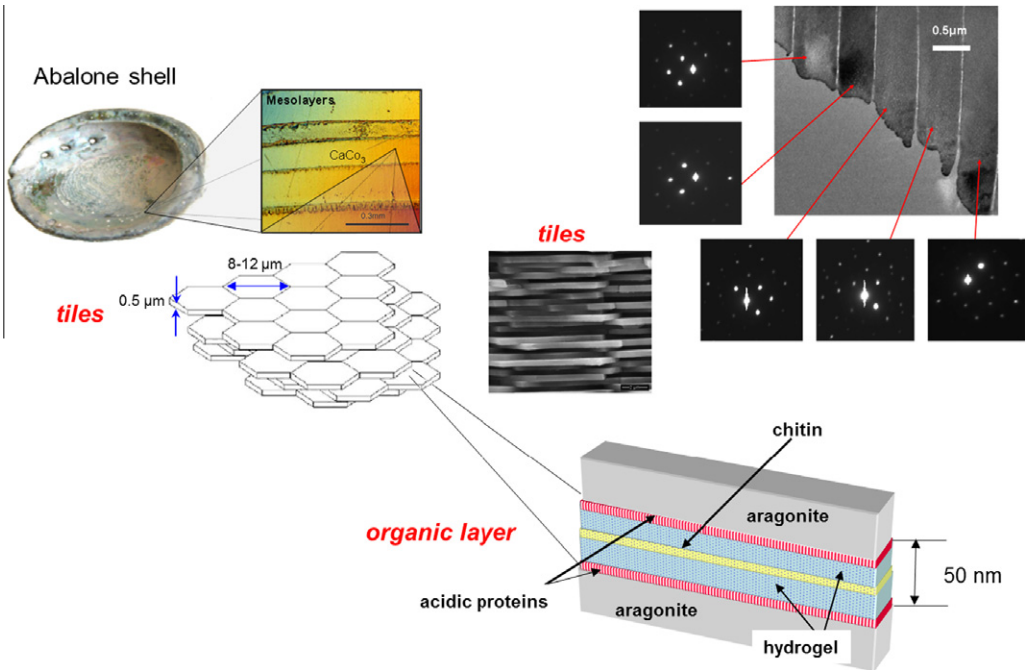


Fig. 66. Hierarchical structure of the abalone shell: The first level is mesolayers of $\sim 300 \mu\text{m}$ in thickness, separated by $\sim 20 \mu\text{m}$ organic. The $\sim 300 \mu\text{m}$ bands are composed of tablets of aragonite (orthorhombic CaCO_3) (95 wt.%) held together by a 10–50 nm layer of an organic biopolymer (5 wt.%) and by mineral bridges $\sim 50 \text{ nm}$. The hexagonal tablets, 8–10 μm in length and $\sim 0.4 \mu\text{m}$ thick, grow in the c -direction exposing the (001) face. TEM selected area diffraction patterns of adjacent tiles show same crystallographic orientation. The organic layer between the tablets has a sandwich structure comprised of a central core of chitin fibers and surface layers with pores 5–80 nm in diameter. Adapted from [21].

can be observed in Fig. 66. The first are mesolayers of $\sim 300 \mu\text{m}$ in thickness, separated by $\sim 20 \mu\text{m}$ organic, designated as the 'green organic' or 'brown organic' [302], which was identified simply as conchiolin. Typically, the age of the abalone is found by counting the 'green' organic rings in the shell; the number deposited per year depends on the species. The $\sim 300 \mu\text{m}$ bands are composed of interdigitated tablets of aragonite (orthorhombic CaCO_3) held together by a 10–50 nm layer of an organic biopolymer of chitin and proteins (5 wt.%) and by mineral bridges. The hexagonal tablets, 8–10 μm in length and $\sim 0.4 \mu\text{m}$ thick, grow in the c -direction exposing the (001) face. Because of the c -axis orientation, nacre has been described as a 'mosaic single crystal' [303]. The thickness of the tablets is on the order of the wavelength of light, which creates the beautiful colored, iridescent surface of nacre. The organic layer between the tablets is comprised of a central core of chitin fibers sandwiched by acidic proteins and has a porous structure with pores $\sim 50 \text{ nm}$ (5–80 nm) in diameter.

3.1.1.1. Abalone biomineralization: nacre growth. Detailed descriptions of the growth of the mollusk shell can be found in [56,69,70,304–321]. The shell grows in the extrapallial fluid from ions and organic matter secreted from the epithelial cells of the mantle. As shown in Fig. 67, the growth is as follows: a biopolymer (periostracum), 100–200 nm thick, is formed, which nucleates prismatic calcite in the (104) direction. Calcite, a polymorph of CaCO_3 (rhombohedral) is the more stable phase under ambient conditions. Fig. 68 shows the calcite forming the external layer of the abalone shell [322]. Its microstructure consists of equiaxed grains with a size of approximately $50 \mu\text{m}$. The calcite external layer will not be discussed in detail here because it does not have mechanical properties that are as outstanding as the aragonite. The interface between the calcitic and aragonitic structure is clear in the figure. After a certain thickness is achieved (0.5–3 mm), there is a spontaneous nucleation of

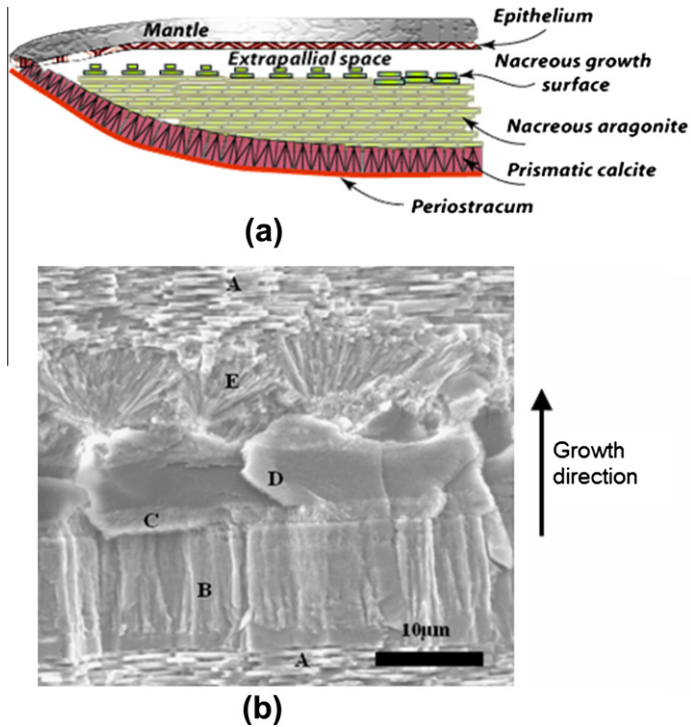


Fig. 67. (a) Structure of the *H. rufescens* shell showing external prismatic calcite and internal nacreous aragonite. Taken from [56]; (b) cross-sectional SEM micrograph showing sequential growth of abalone nacre: regular aragonite tile formation (A), columnar growth of aragonite (B), organic mesolayer (C) and spherulitic growth of aragonite (E) (from [321]).

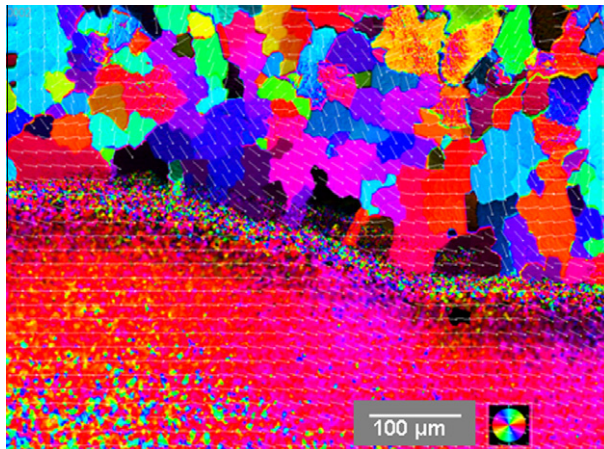


Fig. 68. Calcitic layer in abalone shell; the polycrystalline nature of the layer with equiaxed grains having approximately 50 μm diameter is clearly seen under polarized light (Figure taken from [323]).

aragonite that grows laterally until convergence and the process repeats until aragonite layers are ~300 μm thick [67]. The aragonite structure has a ‘brick and mortar’ configuration (see Fig. 66). The

bricks are the aragonite tablets and the mortar is an organic layer, a sticky substance that holds the tiles together, as shown in Fig. 66.

Fig. 67b shows the growth interruption with the formation of the thick organic mesolayer (C and D); it is preceded by the formation of “blocky” aragonite (B), that transitions from A. Deposition of the so-called ‘green’ organic layer is followed by the formation of spherulitic aragonite (E) ending with the final ‘brick and mortar’ aragonite layers (A). Menig et al. [67] referred to the aragonite-tiled structure interrupted by the green organic layer as mesolayers or growth bands. The construction of the mesolayers, interrupted by the blocky aragonite/green organic, continues during the life of the animal, with some shells reaching up to 30 cm in diameter.

Following the work of Watanabe [304] and Wada [305] who inserted glass cover slips between the mantle and the shell and observed the initial growth, the UC Santa Barbara group showed that these ‘flat pearls’ produced on glass cover slips inserted in the extrapallial fluid grew rapidly (26× that of natural nacre) so the entire structure (organic layer to nacreous layers) could be observed after only a few weeks [312]. This work, along with research from others, has led to a considerably greater understanding of the growth mechanism of the shell [319,321,324]. However, systematic experiments by Lopez [70] demonstrated that the growth velocity in the ‘flat pearl’ technique is affected by water temperature and feeding.

Another important feature of nacre is the topology of the surface of the growing front. As shown in Fig. 69, the tablets grow with a terraced cone structure [309,312,319,321]. Before a layer of aragonite tablets has grown to confluence, there are nucleation events that occur above this base layer, leaving

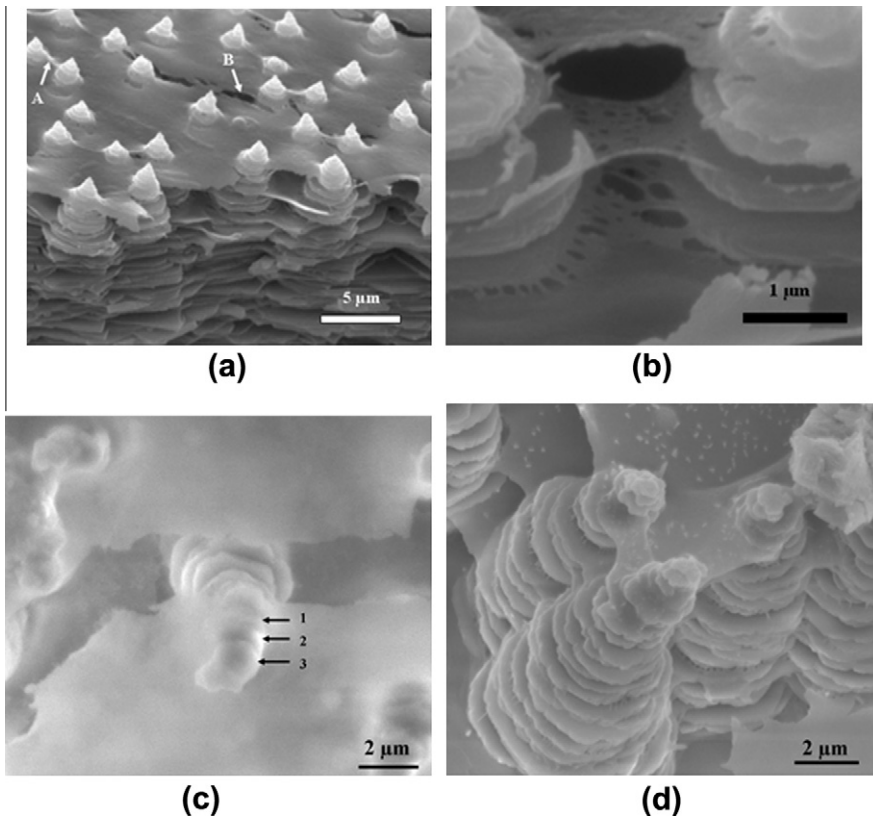


Fig. 69. Growth front of aragonite: (a) terraced cone structure and (b) close up view, showing the porous organic layer. Taken from [69]; (c and d) top views showing terraced cones. Taken from [325].

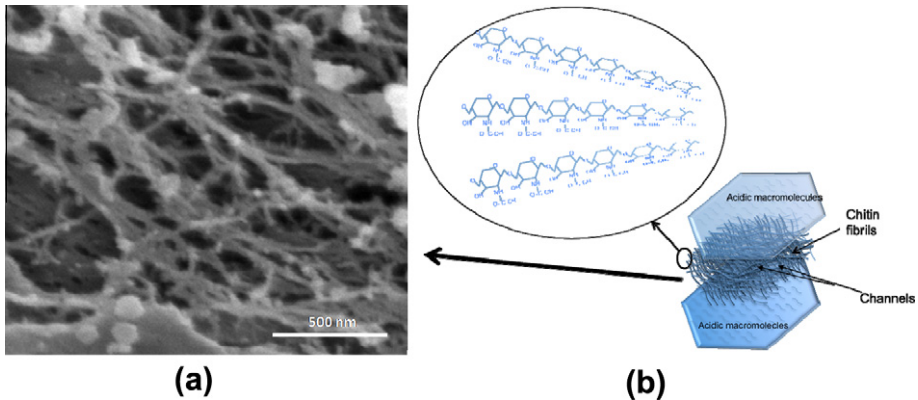


Fig. 70. (a) Randomly oriented chitin macromolecule fibrils (b) schematic representation of organic intertile layer consisting of central layer with randomly oriented chitin fibrils sandwiched between acidic proteins. Adapted from [325].

stacks of smaller diameters, as shown in Fig. 69. This unique, ordered growth of the tablet stacks has been observed and analyzed by several groups [69,310,312,321]. In Fig. 69b, the organic sheet is observed to display a random network of pores. These pores expand when the organic layer is stretched at a rate higher than the overall strain. Thus, nanometer sized holes can grow easily to the sizes shown in Fig. 69b. In Fig. 69c and d one can see the cracked top organic layer that reveals the stacks underneath. Arrows numbered 1, 2, and 3 indicate the top three layers in the stacks that are under the top organic layer. It was proposed by Checa et al. [326] that there is a top layer, or surface membrane, which protects the growing nacre surface from damage. This top layer, surface membrane, contains vesicles that adhere to it on its mantle side. They secrete interlamellar membranes from the nacre side. They observed that this top layer is thicker than the other ones and that it somehow forms the scaffold in which the tiles are mineralized.

The organic layer consists of a core of randomly oriented chitin fibers sandwiched between acidic macromolecules. Fig. 70 shows the configuration. The SEM micrograph shows a layer that was exposed after demineralization of the shell. The organic layer is not continuous, but contains holes (Fig. 71a). These holes have diameters of ~ 50 nm and have an important function in the structure and mechanical properties of aragonite. Seen in Fig. 71b is a schematic showing the growth process. The organic layer containing holes is periodically deposited on the growth surface. The calcium and carbonate ions can penetrate through the organic layer. In this manner, the growth in the *c* direction (perpendicular to the tile surface) is slowed down periodically. The holes in the organic layer enable mineralization to continue from one layer to the next. Hence, tiles on one stack have the same crystallographic orientation. The holes are filled with minerals and form the mineral bridges which connect the different layers. The process by which this sequence takes place is shown in a schematic fashion in Fig. 71b [70]. The SEM insert in this figure shows that the intertile layers (horizontal) are much clearer than the intertabular layers (vertical). The manner in which the chitin fibrils are generated from the internal portion of the mantle (epithelium) is shown in Fig. 72b. This layer has channels in which the fibrils are assembled. They are subsequently (and periodically) squeezed out of the channels and penetrate into the extrapallial layer, being deposited on top of the stacks. A few fibrils embedded in the channels are marked in Fig. 72a. The fundamental sequence of mineral and organic layer deposition that leads to the formation of the tiled arrays is still not completely understood. Thus, it is proposed that these channels create the chitin, which is subsequently deposited on the growing surface to retard the aragonite crystal growth in the *c*-direction. The cells in the epithelium contain microvilli that were originally identified by Nakahara [327]. These microvilli have dimensions of 100 nm diameter and 400 nm height, which correlate well with the pattern of holes in the organic layer and the thickness of the tiles, as shown in Fig. 73. Thus, we propose that a mechanism of templating is taking place.

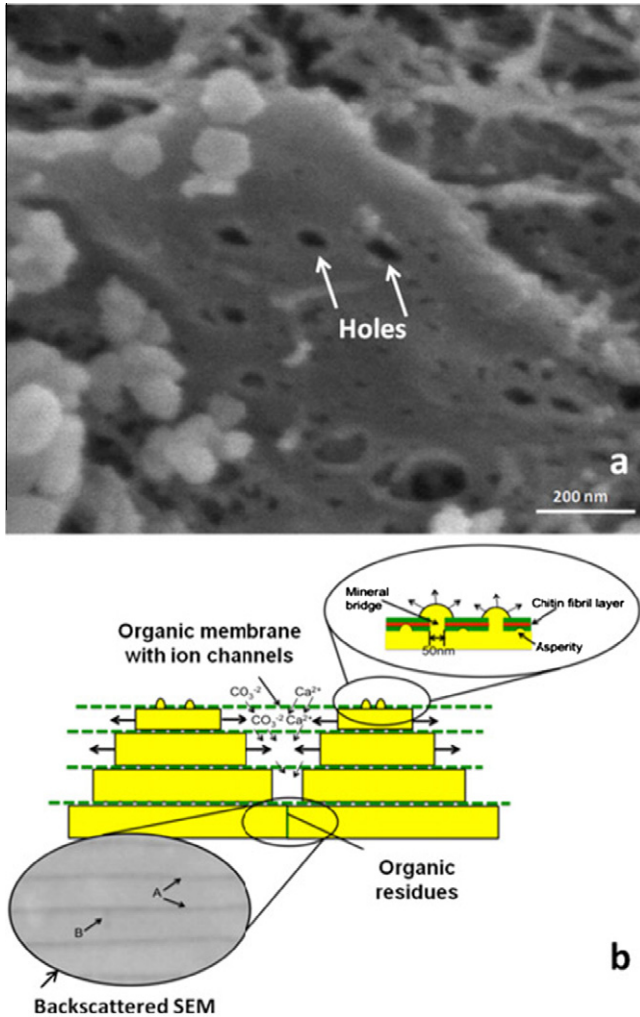


Fig. 71. (a) Thin intertile organic layer showing holes; (b) proposed mechanism of growth of nacreous tiles by formation of mineral bridges; organic layer is permeable to calcium and carbonate ions which nourish lateral growth as periodic secretion and deposition of the organic intertile membranes restricts their flux to the lateral growth surfaces. Arrows A designate organic interlayer imaged by SEM; arrow B designates lateral boundary of tile (schematic representation taken from [325]).

Preliminary experiments conducted by our group [70] have shown significant effects of water temperature and feeding on biomineralization. Fig. 74 shows that the terraced cone configuration that is characteristic of the formation of nacre takes place after 1 week in 21 °C. The growth after 1 week is still columnar when the temperature of the tank is lowered to 15 °C (Fig. 74b).

The organic layer between the aragonite layers has a complex layered configuration and was first discovered and analyzed by Grégoire [315,320,332–336] and subsequently studied notably by Wise [309], Weiner's group from the Weizmann Institute in Israel [328–331] and UC Santa Barbara [316,337,338]. The fibrous and porous two-dimensional network of insoluble proteins (Fig. 70c) is composed of polysaccharide β -chitin with fibrils of ~ 8 nm in diameter [316,339] (see Figs. 66 and 70). β -Chitin is very similar to cellulose in chemistry and organization and is a highly cross-linked biopolymer containing Lustrin A as the major protein [337]. A silk hydrogel sandwiches the insoluble

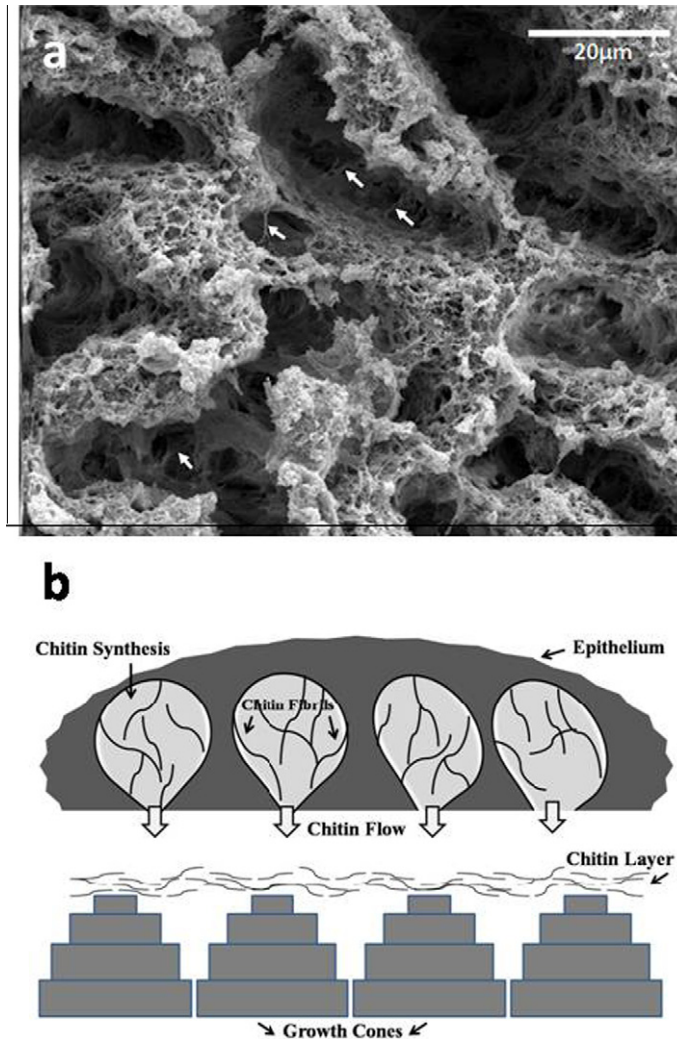


Fig. 72. (a) Array of channels and occasional chitin fibrils in epithelium (marked by arrows); (b) hypothetical mechanism of generation of chitin fibrils and 'squeezing' them onto growth surface. Taken from [70].

matrix and is composed of hydrophobic protein sheets in a β -configuration, similar to that of spider silk [320,337]. The silk-like proteins are amino acids rich in glycine and alanine [328,334,337,340]. Finally a group of hydrophilic proteins, rich in aspartic acid are in direct contact with the aragonite tablets [314,320,333]. As discussed above, the insoluble matrix stabilizes the growth, phase and orientation of the tablets [314,337]. Several groups have identified the soluble proteins that promote either aragonite or calcite formation [314,317,338,341–344]. A matrix protein involved in aragonite formation was recently reported by Suzuki et al. [345]. The protein, which is acidic and contains both an aragonite-binding domain as well as a chitin-binding domain, was found to concentrate calcium carbonate and induce aragonite crystal formation.

Wada [303] first proposed the existence of mineral bridges from one tablet to the next, which grow through the pores in the organic layer; this been further investigated by other researchers [69,309,314,316,321,346–348]. Fig. 75a shows bridges marked by arrows. The density and dimensions

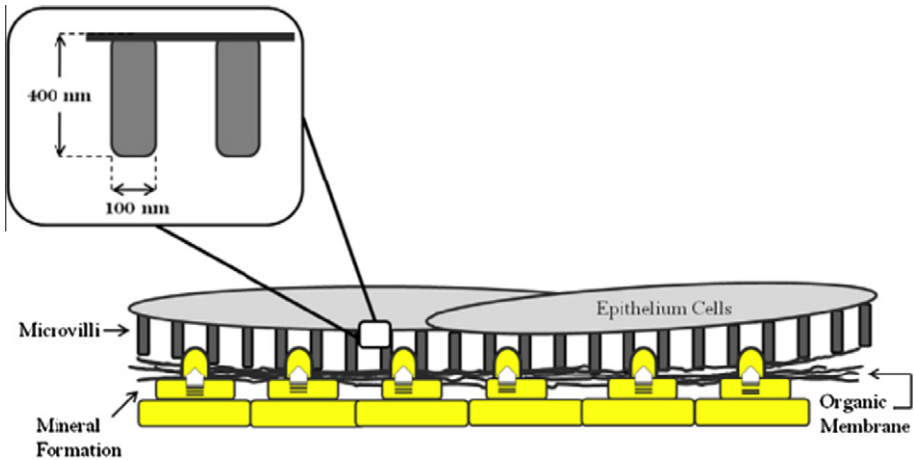


Fig. 73. Microvilli in epithelial layer of mantle facing growth surface of nacre (Courtesy of M.I. Lopez).

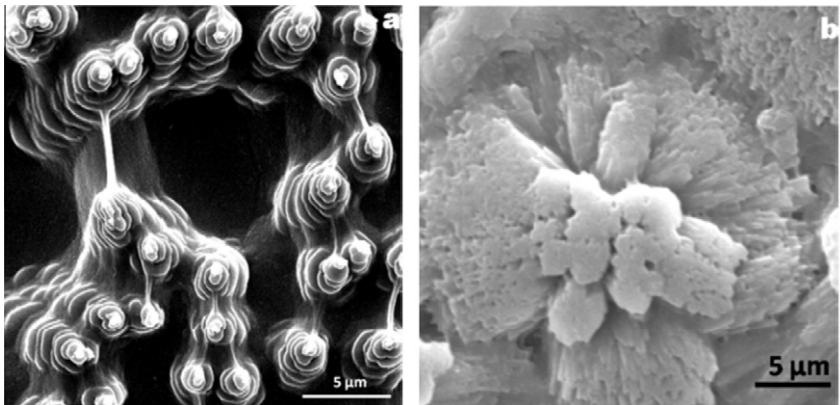


Fig. 74. SEM micrographs of sequential growth results 1 week after implantation of glass slides: (a) growth at 21 °C, (b) growth at 15 °C. Taken from [70].

of the mineral bridges have been under scrutiny in recent years, as they have been proposed to significantly affect the toughening of nacre. First, Schäffer et al. [316] determined in the organic matrix of *H. rufescens*, the density of pores in the sheet to be $97 \mu\text{m}^{-2}$ with an average pore diameter of 30 nm. The density of the mineral bridges was estimated to be $115 \mu\text{m}^{-2}$, which indicates that the pores possess mineral bridges. The average height of the bridges, $\sim 30 \text{ nm}$ [309,339] is similar to the thickness of the organic layer and the number of bridges/tablet was calculated to be ~ 1600 . Song et al. [349] demonstrated that the presence of the mineral bridges decreased the amount of crack extension in the organic matrix by a factor of four. Meyers et al. [69] also verified the presence of mineral bridges (Fig. 75a) and proposed that these bridges have more significance on the mechanical properties of nacre than the organic matrix. Manne et al. [313] did not observe mineral bridges in *H. rufescens* during *in situ* etching experiments with the AFM, however this was the only study that could not verify the presence of mineral bridges.

The presence of nanoasperities on the (001) surface of aragonite has long been documented [69,303,310,313,339,350,351] and an example is shown in Fig. 75b. Schaffer et al. [316] identified 'protrusions' on the surface of aragonite tablets that were suggested to be broken mineral bridges.

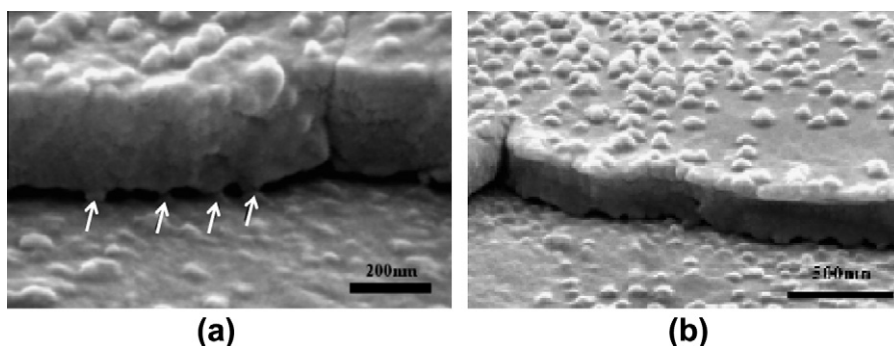


Fig. 75. (a) Examples of mineral bridges (arrows) and (b) nanoasperities on the surface of an aragonite tablet. Taken from [69].

The protrusion density was found to be $115 \mu\text{m}^{-2}$, which is similar to the density of porosity in the organic matrix ($95 \mu\text{m}^{-2}$) and the density of Song's [346,349] asperities ($105 \mu\text{m}^{-2}$). Others have identified the asperities to be 30–100 nm in diameter and 30 nm high [339], 20–30 nm high [347] and densities of $100 \mu\text{m}^{-2}$ [339,351] and $60 \mu\text{m}^{-2}$ [69]. From all of these data, it appears that only a small fraction of asperities form complete and effective bridges. The tensile strength of the nacre perpendicular to the tiles was measured [348] and it was established that there are only ~ 30 – 40 bridges per tile.

As Jackson et al. [55] suggested, the presence of organic matrix not only nucleates CaCO_3 , but also determines the mechanical properties of the shell. The current view is that the bridges ensure the same crystallographic orientation between tiles on different layers and that there is no need for nucleation at each level.

3.1.1.2. Mechanical properties. The nacre is an inorganic/organic composite material with a brittle phase of 95% ceramic. Such materials are not considered in the traditional composite materials literature. In fact, the mechanical properties are expected to be almost identical to what is found for the pure ceramic, if the rule of mixtures holds. However, the work of fracture of nacre was shown to be $3000\times$ higher than single crystal aragonite [55], which was attributed to the presence of the organic layer and its features. This surprising result has led investigators to further study the mechanical properties of nacre.

The mechanical properties of nacre were first studied by Currey [61,62,352–355] followed by Jackson [55,356,357], Heuer [50,358], Sarikaya and Aksay [37,318,324,359–361], Meyers [67–69,348] and Evans [34,218,350]. Some of the mechanical properties of nacre are summarized in Table 7. In some ways, nacre behaves as a typical ceramic: the modulus of rupture (MOR) is higher than the tensile strength and compressive strength higher than tensile strength. However, the ratio of compressive to MOR is low ~ 2 – 3 , which is unusual compared with monolithic ceramics that have ratios >10 [67]. The large variation in the MOR can be fitted with Weibull statistics [67], as is performed with other ceramics. Nacre also behaves as an atypical ceramic—the work of fracture is at least $1700\times$ that of pure aragonite (in contrast to Jackson's $3000\times$ [55]) and the fracture toughness is up to $10\times$ as large. Currey [62] calculated the Griffith flaw size to be $2 \mu\text{m}$ in nacre. This indicates that the tablets of $\sim 0.5 \mu\text{m}$ thick could not contain critical flaws that would grow under loads that would cause nacre to fracture. These remarkable characteristics of nacre have been attributed to the ordered, hierarchical structure. It has been suggested that the aragonite tablets are the primary load-bearing component where the load is transferred through the organic by a shear-lag mechanism [339,355]. Simple examination of the crack features shows two obvious toughening mechanisms. A high degree of crack tortuosity is shown in Fig. 76a and clear evidence of tablet pull-out is shown in Fig. 76b. The length of the crack path divided by the linear distance has been measured to be ~ 3 [62], although it appears to be greater in Fig. 76a. The tortuosity is a result of to crack blunting, branching and deflection and delamination of the layers. Additionally, crack deflection at the mesolayers was detected under compressive loading [67]. Crack tortuosity alone cannot account for the orders of magnitude increase in toughness

Table 7
Mechanical properties of nacre.

	(\perp) ^a	(//) ^a	Ref.
Young's Modulus (GPa)	70		[55]
	69		[349]
Young's modulus for calcite	137		[61]
Young's modulus for aragonite	81		[347]
	100		[55]
Modulus of rupture (MOR) (MPa)	116	56	[62]
	170		[55]
	185–220		[324]
	197	177	[67]
	233	194	[217,218]
	200		[355]
Tensile strength (MPa)	70–110		[62]
Compressive strength (MPa)	540	235	[67]
Compressive strength aragonite (GPa)		11	[339]
Work of fracture (J/m^2)	390–1240 ^b		[55]
	1650	800	[62]
	1000		[357]
Work of fracture for aragonite	0.6		[357]
K_{Ic} ($\text{MPa}\sqrt{\text{m}}$)	4–10		[37]
	4.5		[355]
	5.0	4.6	[55]
K_{Ic} of calcite = $1 \text{ MPa}\sqrt{\text{m}}$			
Vickers hardness (GPa)	2.0		[355]
Hardness (GPa)	10–11		[38]
Vickers hardness of calcite = 3.3 GPa = 3 on Moh's scale			[324]
Elastic modulus of organic sheet	0.01		[21,69,85]
	4		[349]

^a Force applied or // to layers.

^b Depends on span/depth ratio.

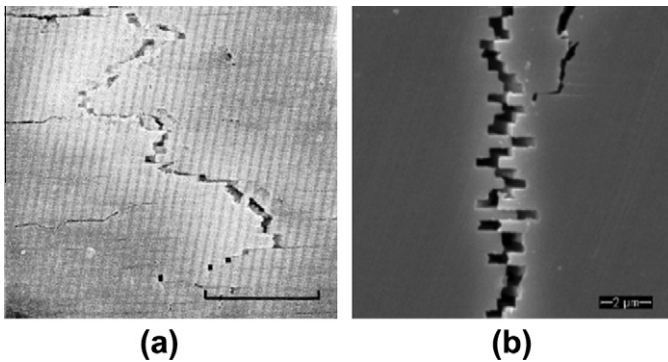


Fig. 76. Two apparent toughening mechanisms (a) crack tortuosity in nacre, taken from [55] and (b) tablet pullout (not tablet fracture), taken from [68].

of nacre over the pure ceramic. Consequently, other mechanisms must be operating in nacre. Sarikaya et al. [37,324,361] were the first to describe toughening mechanisms in nacre and pointed out the major toughening mechanisms as:

- crack blunting, branching, deflection,
- microcrack formation,

- tile pull-out,
- crack bridging.

Meyers et al. [69,87,324,348], Evans et al. [218,350], Bruet et al. [339] and Barthelat et al. [347] followed this work, and identified other mechanisms:

- plastic deformation of the tiles [62,339,35],
- plastic microbuckling under compressive loads [67],
- tile sliding [69,87,324,348],
- viscoplastic shear of organic [319],
- plastic deformation of the asperities [339],
- mineral bridges [69,318,319,346],
- friction from asperities (broken mineral bridges) [218,347,350].

The contribution of the organic layers can be several forms:

- organic viscoelastic stretching of ligaments [37,55,358] [67,68],
- strain hardening of ligaments [362],
- crack bridging of ligaments [55],
- high degree of adhesion of the organic phase to inorganic [55,350,351].

Fig. 77 summarizes the three major modes of opposition to sliding: presence of asperities, occurrence of a viscoelastic layer and presence of mineral bridges. These three mechanisms all contribute significantly to nacre toughness. Greater details of the analysis are provided elsewhere [69,99,348]. It is important to emphasize the controlled sliding of the tiles is such that their fracture strength is not reached. If the tiles were more rigidly bonded, the fracture would transition to the tiles, with a decrease in toughness.

The contribution of the organic layer to the toughness has still not been quantified. An example of ligament formation is shown in Fig. 78. Ligaments are observed between tile layers (a) and between

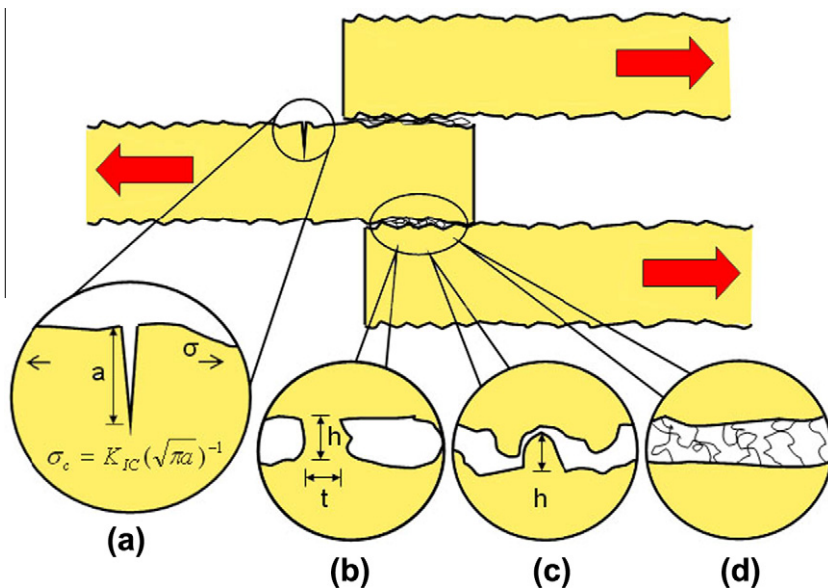


Fig. 77. Different mechanisms providing tensile strength to nacre parallel to tile plane by (a) cracking of tiles; (b) mineral bridges; (c) asperities; (d) organic layer acting as viscoelastic glue. Taken from [348].

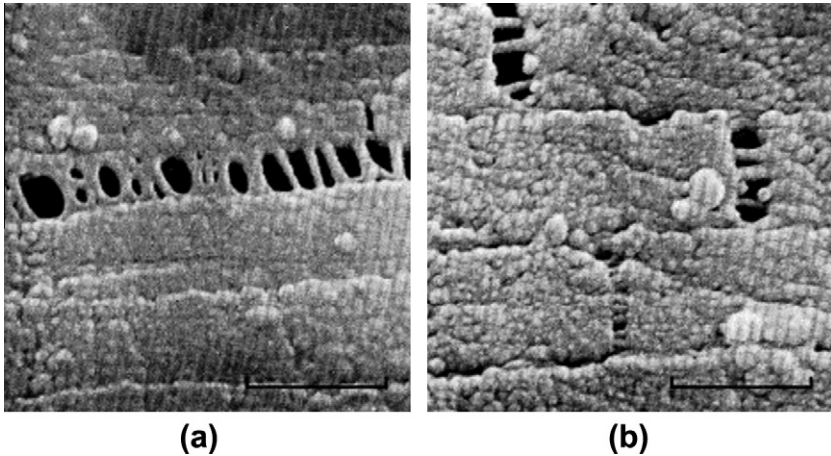


Fig. 78. Ligament stretching from the organic phase between tablets of aragonite. (a) Parallel ligaments between layers and (b) perpendicular ligaments between abutting tablets ligaments are observed. Scale bar = 0.6 μm . Taken from [55].

abutting tiles (b). From Jackson et al. [55] who supposed that the organic layer was primarily responsible for the enhanced toughness to Meyers et al. [69] who conclude that it is only important as a glue, and Evans et al. [350] who believe it is a lubricant, the contribution of the organic layer to the toughness has not yet been ascertained.

Examination of Fig. 78 reveals that the mineral bridges must be broken and the organic filaments are holding the tablets together. The length of the filaments is 190 nm, which far exceeds the height of the mineral bridges (~ 30 nm). Barthelat, Espinosa and co-workers [363–365] proposed that the wedge effect, produced by an irregular tile thickness, was important in toughening. However, we failed to see this thickness variation in our abalone nacre studies.

3.1.2. Clams

3.1.2.1. *Saxidomus purpuratus*. This shell is a representative of bivalves, which have two valves connected by a junction. Clams and mussels are bivalves. The *Saxidomus purpuratus* shells show a crossed lamellar structure in the inner and middle layers and a fibrous/blocky and porous structure composed of nanoscaled particulates (~ 100 nm diameter) in the outer layer. Fig. 79 shows the overall view of the *Saxidomus*' structure with an external layer that is blocky/fibrous and an internal layer crossed lamellar structure. The crossed lamellar structure is composed of domains of parallel lamellae with approximate thickness of 200–600 nm. These domains have approximate lateral dimensions of 10–70 μm with a minimum of two orientations of lamellae in the inner and middle layers. Neighboring domains are oriented at specific angles and thus the structure forms a crossed lamellar pattern. The microhardness across the thickness was lower in the outer layer because of the porosity and the absence of lamellae. The bending and compressive strengths were analyzed by means of Weibull statistics. The mean bending strength at a probability of failure of 50%, 102–104 MPa, is shown for two valves of the same shell in Fig. 80. There is little difference between the two valves (halves) [366].

The compressive strength (~ 50 –150 MPa) is on the same order as the tensile strength (Fig. 81). The compressive strengths were obtained along three loading orientations and the results vary somewhat. Indeed, the *Saxidomus*, as well as most shells, has anisotropic mechanical properties that are the result of the aligned microstructure. The compressive and flexure strengths are significantly lower than abalone nacre, in spite of having the same minerals. The lower strength may be attributed to a smaller fraction of the organic interlayer. The fracture path in the specimens is dominated by the orientation of the domains and proceeds preferentially along lamella boundaries.

3.1.2.2. *Araguaia river clam*. The Araguaia river clam is found to exist in fresh water of the Amazon basin. In its natural environment it sits upright with its flat bottom base seated in the floor of a sandy

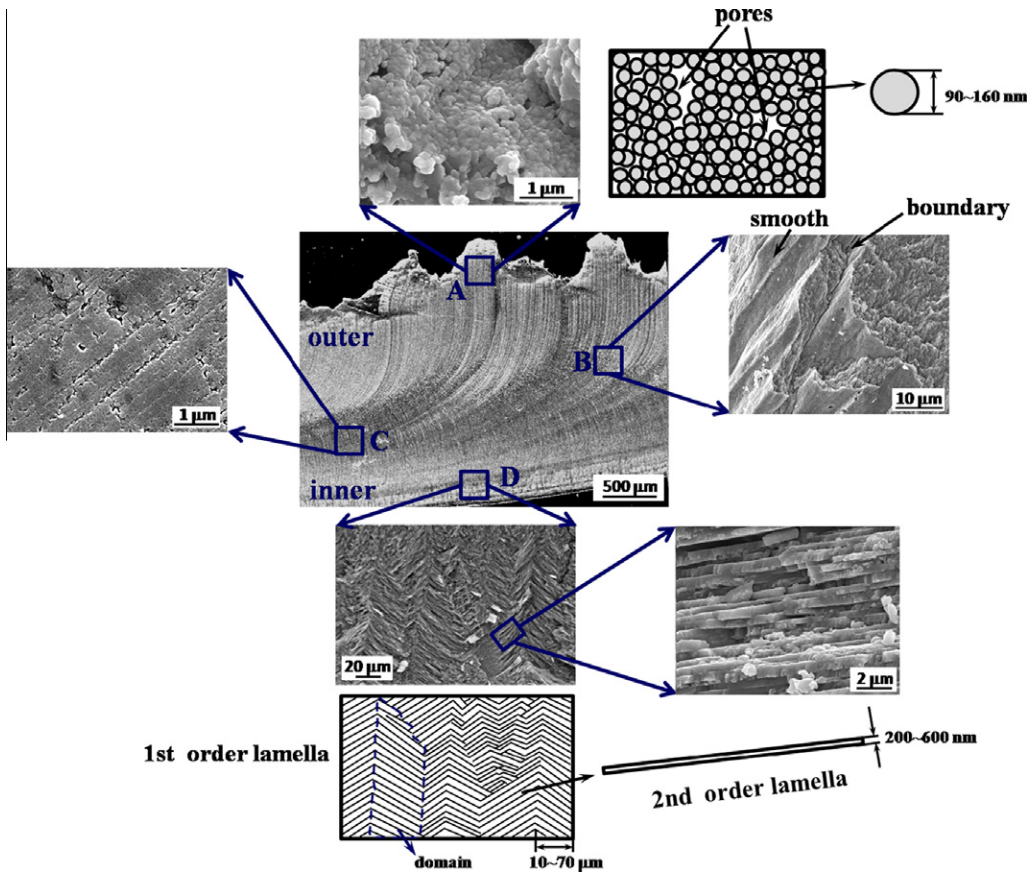


Fig. 79. Overall view (center) of section of *Saxidomus purpuratus* shell showing different morphologies in inner layer (bottom), middle layer (left) and outer regions (top and right). Taken from [366,367].

river bed. Protruding upward, its shell makes a finlike arc (Fig. 82a) cutting through the current of the moving river, allowing the capture of passing food. Although the environment of this freshwater bivalve differs greatly from that of the red abalone, their structures both consist of aragonite tiles. However, there are significant differences in this structure and, thus, differences in their mechanical response. The shell of the Araguaia river clam consists of parallel layers of calcium carbonate tiles, approximately 1.5 μm in thickness and 10 μm in length. This is three times thicker than the previously described abalone nacre, implying a higher inorganic to organic ratio. Furthermore the uniformity of the tiles is far less apparent in the shell of the river clam than the abalone. Although a uniaxial alignment is observed along the *c* axis (the axis parallel to the direction of growth), the consistency of layer thickness is less pronounced than its saltwater counterpart. The wavy structure is observed in Fig. 82c and can be seen throughout. Indeed, the “wedging” mechanism proposed by Barthelat et al. [364,365,22] for nacre is quite applicable for the Araguaia river clam shell and not to the abalone, which exhibits regular tile thickness. The Barthelat mechanism requires irregular thickness, by which the tiles effectively act as wedges, their displacement requiring dilatation.

The greatest difference between the two structures, however, is at the macrolevel. In contrast to the abalone shell, there were no observed mesolayers marking inorganic growth interruption. Fig. 82b provides an optical view of the cross section of the river clam shell. The missing growth bands and decreased organic composition lead to a more classically brittle ceramic. While mechanisms such as crack deflection and microbuckling are characteristics of the abalone nacre, they were lacking in the

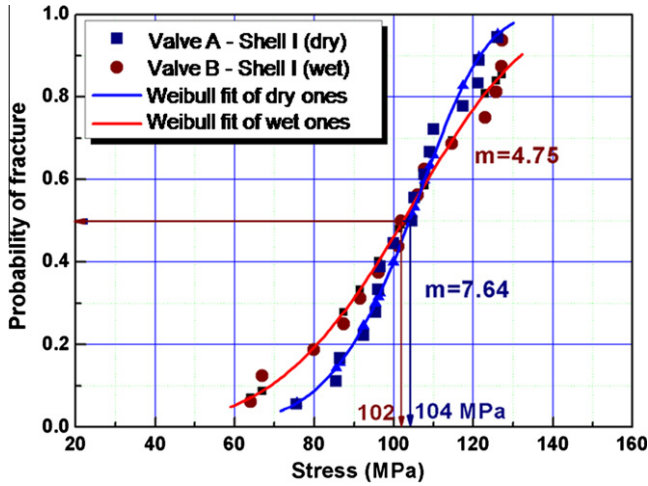


Fig. 80. Weibull plots of bending strengths from two valves of a same *Saxidomus purpuratus* shells. Note that differences are minor. On the other hand, different shells have significantly different bending strengths. Taken from [366].

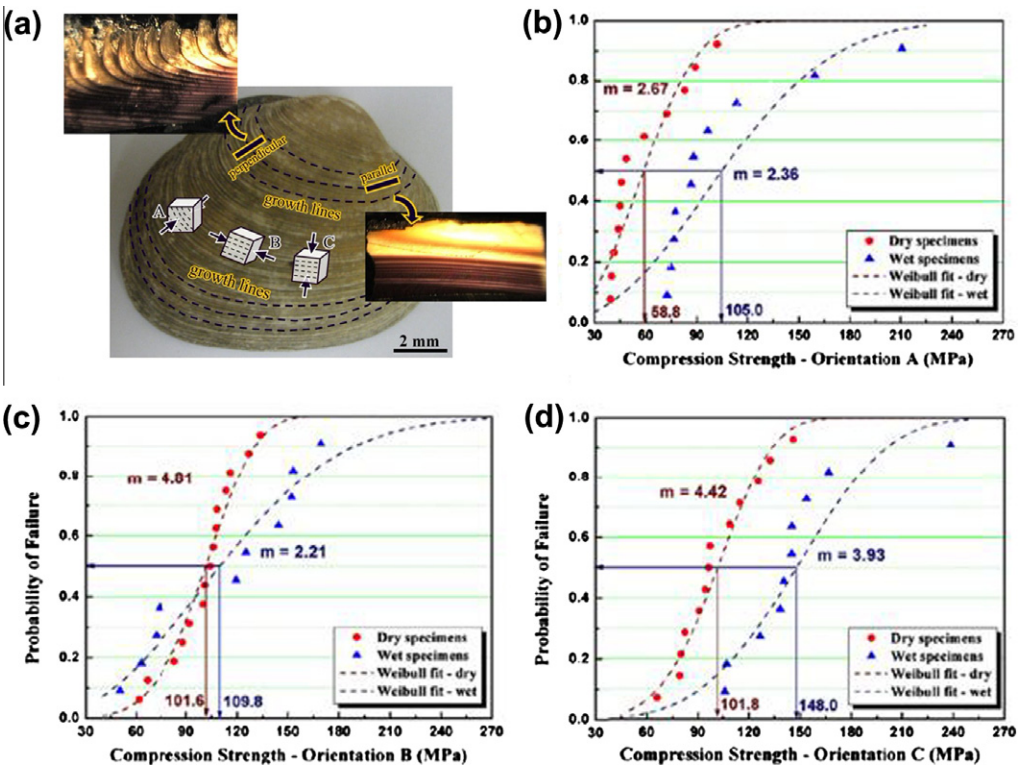


Fig. 81. (a) Cross sections parallel and perpendicular to growth lines of *Saxidomus purpuratus* shell and the orientations of compression specimens: Orientation A, loading perpendicular to the shell surface; Orientation B, loading parallel to the shell surface and growth lines; Orientation C, loading parallel to the shell surface and perpendicular to the growth lines. (b)–(d) Compression test results in Orientations A, B, and C, respectively. Taken from [367,368].

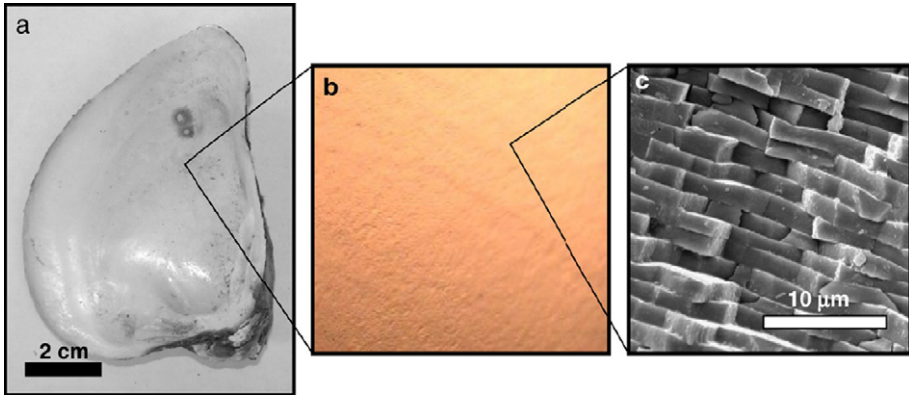


Fig. 82. Structural hierarchy of the Araguaia river clam. (a) Note flat bottom which ensures that the clam stays upright on the sandy river bed. (b) There is little or no observable mesolayers at the mesoscale. (c) Thick wavy tiles of 1.5–2 μm in thickness and 10 μm in length are observable at the microscale. Taken from [23].

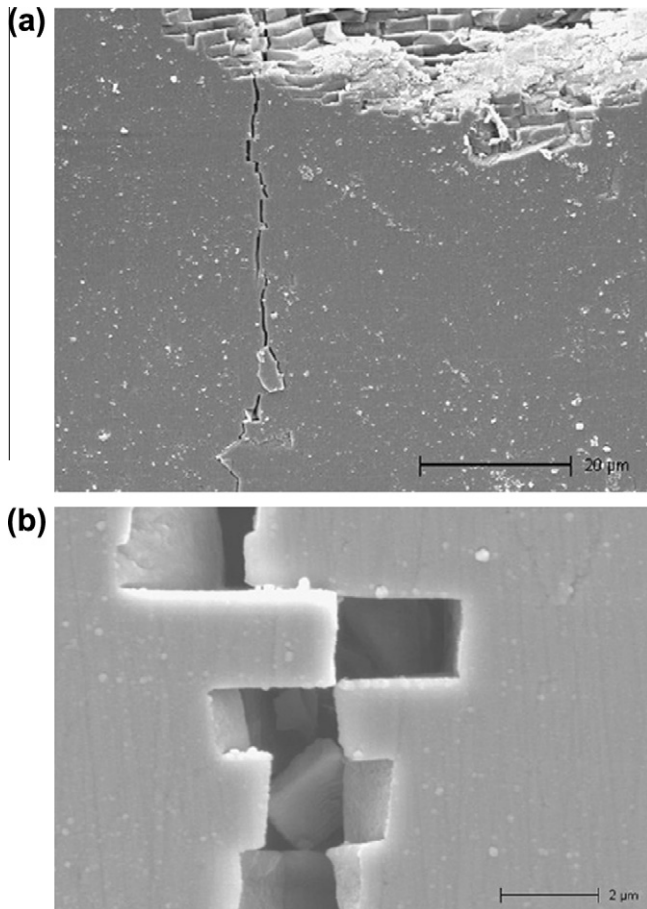


Fig. 83. Crack propagation in fractured Araguaia river clam shell; (a) through-tile fracture; (b) region with tile pull-out.

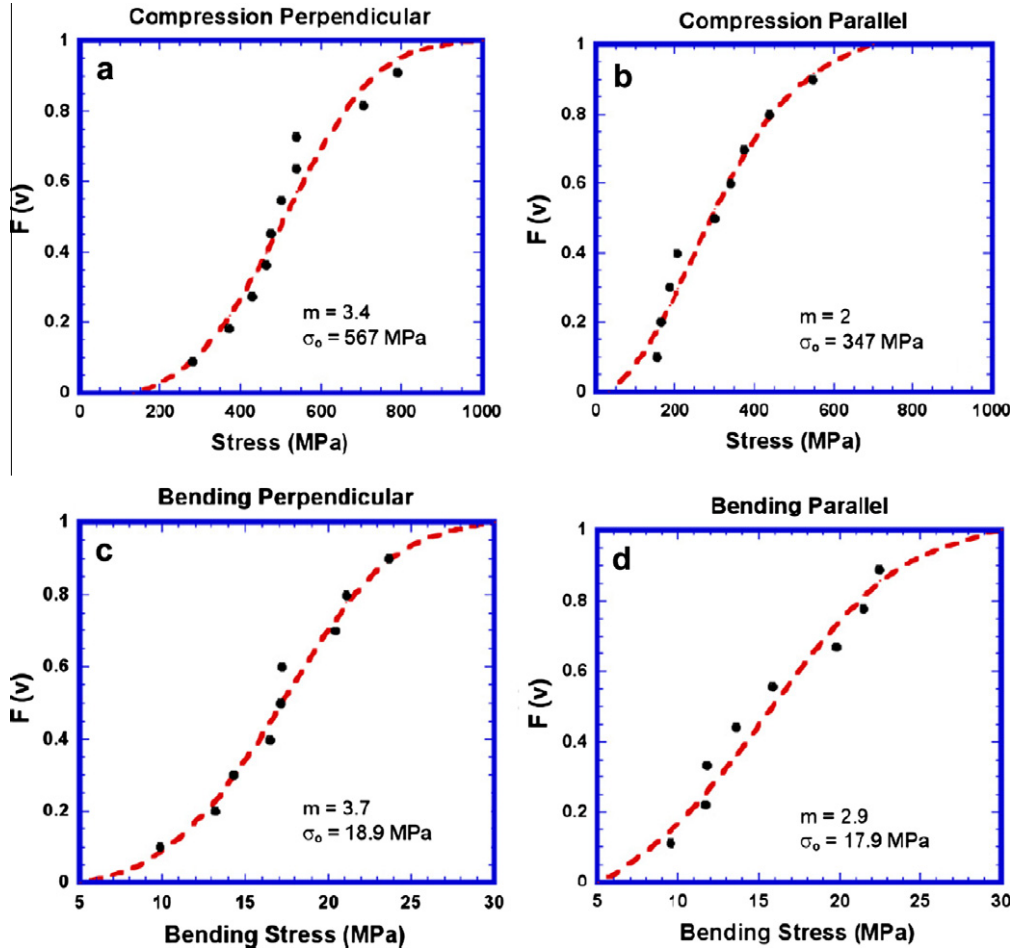


Fig. 84. Strength (Weibull) distribution for Araguaia river clam: (a) compression perpendicular to layered structure; (b) compression parallel to layered structure; (c) three-point bending perpendicular to layered structure; (d) three-point bending parallel to layered structure. m = Weibull modulus, σ_0 = characteristic strength. Taken from [23].

river clam shell. Fig. 83a shows the unobstructed crack propagation in the river clam shell. In some places, plate pullout was observed (Fig. 83b), but this was not the most common response. Three point bending and quasistatic compression tests were conducted in various orientations of shell microstructure. The compressive strength when loaded perpendicular to the layers is 40% higher than when it is loaded parallel to them. The 50% fracture probability is 567 MPa for the perpendicular direction and 347 MPa for the parallel (Fig. 84a and b). This compressive strength is roughly 20–35 times greater than flexural strength of 15 MPa observed in both directions of loading (Fig. 84c and d). This ratio of compressive to flexural strength is far greater than what is found in abalone nacre, and represents a brittle ceramic. This may be attributed to the lack of the macroscaled organic laminate mesolayers.

In conclusion, there is a great variation in the strength of shells, correlated to their structure. A complete tabulation of values is given by Yang et al. [366,367].

3.2. Sea urchins (*Echinoidea*) and sponge spicules

Another interesting example is the calcite structure of the sea urchin (*Echinoidea*) spines. Sea urchins are found in all marine environments. The spines can be up to 30 cm in length and 1 cm in

diameter and either sharp or blunt [368,369]. The spines are a highly Mg-substituted calcite, $Mg_xCa_{1-x}CO_3$, $x = 0.02-0.15$ with crystallites 30–50 nm in diameter [370]. Substitution of Ca by Mg ions increases the strength of the crystallites; it tends to be at a higher concentration at the base than at the tip. The concentration of Mg is directly related to the water temperature – higher Mg concentrations are found at higher temperatures. The calcite crystal orientation, interdigitated microstructure and self-sharpening capability of sea urchin tooth have recently been investigated by Ma et al. [371,372].

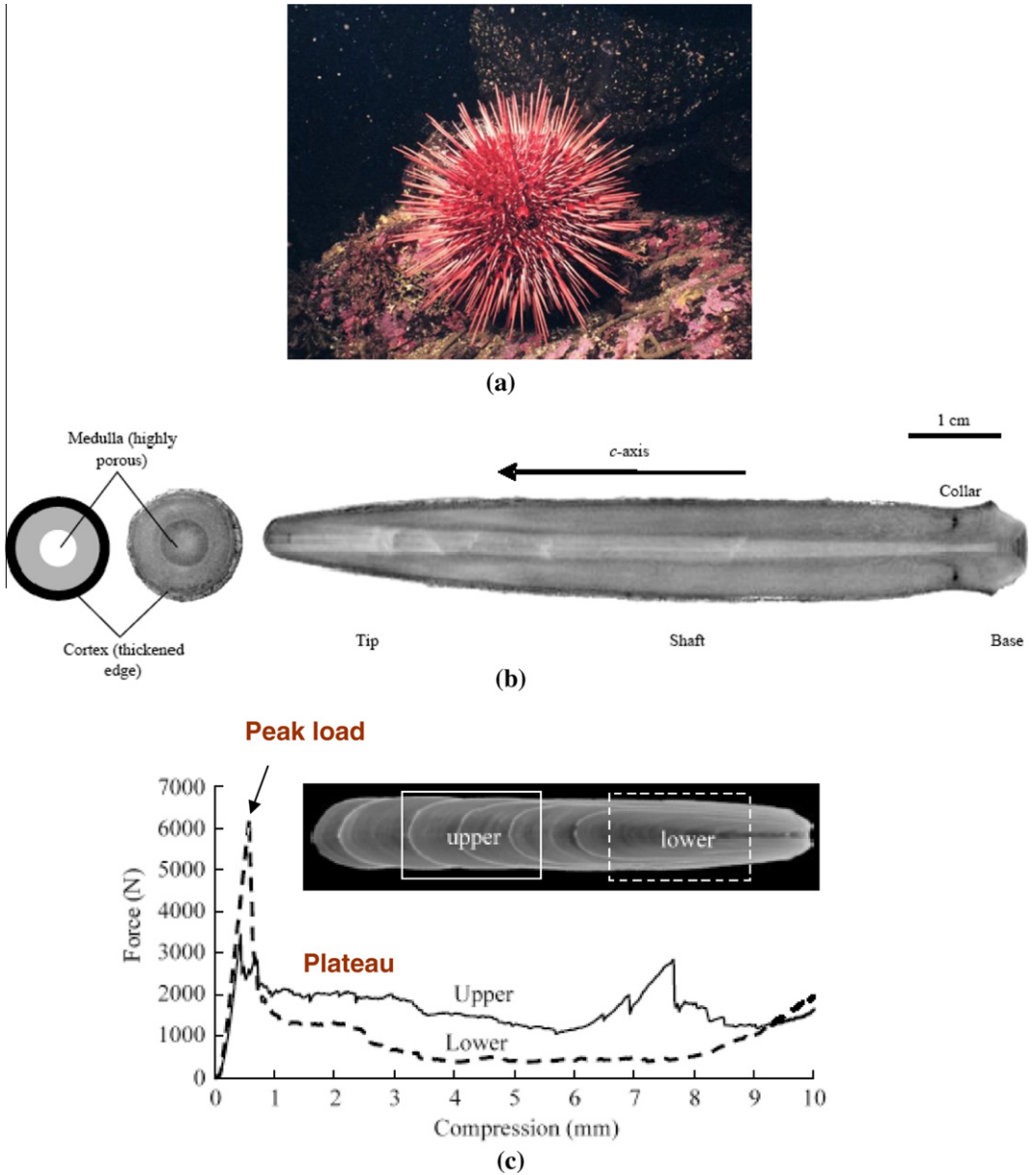


Fig. 85. (a) Photograph of a sea urchin; (b) cross-sectional and longitudinal views; (c) compressive force–deflection curve, showing a peak load and then graceful failure during the plateau region. Taken from [370].

Fig. 85 shows a sketch of the cross section and an X-ray computer tomography micrograph along the length of a *Phyllacanthus imperialis* spine [370]. As shown, there is a gradient in porosity with porosity increasing substantially from $\sim 10\%$ on the surface to $\sim 60\%$ in the medullary core. What can possibly be gained from such a configuration? Because the spines are used for protection, the compressive strength is more important than the tensile strength. The compressive force–displacement curve displays a graceful failure instead of a catastrophic failure typified of monolithic ceramics. Interestingly, the stress–strain curve resembles that of a classical cellular solid, as described by Gibson and

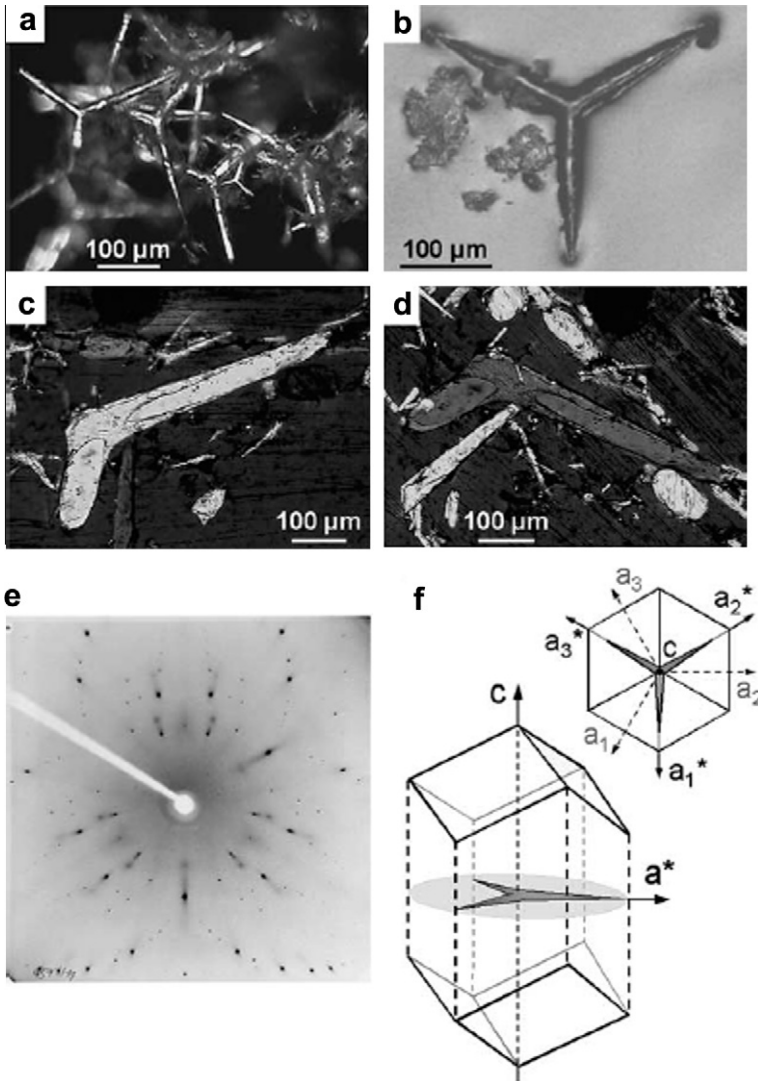


Fig. 86. (a) Sponge skeleton, consisting of an array of spicules; (b) small calcareous spicule of the sponge *Pericharax heteroraphis* (optical micrograph, reflected light); (c) and (d) thin section of variously oriented spicules embedded in resin. In transmitted light with crossed polarisers the spicules behave as single-crystals. The large spicule in the center, embedded and cut obliquely to the plane of the actines, is shown in bright orientation (c) and rotated by 45° in extinction orientation (d), with the extinction being incomplete; (e) X-ray diffraction (Laue pattern) confirms the calcitic single-crystalline behavior of the spicules (spicule orientation as in (b), irradiation parallel to the c -axis) and (f) drawing of a spicule in relation to the crystallographic axes, according to (e), and to a calcite $\{1014\}$ rhombohedron in different view directions. Taken from [373].

Ashby [166]. The peak stress is related to the strength of the dense outer sheath while the plateau region relates to the failure of the highly porous region, dependent on the density and other elastic properties of the solid material.

Sea sponges (Porifera) have fibrous skeletons that are classified depending on their chemical constituents. Skeletons made of calcium carbonate are in the class Calcarea, those with silica are in the class Hexactinellida and those of protein fibers (spongin) are in the class Demospongiae. The inorganic sea sponge spicule is an excellent example of a well-designed ceramic rod. It can be up to 3 m in length and 0.8 cm in diameter [374] and displays high fracture resistance, and in the case of Hexactinellida, high flexibility.

In the calcareous sponge, *Pericharax heteroraphis* the spicules behave as single crystals, verified by Laue diffraction that show a single orientation (Fig. 86). High-resolution TEM and AFM studies showed that the 'single crystals' are actually composed of ~ 5 nm nanoclusters with the organic matter between them, as shown in Fig. 87a. [373]. This is similar to the 'single crystal' tablets in sea urchin spicules, which are also composed of nanocrystals. In Fig. 87b, the conchoidal fracture surface characteristic of a single crystal is evident.

Fig. 88 shows the siliceous Venus flower basket (*Euplectella aspergillum*). It has an elaborate structure that appeals to mechanical engineers due to the regular arrays of longitudinal, radial, and helical fibers (both right hand and left hand) that provide strength with a minimum of silica. The basket holds prison a pair of breeding shrimp that keep the basket clean and protects them from predators. The offspring are small enough to escape, thus is an example of a symbiotic relationship.

Fig. 89 shows the hierarchical nature of the glass fibers from the sea sponge *Euplectella* sp. [375]. Each of the fibers or struts of the cage is a bundle of spicules (~ 100 μm diameter). The spicule consists of layers of concentric lamellae; the lamella thickness ranges from ~ 1.3 μm near the core and gradually becomes thinner to ~ 0.3 μm at the outer surface. The thickness of the lamellae scales with the diameter of the overall spicule – larger diameter spicules have thicker lamellae. Sandwiched between the lamellae is a thin layer of a protein 'glue' that binds the layers together. Closer inspection of a lamella reveals it is composed of spherical nanoparticles (~ 100 nm) that are also held together by proteins. Cha et al. [376], Cha et al. [377] identified the protein and named it silicatein.

The surprising flexibility of these ceramic fibers is demonstrated in Fig. 90. The basket is held to the ocean floor from spicules radiating from the basket (Fig. 90a), which also has the unique concentric laminated structure. These fibers must flex with wave action but remain firmly embedded in the floor. In Fig. 90b, the flexibility of the anchoring fiber is demonstrated by showing the spicule curved into a circle. This is unusual behavior for a ceramic material, where small deflections usually result in brittle

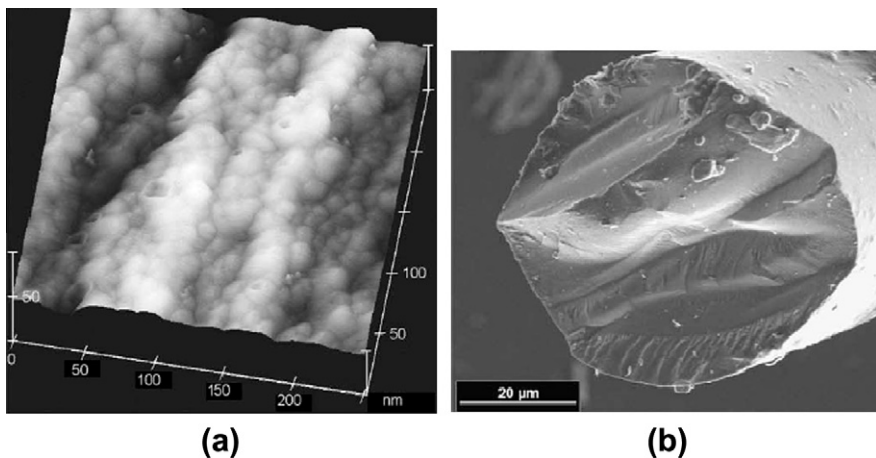


Fig. 87. (a) AFM height image of the fracture surface, revealing the nano-cluster structure, (b) SEM micrograph of the conchoidal fracture surface of a spicule from the calcareous sponge (*Pericharax heteroraphis*). Adapted from [373].

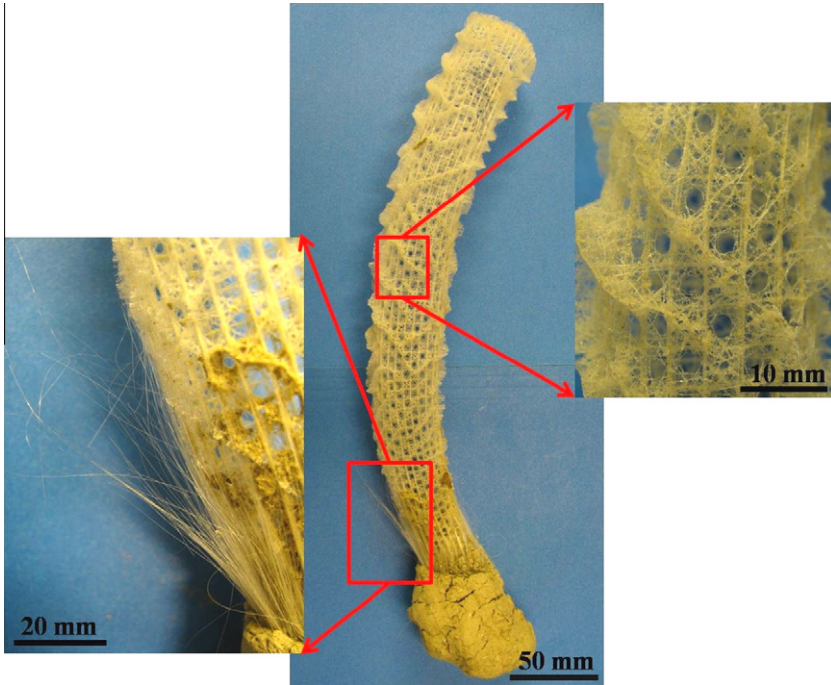


Fig. 88. Venus flower basket (*Euplectella aspergillum*); two shrimp live inside the cage and procreate, their offspring being able to escape. This is a symbiotic relationship whereby shrimp are fed and clean cage. Left, spicules: right, detail of structure.

failure. Fig. 90c shows the uneven fracture surface of a sponge spicule, where the onion-like layers are observed. This structure of concentric rings has some analogy with osteons in cortical bone, another example of a material with excellent crack arresting capability. Fig. 90d shows a cross-sectional SEM micrograph of the fracture path across the spicule shown in (c). The step-wise shape demonstrates that the cracks cannot travel in a straight path; there is increased toughening over a monolithic material. The mechanical behavior of giant sponge spicule (*Monoraphis chuni*) has been studied quantitatively using indentation techniques [378]. It has been shown that the lamellar structure increases by 2-orders of magnitude the load P_c necessary to nucleate a crack (and hence damage). This is because P_c scales as (Kc^4/E^2H) ; hence a small increase in fracture toughness (for instance 2-fold) has significant impact on the damage tolerance, together with the reduction in modulus due to hydration (which slightly decreases E and H). The sponge spicule is multifunctional [245]. It will be seen in Chapter 7 how this structure inspired Aizenberg and Hentler [379] to create biologically inspired wave guides.

Cha et al. [376,377] demonstrated that silicatein can hydrolyze in spicules of the sponge *Tethya aurantia*, and condense the precursor molecule tetraethoxysilane to form silica structures with controlled shapes at ambient conditions. This principle was used to generate bioinspired structures by using synthetic cysteine-lysine block copolypeptides that mimic the properties of silicatein [377]. The copolypeptides self-assemble into structured aggregates that can produce regular arrays of spheres and columns of amorphous silica.

3.3. Diatoms and radiolarians

Diatoms are unicellular algae that have a mineralized shell acting as protection. There are 10,000 species of diatoms and their shells, called frustules, have a large number of shapes. Nevertheless, they have in common the pillbox construction with an overlap belt. Diatoms secrete a hydrated silica cage

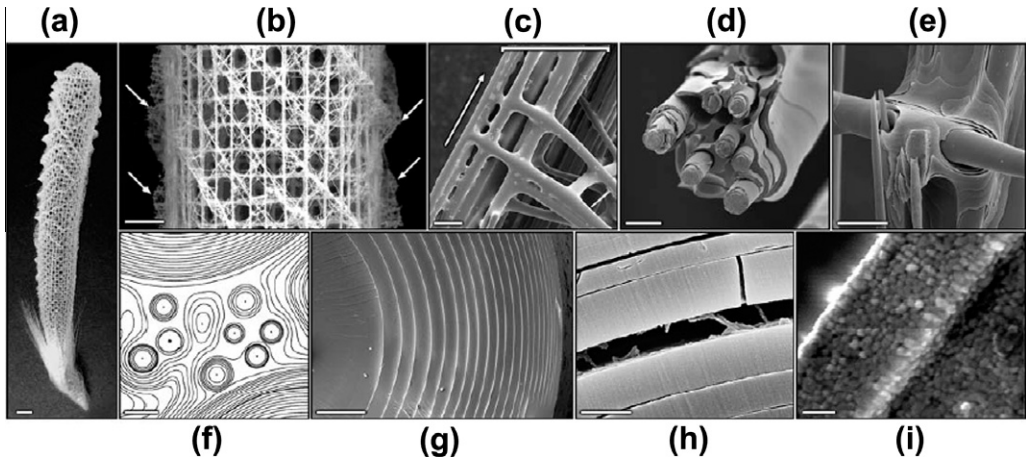


Fig. 89. Structural analysis of the mineralized skeletal system of *Euplectella* sp. (A) Photograph of the entire skeleton, showing cylindrical glass cage. Scale bar, 1 cm. (B) Fragment of the cage structure showing the square-grid lattice of vertical and horizontal struts with diagonal elements arranged in a chessboard manner. Orthogonal ridges on the cylinder surface are indicated by arrows. Scale bar, 5 μm . (C) Scanning electron micrograph (SEM) showing that each strut (enclosed by a bracket) is composed of bundled multiple spicules (the arrow indicates the long axis of the skeletal lattice). Scale bar, 100 μm . (D) SEM of a fractured and partially HF-etched single beam revealing its ceramic fiber-composite structure. Scale bar, 20 μm . (E) SEM of the HF-etched junction area showing that the lattice is cemented with laminated silica layers. Scale bar, 25 μm . (F) Contrast-enhanced SEM image of a cross section through one of the spicular struts, revealing that they are composed of a wide range of different-sized spicules surrounded by a laminated silica matrix. Scale bar, 10 μm . (G) SEM of a cross section through a typical spicule in a strut, showing its characteristic laminated architecture. Scale bar, 5 μm . (H) SEM of a fractured spicule, revealing an organic interlayer. Scale bar, 1 μm . (I) Bleaching of biosilica surface revealing its consolidated nanoparticulate nature. Scale bar, 500 nm. Adapted from [375].

($\text{SiO}_2 \cdot n\text{H}_2\text{O}$), which is not as stiff as calcite; thus, it can undergo more deformation per unit load, making it more flexible. The Young's modulus of the glass sponge spicule is ~ 40 GPa [374] and the diatom frustule is 22.4 GPa [138] whereas that for calcite is ~ 76 GPa. They contain two valves with a regular set of perforations through which they filter the nourishment from the ocean. Fig. 91 shows several types of diatoms. In diatoms, the silica is formed in the surface of the cell in a complex tridimensional network that is only partially understood. Each diatom species has a specific biosilica cell wall with regularly arranged slits or pores in the size range between 10 and 1000 nm. Biosilica morphogenesis takes place inside the diatom cell within a specialized membrane-bound compartment termed the silica deposition vesicle. It has been postulated that the silica deposition vesicle contains a matrix of organic macromolecules that not only regulate silica formation but also act as templates to mediate the growth of the frustules and the creation of the holes and slits (nanopatterning). Using of these biosilica-associated phosphoproteins, known as silaffins, Poulsen et al. [380] were able to create a silica assembly with pores having 100–100 nm diameters.

Progress toward the goal of creating, synthetically, frustules, was made when the genome of the marine diatom *Thalassiosira pseudonana* was established [381] including novel genes for silicic acid transport and formation of silica-based cell walls. Based on this, [160,382,383] proposed that the first step is to identify cell wall synthesis genes involved in structure formation and stated that the completed genome sequence of *Thalassiosira pseudonana* opens the door for genomic and proteomic approaches to accomplish this. An approach that is also used in other organisms is to modify gene sequences or expression, introduce the modified genes into the diatoms, and to monitor the effect on structure. The ultimate goal of this approach is to produce genetically modified frustules that can be tailored to specific applications through biosilicification processes. Indeed, some progress has been made in this direction, illustrated in Fig. 92. The picture on top represents the valve of a normal diatom; the one in bottom shows the effect of treating the culture with 1,3-diaminopropane dihydrochloride. The silicification is altered and the arrows show regions in which it has not occurred.

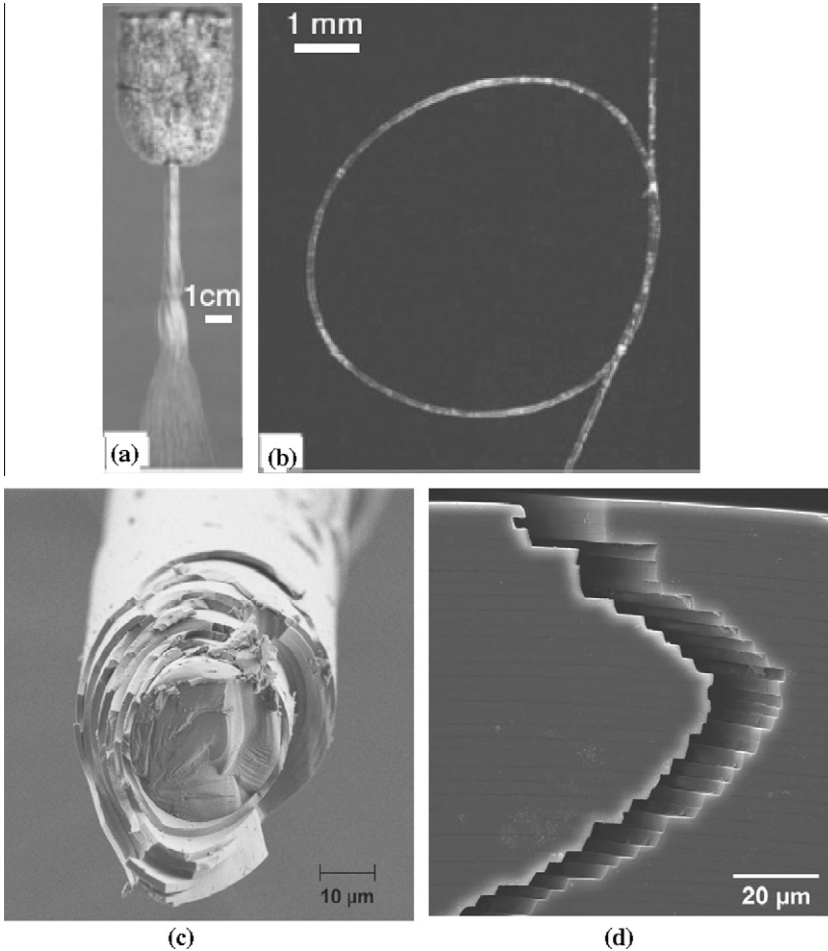


Fig. 90. (a) Photograph of basal spicules of the glass sponge *Hyalonema siebody*, showing (b) flexibility. Adapted from [384]. (c) Fracture path across a spicule of *Monorhaphis chuni* and (d) SEM image fracture surface of a *Euplectella aspergillum* spicule. Taken from [374].

Radiolarians have some similarities to diatoms, since they also ‘float’ in the ocean as zooplankton. However, they are ameboid protozoa. Their dimensions vary from 30 μm to 2 mm. Some are icosahedral shaped, as shown in Fig. 93. They often have spikes (for protection), in contrast to diatom frustules. Of the 10,000 diatom types, 90% are alive today, while 90% of the radiolarians are extinct. They prey on diatoms.

3.4. Skin

The skin is an orthotropic material, i.e., the mechanical response has defined and different trajectories for the perpendicular orientations defined by a coordinate system in which two axes are parallel to the skin surface and the third axis is perpendicular to it. The Langer lines cover the entire skin and mark the directions along which the mechanical stiffness is highest. Fig. 94 shows the Langer lines on the human body. Fig. 95 shows the tensile stress–strain curves for the skin of pig belly along two orientations: parallel and perpendicular to the spine. The Langer lines for pigs should be analogous to

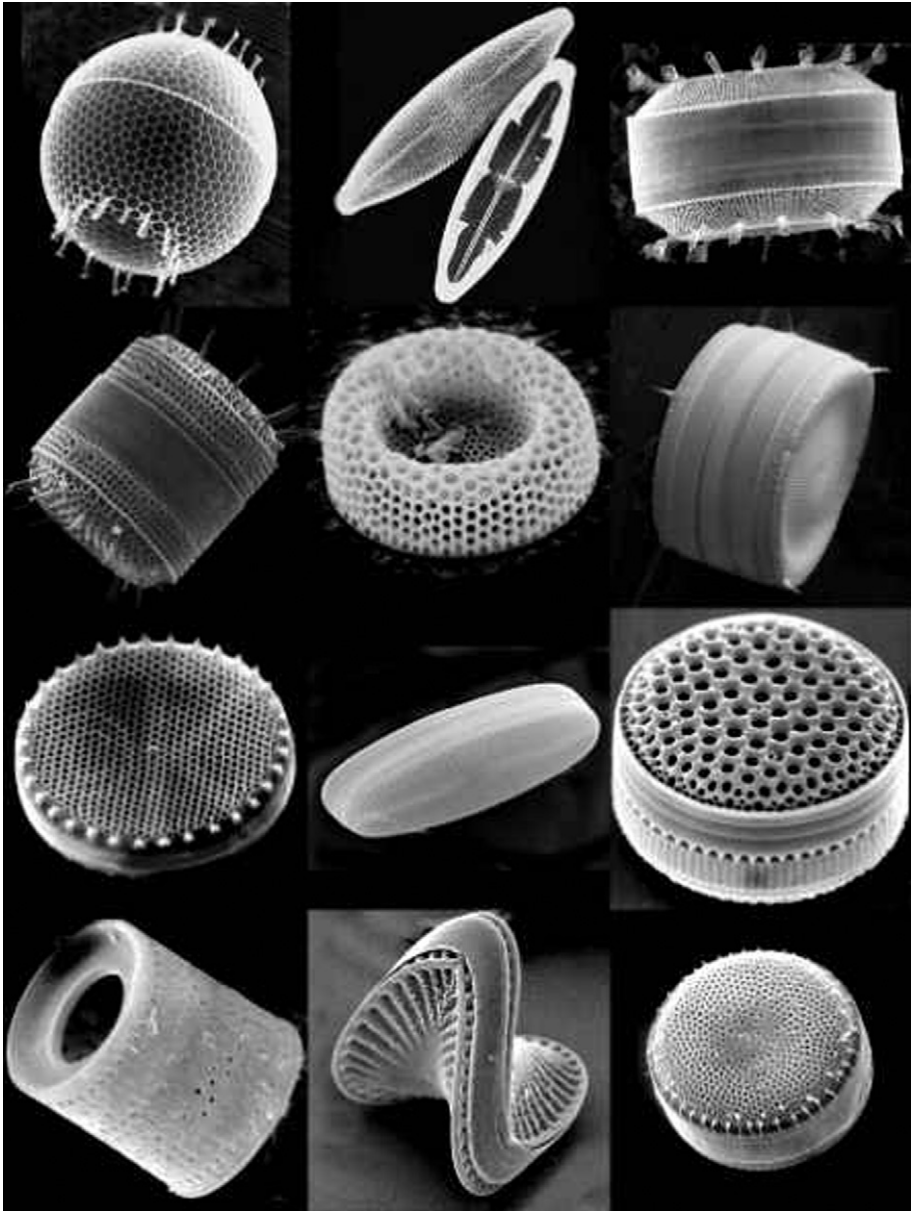


Fig. 91. Different morphologies of diatoms. Taken from <http://ecogadget.net/page/5/>.

those of humans since they are close cousins in voracity and beauty. The stress–strain curves are of the *J* type, discussed previously in Section 1.3, the stiffness gradually increasing with strain (or stretch ratio λ). There is a considerable difference in the total elongation, increasing from 0.2 parallel to spine to 0.8 perpendicular to it. The mechanical properties of mammalian skin are dominated by the dermis, which is 90–95% of the total. The dermis is composed primarily of collagen (60–80%), elastin, and a hydrated gel-like substance. A phenomenological model is the Ogden equation (Eq. (1.15)), that is

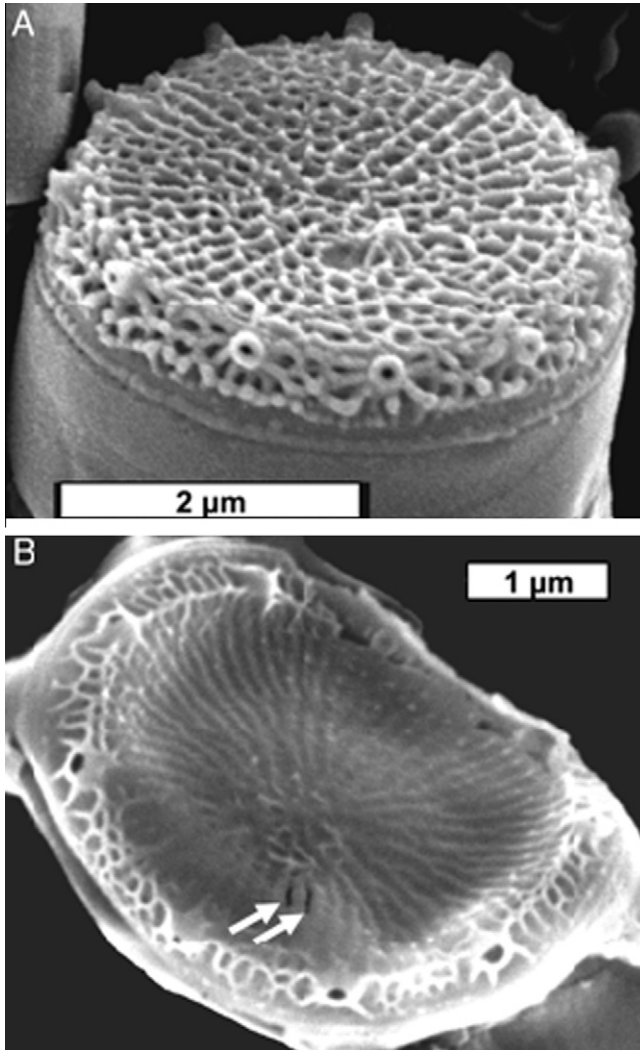


Fig. 92. Effect of the polyamine synthesis inhibitor DAPDH on valve formation in *Thalassiosira pseudonana* diatom. (A) Valve from untreated culture; (B) Valve from culture treated with 10 mM 1,3-diaminopropane dihydrochloride. Arrows denote areas where silicification has not occurred. Taken from [383].

presented in Chapter 1. It was applied to skin by Shergold et al. [385]. In the case of human and pig skin, [385] obtained a best fit with $\alpha = 9$ and $\alpha = 12$, respectively. However, as will be seen below, this is dependent on orientation, strain rate, and temperature. The effect of temperature can also be incorporated into the Ogden equation. Another effect needs to be incorporated into the Ogden equation: the strain rate sensitivity,

$$\sigma = \frac{2\mu_0}{\alpha_0} \left(\frac{T}{T_0}\right)^n \ln\left(\frac{\dot{\epsilon}}{\dot{\epsilon}_0}\right) \left(\lambda_1^{\alpha-1} - \lambda_1^{-1-\frac{\alpha}{2}}\right) \quad (3.1)$$

where n is a temperature softening parameter, $\dot{\epsilon}$ is the strain rate, and the strain rate sensitivity is expressed by the well-accepted logarithmic behavior. α_0 , μ_0 , T_0 , and $\dot{\epsilon}_0$ are reference values.

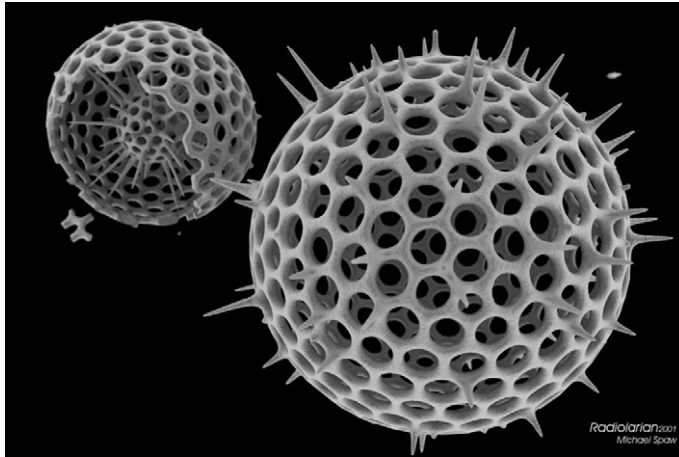


Fig. 93. SEM micrograph showing two radiolarians. The silica-made shells are perforated with holes and have little spikes (spicules). Taken from <http://allencentre.wikispaces.com/Oceans>.

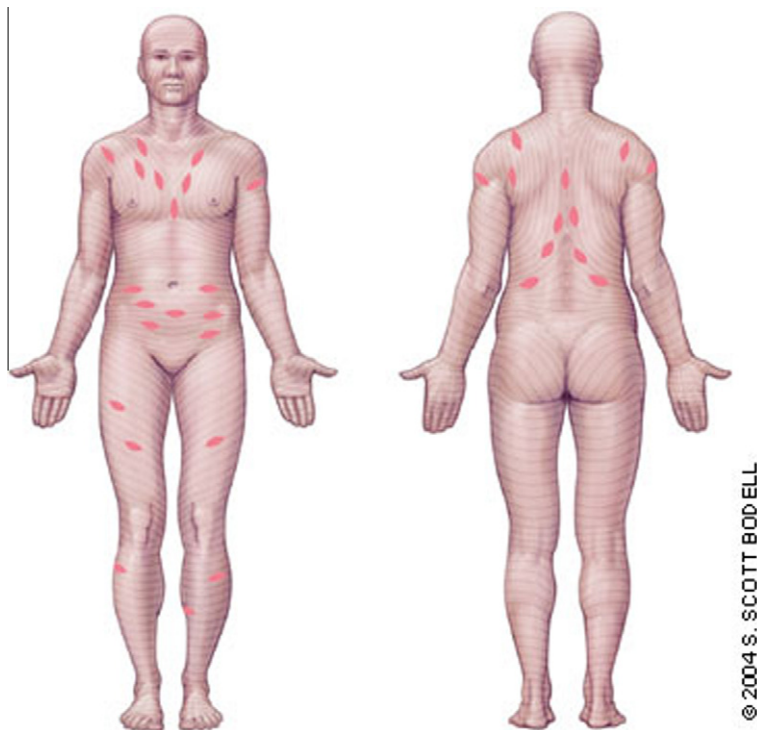


Fig. 94. Langer lines indicating the direction of alignment of the collagen molecules. Taken from <http://www.aafp.org/afp/2004/0101/afp20040101p87-f4.jpg>.

Indeed, Fig. 96 shows the effect of the strain rate on the compressive strength of pig skin; both experimental and computational results are shown. Different values of the shear modulus μ were used to obtain a satisfactory fit. It is possible to incorporate the effect of strain rate into the Ogden equation by using the following form of the shear modulus:

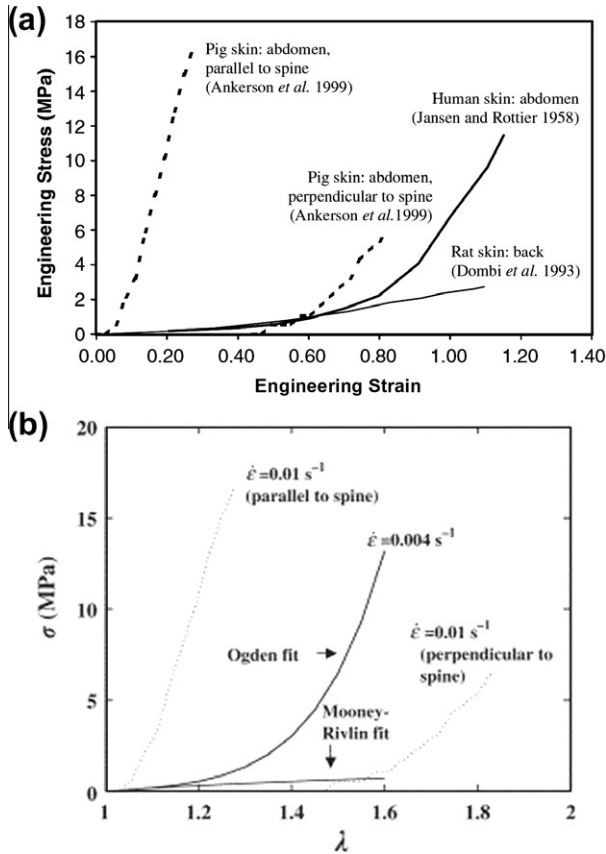


Fig. 95. Stress strain curves for pig belly skin parallel and perpendicular to the Langer lines and for human and rat skin. Taken from [385].

$$\frac{2\mu}{\alpha} = \frac{2\mu_0}{\alpha_0} \left(\frac{T}{T_0}\right)^n \ln\left(\frac{\dot{\epsilon}}{\dot{\epsilon}_0}\right) \tag{3.2}$$

Zhou et al. [386] showed that there is a significant variation in skin tensile behavior with temperature and strain rate. They used the Ogden model to represent the effects of strain rate and temperature on the measured constitutive response through two parameters (α and μ). Fig. 96 shows the effects of strain rate and temperature on the tensile stress strain (or stretch) curves. There is significant effect of strain rate in the range of $0.0025\text{--}0.1 \text{ s}^{-1}$. Similarly, the maximum strain increases with temperature. They obtained a best fit with $\alpha \sim 9$. The ‘effective’ shear modulus, μ (Eq. (3.2)), depends on strain rate. Shergold et al. [385] quote values varying between 0.4 and 7.7 MPa for strain rates ranging from 0.004 s^{-1} to 4000 s^{-1} . In contrast, for an elastomer tested by Shergold et al. [385] the value of α was much lower: ~ 3 . This is much closer to the entropic equation for rubber, for which $\alpha = 2$. Thus, skin ‘stiffens up’ much faster than rubber. More sophisticated constitutive models of skin can be developed, incorporating the mechanical response of the individual collagen and elastin fibers and their dependence on orientation.

3.5. Osteoderms

The osteoderm, as the name implies, is a ‘bony skin.’ Osteoderms are found on both mammals (Cingulata–armadillos) and reptiles (testudines, crocodilia). The osteoderms are attached to the

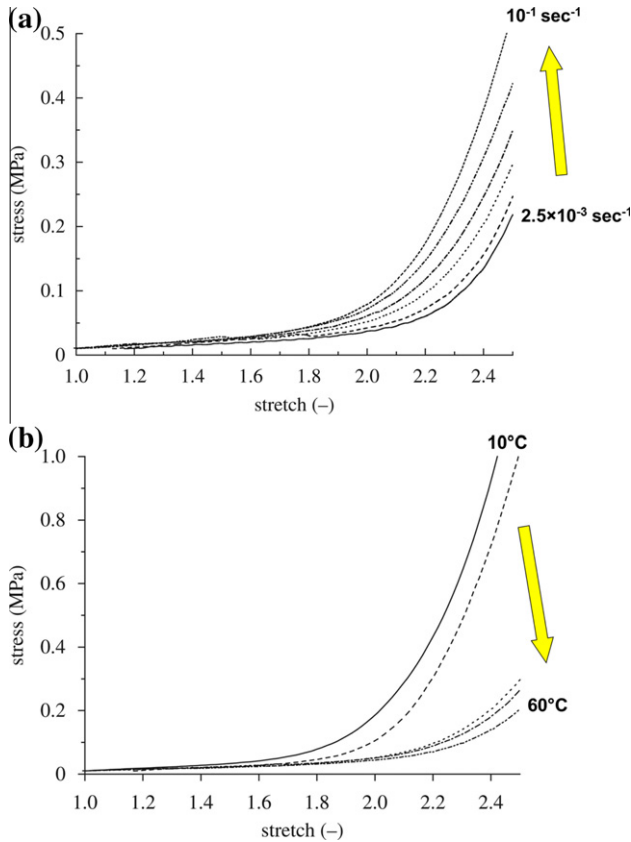


Fig. 96. Effect of (a) strain rate ($0.0025\text{--}0.1 \text{ s}^{-1}$) at $45 \text{ }^{\circ}\text{C}$ and (b) temperature ($10\text{--}60 \text{ }^{\circ}\text{C}$) at 0.01 s^{-1} on the tensile mechanical response of pig belly skin. Taken from [386].

animals by blood vessels, or in the case of testudines, are fused to the skeleton. Armadillo pups are born with a soft carapace that ossifies as they mature. In the reptiles, the osteoderms grow as the animals mature and growth rings, similar to those observed in trees, can be identified. There are surprisingly structural similarities between these osteoderms of these different classes, as described below.

3.5.1. Armadillo

The armadillo (“little armored one”, in Spanish) is indigenous to and is found throughout South America and as far north as Kentucky in North America. The South American three-banded armadillo (*Tropeutes tricinctus*) can curl up completely into a ball, protecting its soft underbelly. The nine-banded armadillo (*Dasypus novemcinctus*), found in North America, cannot curl up into a ball, thus its armor provides a shield not only from some predators, but also from thorny bushes and cacti, well-known flora in the southwestern USA. Fig. 97a shows the hierarchical structure of the nine-banded armadillo osteoderm. The carapace is composed of bony tiles (osteoderms or scutes) with two different morphologies – hexagonal and trapezoidal, which are covered by keratin. The hexagonal tiles appear on the pectoral and pelvic areas whereas the triangular ones are along the torso. The hexagonal tiles have a uniform shape of $\sim 5 \text{ mm}$ in diameter and $1\text{--}2 \text{ mm}$ thickness. The bands of the trapezoidal tiles overlap and can slide relative to each other, thereby providing flexibility to the torso. A photograph of the carapace, with some of the keratin removed to more clearly see the underlying

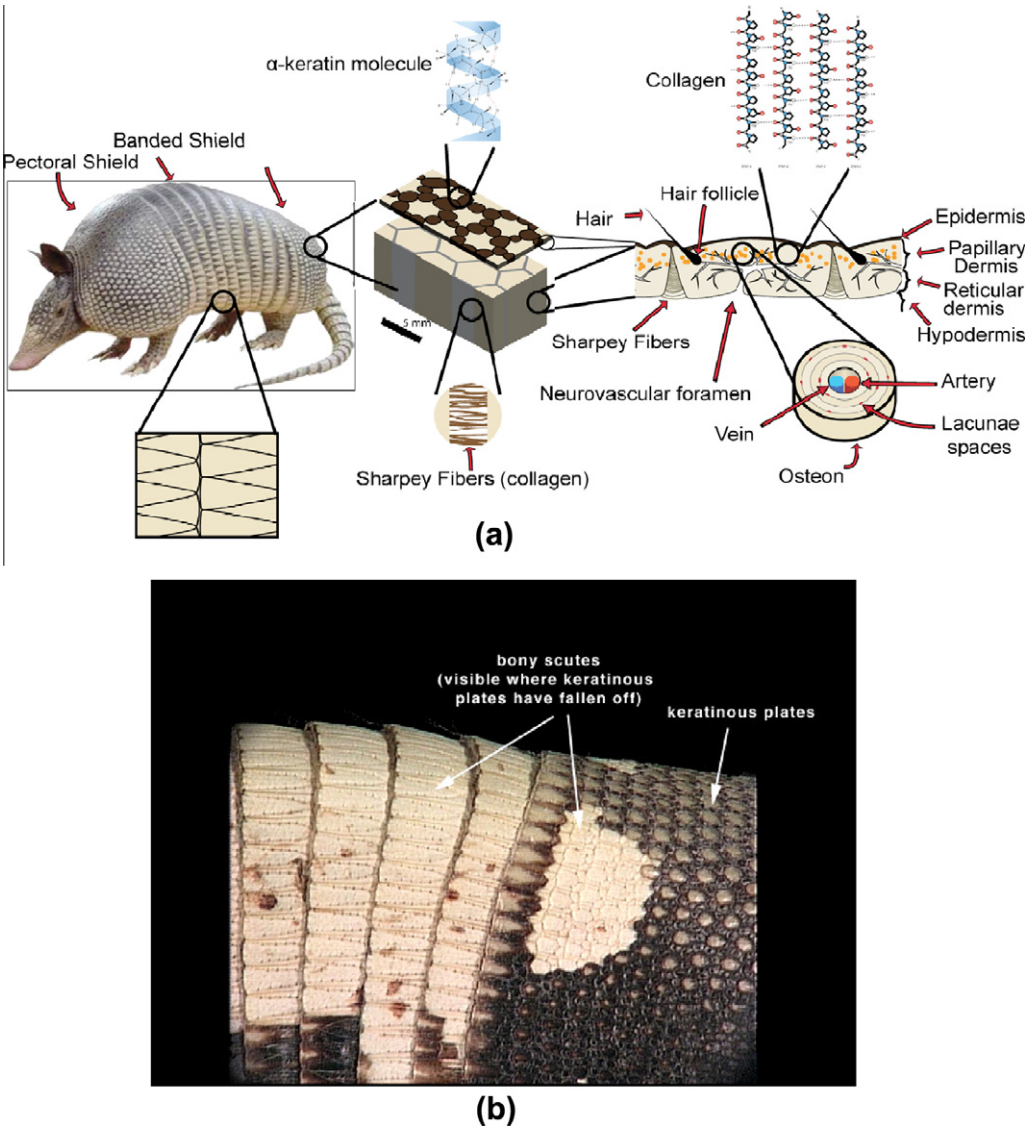


Fig. 97. (a) Hierarchical structure of the nine-banded armadillo. The carapace consists of hexagonal (pelvic and pectoral shield) or trapezoidal (trunk) bony tiles (osteoderms). The osteoderms are covered by a water repellant keratin epidermis below which is the bone, consisting of both dense and porous (middle) regions. The tiles are held together by non-mineralized collagen fibers (Sharpey's fibers) that provide flexibility to the carapace. Taken from [205]. (b) Osteoderm with some of the keratin scutes removed to reveal underlying bone structure. (http://animaldiversity.ummz.umich.edu/site/resources/anatomical_images/family_pages/xenarthra/armadillo_shell.jpg/view.html).

osteoderms, as shown in Fig. 97b. A photograph of the hexagonal keratin scales (Fig. 98a) illustrates their bimodal distribution. Tiles were baked at 550 °C to remove the organic constituents and are shown in Fig. 98b. Based on the drying and ashing experiments, tiles have 14 wt.% water and 65 wt.% ash (mineral) [205].

The bone structure of the hexagonal tiles is shown in Fig. 99. The keratin component on the top epidermis layer is ~120 μm thick, followed by a thicker papillary layer (350 μm) composed of dense

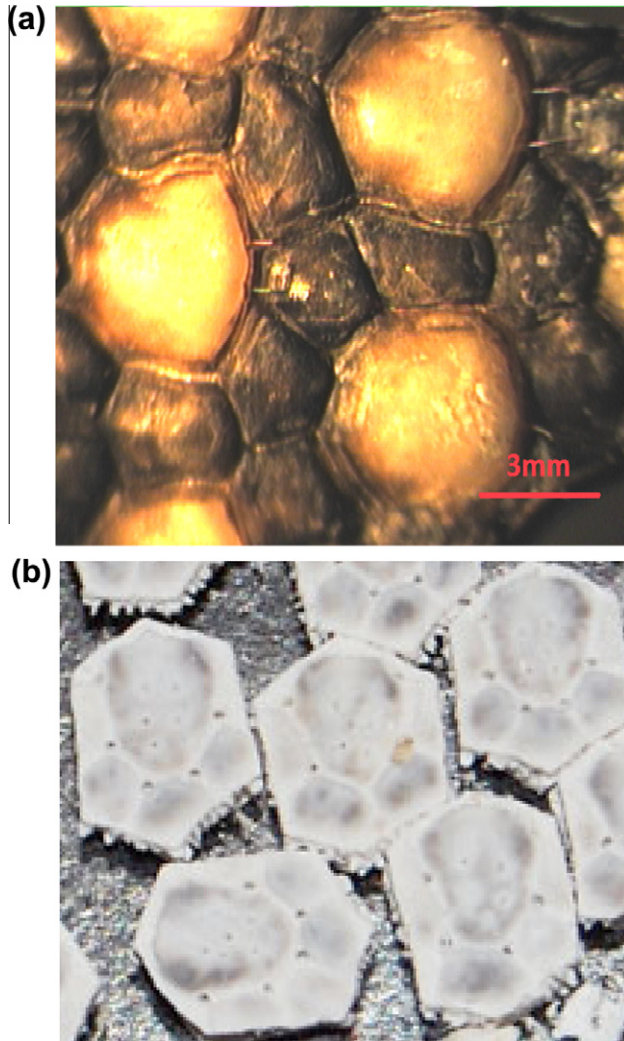


Fig. 98. (a) Surface of the shell (keratin layer) showing bimodal distribution of scales with larger (light) scales surrounded by smaller (dark) scales and (b) osteoderms after heating in a furnace to 550 °C for 24 h. The organic substance and water were baked off, leaving only the mineral phase. Taken from [205].

bone. Several small hollow spaces with layers of concentric lamellae of diameters 120–150 μm found at the bottom of papillary layer correlate to osteons with vascular channels ranging from 10 to 15 μm . There are evenly distributed lacunae spaces of diameter 10 μm found surrounding and internal to these osteons. The armadillo osteons are slightly smaller than those of bovine femur bone ($\sim 200 \mu\text{m}$). The collagenous high porosity region (reticular dermis layer) has larger cavities of diameters of 100–400 μm along with some evenly distributed lacunae spaces of 10 μm . These cavities are thought to be derived from the complex branched structure of the vascular channels that stem from the ones that attach the osteoderm to the dermis. In the hypodermis layer, limited traces of blood vessels were observed; they are oriented parallel to the surface. As shown in Fig. 99, the tiles are held on the body by blood vessels that extend through the dermal layer into the tile, and have a sandwich structure (dense cortical bone surrounding porous bone).

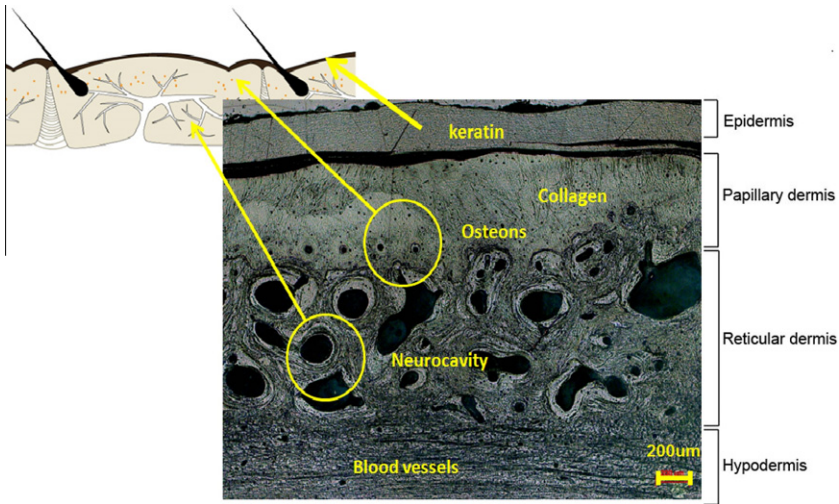


Fig. 99. Optical microscope of a cross-section of a hexagonal tile from the armadillo. The image shows osteons and interior porosity at different depth. The epidermis consists of a keratin layer. The papillary dermis is dense bone that sandwiches the reticular dermis consisting of porous bone, arising from the complex branched vascular network (neurocavities) that stem from the vascular channels that attach the osteoderm to the dermal layer. The hypodermis is another layer of dense bone. Taken from [205].

An important feature is the manner in which the tiles are held together laterally. The carapace can have a varying curvature and this is enabled by the structure composed of tiles held together by non-mineralized collagen fibers (also known as Sharpey's fibers after the Scottish anatomist who discovered them in 1846). These fibers are found in the skeletal tissue where some amount of movement is required. For example, the bones of the cranium are attached by Sharpey's fibers, as is the periosteum to bone; so are the roots of the teeth, attached to bone. The stretched (Fig. 100a) and curved states (Fig. 100b) are accompanied by extension and retraction of the Sharpey's fibers, respectively. The inner dimensions (D_1) of the tiles are smaller than the outer ones (D_2). The curved configuration represents the typical armadillo carapace in nature. The length of the collagen fibers can be varied to give the entire carapace structure the desired curvature. There is a high density of these fibers, which provides some flexibility to the carapace, as shown in Fig. 100c. X-ray fluorescence mapping in Fig. 100d and e confirms that hexagonal and rectangular tiles are calcium rich, whereas the junction (location of the collagen fibers) between the tiles have little or no traces of calcium, confirming that the Sharpey's fibers are non-mineralized.

The tensile failure strengths of the osteoderm are 16 MPa in the hydrated condition and 20 MPa in the dry condition. In the hydrated condition, the failure was along the Sharpey's fibers whereas the dry failure occurred in the tiles. The Young's modulus was quite different in the hydrated (150 MPa) and dry (425 MPa) samples. The Young's modulus of cortical bone is ~ 20 GPa, over an order of magnitude higher than the dry osteoderm. Under tensile stress, the mineralized tiles and the Sharpey's fibers can be considered to be under isostress conditions. The fibers undergo more strain than the bony tiles.

One interesting aspect is that the shear strength of the (hydrated) tiles (the stress necessary to push out a tile from the carapace) is similar to the tensile strength of the hydrated samples (Fig. 101a and b). Fig. 101c illustrates how the samples were loaded in tension and shear. The shear strength is half the tensile strength for most materials ($\tau_{xy} \sim \sigma_y/2$). This unusual behavior is attributed to the fact that the failure in both cases is due to tensile stretching of the Sharpey's fibers.

Rhee et al. [204] examined the compressive properties and found the osteoderms behave as a cellular solid, having in the stress–strain curve an initial linear elastic region followed by a plateau

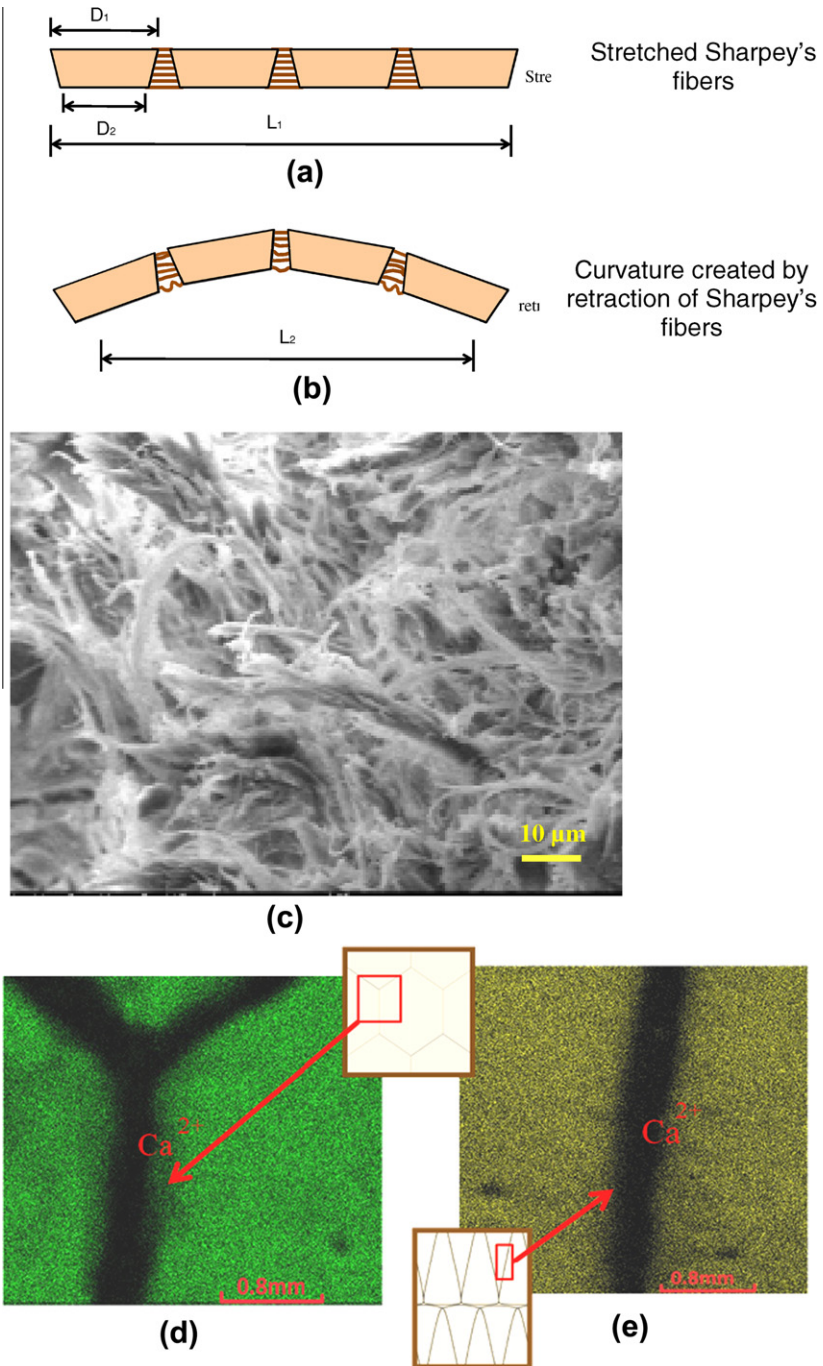


Fig. 100. Cross-sectional morphology of osteoderm scales of the (a) stretched and (b) flexed carapace ($D_1 > D_2$). Sharpey's fibers create a variable curvature with retraction of the fibers. (c) SEM micrograph of fractured Sharpey's fibers from the armadillo carapace. X-ray fluorescence images taken on (d) the hexagonal tiles. The bright green color corresponds to calcium. Calcium is not found between the tiles, indicating that the Sharpey's fibers are not mineralized and, (e) same for rectangular tiles. These images also show high calcium concentration in the tiles and little or no calcium between the tiles. Taken from [205].

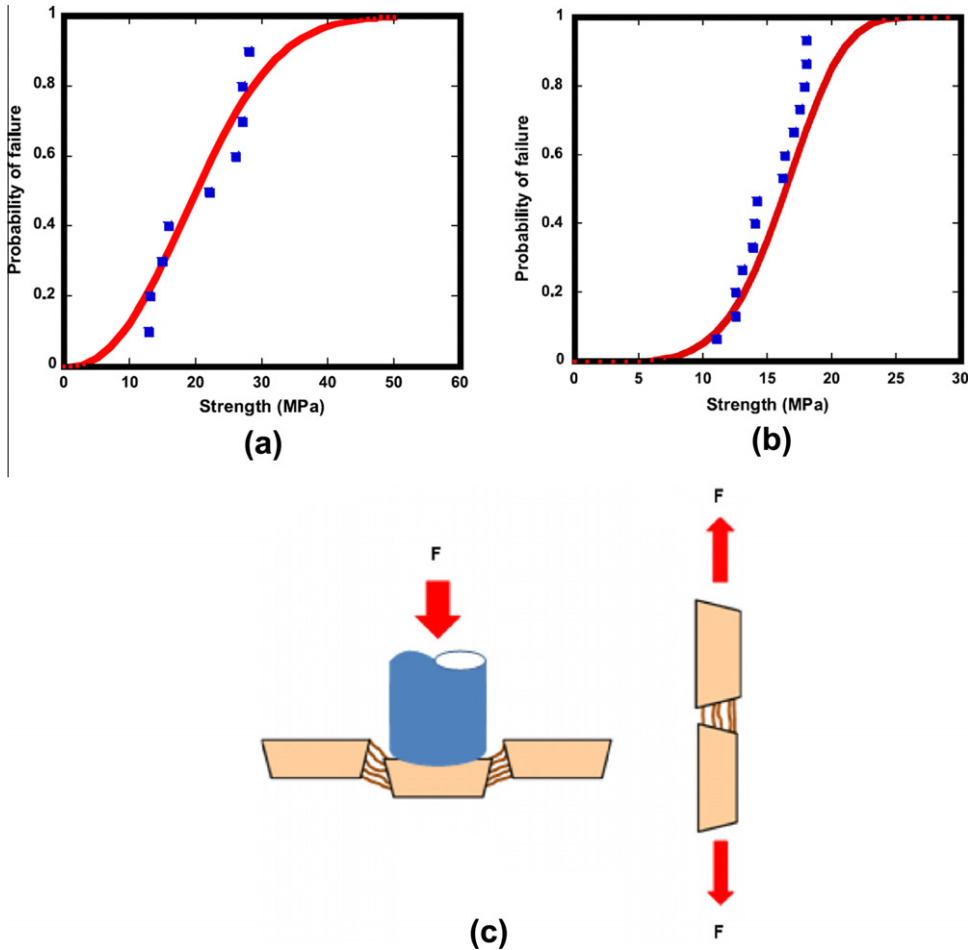


Fig. 101. Weibull probability distribution function as a function of failure strength for hydrated sample for (a) shear test results and (b) tensile tests results. The mean stress is defined as a 50% probability of failure. (c) Configuration of the hexagonal tiles of the armadillo tested in tile puncture (left) and in tile tension (right). Taken from [205].

region, attributed to deformation of the interior porous bone, and a final upturn assigned to crushing of the porous bone. The large plateau region, up to $\sim 50\%$ strain, demonstrates that the application of a compressive force will lead to extensive distortion of the osteoderm before failure. They found the compressive strength to range from 500 to 1500 MPa, significantly higher than the tensile strength.

3.5.2. Testudine

The order testudine includes turtles, tortoises and terrapins. The carapace (top shell) and plastron (base of shell) have a keratin covering (for water proofing) that has bone underneath. The shell, $\sim 6\text{--}120$ cm in length, is composed of large osteoderms (compared with the armadillo) that range from millimeter to centimeter diameters, depending on the species. There are about 38 scutes on the carapace and 12–14 on the plastron for the Red-eared slider turtle (*Trachemys scripta elegans*). The osteoderms have cortical bone on the top and bottom layer with a cancellous bone sandwiched between, similar to the armadillo, as shown in Fig. 102. The osteoderms have sutures between them, instead of the Sharpey's fibers. These sutures, also of non-mineralized collagen, and have a 'zig-zag' shape that serves to interlock the osteoderms together. These provide more rigidity

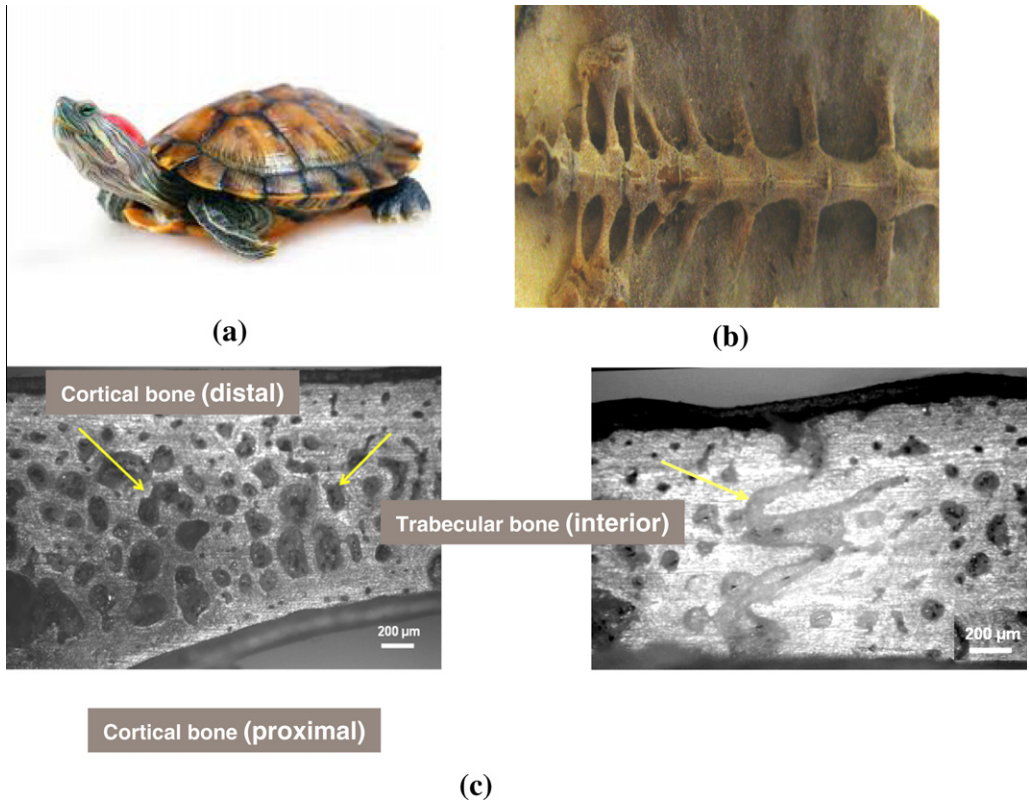


Fig. 102. Red-eared slider turtle carapace: (a) overall picture of the shell and (b) micrograph showing that the skeleton (ribs) are fused to the carapace. Cross-sectional micrographs showing (c) trabecular (porous) bone surrounded by dense cortical bone. Arrows point to the pores in the trabecular bone and (d) the 'zig-zag' suture (non-mineralized) between the osteoderm (arrow).

to the carapace, in comparison to the more flexible shell of the armadillo. Fig. 103a shows a diagram of the sutures in the normal and displaced state [201]. In Fig. 103b the three-point bending force–displacement curves for the carapace with and without sutures, illustrating that samples with the sutures result in a lower stiffness compared to that of a single scute. Rhee et al. [203] examined the carapace of the *Terrapene carolina* turtle shell, performing compression and bending tests. The three-point bending stress–strain curve is shown in Fig. 103c. The Young's modulus was found to be 7.1 GPa, which is over an order of magnitude greater than that of the armadillo carapace (425 MPa).

3.5.3. Crocodylia

The order crocodylia contains notably crocodiles, alligators and caimans. All have osteoderms that cover the head, back and tail of the animal. Crocodiles are 'living fossils' in that they have not changed much over 250 M years of evolution, indicating that they did not find the need to adapt. Crocodile osteoderms have been known for centuries as being repellent to arrows (even bullets). A cross-section of a crocodile osteoderm (Fig. 104a) shows dense bone surrounding porous bone, similar to the armadillo and testudine osteoderms. This can also be compared to the armor of the stegosaurus, shown in cross-section in Fig. 104b. Thus, osteoderms of extant and extinct species have great similarities in architecture and all can be considered to be flat sandwich panels that consist of a porous core (cancellous bone) that is surrounded by dense sheaths (cortical bone).

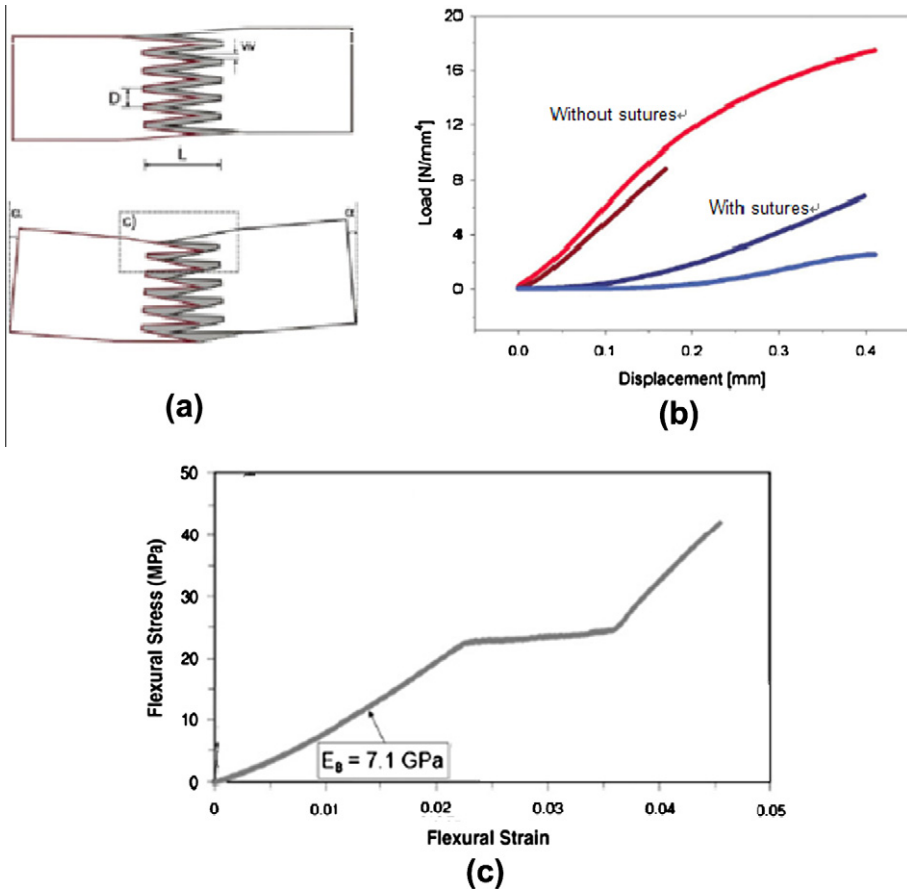


Fig. 103. (a) Mechanical deformation of red-eared slider turtle carapace. The sutures (non-mineralized) allow for some flexibility, but mostly the osteroderms are interlocked with each other. (b) Force–displacement curves from two carapaces with (blue) and without (red and brown) sutures. Taken from [201]. (c) Flexural stress–strain curve for a *Terrapene carolina* turtle carapace specimen. The plateau region corresponds to deformation of the interior trabecular bone and the upturn results from crushing of the bone. Adapted from [203].

3.6. Fish scales

A number of studies on fish scales have been conducted including the structural arrangement, collagen formation and orientation [387–389], and the mechanical properties [88,390,391]. The fish scales provide protection from the environment and predators. Surprisingly, most fish scales have similar material components to other hard tissues such as bones and teeth. They are mainly composed of type I collagen fibers and calcium-deficient hydroxyapatite. The collagen fibers are usually densely packed lamellae with different orientations from layer to layer, forming a plywood structure [161,388]. Such is the case for the *Pagrus major* (sea bream) scales reported by Ikoma et al. [392]. Fig. 105 shows a TEM micrograph for *P. major* in which several layers are imaged. The different alignment of the sequential layers is clearly seen. Both orthogonal and double twisted plywood patterns are reported. This plywood structure has been proposed to form a Bouligand arrangement. The concept of the Bouligand arrangement will be further discussed at the end of this section.

A fascinating fish is *Polypterus senegalus*, a smallish fish, ~100 mm long, living in estuaries and muddy bottoms in Africa. It is an example of a living fossil, such as the coelacanth, thought to be

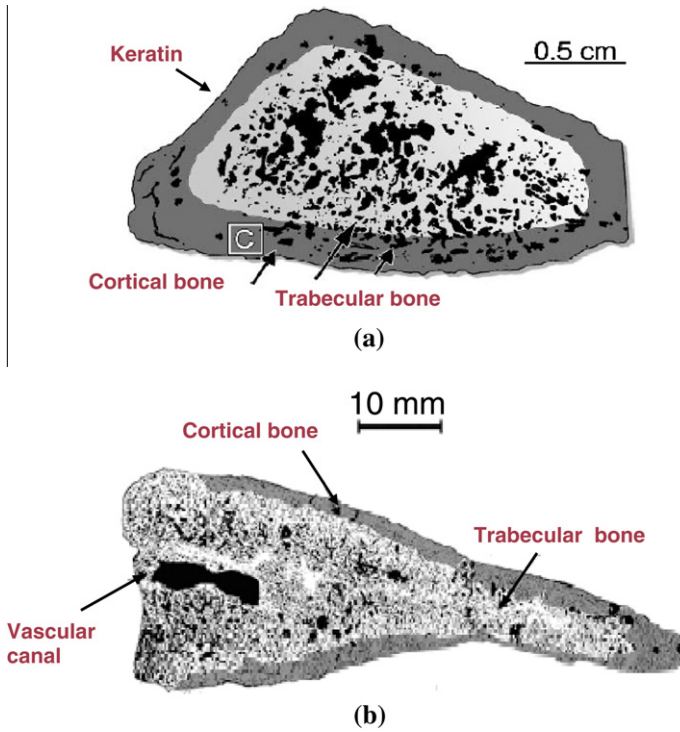


Fig. 104. (a) Cross-section of a crocodile osteoderm. Taken from [393]. (b) Cross-section of the dermal plate of a stegosaurus. Taken from [394]. Both (a) and (b) show similarities in structure with the armadillo and turtle osterderms.

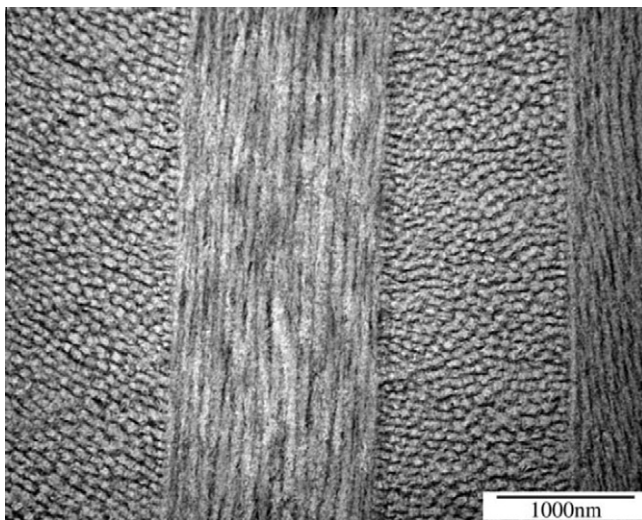


Fig. 105. Transmission electron micrograph of the cross section of scale of *Pagrus major*. Taken from [392].

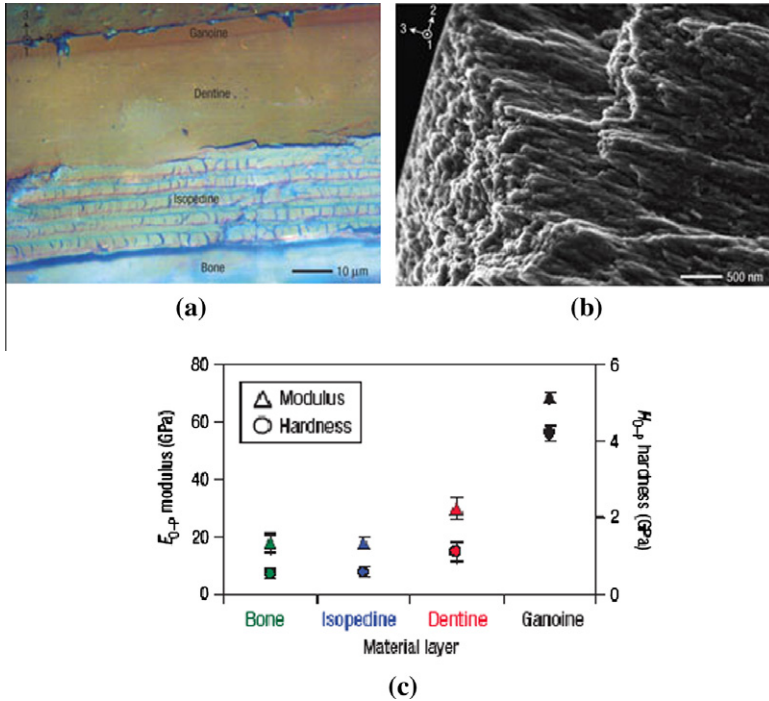


Fig. 106. (a) Cross-section showing laminate composite structure of living fossil *Polypterus senegalus* with inside layer comprised of bone and outside layer of ganoine, one of the hardest biominerals; (b) microstructure of ganoine, similar to enamel, containing less than 5% collagen; (c) variation in nanoindentation hardness from the inside (bone) to the outside (ganoine). Taken from [390].

extinct since the late Cretaceous but rediscovered in 1938. Bruet et al. [390] have recently demonstrated that it has a multilayered dermal armor. Following this, Song et al. [395] analyzed the threat protection mechanisms offered by the dermal layer against biting attacks from the same species. Nanoindentation measurements on the scales show that distinct reinforcing layers with different moduli and hardness offer a graded protection mechanism. Fig. 106a shows four different organic–inorganic nanocomposite material layers (from outer to inner surface): ganoine, an enamel-like material (thickness: 10 μm), dentine (thickness: 50 μm), isopedine (thickness: 40 μm) and a bony basal plate (thickness: 300 μm). The nanoindentation hardness (Fig. 106c) is seen to vary systematically with the composition of the layer, being highest for ganoine (4.4 GPa) and lowest for bone (<1 GPa). The more collagenous dentine layer has a lower mineral content than ganoine, but is more mineralized than the bone basal plate with a nanoindentation hardness of 1.2 GPa. The third layer, isopedine, consists of superposed orthogonal collagenous layers forming a laminate structure. The bone is under this layer.

On the other side of the size spectrum is the *Arapaimas gigas*, a freshwater fish that lives primarily in Amazon basin lakes and can weigh as much as 200 kg. Fig. 107 shows the hierarchical structure of the scales, which are quite large and can be up to 10 cm in length. The collagen fibrils form fibers, which, on their turn, form bundles with diameters on the order of 1–5 μm. The latter are aligned and organized and into lamellae with an average thickness of 50 μm. The collagen fiber alignment has been described by Onozato and Watabe [396] and Zylberberg et al. [397], among others. The fibril orientation varies from layer to layer. A rough external layer, ~600 μm thick is highly mineralized with hydroxyapatite. As shown later on, this structure can undergo significant non-elastic deformation prior to failure, providing considerable toughness.

A cross-section of a scale is shown in Fig. 108a, confirming the uniformity of the layer thickness. The cracks present in some of the layers are due to the drying process. When the collagen fibrils

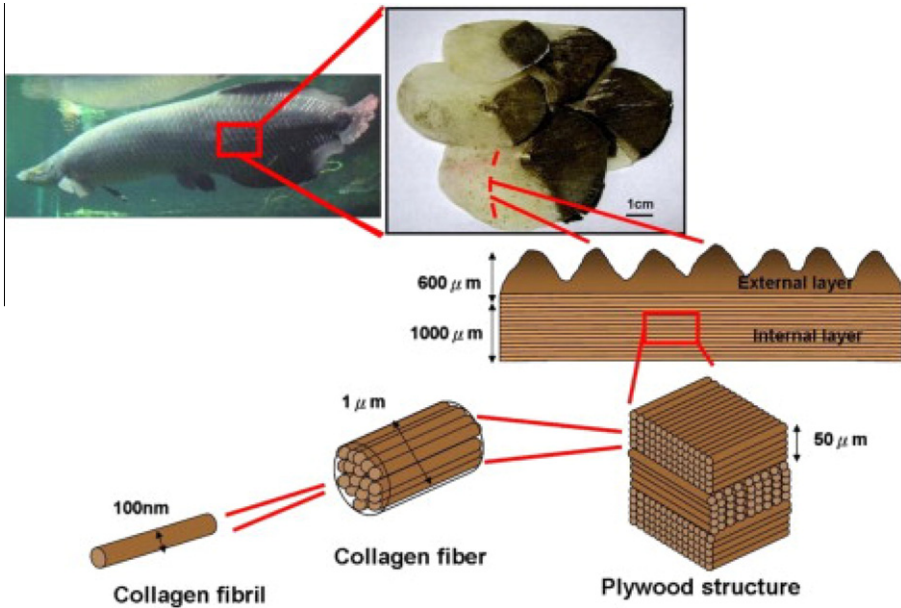


Fig. 107. Hierarchical structure of the *Arapaimas gigas* scales. Angle between lamellae, which is schematically drawn as 90° is actually close to 75° . Taken from [88].

are parallel to the plane of observations the cracks can no longer be seen. Fig. 108b shows the micro-indentation hardness across the cross section. The external layer (550 MPa) is harder than the internal layer (200 MPa), consistent with its higher degree of mineralization.

SEM observation of the scales reveals layers which consist of collagen fibrils with diameters of ~ 100 nm and the characteristic banding pattern with periodicity of 67 nm is seen in Fig. 109. These collagen fibers were revealed by demineralizing the scales. Adjacent lamellae have the fibrils rotated at an angle of $\sim 75^\circ$. This is shown in the SEM micrograph of Fig. 110a. It can be understood that the 75° rotation or multiples thereof (150° , 225° , 300° , etc.) does not bring the structure into a cross-lamellar configuration into which layers have the same orientation. This is the essence of the Bouligand arrangement, which produces the closest to isotropy. Thus, the scale is a collagen composite laminate. This structure is analogous to that observed in other fish scales, apart from the dimensions. In *P. reticulata* (guppy), the lamellae are ~ 1 μm thick; in *C. auratus* (goldfish), they are around 5 μm [388]. The angles between layers have also been found to vary from 36° for some teleosts [388,389,397], to 90° for *P. major* [392], to less than 90° for *H. bimaculatus* (jewelfish).

The *A. gigas* scales play an important role in protecting this large Amazon basin fish against predators such as the piranha. The piranha teeth form triangular arrays that create a guillotine-like cutting action and are highly effective in slicing through fish tissue. Piranhas are primarily piscivores, as opposed to the carnivorous nature portrayed by the popular media. It was demonstrated that the puncturing ability of the piranha teeth could not penetrate the *Arapaimas* scales [398]. This was done by pushing a piranha tooth against the arapaima scale. The tooth penetrated but broke at loads on the order of the biting force of piranha (~ 20 N). The ability of the *Arapaimas* to resist the attack of piranha is clearly the result of the hierarchical structure displayed in Fig. 109.

Fig. 110b shows the typical tensile stress–strain curves in the hydrated condition. The Young's modulus is ~ 120 MPa. The strengths of the hydrated samples range from 15 to 30 MPa. The failure strain is 30–40% indicating that the scales are quite flexible in water, a requirement for swimming. The high failure strain is attributed to the high collagen content (85 vol.%) and much lower mineral content (15 vol.%) in fish scales [88]. The tensile strength obtained is in agreement with the test results

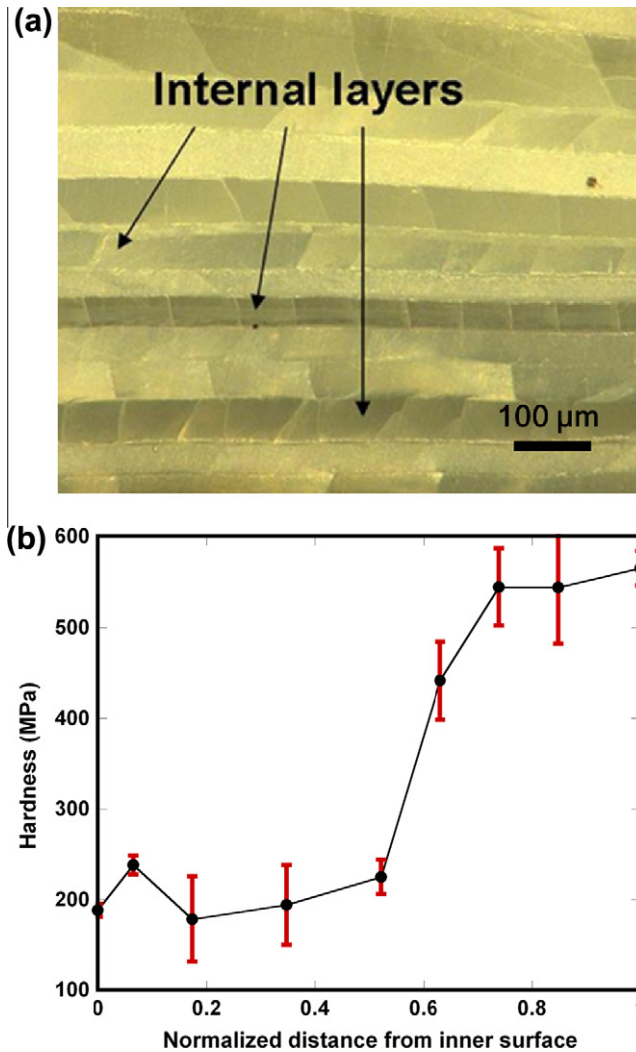


Fig. 108. *Arapaimas gigas* scale; (a) SEM image of the cross-section showing the laminated structure in the internal layers; (b) microindentation through the cross section from inner surface to outer surface showing that hardness is higher in the external layer. Taken from [88].

of Torres et al. [399] which yielded a value of 22 MPa. Their curves also exhibited stress drops, evidence of “graceful” failure, as the experiments by Lin et al. [88]. Several local discontinuities correspond to either the breakage of different layers or the sliding between layers. They are marked by arrows in Fig. 110b. Ikoma et al. [392] reported that the tensile strength of *Pagrus major* scales was 93 MPa which is higher than the results for the *Arapaima* [88]. The strength of the *A. gigas* scale in the dry condition is about one half of that of the *P. major*. It is inferred from the low ductility (~5%) that the *Pagrus major* scales were tested in the dry condition, which would increase the tensile strength. The tensile curve also exhibited a pseudo-plastic behavior, i.e., the curve shows non-linearity prior to failure.

The fracture surface (Fig. 110a) of a demineralized scale clearly shows the different collagen fibril orientations in the lamellae. The angle between two adjacent lamellae seem close to 75°, thus forming

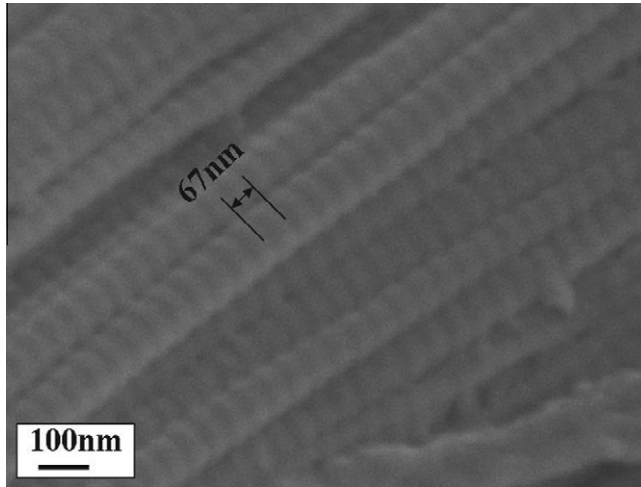


Fig. 109. Collagen fibers in Arapaima scale after demineralization process; note 67 nm periodicity in structure. Taken from [88].

a plywood structure. Fig. 110b shows on the stress–strain curves pulled out or distorted collagen fibrils have damaged during tensile testing. Tensile load not only breaks the collagen fibers but also tears the collagen fibers away from each other. The fracture mechanism seems to be a combination of collagen fracture and the pulling out of the collagen fibers in a single layer. Tensile testing of the scales carried out in the dry and wet conditions shows that the strength and stiffness are hydration dependent. As is the case in most biological materials, the elastic modulus of the scale is strain-rate dependent. The strain-rate dependence on the Young's modulus, can be expressed by the Ramberg–Osgood equation:

$$E = A\dot{\epsilon}^n \quad (3.3)$$

where n is equal to 0.26, which is approximately ten times higher than that of bone [400]. Thus is attributed to the higher fraction of collagen in the scales and to the high degree of hydration (30% H_2O).

3.7. Arthropod exoskeleton

The exoskeleton (cuticle) of arthropods is a laminated biological composite composed of chitin fibers embedded in a protein matrix. The cuticle is multifunctional: it supports the insect, gives it its shape, means of locomotion, waterproofing and a range of localized mechanical specializations such as high compliance, adhesion, wear resistance and diffusion control. It can also serve as a temporary food store and is a major barrier to parasitism and disease, e.g. fungal invasions (Vincent, 2004). Fig. 111 is a section cut from the hind leg of a large adult grasshopper (locust). The layers can be clearly seen as a succession of darker and lighter regions, which constitutes the endothelium. Daily layers are created by the epidermal cells, on the bottom. The top layer is the epicuticle and is, in terrestrial insects, waterproofed by lipids. Its thickness is $\sim 1\text{--}2\ \mu\text{m}$ and it is harder than the endocuticle. This layer is created before molting whereas the endocuticle is created after molting. Fig. 112 is a schematic representation with the principal components labeled. In locusts, the deposition that occurs during the day consists of a layer of parallel fibers. Nightly deposition is in a helical sequencing of fibers, creating a Bouligand [401] pattern. Fig. 112 shows a 180° rotation in the night layer. Arthropods have pore canals that join the epidermal cells to the epicuticle. These hollow tubes transport waxes to the epicuticle, ensuring that it is water proof. Several of these pores are shown in Fig. 112. The pores canals are 'squeezed' by the chitin fibers and take on the flattened configuration, which twists according to the helical shape of the layers.

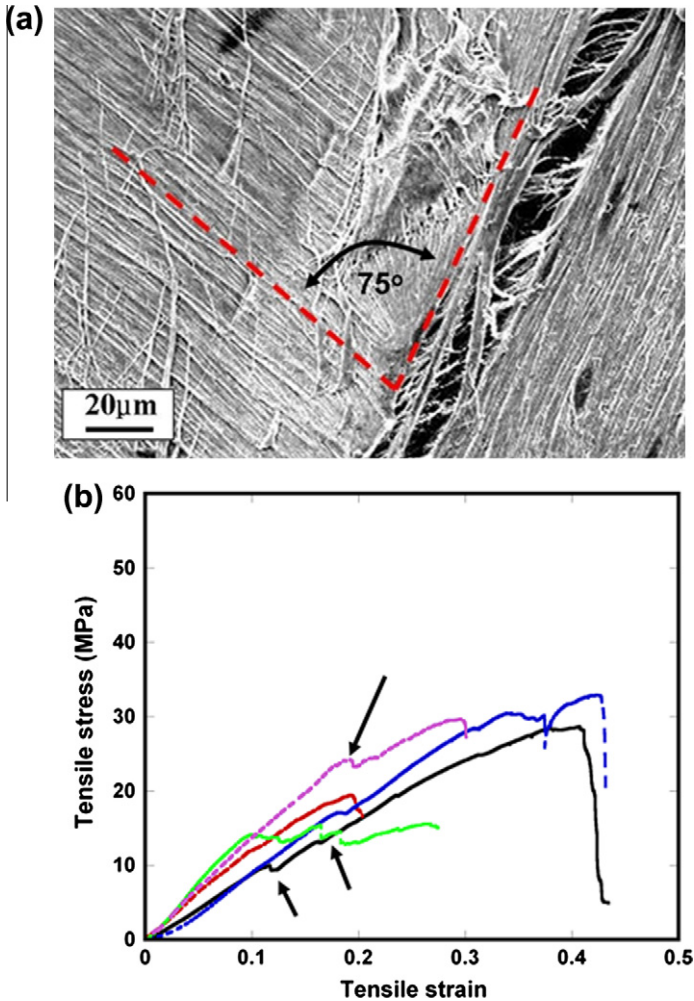


Fig. 110. (a) SEM image of scale fracture surface showing different orientations of the collagen fibers (75°); (b) Tensile stress vs. strain curve for hydrated scale of *Arapaima gigas* at 10^{-4} s^{-1} ; arrows indicate partial failure of collagen layers. Taken from [398].

The succession of layers in the wing case (elytron) of a scarab beetle is shown in Fig. 113. It should be noted that they are not quite orthogonal, providing a ‘twist.’ The thickness of the exo- and endocuticle in insects can vary considerably: it can be as small as $1 \mu\text{m}$ in the hindgut over gills of larvae and as thick as $200 \mu\text{m}$ in the elytra of large Coleoptera [18]. Fig. 114 shows the microstructure of lateral sections of elytra in three types of beetles, revealing a well organized cellular structure [402]. The center portion has pores around which the chitin fibers wrap. This is especially clear in Fig. 114a. This structural arrangement increases the stiffness/weight.

The mechanical properties of arthropod exoskeletons show a great range of variation. This range is needed for the different functions and is highly dependent on the degree of hydration. A fascinating aspect is the hardness of some regions that can reach extraordinary values, which is associated with an increase in concentration of the metals Zn, Mn, and Fe. The microhardness of the mandible of ground beetle (*Scarites subterraneus*) is comparable with enamel, $\sim 5 \text{ GPa}$ [403]. It is not known what form the metal has in the mandible. It is possible that it is present as an ionic cross-linker, similar to the unmineralized Zn ions found in *Nereis virens* polychaete jaws, which formed coordination

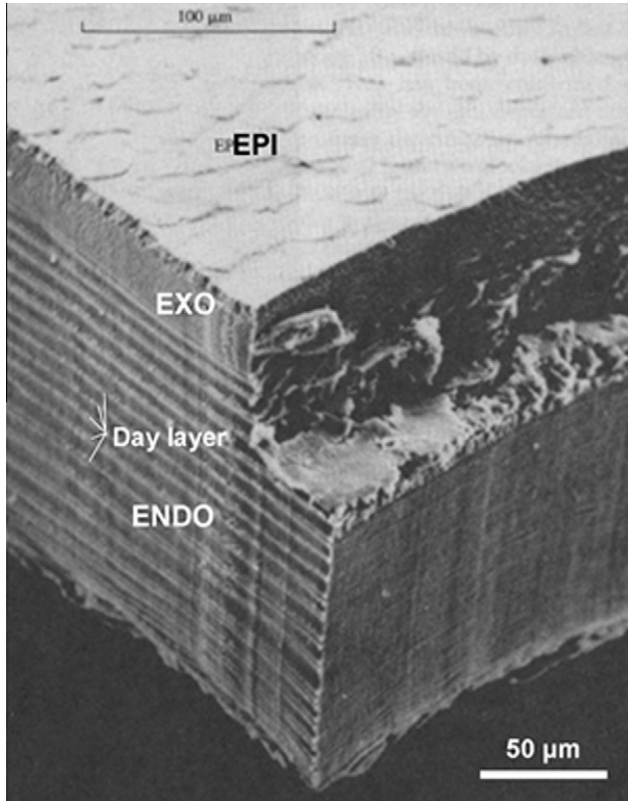


Fig. 111. SEM micrograph showing exoskeleton of adult grasshopper. Epicuticle (EPI), exocuticle (EXO), endocuticle (ENDO) and day layers (from top to bottom) can be observed. Taken from [404].

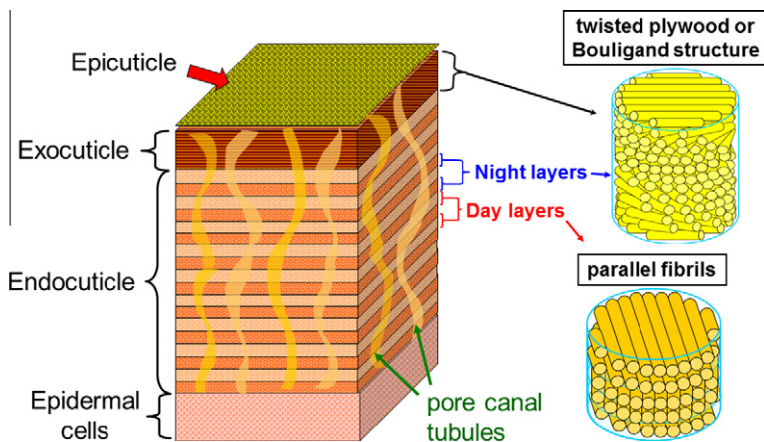


Fig. 112. Schematic representation showing structural components an insect exoskeleton: epicuticle, exocuticle, endocuticle, epidermal cells, and pore canal tubules. Endocuticle consists of night and day layers. The chitin fibrils in night layers arrange into a twisted plywood structure and those in day layers align in a parallel stacking. Adapted from [71].

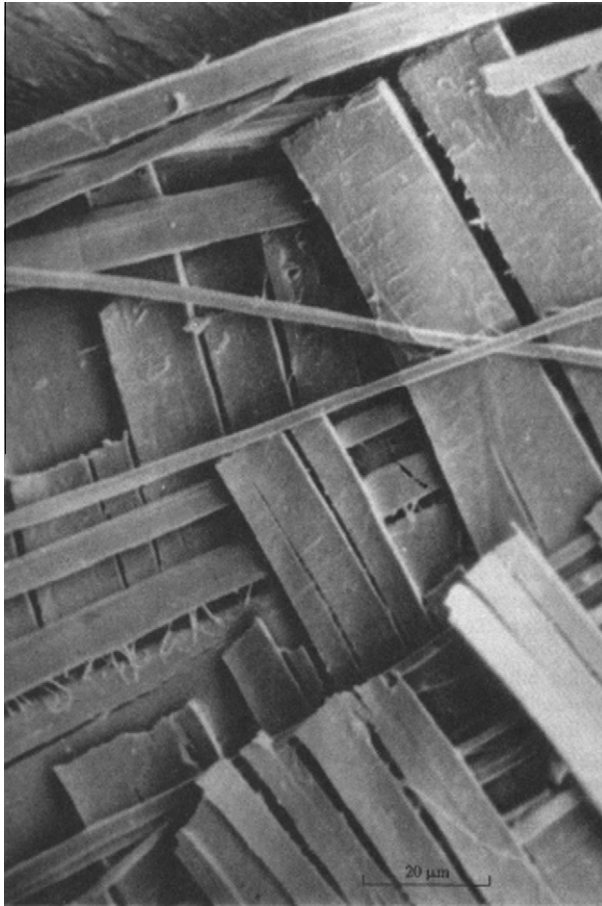


Fig. 113. Scanning electron micrograph showing successive layers with orientation close to (but not equal) to 90° in the wing case (elytron) of scarab beetle. Taken from [18], Fig. 2.39, p. 79.

complexes with Histidine residues [405–407]. The Young's modulus varies from 1 kPa to 20 GPa, for adult insect wing, tibia, and elytron. This is understandable, since the cuticle is a composite of chitin nanofibers that are among the stiffest of the natural fibers. The elastic modulus of crystalline α -chitin measured by *in situ* tensile testing under synchrotron X-ray is reported to be ~ 40 GPa [408]. 'Compliant' cuticles contain 40–75% water whereas stiff cuticles contain only 12% water. The tensile strength of femoral cuticle in locust is 60–200 MPa and the failure strain is as high as 5% [409].

One of the important components in the efficient strengthening of the organic matrix by the chitin nanofibrils is the bonding between the two. If the fibers were only weakly bonded this strengthening effect would not occur, such as in polymer synthetic composites. Fig. 115 shows a chitin chain, aligned with the beta pleated protein. There is an almost exact coincidence between nearly every fourth sugar residue in the chitin chain with every sixth amino acid residue in the protein. This can be verified by multiplying 1.032 nm by four (4.128 nm) and 0.69 nm by 6 (4.14 nm). These sites are proposed to provide hydrogen bonds. Vincent and Wegst [409] estimated the shear strength of the chitin–protein interface by assuming that each bond has a strength of about 30 pN. Considering nanofibrils with a diameter of 3 nm and length of 300 nm containing 19 chains, they obtained a shear strength of approximately about 30 MPa, or about half of that measured for carbon fibers in a resin matrix. This is indeed significant and explains the excellent stiffness and strength of the cuticle. In addition, there

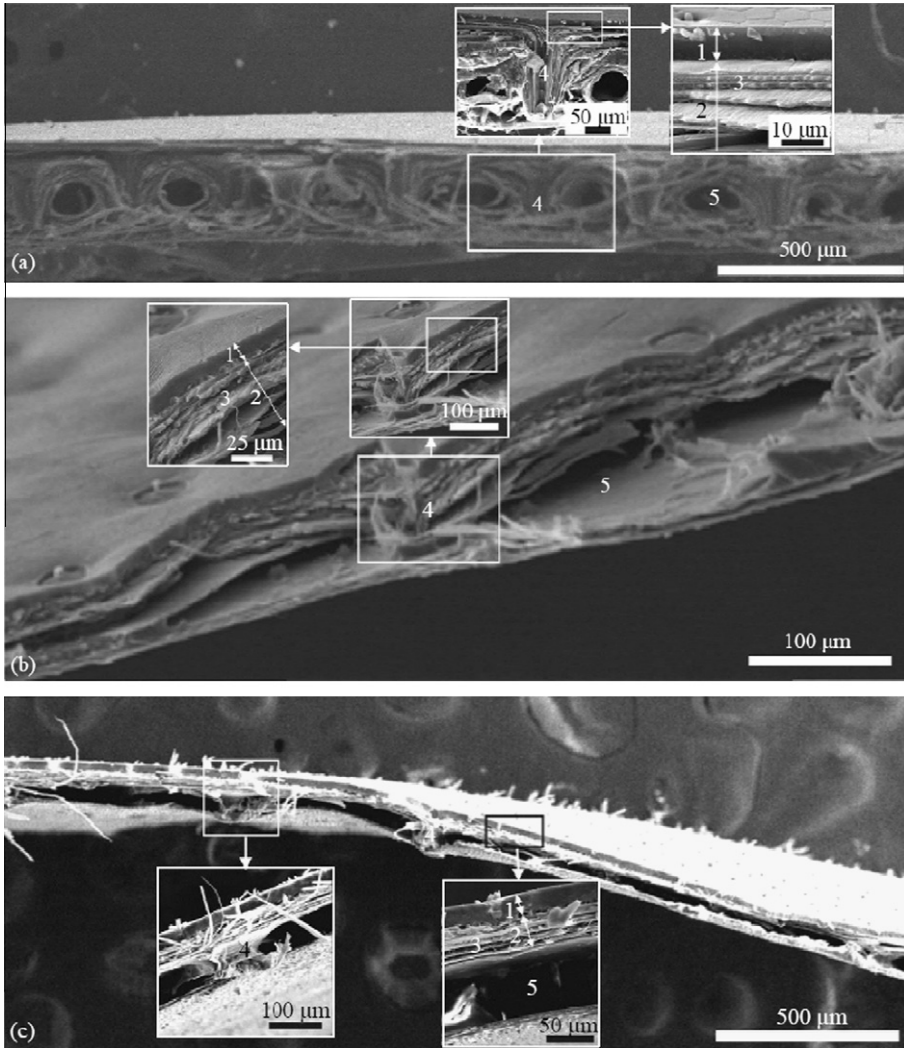


Fig. 114. Scanning electron micrographs showing microstructure of lateral section in three beetle's elytra. (a) *C. japonicus* (b) *A. dichotoma* (c) *P. brevitarsis* (1: epicuticle; 2: exocuticle; 3: fiber layers; 4: bridge pier connecting the exocuticle and endodermis; 5: cavity). Taken from [402].

must also have covalent attachment between chitin and cuticle proteins. Such sites have been detected in various insect cuticles by Rebers and Willis [410] and Hamodrakas et al. [411].

In crabs, lobsters, and shrimps, also arthropods, the exoskeleton is highly mineralized with CaCO_3 in the form of calcite and some amorphous CaCO_3 , deposited within the chitin–protein matrix. Chen et al. [71] investigated microstructure and mechanical properties of sheep crab (*Loxorhynchun gandis*) and the tensile properties both in the thickness and in the lateral directions were measured. The results showed that the mechanical properties of crab exoskeletons are highly anisotropic. The mineralized chitin–protein fibers arranged in a Bouligand structure provide strength in the in-plane (x or y) directions and can be considered as the hard or brittle component. The flat fracture surface shown in Fig. 116 is clear evidence of brittle failure. The pore canal tubules in the vertical or thickness direction (z -direction) are ductile and can undergo a large amount of plastic deformation before

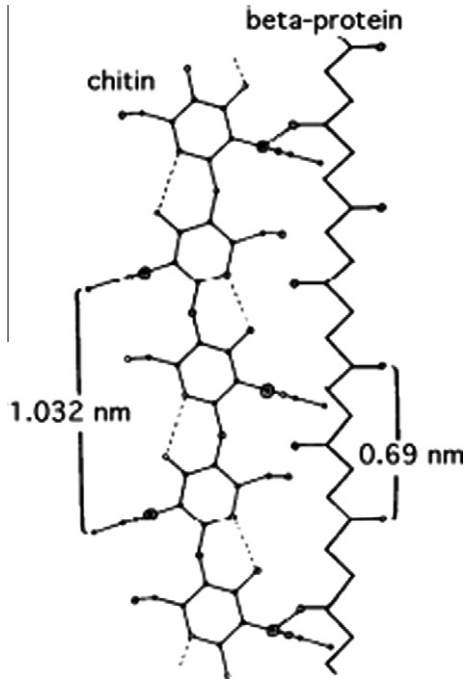


Fig. 115. Schematic diagram showing how chitin and protein can bond in cuticle. Every fourth amino-sugar residue of the chitin molecule ($4 \times 1.032 = 4.128$ nm) nearly coincides with every sixth amino acid residue of the protein $0.69 \times 6 = 4.14$ nm). Taken from [409]. Fig. 2).

fracture, providing the toughness and stitching the layers together. The shape of these pore canals is better understood by referring to Fig. 112.

The design of crab exoskeleton is an example illustrating how natural composite combines brittle (mineralized chitin–protein fibers) and ductile (organic tubules) components in a highly sophisticated manner, yielding enhanced mechanical properties. The mechanical properties of American lobster have been extensively studied by Raabe and co-workers [412–416]. A hierarchical multi-scale mechanical modeling was used to elucidate the structural and mechanical design of the lobster exoskeleton [415]. Fig. 117 is an overview showing key structural features at varying length scales and the methods used to model the mechanical anisotropy. The results showed that the twisted plywood structure provides isotropic in-plane strength, prevents microcrack propagation, and plays a role in energy dissipation during impact loadings. The nanosized CaCO_3 minerals and mineral–protein interfacial interactions further stiffen the exoskeleton. The multifunctional, hierarchically structured arthropod exoskeleton provides inspirations for the novel design of high-performance composites.

3.8. Egg shells

Oviparous animals produce eggs that protect the babies before they hatch. These eggs have mechanical properties that are adjusted to the environment encountered. They also have to be sufficiently weak to be penetrated or broken by the hatchlings. In the case of birds, the eggs are primarily calcite (96–98% by volume), the rest being hydrated organic material. Fig. 118a shows a schematic of the cross-section of a chicken egg shell. It contains three layers: an inner membrane, the mineralized shell, and an outer epithelium. Fig. 118b is a SEM micrograph showing the cross-section of an egg shell.

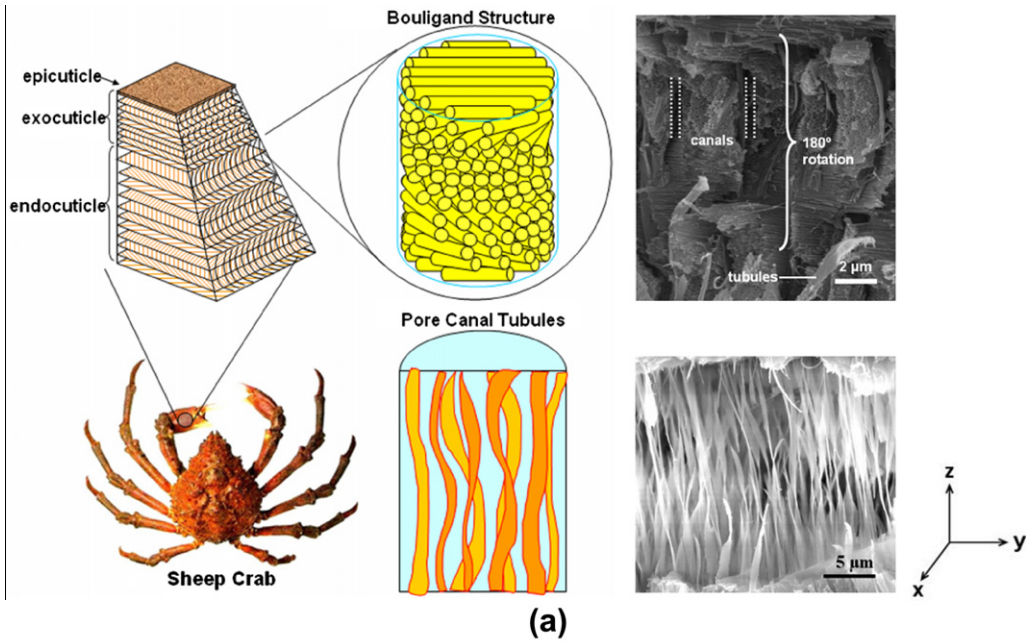


Fig. 116. Mechanical design of the crab exoskeletons: mineralized chitin–protein fibers arranged in the Bouligand structure provide in-plane (*x*–*y*) stiffness and ductile pore canal tubules in the *z*-direction stitch the layers together and enhance toughness. Taken from [71].

We are all familiar with an inner porous membrane from peeling boiled eggs. The structure of this membrane is shown in Fig. 118c. It consists of a network of collagen fibers. The density can be calculated from Gibson and Ashby [166] equation:

$$\frac{\rho_c}{\rho_s} = C_1 \left(\frac{t}{l} \right)^2 \tag{3.4}$$

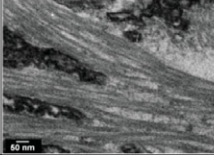
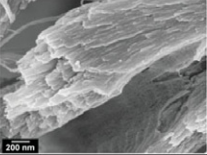
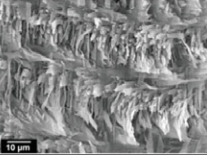
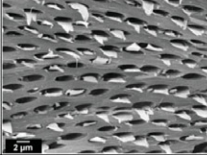
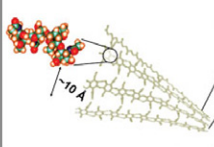
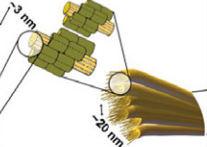
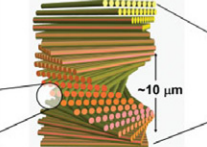
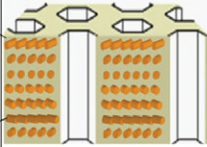
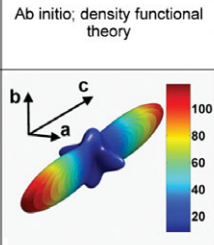
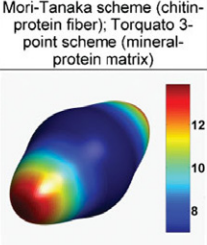
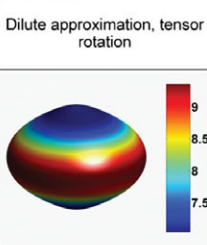
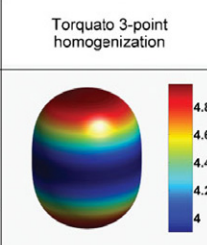
Scale	0.1 nm – 10 nm	10 nm – 100 nm	100 nm – 10 μm	10 μm – 1 mm
Hierarchical structure unit	α -chitin (H-bonded anti-parallel N-acetyl-glucosamine molecular chains)	Mineralized chitin-protein nanofibrils in a planar array	Twisted plywood stack of mineralized chitin-protein planes without pore canals	Twisted plywood stack of mineralized chitin-protein planes with pore canals
Experimental method	Transmission electron microscope	Field emission scanning electron microscope	Field emission scanning electron microscope	Field emission scanning electron microscope
Microstructure				
Schematic				
Simulation method	Ab initio; density functional theory	Mori-Tanaka scheme (chitin-protein fiber); Torquato 3-point scheme (mineral-protein matrix)	Dilute approximation, tensor rotation	Torquato 3-point homogenization
Elastic behavior, 3D maps of Young's modulus [GPa] a, b-axes: basal directions of the chitin unit cell c-axis: longitudinal (chain) axis of the chitin molecule				

Fig. 117. Overview of key structural features of a lobster exoskeleton at different hierarchical length scales and the corresponding mechanical modeling methods. Taken from [415].

where ρ_c is the density of the cellular structure and ρ_s is the density of the solid material, respectively. There are two characteristic dimensions: the cell size, l , and the strut thickness, t . C_1 is a proportionality constant. In Fig. 118c, $t \sim 1 \mu\text{m}$ and $l \sim 10 \mu\text{m}$, thus, the relative density is a very low value. This inner membrane is quite elastic and has several functions, one being to ensure that shell fragments stay in place in case of egg fracture. Thus, it serves as an inner scaffold. This can be readily seen by removing an egg from the refrigerator, hitting it on the counter until it fragments. The egg will maintain structural integrity. This additional mechanical property is achieved without significant weight penalty.

The calcite in eggs nucleates in the inside and forms radiating growth rods. This type of growth is also known as 'spherulitic' and is also observed in polymers and in the aragonite growth after interruption and prior to the formation of regular tiles (Fig. 67b). The crystals that grow toward the outside have a free path and therefore propagate until the external surface. These crystals grow in a spongy organic matrix. This spherulitic growth is also similar to the ones in the nacreous portion of the abalone shell, after growth interruption and the formation of a mesolayer. The external surface of the egg shell is comprised of an epithelium. The aligned calcite crystals are shown in the SEM micrograph of Fig. 118d.

It should be mentioned that turtle eggs are not rigid but can undergo considerable deformation. This is a requirement of the manner in which they are laid and covered by sand.

3.8.1. Whelk eggs

Oviparous marine snails (such as *Busycon canaliculum*) secrete peculiar egg case membranes that protect their growing embryos. In *Busycon*, it forms a helical strand as long as 1 m. This has been nicknamed 'mermaid's necklace.' These strands contain up to 160 capsules (Fig. 119a) and are repeatedly

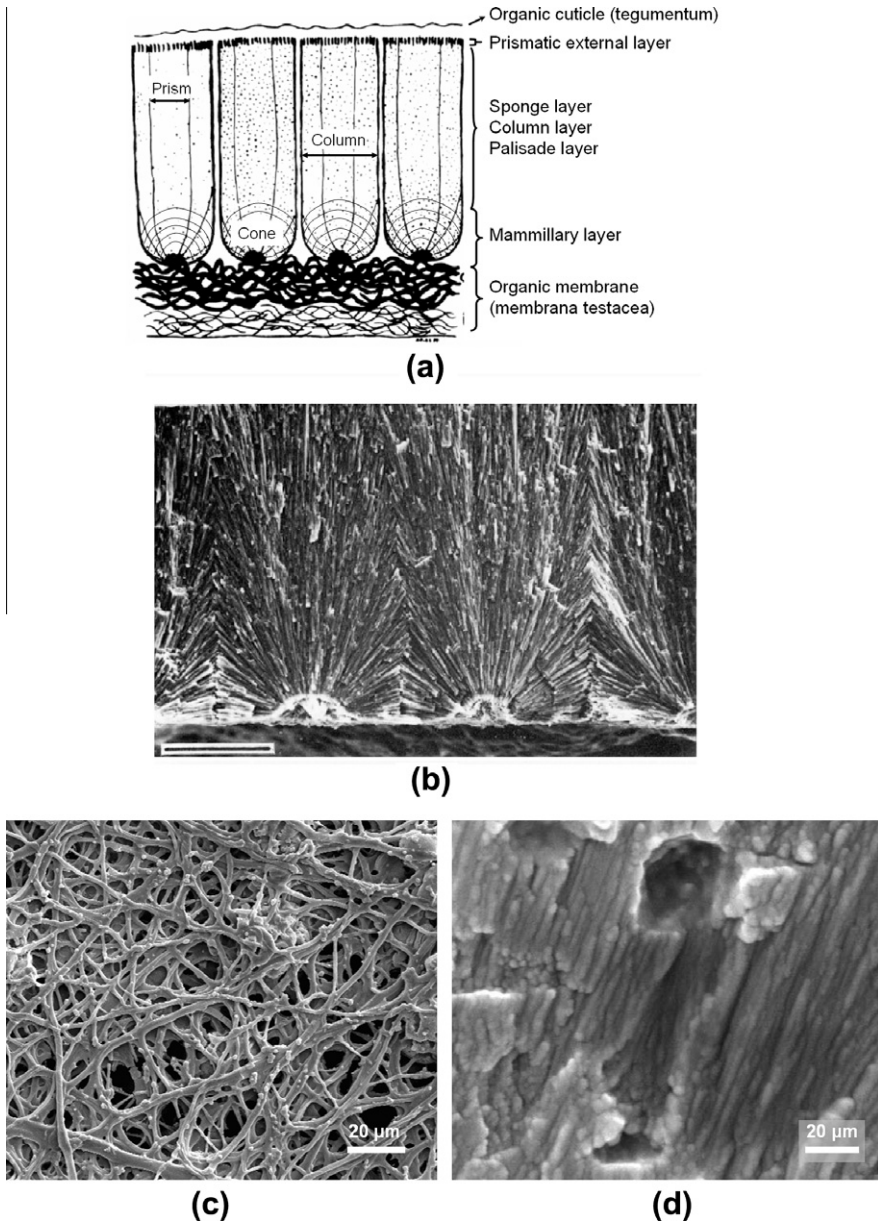


Fig. 118. (a) Sketch of cross section of an egg shell showing inner membrane and growth of spherulites of calcite crystals. Adapted from [417]; SEM micrographs showing (b) cross section of an egg shell. Adapted from [418]; (c) structure of organic layer underneath shell; (d) calcium carbonate crystals growing from the internal surface toward outside.

hit by seashore waves. Thus, the capsules containing the whelk embryos have to have unique mechanical properties to resist the onslaught of coastal waves. In addition to the mechanical impact of coastal waves, the cases must also resist chemical, bacterial, and predator attacks. They can undergo large reversible deformations akin to the synthetic elastomers (rubber). The mechanical response is analogous to the superelastic effect of the Ni–Ti (Nitinol) and other alloys. In Nitinol, the martensitic

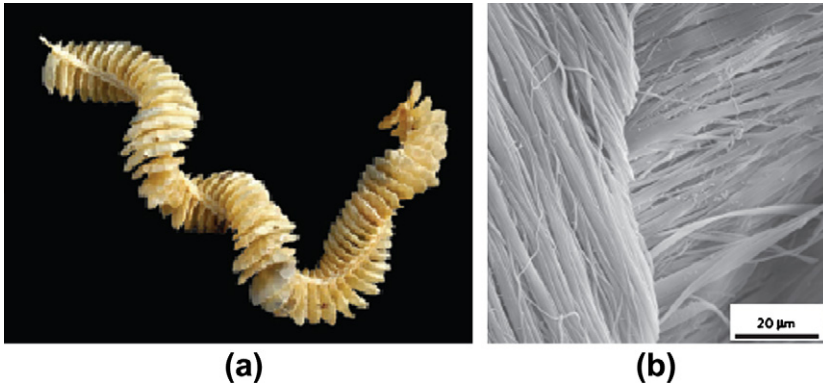


Fig. 119. (a) 'Mermaid necklace' (whelk eggs) of interconnected capsules forming a helical pattern around strand; (b) pattern of cross-plywood structure of fibers from whelk egg capsules, each with 0.2–0.5 μm diameter. Taken from [180].

transformation induced by stress is reversible. Upon unloading, the alloy returns to its original structure. Reversible strains of up to 0.06 can be obtained in these shape memory alloys. In contrast, in conventional metals, the reversible (elastic) strains rarely exceed 0.01.

The same response is obtained when specimens from the capsule of whelk eggs are subjected to tension. The results of stress–strain tests in tension at temperatures ranging from -1 to 80 $^{\circ}\text{C}$ are shown in Fig. 120a, showing the characteristic inflection ($d^2\sigma/d\varepsilon^2 = 0$) (discussed in Section 1.3). The stress–strain curves have three stages:

- (a) an initial region with elastic modulus of ~ 100 MPa;
- (b) a plateau covering strains up to 0.7;
- (c) a stiffening beyond 0.7.

Upon unloading the three stages are again observed, albeit with a hysteresis. The region from $\varepsilon = 0.05$ to $\varepsilon = 0.7$ corresponds to the structural transition of the bioelastomer, which changes from α -helix to β -sheet configuration, in the same manner as wool upon being tested in tension. The structural change of the biopolymer is shown in Fig. 120b. Initially, the fibers are comprised of coiled-coil α -helices (described in Section 1.1.1). These helices open up (unravel) under the effect of stress, being bonded by van der Waals and hydrogen bonds. The stretched chains subsequently organize into β -sheets. Upon unloading, the opposite effect happens and the process is reversible. Miserez et al. [180] analyzed this phenomenon thermodynamically and compared it with rubber elasticity. As the polymer chains in rubber are extended, they align themselves with the tensile axis, decreasing the disorder (entropy) of the system. The Treloar equation (Eq. (1.8)) shows that the stiffness increases with increasing temperature, at a fixed value of the extension ratio (strain). The experimental results shown in Fig. 120a do not agree with this behavior. The analysis by Miserez et al. [180] uses two terms: a term due to the internal energy increase (σ_U) and one due to the entropy decrease (σ_S):

$$\sigma = \sigma_U + \sigma_S = \left(\frac{\partial U}{\partial l}\right)_{v,T} - T \left(\frac{\partial S}{\partial l}\right)_{v,T} \quad (3.5)$$

The application of Maxwell's relationship gives:

$$\sigma = \left(\frac{\partial U}{\partial l}\right)_{v,T} + T \left(\frac{\partial \sigma}{\partial T}\right)_{v,l} \quad (3.6)$$

The stress vs. strain plots in the range 10–100%, Fig. 120a, at various temperatures unequivocally show that the stress decreases with temperature at all strains tested, contrary to rubbery elastomer behavior governed by entropy.

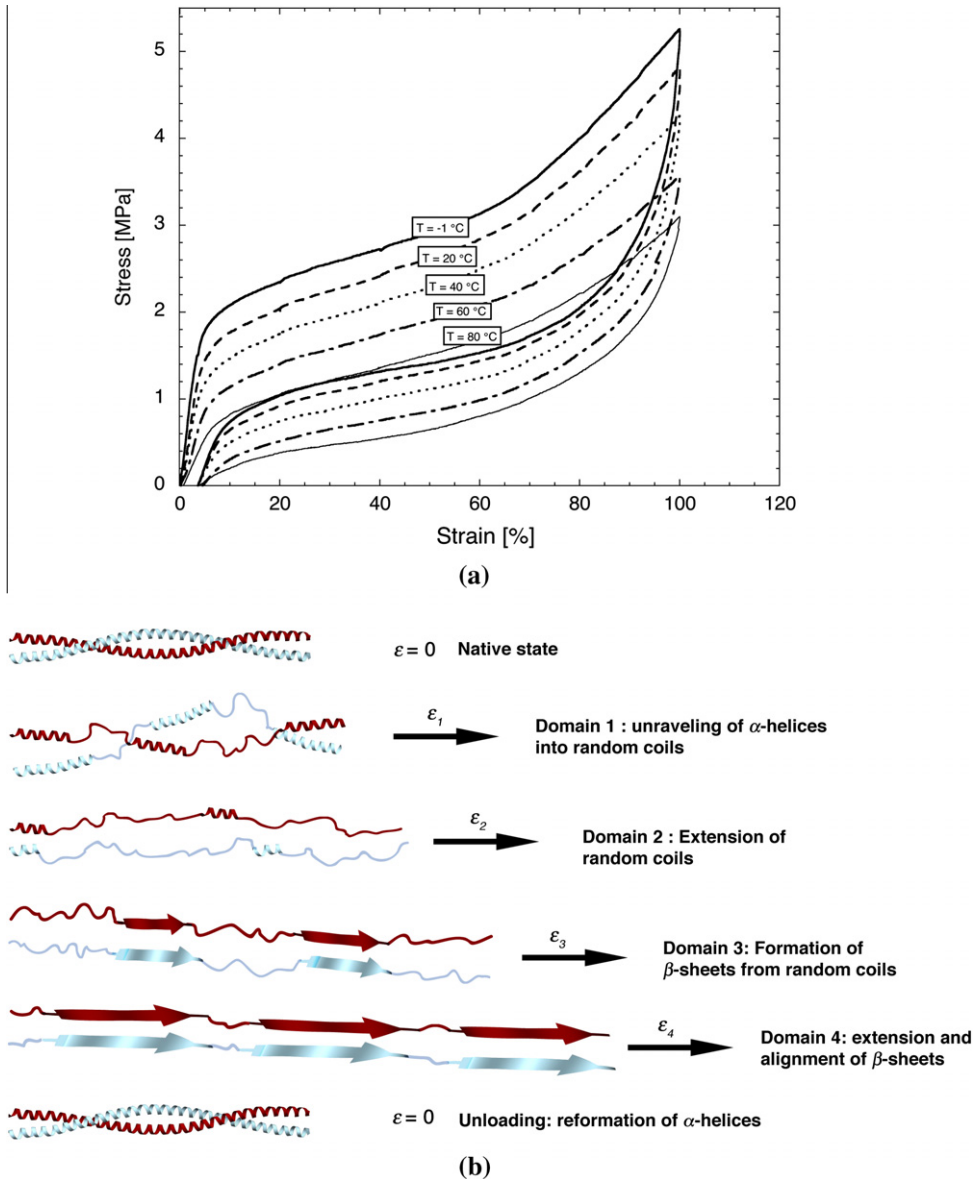


Fig. 120. (a) Engineering tensile stress–strain curves of whelk egg capsules in loading and unloading, up to a strain of ~ 1 ; notice superelastic effect and hysteresis; (b) schematic representation of presumed reversible structural transformation. Taken from [180].

The decrease in the strength at a constant strain with increasing temperature suggests that the internal energy term dominates over the entropy decrease in Eq. (3.5) above. This argument is in agreement with Flory's theoretical analysis [419] of elastic proteins showing that strains can be due to internal-energy dominant mechanisms. However, entropic effects can be and probably are present.



Fig. 121. (a) Pangolin (*Manis temmincki*) showing scaly exterior made of keratin (<http://letopis.kulichki.net/2001/image2001/pangolin.jpg>). (b) Close-up view of the overlapping keratin scales (<http://www.itsnature.org/ground/mammals-land/pangolin/#ixzz1067QifR5>).

3.9. Keratin armor

3.9.1. Pangolin scales

An unusual armor is found on the pangolin, a small insectivore that lives in the rain forests of Asia and Africa. It ranges from 40 to 100 cm in length and weighs up to 18 kg. The exterior of the animal is covered with non-mineralized keratin scales, as shown in Fig. 121a, which weigh up to 20% of the total animal. When curled up, these scales extend from the body producing a barrier of razor-sharp edges, as shown in Fig. 121b. These scales have been used to create a coat of armor that was presented to King George III.

3.9.2. Quills

Some mammals have developed hair that is coarse, stiff and sharp for defense and protection. These animals include porcupines, hedgehogs, echidnas, tenrecs and spiny rats and mice. Like hair and fur,

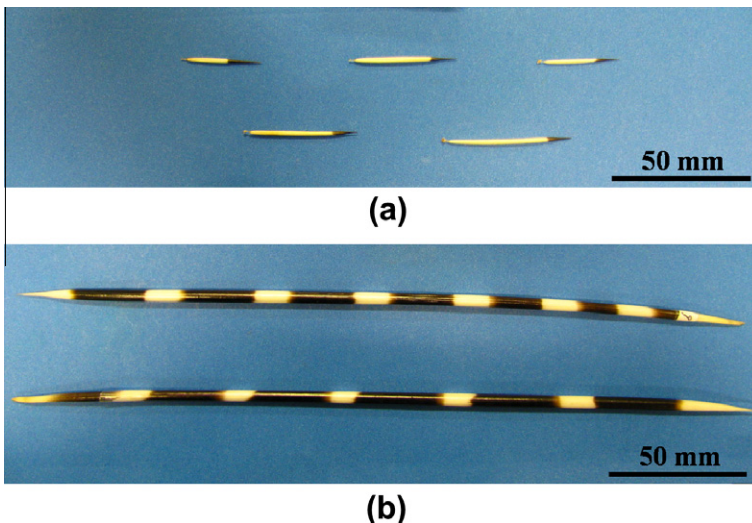


Fig. 122. Photograph of (a) Erethizontidae (North American) and (b) Hystricidae (African crested) porcupine quills. Taken from [89].

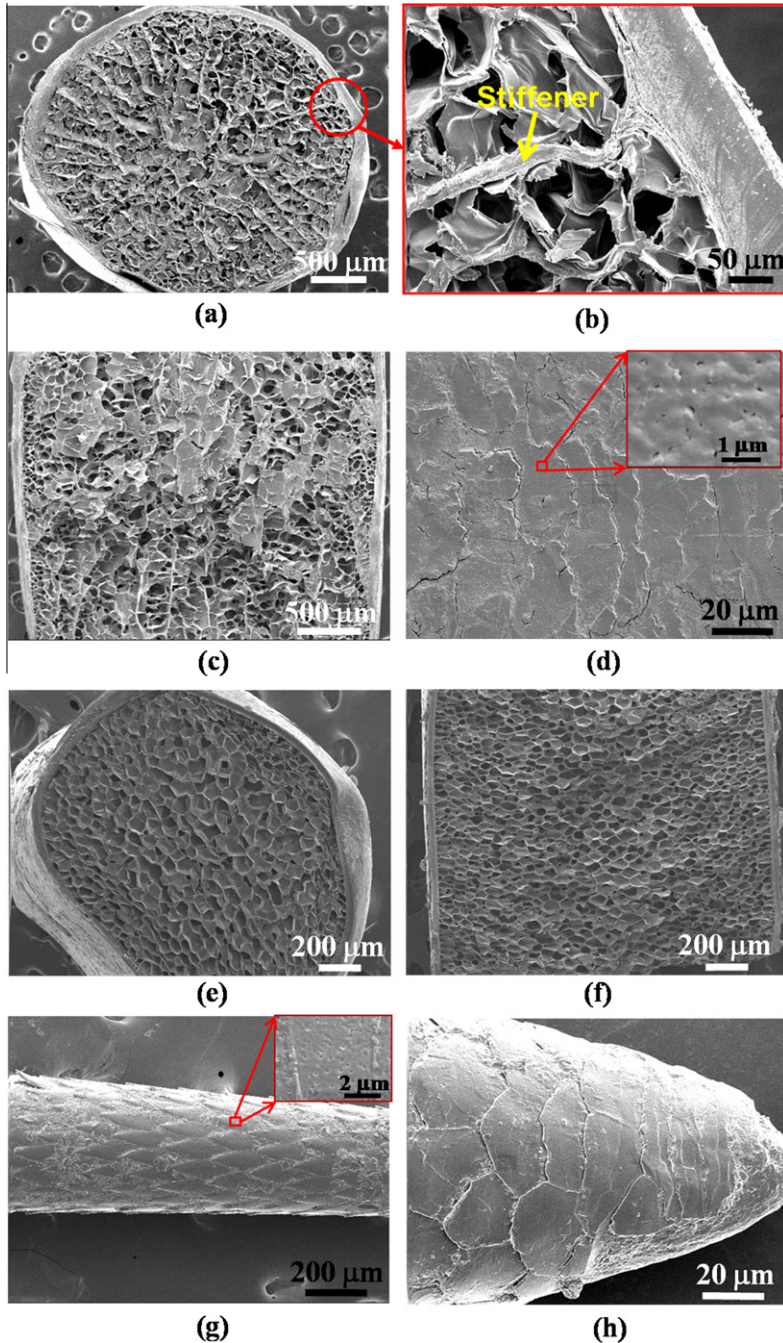


Fig. 123. Cross-sections and surface morphology of Old (Hystricidae) and New World (Erethizontidae) porcupine quills. (a) Transverse section of the Hystricidae (African crested) quill showing stiffeners that extend through the core, (b) higher magnification of the stiffener, (c) longitudinal cross-section. The areas where the core is obscured are remnants of the stiffeners, (d) surface of the quill, showing the plate-like morphology of the keratin tiles. Structure of Erethizontidae (North American) quill; (e) whole morphology in transverse orientation, (f) morphology in longitudinal orientation, (g) and (h) scales on the cortex surface of the black tip with pores on the right hand of (g). Taken from [89].

the quills (spines) are composed of α -keratin, which are long tubes (cortex) with tapered ends filled with a closed cell foam (core). Unlike Old World porcupine (Hystricidae, African or Indian ‘crested porcupine’) quills, some of the New World (Erethizontidae) quills have a hooked end that ends up embedded in a predator if the porcupine is attacked. Both families have muscles on the base of the quill allowing them to stand up, thereby making the animal look larger if threatened. The Erethizontidae quills can be as long as 8 cm while the Hystricidae are longer – up to 50 cm – and also have a proportionally larger diameter.

The cores have several morphologies, depending on the species: isotropic (Erethizontidae and echidnas), isotropic with longitudinal stiffeners (Hystricidae) or a honeycomb with longitudinal cortex ribs and septae (hedgehog) [291,420,421]. The septae are thin membranes that are connected to the cortex and periodically separate the foam in the longitudinal direction. Fig. 122 shows a photograph of Hystricidae and Erethizontidae quills side by side for comparison. Fig. 123 shows SEM micrographs of the transverse and longitudinal cross-sections of Hystricidae and Erethizontidae quills.

Fraser and MacRae [117] examined the elastic modulus of Hystricidae quills and, as with other keratinous materials, found it to be highly dependent on the relative humidity (3.4–6.7 GPa, 100–0% humidity). Vincent and Owers [291] examined microstructure and Euler buckling stress for a variety of quills (porcupines, hedgehogs and tenrecs). The Euler buckling stress was higher for the hedgehog, which was attributed to the presence of the septae. They concluded that the hedgehog quills are designed for energy absorption by buckling elastically under large forces (falling from heights or from attack of a predator) whereas the porcupine quills are designed for piercing opponents.

Karam and Gibson [171] examined the structure of quills from the hedgehog, Hystricidae, Erethizontidae, and echidna and applied equations they developed to predict the elastic modulus. They estimated the axial buckling load and local bending moment based on equations they had developed for cylindrical tubes filled with compliant cores [171]. They found that the axial buckling load and the critical bending moment of the hedgehog spines were greater than that of an equivalent diameter unfilled cylinder, thus optimized for resistance to bending. The Brazier ovalization (Fig. 124) was significantly reduced for the quills, in comparison to hollow cylinders due to the presence of the foam, which does not separate from the cortex under deformation.

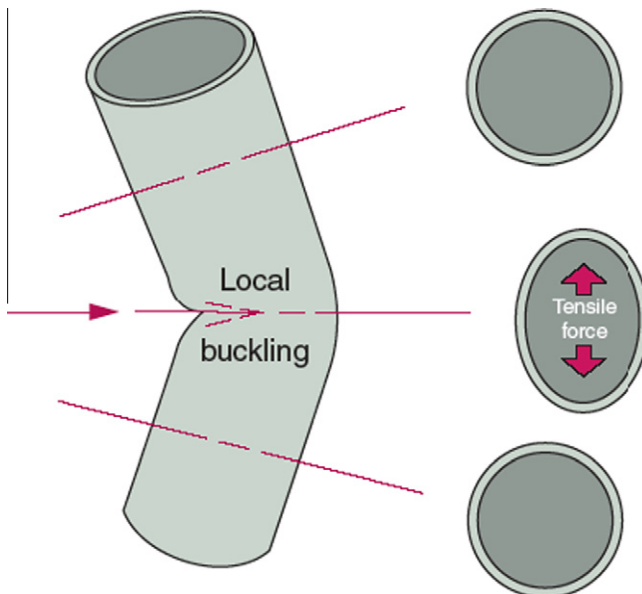


Fig. 124. Brazier ovalization of a cylindrical shell. Taken from [420].

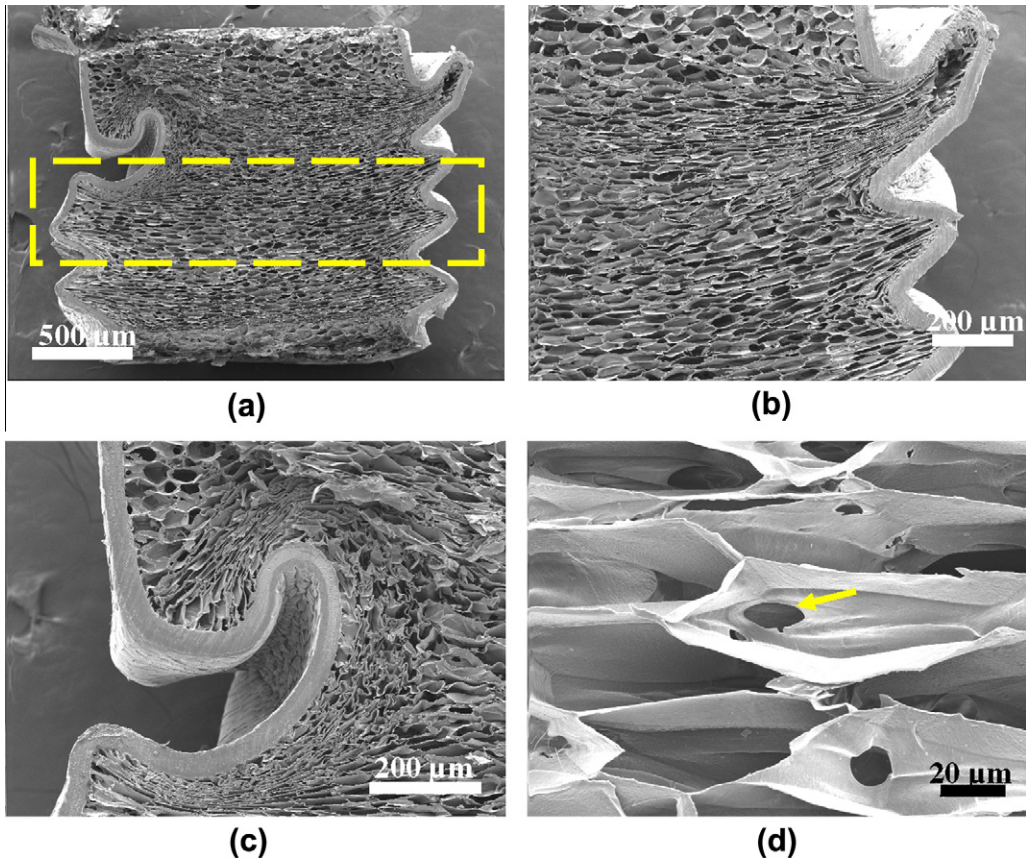


Fig. 125. SEM micrographs of a compressed *Erethizon* (North American porcupine) quill: (a) morphology of the longitudinal cross-section, (b) and (c) foam and cortex at the buckling part, (d) damaged cores. The yellow rectangle indicates lateral tensile deformation of the foam. The arrow in (d) points to a tear produced by compressive load. Taken from [89].

Fig. 125 shows SEM micrographs of a *Erethizontidae* quill after compression testing (not to complete densification). Buckling of the cortex is clearly observed with a periodic wavelength on one edge (Fig. 125a). The cells deform significantly around the buckled cortex and flatten in the center (Fig. 125b), but almost all the foam remains attached to the cortex. Higher magnification shows that the cell walls tear prior to complete densification. Thus, the cortex remains attached to the foam, even after severe deformation.

4. Cutting edges

These are important survival and predating mechanisms in a number of plants, insects, fishes, and mammals based on sharp edges and serrations. Some plants (e.g., Pampas grass: *Cortaderia scilloara*) have sharp edges covered with serrations. The proboscis of mosquitoes and stinger of bees are examples in insects. Serrations are a prominent feature in many fish teeth. We discuss the teeth of the piranha and various sharks, focusing on the hierarchical aspects. The chiton radula is composed of magnetite, the hardest biomineral with Vickers hardness number (HVN) 9–12 GPa. On the opposite side of the spectrum, squids do not have minerals and have sharp beaks that use an ingenious tanning process, providing a graded structure with HVN up to 5 GPa. Rodents have teeth that are sharpened continuously, ensuring constant sharpness and efficacy. Insect stingers and ovipositors, that penetrate into the dermis and wood, respectively, are also presented.

We illustrate these unique aspects by focusing on one characteristic of biological materials: their ability to puncture, cut, and shred. The fact that serrations and needles are present in many species and in diverse configurations is direct evidence that they developed independently, by a mechanism that is called convergent evolution. This chapter contains extensive material from Meyers et al. [86].

4.1. Plants

Fig. 126 shows a blade of pampas grass (*Cortaderia selloana*) with serrations along its outer edge. Each serration is in the shape a thorn protruding upward along the side of the blade. They extend approximately 50 μm from the body of the leaf and form sharp points with an apex angle of roughly 20°. This sharp cutting edge was evolutionarily designed as a defense mechanism against grazing animals. This feature is also prominent in other grasses, such as *Hypolitrium sharaderenium*. Another example can be found in cacti, which have their bodies covered in thorns for protection.

4.2. Fish teeth

We discuss a few fish teeth with emphasis on their function. The “big teeth” of the Amazon dogfish have a piscivorous evolutionary design. They are used to puncture and hold prey and are thus designed in a hook-like fashion facing inward toward the mouth of the fish. This can be seen in Fig. 127.

Fig. 128a shows structural hierarchy of the cutting mechanisms found in the jaw of a piranha (*Serrasalmus manuelyi*). The jaw is designed with sharp triangular teeth aligned so that as the mouth of the fish closes the initial points of puncture of both the lower and upper jaw are superimposed. Each tooth exhibits microserrations along its cutting edge, seen in the detail of Fig. 128a. These serrations, approximately 10–15 μm in wavelength, are used to create a highly efficient cutting effect which converts some of the dragging force into normal force at localized points. As the jaw further closes any tissue caught in the trough of the aligned teeth are caught in a guillotine-like confinement of teeth. This is shown in Fig. 128b and c. There is a superimposed compression stress P and shear stress S which effectively cut through the skin and muscle fibers. The mechanics of cutting is rather complex and is presented by Atkins [422]. Meyers et al. [398] calculated the bite force of a piranha from the biomechanics of the muscles and the value is surprisingly low: ~ 17 N. Thus, the cutting ability is derived from the sharpness and angle of the cutting edges, and not from a powerful jaw action. The piranha tooth has an external layer of enameloid, highly mineralized with hydroxyapatite (>95 wt.%) enclosing an internal region of dentin, which is a composite of collagen fibril and hydroxyapatite crystals. The hardness and reduced modulus of piranha tooth measured by nanoindentation are reported

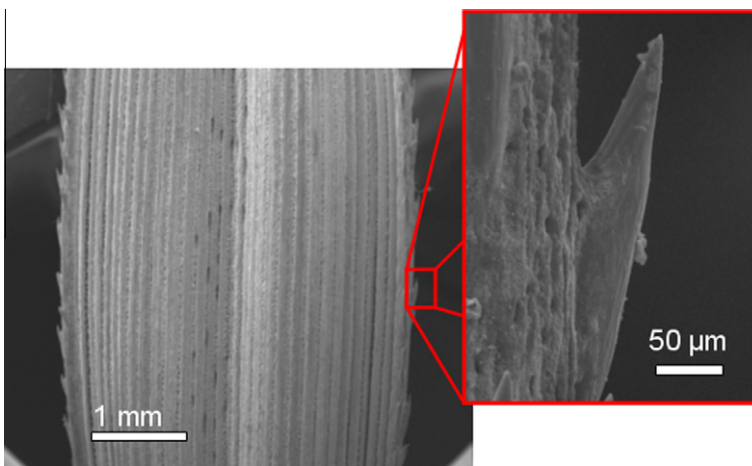


Fig. 126. Pampas grass leaf; note serrations at edges. These serrations, with approximately 150 μm barbs, protect grasses against herbivores.

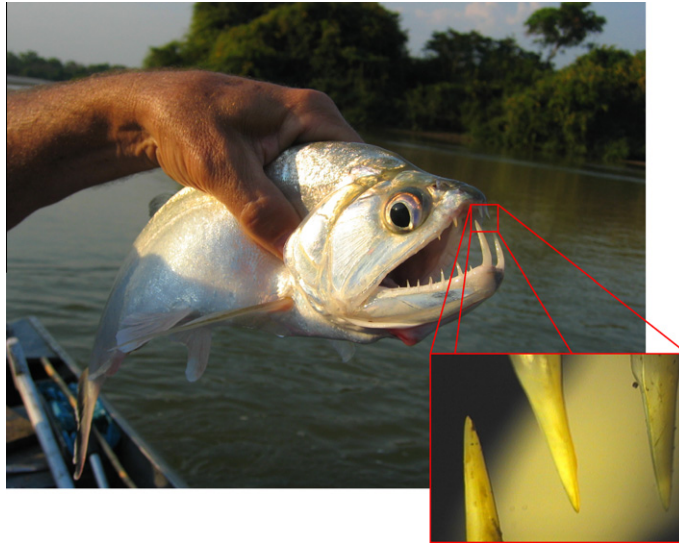


Fig. 127. Dogfish and teeth. A unique characteristic of this fish is that the teeth from the lower mandible penetrate through the skull. Their tips actually protrude out of the skull when the mouth is closed.

to be 4–5 times higher than those of dentine [423]. Similar microstructural and mechanical design have been found in teeth from shark [423] as well as a variety of animal species [69].

The great white shark (*Carcharodon carcharias*) evolved teeth from the scales of its ascendants. It uses these extremely sharp teeth to perform a very specific function: to cut through the skin and flesh of mammals. To avoid self-injury the great white shark takes one efficiently large bite out of its prey then retreats and waits for its victim to undergo shock or hemorrhaging before final consumption. This bite takes only one second to complete [424] and thus extremely sharp teeth are required. Each tooth is outfitted with a line of large serrations, with up to 300 μm between points. The serrations are perfectly aligned along the cutting edge of the tooth, each creating a mini tooth on the side of its parent tooth. Similar to the piranha tooth the serrations on this edge maximize the efficiency of the drag force and convert it into points of normal force summed along the side of each serration. Fig. 129 shows (a) a photograph of great white shark jaw with multiple rows of teeth and two SEM micrographs showing serrations on the teeth at increasing magnifications, (b) serrations in teeth and comparison with cycloid. Cycloid is a curve generated by a point on the surface of a circle rolling on a plane. The radius of the circle that defines the cycloid is r and x, y are the coordinates of a point on the cycloid. It is interesting that this serrations are well represented by a cycloid equation, which is shown in Fig. 129b in comparison with the actual profile of the tooth:

$$y = \frac{1.2(1 - \cos r)}{(r - \sin r)x} \quad (4.1)$$

In Eq. (4.1), the radius of the circle that defines the cycloid is r and x, y are the coordinates of the points on the cycloid. In a manner similar to the piranha, the bite force is not very large; its maximum was measured to be ~ 2000 N. The cutting action is due to the sharpness of the teeth and not due to a large pressure. In contrast, the jaws of a crocodile can apply forces that are eight times larger.

In contrast with great white shark, there are no serrations on the edge of the Shortfin Mako shark (*Isurus oxyrinchus*) tooth [425]. The teeth are slender and slightly curved in a hook-like fashion. The function of these teeth is primarily to puncture and capture prey while in the Great white shark the teeth are used more as cutting tools. It is clear in Fig. 130 that the angle of the apex of the tooth of a Mako shark is much smaller than that of the great white shark. Again, this sharp angle, similar to that of the dog fish, is used to puncture the prey. Piscivorous fish do not have to penetrate the tough skin of

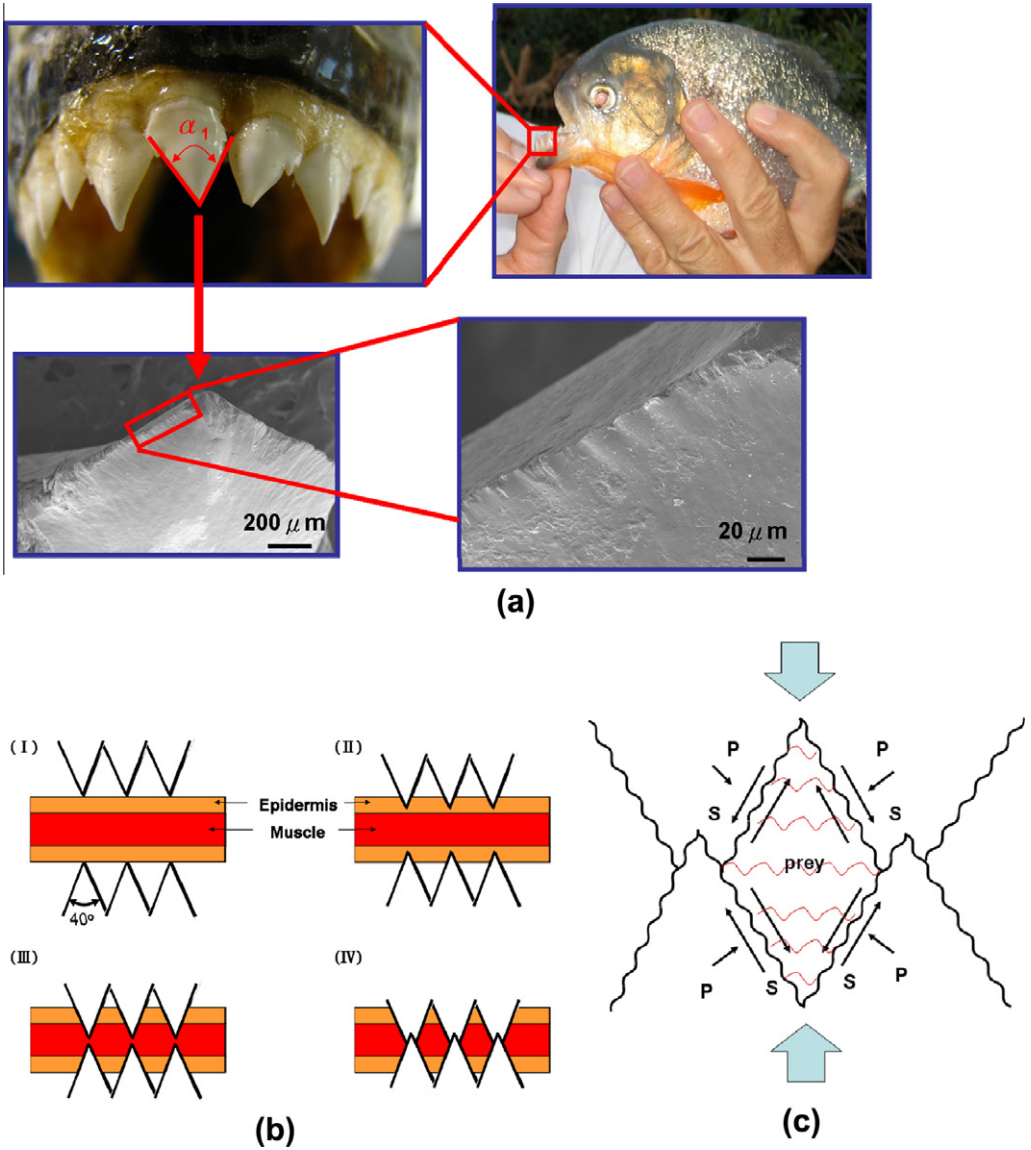
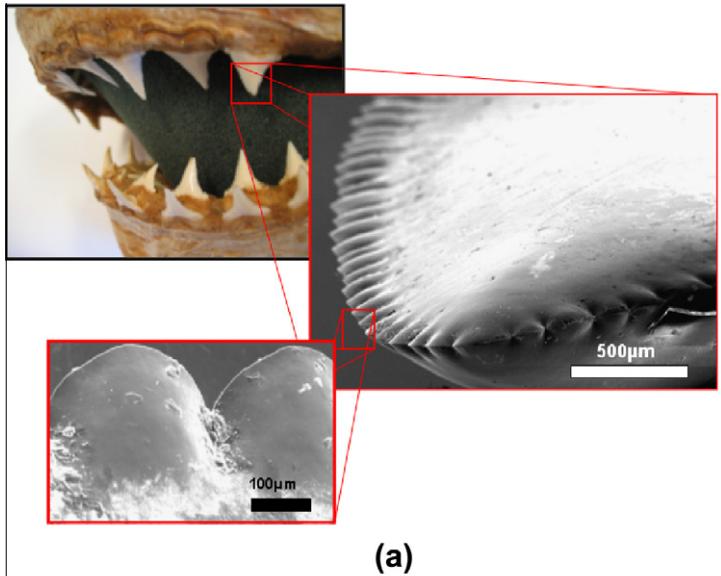


Fig. 128. Piranha, teeth, and biting action: (a) progressively higher magnifications showing SEM micrographs of a single tooth; higher magnification micrograph on right shows small serrations on cutting edge; (b) diagram of guillotine-like confinement of material during the biting action. I–IV: teeth closing and slicing through epidermis and muscle; (c) applied force from jaws generating pressure P and shear stress S .

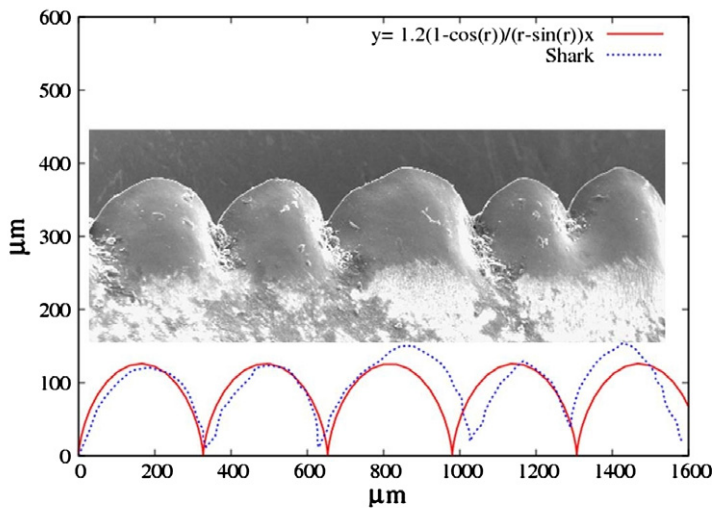
mammals against which serrations are needed. The analogy with knives is applicable here. A butter knife is smooth whereas a steak knife is more effective if it has serrations.

4.3. Rodent incisors

The incisor teeth of rodents such as the rabbit and rat (Fig. 131a and b, respectively) have been evolutionally designed to “self-sharpen” through a process which takes advantage of natural wear and



(a)



(b)

Fig. 129. Great white shark (*Carcharodon carcharias*) teeth; (a) Shark mouth and detail of teeth at increasing magnifications, showing serrations; (b) serrations in teeth and comparison with cycloid. Cycloid is a curve generated by a point on the surface of a circle rolling on a plane. The radius of the circle that defines the cycloid is r and x, y are the coordinates of a point on the cycloid.

differences in the wear rates depending on the hardness of the materials. These teeth are designed in a way so that a softer dentine backing is worn away at a faster rate than the hard enamel cutting edge. This action continuously exposes new sections of the enamel material, creating a self-sharpening effect. The teeth of rodents continuously grow. Hence, the selective wear is necessary to maintain their sharpness.

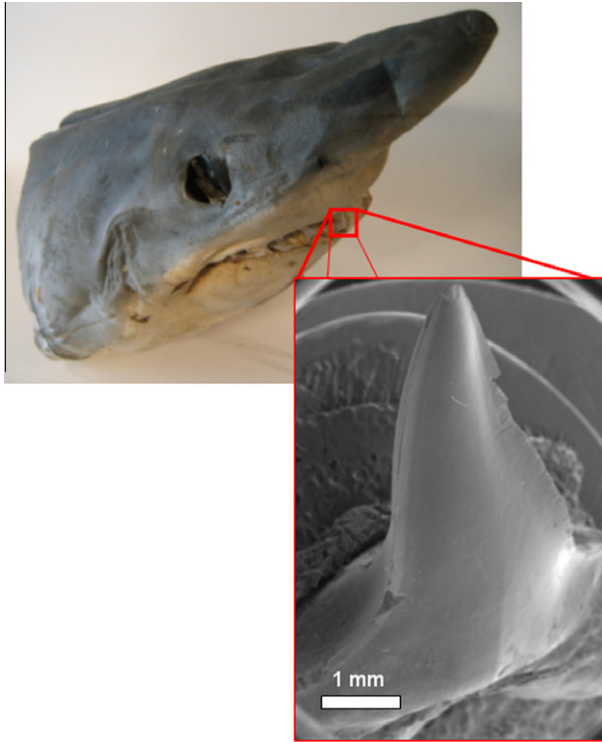


Fig. 130. Mako shark and tooth. The teeth are sharp and do not contain serrations, in contrast with great white shark teeth.

4.4. Squid beaks

Squids are mollusks that in the class cephalopods. They have a head, mantle, and eight arms and two tentacles. They have some uniquely interesting aspects due in part to the fact that they do not contain minerals. Their mantle, beak and suckers will be presented here.

The mantle of the squid is a hollow cylinder. Biopolymers are strong in tension but cannot resist compression without buckling. The mantle is rigid because of the internal water pressure. The principal locomotion method is through an ingenious water jet mechanism. The water stored inside the mantle is expelled through an orifice by the contraction of the muscles that form a special pattern of orientations (Fig. 132). There are inner and outer layers of collagen fibers that are called tunics. These collagen fibers are oriented at $\pm 27^\circ$ to the longitudinal axis of the mantle. The collagen layers sandwich the central region, which is the muscle. This muscle, upon contraction, creates the water jet. The muscle fibers are oriented in two directions: radially, connecting the outer and inner collagen tunic, and circumferentially. The propulsion takes place by the contraction of the circumferential muscle fibers and consequent reduction of the cavity volume. The length of the mantle is unchanged and therefore the wall thickness increases correspondingly. The jet propulsion in the squid can create significant velocities. For a 350 gram *Loligo* squid [426], this velocity is on the order of 2 m/s.

The squid beak is another component with unique characteristics. The necessity of the beak to tear flesh from its prey in the absence of a biomineral poses a significant challenge. The beak resembles somewhat a parrot's beak, with two sharp parts. The beak of a Humboldt squid (*Dosidicus gigas*) is shown in Fig. 133. The beak is embedded into the softer tissues of the squid head. The beak is much darker and the coloration gradually lightens as one moves away from its tip. This change in color (the dark is called 'tanned') is related to an increase in cross-linking of proteins in the structure. Whereas the lighter part is primarily a network of chitin in water, the tanned region contains His-rich and

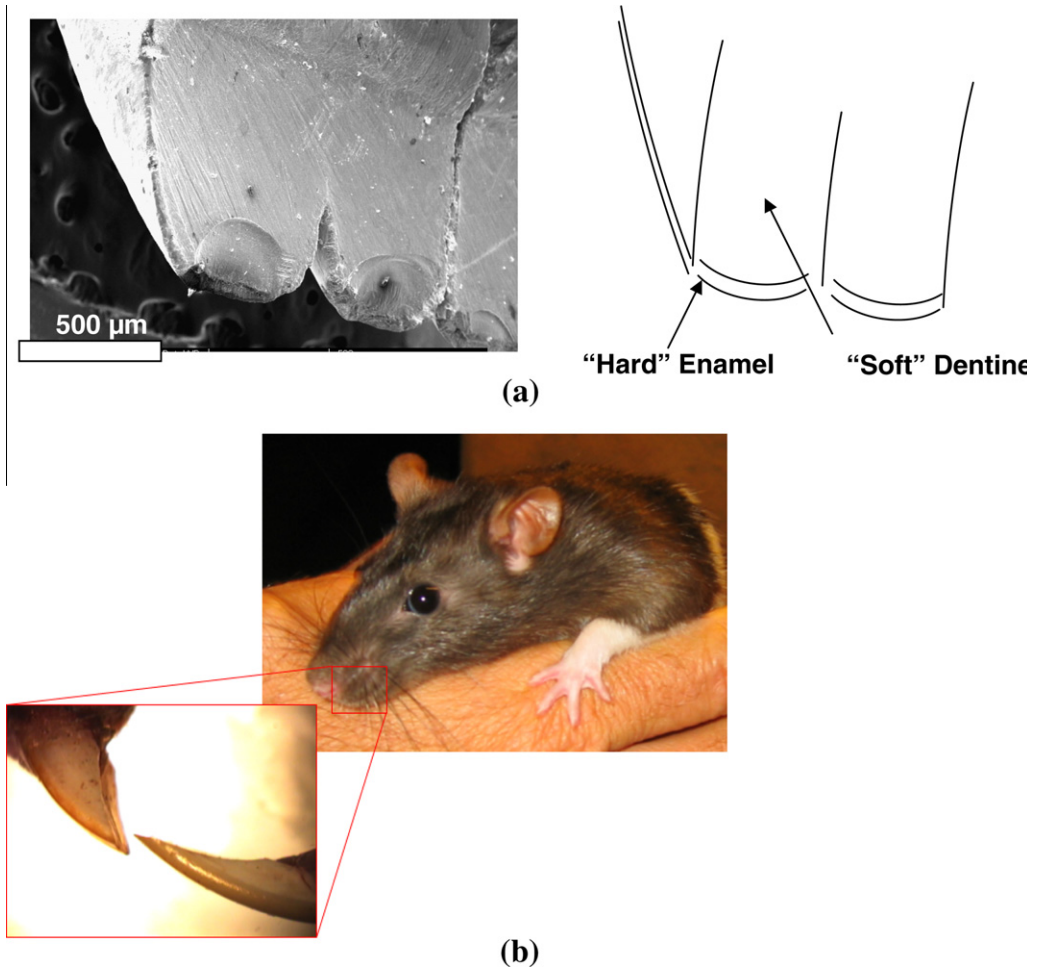


Fig. 131. (a) Rabbit tooth (incisor). The outside is hard enamel and the inside much softer dentine. The rabbit keeps the teeth sharp by wearing down the dentine and keeping a sharp protruding enamel layer. (b) Rat incisors. The enamel is the outside layer and the softer dentine is the inside. The action of incisors rubbing against each other ensures that the teeth remain sharp.

DOPA-containing proteins [378]. DOPA is an amino acid synthesized in the body from Tyr and is a neurotransmitter. It is surprising that it is a key ingredient in producing the hard tip of the squid beak. These amino acid residues are critical because they create strong cross-link networks by forming covalent bonds with each other. Additionally, low-molecular weight catechols also cross-link the protein network [427]. When the entire beak and surrounding region are dried, the Young's modulus is the same: 5–10 GPa. However, in the hydrated condition, the Young's modulus of the tanned region corresponding to the beak tip is ~ 5 GPa, while it drops to 0.05 GPa in the farthest regions. This indicates that there is a gradient in mechanical stiffness provided by the gradual change in hydration of the chitin network which is itself modulated by the gradient of His-rich proteins. It should be noted that there are other proteins mixed with the chitin.

The squid tentacles are another example of the ingenious design to accomplish necessary performance [428]. They have 'suckers' which attach themselves to the prey by suction, while resisting any shear action that would allow the prey to slide off. The suckers contain sharp edges along the periphery which can penetrate into the flesh of the prey. The suckers also have a gradient in

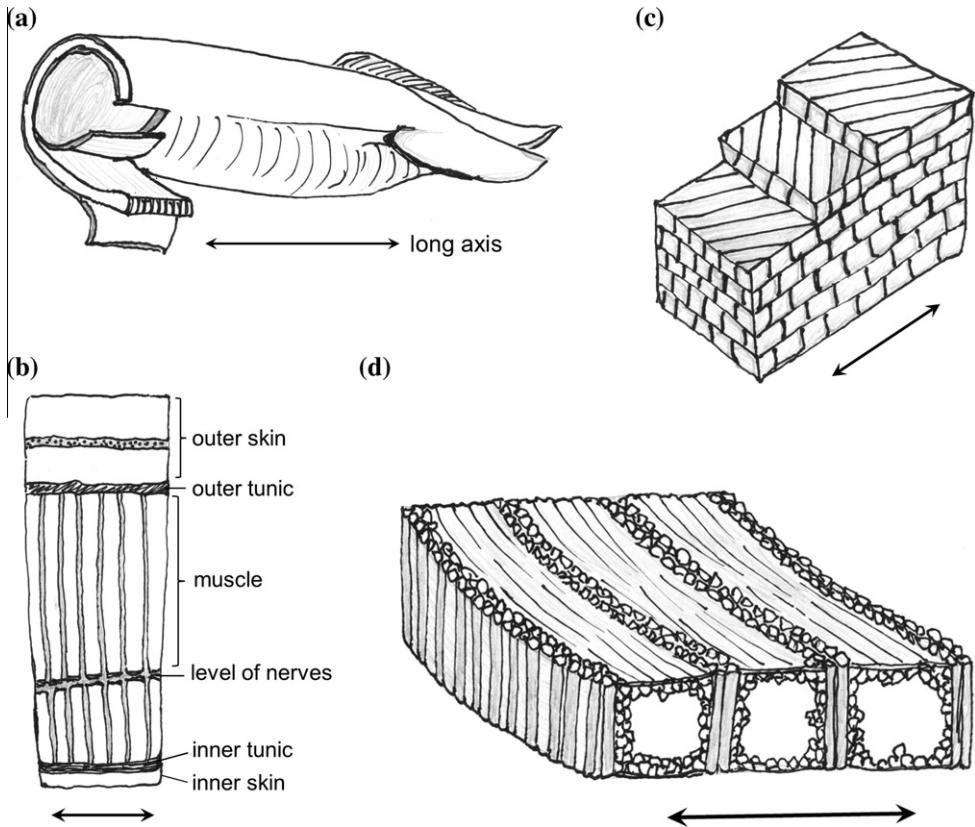


Fig. 132. Structure of squid (*Lolliguncula brevis*) (a) cross and longitudinal sections of body; (b) cross-section showing muscle sandwiched between inner and outer tunic; (c) outer tunic consisting of a pattern of collagen molecules forming a cross pattern; (d) muscles forming a pattern that is symmetrical with respect to longitudinal axis (taken from [426], Fig. 1).

mechanical properties. In this case, however, the gradient is accomplished by the controlled presence of aligned ducts. The section of the sucker in Fig. 134 shows the elongated proteinaceous tubules with pores between them. The greater the porosity is, the lower the elastic modulus.

4.5. Polychaete worm jaws

Polychaetes are another type of invertebrate that use a mostly non-mineralized strategy in their jaws. In *Glycera*, copper is present in both mineralized (atacamite) [156] and non-mineralized form [429]. While at first it was speculated that the atacamite fibers were involved in increasing the abrasion resistance, it was later shown that it is rather involved in improving the bending stiffness of the jaw, whereas nano-friction and nano-wear testing have shown that the non-mineralized domains improve the wear and abrasion resistance [158,430]. *Nereis*, which are a cousin species of *Glycera* use mostly Zn in unmineralized form to improve the jaws' mechanical properties. Broomell et al. [406] showed that Zn directly cross-links the jaw by forming coordination complex with His residues. This was done by chelating Zn ions with EDTA and measuring the properties by nanoindentation. The regions that were depleted in Zn had a decrease in hardness and modulus. When treating again the surface with Zn salt, the Zn ion replenish the coordination sites, and E and H values are largely recovered, highlighting the reversibility of the process [93,406]. These systems have been reviewed in more details by Broomell et al. [407] and Rubin et al. [431].

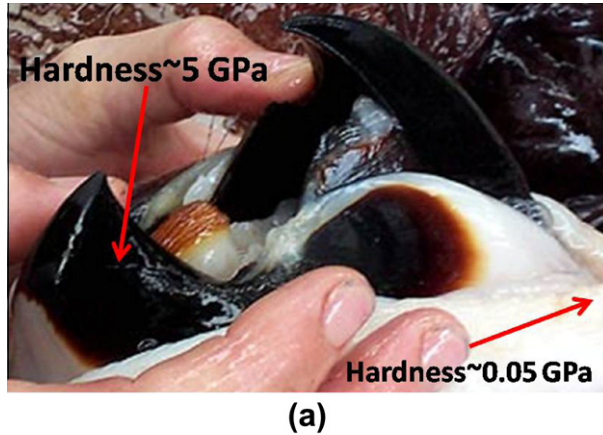


Fig. 133. (a) Squid beak (black) embedded in body (lighter); nanoindentation hardness of two regions marked; (b) beak extracted from animal showing gradient in tanning.

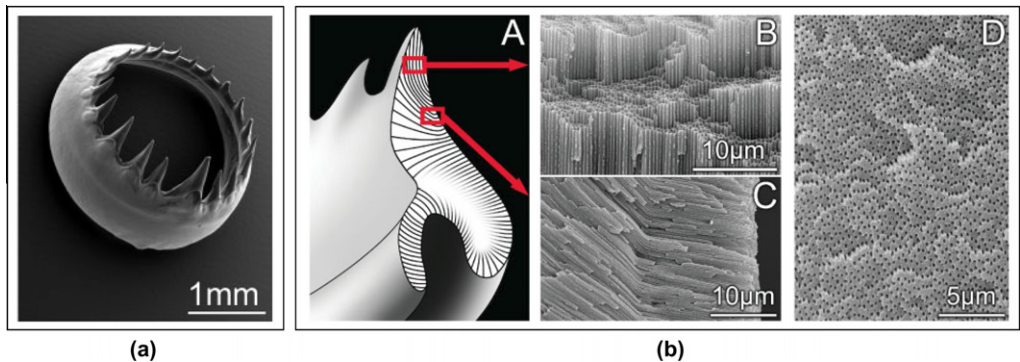


Fig. 134. (a) Squid sucker; (b) sketch of section (A) section showing array of elongated proteinaceous material arranged in a tubular architecture fashion. Taken from [428], Figs. 1 and 2.

4.6. *Chiton radula*

Chitons are marine mollusks whose dorsal shell is composed of not one, but eight separate plates. They belong to the class *Polyplacophora* (from Greek: *poly*-many; *plako*-plates; *phorous*-bearing). These mollusks have a skirt around their periphery. They have also received the nickname of ‘coat-of-mail’ shells.

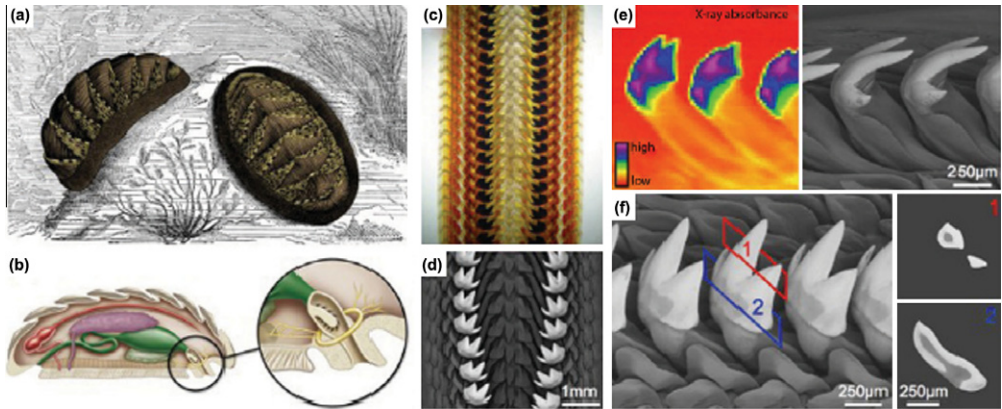


Fig. 135. Chiton, a mollusk containing eight plates. External (a) and internal (b) anatomy of chiton with detail showing the radula, a rasping, toothed conveyor belt-like structure used for feeding. (c–f) Optical (c) and backscattered SEM (d) imaging and X-ray transmission studies (e) reveal the nature of the electron density distribution of the tricuspid tooth caps. Cross-sectional studies through the teeth from *C. stelleri* (f1,2) reveal a concentric biphasic structure. Taken from [106].

The plates are composed of aragonitic calcium carbonate and are held together by a muscular girdle that surrounds the body (Fig. 135a and b). Thus, the name chiton, also derived from Greek, meaning tunic. One unique aspect of the chiton that will be presented here is its radula, or raspy tongue. This radula is a conveyor-belt like structure containing magnetite teeth. Fig. 135c–f shows the conveyor-belt appearance of the radula [106]. Chitons derive their nourishment from algae that form on rock and therefore their teeth have to resist this action of grazing on the rock that can wear them. The teeth have three cusps and are attached to underlying cuticles that ensure proper alignment. This can be seen in Fig. 135c and d. When the teeth are worn, new teeth form. Lowenstam and Weiner [14] described it as magnetite. Its hardness is 9–12 GPa, the highest of any biomineral. In comparison, dental dentine has a hardness of 3.5–4.5 GPa. Ganoine, hard layer present on the fish scales (see Section 3.6), has a hardness of 4.5 GPa.

The structure of the tooth is similar to the teeth of vertebrates, having an external layer that is harder and a more compliant core. The external layer is pure magnetite organized in parallel rods and the internal core is made of an enriched iron phosphate interspersed with chitin fibers; correspondingly, its hardness is lower, ~2 GPa.

4.7. Insect mandible and proboscis

Insect mandibles (“jaws”) are a pair of attachments near the mouth that are multifunctional: they gather, manipulate and process food, catch and attack prey, build nests, and in some ants, provide propulsion. The mandibles have evolved from legs and move with a horizontal motion unlike the jaws of vertebrates. Fig. 136 is an SEM micrograph of the mandible of a bleach beetle (*Priacma serrata*) that is as long as the head, showing four teeth on each side. Mandibles, like the rest of the cuticle, are composed of waxes, polysaccharides and proteins. Chitin provides strength and sclerotized proteins bind them together, much like polymer–matrix fiber reinforced composites. They have a large variety of morphologies – some insects have no teeth on the mandible (nectar feeding), some have serrated-like teeth (grasshoppers) or some have needle-like teeth in piercing or sucking insects (tree bugs). They are the hardest part of the insect integumentary system and are found to be twice as hard as the rest of the exoskeleton [432]. This is attributed to the presence of metals such as zinc, manganese, iron and in some cases, calcium [432–437]. Zinc, in particular, is connected with a 20% increase in hardness [436]. Again, it is likely that the Zn-containing mandibles are hardened through complex coordination as described earlier for *Nereis* jaws. The ‘tools’ of an insect (mandible, ovipositor, claws) undergo sclerotization (tanning), which involves extensive cross-linking of the proteins

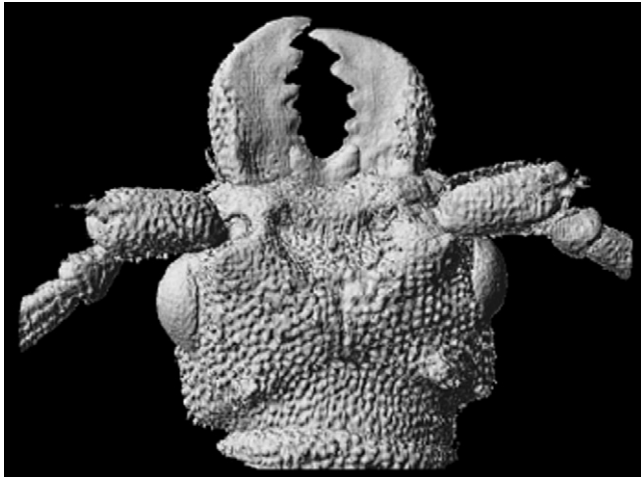


Fig. 136. Head and mandibles of a bleach beetle (*Priacma serrata*). Taken from [438].

thereby darkens and hardens the material. It is during the sclerotization process that the transition elements are incorporated.

One interesting recent study has been on the comparison of adult and larvae jewel beetles (*Pseudotaenia frenchi*) mandibles [439]. The dry larval mandible was found to have a higher hardness than the adult one, despite not having any metals incorporated into the structure, as shown in Fig. 137. The larvae must bore through wood to emerge and thus develop a hard mandible that is crucial to their survival. This work provides evidence that a purely organic material has a hardness that is higher than cortical bone and even approaches values for stainless steel.

Mandibles can snap at incredible speed and with surprisingly high forces. The speed of the trap-jaw ant (*Odontomachus bauri*) has been measured at up to 60 m/s with an acceleration of 100,000 g and a dynamic force that exceeds the body weight (12–14 mgf) [440]. Within the animal kingdom, this is one of the fastest measured predatory strike. Additionally, by striking their mandibles on a surface,

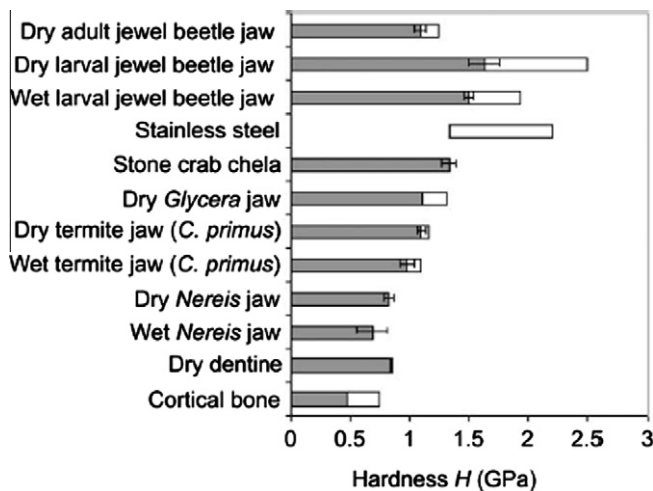


Fig. 137. Comparison of the hardness of insect mandibles with other materials. Taken from [437].

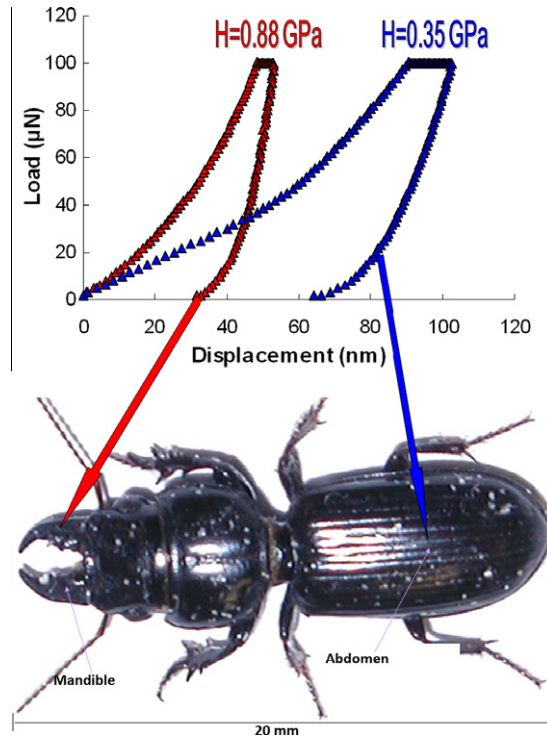


Fig. 138. (a) Representative load displacement curves and hardness values (H) generated from nanoindentation of mandibular and abdominal exoskeleton of *Scarites Subterraneus* beetle; (b) photograph of beetle showing the two regions where nanoindentation tests were performed. Taken from [439].

these ants can jump vertically ~ 8 cm and horizontally ~ 40 cm to evade predators. The mechanical properties of the mandible of a ground beetle (*Scarites suterraneus*) were tested using nanoindentation [439] and compared with those of the abdomen, as shown in Fig. 138. The hardness (~ 1 GPa) and reduced elastic modulus (~ 30 GPa) of the mandible are much higher than those at the abdomen (hardness, ~ 0.35 GPa; reduced modulus ~ 9 GPa). This may be attributed to an increased level of heavy metals (such as Zn and Mn) and halogens incorporating into the nanoscale structure of the exoskeleton during maturation and likely correlate to the different functions of fighting and protection of the two areas.

The proboscis is an organ that can be inserted into tissue (plant or animal) to suck out nutrients. It is a modification in which the mandible and maxilla (upper jaw) are combined to form a needle-like appendage. Insects of the order *Hemiptera* (e.g. cicadas, aphids) and *Diptera* (mosquitoes) employ the proboscis to pierce plants to suck out the sap. Additionally, the female mosquito needs blood to lay eggs. Butterfly and moth proboscises are long and tubular, having a sharp tip, and are coiled under the face when not in use.

Fig. 139 shows the proboscis of the mosquito (*Culex pipiens*). The proboscis is composed of an outer sheath which is used to detect the surrounding environment such as temperature and chemical balance while there are two tubes which enter its unsuspecting prey. One of them is terminated with an inner stylet that is used to pierce through the skin and draw blood while the other injects an anticoagulant into the host to keep the blood flowing. The figure shows that there are serrations on the edge of the stylet possibly designed to reduce nerve stimulation during a bite by increasing the efficiency of the cutting edge [441]. This is in congruence with Oka et al. [242], who concluded that the initial bite of a mosquito is painless because of the highly serrated proboscis. They used this concept and

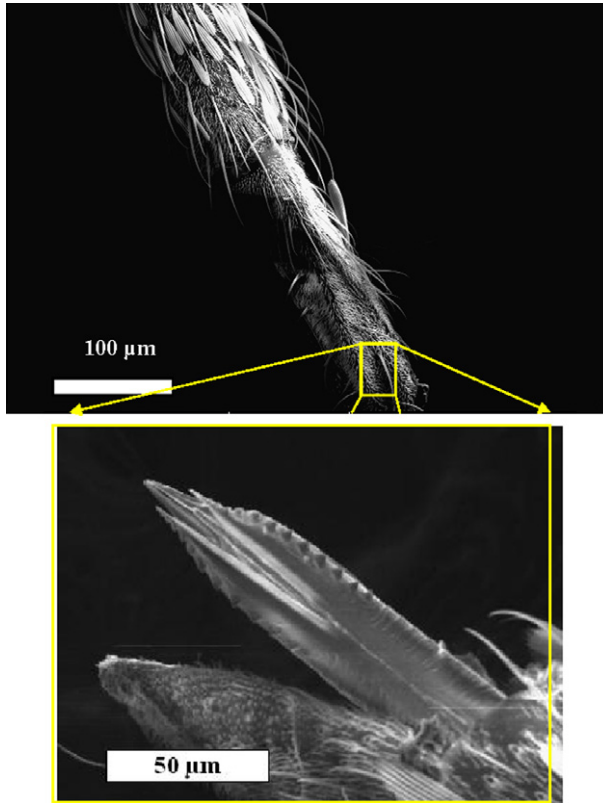


Fig. 139. SEM micrographs of a mosquito proboscis; top: proboscis covered with hairy sheath; bottom: serrated stylet designed to section tissue for dual needle penetration.

developed a mosquito-inspired hypodermic needle, which is discussed in Section 7.4. Atkins [422] analyzed the mechanics of cutting which explains the importance of serrations in severing skin.

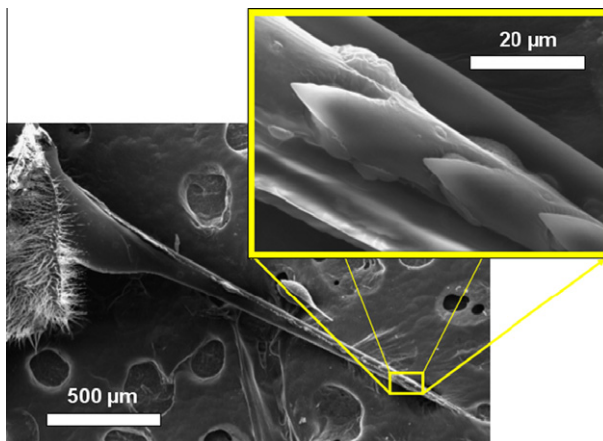


Fig. 140. Bee (*Apis mellifera*) stinger; notice directional serrations that are responsible for the stinger staying embedded in epidermis, in contrast with mosquito proboscis (Figs. 4–14), which is removed after blood extraction.

The stinger of the common bee (*Apis mellifera*) is yet another example of the efficiency of serrations, as shown in Fig. 140. It is equipped with reverse facing barbs which are used to propel the needle deep into the tissue of its prey. These backward facing barbs are approximately 10–20 μm long and run along the shaft of the stinger. When the insect has used the stinger it stays embedded in the skin.

4.8. Wood wasp ovipositor

The wood wasp uses its ovipositor (egg laying organ) to drill holes in wood to deposit eggs. The ovipositor can be as long as 10 cm, as in the parasitic wasp (*Megarhyssa ichneumon*). The wasps can drill to depths of over 20 mm without causing much damage to the plant. Vincent and King [443] examined the ovipositors of two wood wasps, the *Sirex nocitilo* (10 mm length) and the *Megarhyssa nortoni nortoni* (50 mm length), both with diameters of $\sim 200 \mu\text{m}$. The ovipositor was found to have an unusual structure – there are two halves, called valves that slide relative to each other. No rotary motion is involved, rather the wood is scraped out with ‘teeth’ that surround each valve. Fig. 141 illustrates the method of drilling: one valve penetrates the wood, creating a tensile force, while the other

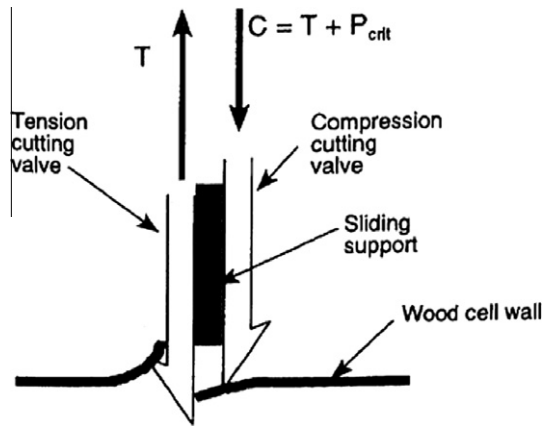


Fig. 141. Three-part ovipositor cutting into wood. The left valve pulls with a force T . The right valve is under a compressive force, C , that is enough so that Euler buckling at P_{crit} does not occur. Taken from [440].

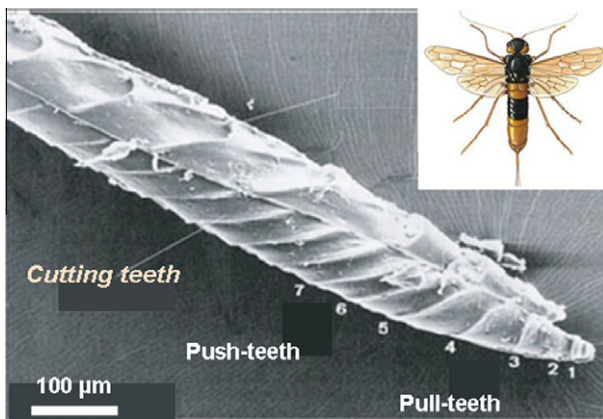


Fig. 142. Ovipositor of the wood wasp, *S. nocitilo*. The push teeth are pointed down the shaft and the pull teeth point up the shaft, allowing for cutting in both directions. Adapted from [443].

valve is placed in compression. Once the tensile side is stabilized in the wood, the compressive side can then be inserted and the motion is repeated. Because the tensile and compressive forces are balanced, there is not net force on the ovipositor, or the net force is below the critical load for Euler buckling [443]. Fig. 142 shows an SEM micrograph of the ovipositor of the *S. noctilio*. The valve separation is shown as the light colored line bisecting the ovipositor. The push and pull teeth are at the proximal and distal ends, respectively.

5. Avian materials: lightweight and aerodynamic

Aerodynamic activity requires stiff, lightweight structures, exemplified by avian components – feathers, bones, and beaks all have cellular elements in their structures. They are surrounded by a stiffer, denser sheath. Flying requires materials with a combination of properties that demand the greatest ingenuity of materials engineers and designers because the strength/density ratio is the guiding rule. Thus, the study of these biological materials is especially fruitful because of the unique solutions developed by nature.

5.1. Feathers

Feathers are lightweight, complex, multifunctional integumentary appendages that are entirely composed of β -keratin in the form of β -pleated sheets. They have a variety of functions that include flight, camouflage, courtship, thermal insulation and water resistance. Feathers form from follicles in the epidermis that are periodically replaced by molting. The hierarchical structure of a feather of a toucan (*Ramphastos toco*) is shown in Fig. 143. The rachis is the long shaft that extends the length of the feather and supports the barbs, which form the herringbone pattern along the rachis. It has a design that satisfies resistance to rupture during flexure without a proportionate increase in weight [445]. The barbs have smaller barbules extending from them. The cortex of the rachis is constructed of fibers, $\sim 6\ \mu\text{m}$ in diameter, which are aligned along the long axis and consist of $0.3\text{--}0.5\ \mu\text{m}$ diameter bundles of barbule cells that are connected end-to-end. A cellular material is in the center of the rachis, thus, a feather has a sandwich construction that gives a maximum flexural strength to weight ratio. The SEM micrographs of dorsal (Fig. 143b) and ventral (Fig. 143c) surfaces reveal relatively smooth topography compared to that of lateral surfaces (Fig. 143d) which exhibit intersecting ridges with a spacing of $10\ \mu\text{m}$ to $20\ \mu\text{m}$, with considerable overlap in diameter of cells of the medullary core (Fig. 143e) ranging from 20 to $30\ \mu\text{m}$. The smoothness, at microscale, of the dorsal and ventral surfaces is remarkable, as it is expected that surface roughness would serve to decrease drag (i.e. if the laminar-to-turbulent transition occurs before the point of boundary layer separation), as proposed regarding microscale features observed on the surface of barbs [446].

A more detailed schematic drawing of the fiber orientation is shown in Fig. 144a and b. In (a) a cut-away shows the longitudinal orientation of the fibers along the cortex and in (b) the thin layer of circumferentially wound fibers is illustrated. Lingham-Soliar et al. [447] propose that the circumferentially wound fibers could control the hoop and longitudinal stresses thus preventing ovalization and axial splitting of the rachis. The fibers in the common chicken (*Gallus gallus*) show protuberances similar to a bamboo pattern (Fig. 145). These protuberances may minimize sliding between fibers thereby increasing stiffness.

Fig. 146 shows a schematic of feather foam and several SEM micrographs at increasing magnifications for a falcon (*Falco sparverius*). The internal foam has a fascinating structure. It consists of cells with approximate diameter of $10\ \mu\text{m}$. If one images the cell walls at a higher magnification, one recognizes that they are not solid but are, in turn, composed of fibers with a diameter of $\sim 200\ \text{nm}$. Thus, one has a two-level cellular structure that minimizes, as required, weight.

Typical stress–strain curves for the tail feathers of a Toco toucan are plotted in Fig. 147. As shown, there is considerable variability in mechanical properties. Most dorsal and ventral samples failed at strains higher than 5% and some even in excess of 10%, while the majority of lateral samples failed at less than 5% strain. The samples excised from the left rectrices demonstrate marginally higher stiffness than those from the right rectrices. It has been reported that among parrots observed in captivity,

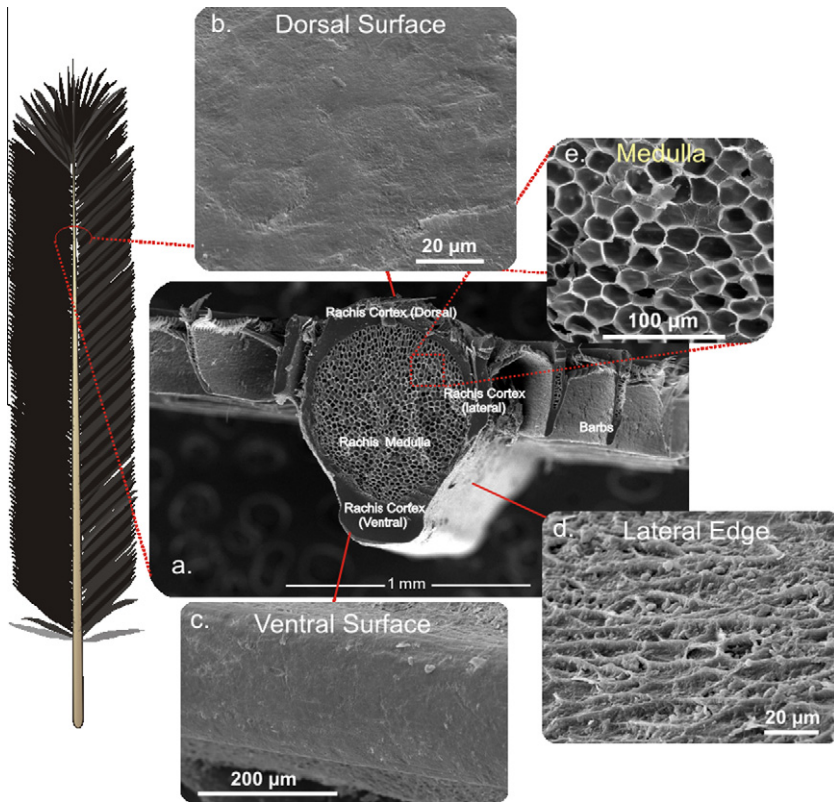


Fig. 143. Hierarchical structure of a feather (Toco toucan). SEM of the surface microstructure of the cortex and (a) the cross-section of a distal section of rachis. This sandwich construction of the rachis is repeated in the barbs as well. The (b) dorsal and (c) ventral cortical rachis keratin is smooth at the micron scale, while the (d) lateral cortical rachis keratin is fibrous and textured with ridges separated by 10–20 μm . Enclosed by a thin-walled shell or cortex is a (e) medullary core constructed of cells ranging from 20 to 30 μm in diameter. Taken from [76].

left-handedness (or rather left-footedness, in the sense that parrots use their feet to manipulate toys or food) is prevalent [448]. The average tensile modulus was 2.6 GPa and the average strength ranged from 33–141 MPa [77].

Samples of dorsal and ventral cortex were found to be significantly stiffer and stronger than those of the lateral edges. Samples from the dorsal surface sustain both the highest stress and the highest stiffness. The discrepancy in mechanical properties on the surfaces of the cortex may be related to the role of melanin, which provides the black coloration in plumage in the form of rod-like granules [449]. Note that melanin has been shown to play an important structural role in *Glycera* jaws described earlier [429]. The dorsal surface, appears to be uniformly and densely melanized; the ventral surface, based on visual inspection, is less melanized, appearing brown in color in some places, and the lateral surfaces are non-melanized. Bonser [450] reported a 39% increase in microhardness of melanized dorsal cortex from the wing feather of a ptarmigan compared to non-melanized ventral surfaces.

Distal samples of cortical rachis were weakest and least stiff compared to proximal and middle specimens, but not significantly so. The fracture strength and stiffness of proximal and middle specimens were approximately equivalent. This result is in contrast to the proximal to distal increase in stiffness reported by Bonser and Purslow [451] for the case of the wing feathers of the swan and suggested to be correlated to the increased proportion of the axially oriented fibers in the cortex. An increasing stiffness gradient from proximal to distal end may serve to compensate for the effect

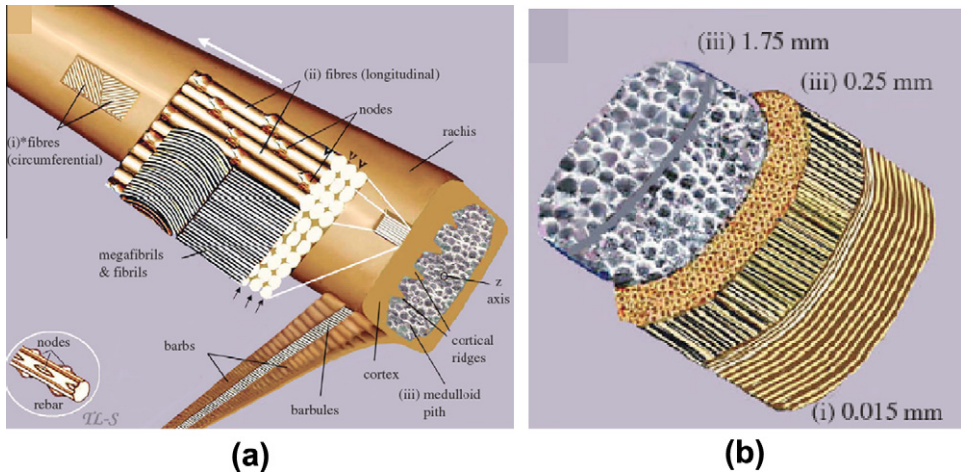


Fig. 144. Schematic representation of fiber orientation (a) the majority of the fibers ($\sim 6 \mu\text{m}$ diameter) are oriented along the main axis of the shaft (rachis). (b) Illustration of a thin sheath of circumferentially oriented fibers on the surface of the rachis. Taken from [447].

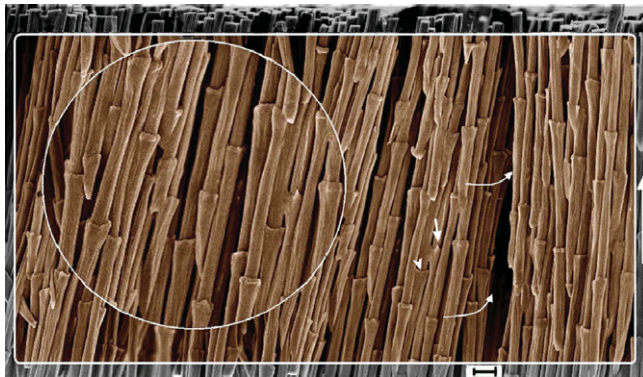


Fig. 145. SEM image of the aligned fibers (syncytial barbules) from the cortex of a chicken (*Gallus gallus*) rachis after fungal biodegradation. The arrows show hooked ends to the barbules or rings (arrow head). The densely packed fibers (curved arrows) show a staggered arrangement. Bar = $10 \mu\text{m}$. Taken from [447].

of decreased cross-sectional area along the length of the feather, if flexural stiffness, EI , where I is the second moment of inertia, is to be conserved or compensated. However, this increase in strength and stiffness may be confounded by a temporal or aging effect of keratin, as the more distal cortex is more mature [452]. The cortex sampled from distal regions of peacock tail coverts is significantly less crystalline than in other regions along the length of the feather [453]. Therefore, the cortex of the rachis, in addition to being a fiber-reinforced bi-laminate composite, may also be described as functionally graded.

The male peafowl (peacock) tail feathers are one of the most beautiful and colorful in nature. The fanned out feathers are used to attract peahens. Several structural features are required for these feathers: the fanned out feathers must support their own weight but must be lightweight enough because peacocks can fly, a minimal amount of material must be used for energy conservation and finally, they must have sufficient strength and stiffness so that buckling during natural bending does not occur [454]. There are ~ 300 feathers on the tail and they range in length from a few cm up to 1.5 m.

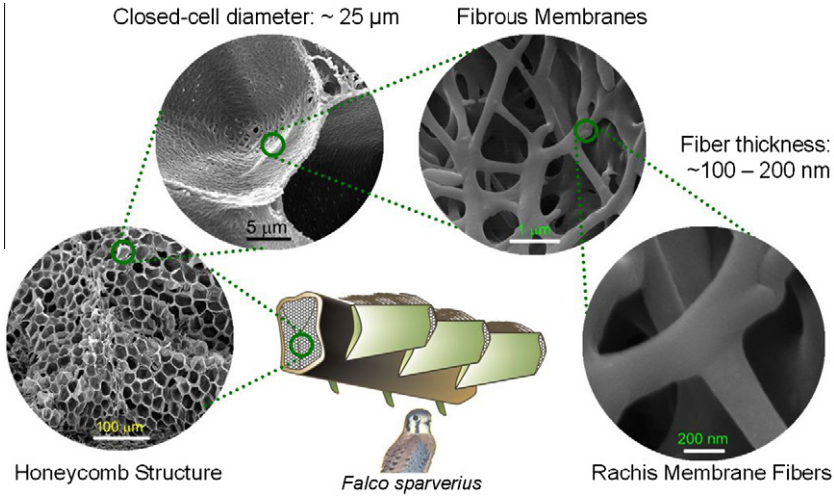


Fig. 146. Schematic of falcon (*Falco sparverius*) feather internal foam along with scanning electron micrographs of the medullary core (courtesy of S.G. Bodde, unpublished research).

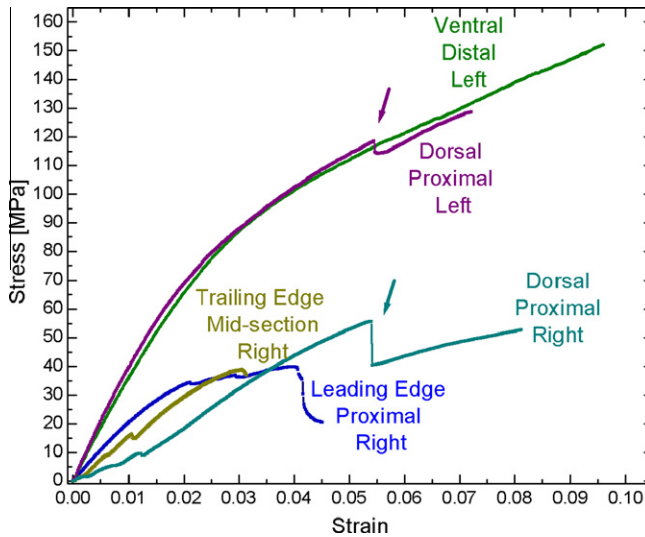


Fig. 147. Typical tensile stress–strain curves for Toco toucan cortical rachis keratin. Rachis cortex sample from dorsal and ventral surfaces exhibits linear elasticity over a larger strain range than lateral samples. Variation in stiffness and maximum tensile strength is high. Arrows denote localized failures. Taken from [76].

The rachis has ~ 300 barbs covered with 10^6 barbules. The barbules contain ~ 20 indentations along the length, which produces the color [454]. Weiss and Kirchner [455] examined the strength and stiffness and found the longitudinal stiffness of the cortex to be 3.3 GPa while the transverse one was 1 GPa. The medullary foam had a stiffness of 10 MPa. The foam played no significant role in the tensile properties, but provides 96% of the transverse compressive stiffness. It is unclear what the role of the circumferentially wound fibers are in the compressive stiffness. The fracture strength of the cortex, both longitudinal and transverse was found to be 120 MPa, similar to what is found for the Toco toucan feathers.

5.2. Bird beaks

Whereas birds usually have either short and thick beaks or long and thin beaks, toucans have long and thick beaks. The Toco Toucan (*Ramphastos toco*) has the largest beak among the species. The large beaks help in picking up fruits at the tips of branches in the canopy and extracting prey (little baby birds!) from holes in trees. They also assist in combat and bill fencing. The Toucan beak is one-third of total length of the bird; nevertheless the weight is 1/30th–1/40th of its mass. The African Hornbill also has an extraordinarily large beak; it is, however, heavier. This accomplished by an ingenious solution, enabling a low density and sufficient rigidity. The outside shell (integument) of beak consists of β -keratin. The inside is filled with a cellular bone. This internal foam has a closed-cell structure constructed from bony struts with thin membranes. We summarize here the principal results obtained by our group [72–74,456,457].

Fig. 148 shows photographs and schematics of the toucan and hornbill beaks. This structure was found by Seki et al. [72] to have a bending strength (Brazier moment) that is considerably higher than if all the mass were concentrated in the shell as a solid hollow cylinder by applying the analysis developed by Karam and Gibson [171]. Seki et al. [72,73] showed that the internal cellular core serves to increase the buckling resistance of the beak and demonstrated a synergism between the two components that provides the stability in bending configuration. Thus, there is clearly an advantage in having an internal foam to support the shell. The nature of the internal foam structure is revealed in considerable detail by micro computerized tomography.

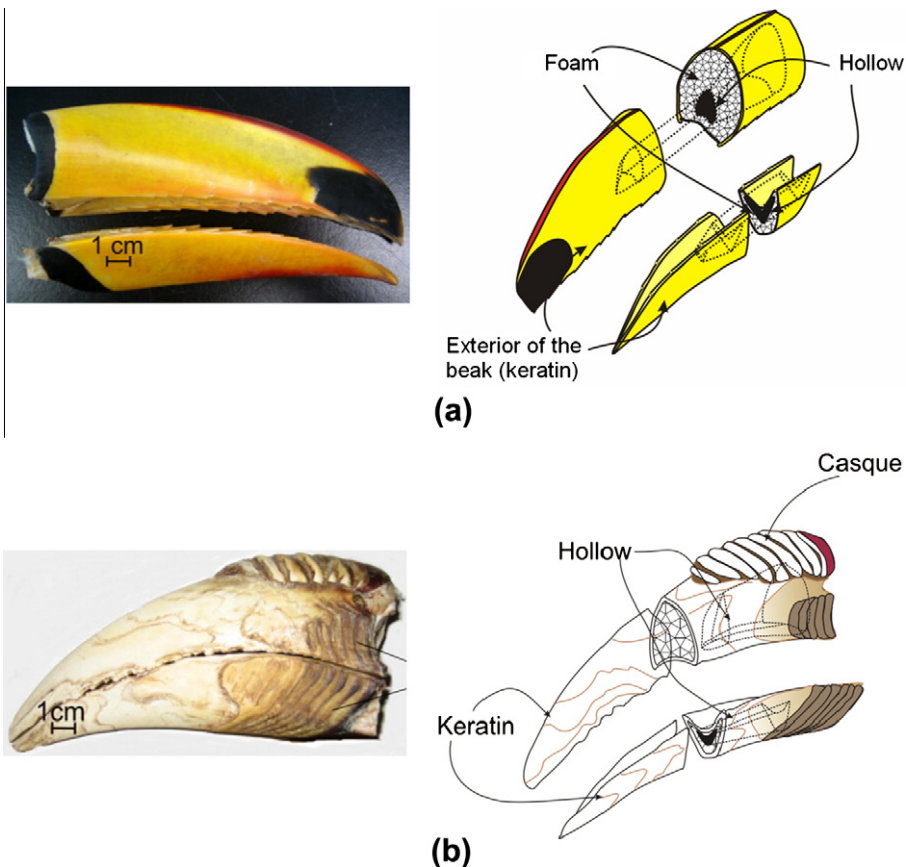


Fig. 148. Photographs and schematic drawings of (a) toucan and (b) hornbill beaks. Adapted from [74].

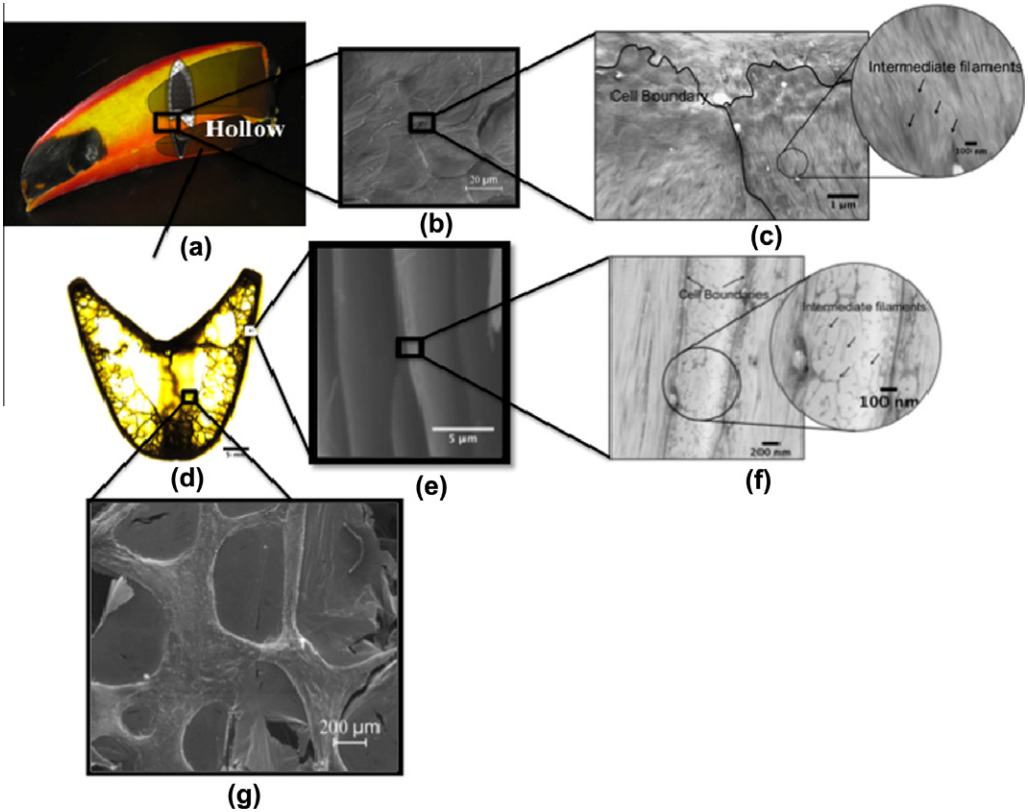


Fig. 149. Hierarchical structure of Toucan beak; (a) picture of the beak, hollow parts are indicated by schematics; (b) surface morphology of beak keratin by SEM; (c) keratin scale structure by TEM, intermediate filaments are indicated by arrows; (d) cross sectional mosaic of lower beak by confocal microscope; (e) cross section of keratin exterior by SEM; (f) TEM of cross section of beak keratin, arrows indicate intermediate filaments; (g) scanning electron micrograph of the foam structure, the cells are sealed by membranes. Taken from [456].

The outer surface of the beak is covered by a thin horny sheath called rhamphotheca, which consists of polygonal keratin tiles shown in Fig. 149b. The keratin tile boundaries are wavy, traced by black lines for greater clarity, are shown in the longitudinally sectioned beak keratin in Fig. 149c. The intermediate filaments (IFs) indicated by arrows in Fig. 149c are surrounded by the matrix proteins. The cross sectional mosaic image of lower beak was captured by confocal microscope in Fig. 149d. The transverse section of the beak keratin exhibits layered structure in Fig. 149e and the tiles are connected by organic glue, shown in Fig. 149f. The intermediate filaments, embedded fibers in the keratin matrix, are either aligned along the cell boundaries or spongy structure in Fig. 149f. It appears that there is a difference in orientation of the IFs from one layer to the next, similar to a $0^\circ/90^\circ$ laminated composites. The Toucan beak trabeculae are composed of cylindrical or elliptical rods with $\sim 200 \mu\text{m}$ in diameter. The porosity of the trabecular bone in beak is enclosed by thin membranes; the typical pore size is 1 mm, Fig. 149g. This is a different structure from human trabecular bone, which has no membranes. The average edge connectivity of pores is approximately 3. The trabecular bone is enclosed by a thin cortical shell.

Fig. 150 shows a typical tensile stress–strain curve of a single trabecula of the Toucan beak. The Young's modulus ranges from 0.4 to 7 GPa. The average Young's modulus, obtained from 29 measurements, is 3.0 GPa. Values reported in the literature have varied from 1 GPa to 19 GPa in tension [458–461]. Lucchinetti et al. [459] discussed the limitations and error sources associated with mechanical testing at the micrometer scale.

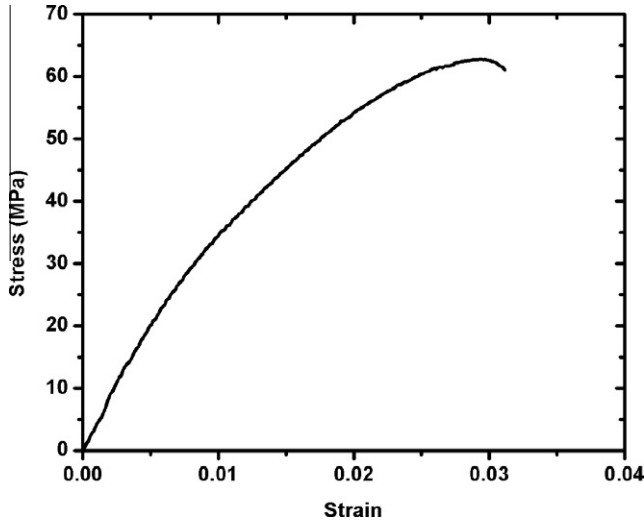


Fig. 150. Typical stress–strain curve of toucan beak trabecula in tension. Taken from [74].

In most cases, the trabecular bone failed after buckling and bending of the struts. Therefore, it is important to evaluate the buckling of a single trabecula in compression to obtain material parameters for the beak foam. The elastic buckling load of a beam is given by the Euler equation:

$$P = \frac{n^2 \pi^2 EI}{L^2} \quad (n = 1, 2, 3, \dots) \quad (5.1)$$

where n is defined by the supports, E is Young's modulus, I is the moment of inertia, and L is the length of beam. If both ends are pinned and fixed, one has $n = 1$ and $n = 2$, respectively.

The corresponding critical stresses σ_{cr} are, for pinned supports and fixed ends:

$$\sigma_{cr} = \frac{\pi^2 E}{(L/r)^2} \quad \text{and} \quad \sigma_{cr} = \frac{4\pi^2 E}{(L/r)^2} \quad (5.2)$$

where A is the cross sectional area and $r = \sqrt{I/A}$ is the radius of gyration.

The equations for critical stresses are valid for ideal, relatively long columns. In this study, the column slenderness ratio (L/r) is less than 100, which leads to inelastic buckling. Therefore, the tangent modulus theory for inelastic buckling was applied [456].

Fig. 151 shows the two Euler curves with predicted values for pinned and fixed ends trace experimental results. A Young's modulus of 3 GPa (from tensile testing) was used to draw Euler curves. It is simple to envisage that the supports can undergo damage in assembly of the test setup. If the ends are cracked, a fixed support becomes essentially pinned. The Euler curve for pinned ends tracks the lower buckling stresses and that for fixed ends represents the upper bound for the buckling stresses, Fig. 151. The Euler equation suggests that the estimated Young's modulus matches the assumed 3 GPa value used for elastic buckling.

The experimentally-obtained material parameters of the trabeculae and cortical bone were used for the FEM calculations. Yield stresses of $\sigma_y = 20$ MPa for trabeculae and $\sigma_y = 10$ MPa for the cortical shell were used. The Young's moduli were taken as 3 GPa for trabeculae and 0.3 GPa for the cortical shell. The trabecular and cortical bone were deemed to have failed at strains of 0.03 and 0.1, respectively.

In order to create a FE model, 150 images scanned at 93 μm resolution by microtomography (μCT) were used. With this resolution, the main structure of the trabeculae was captured, which contribute to the stiffness of the foam. The CT images were converted to tri-dimensional structure of the trabeculae and the cortical shell by a marching cube algorithm, shown in Fig. 152. The core part (trabeculae)

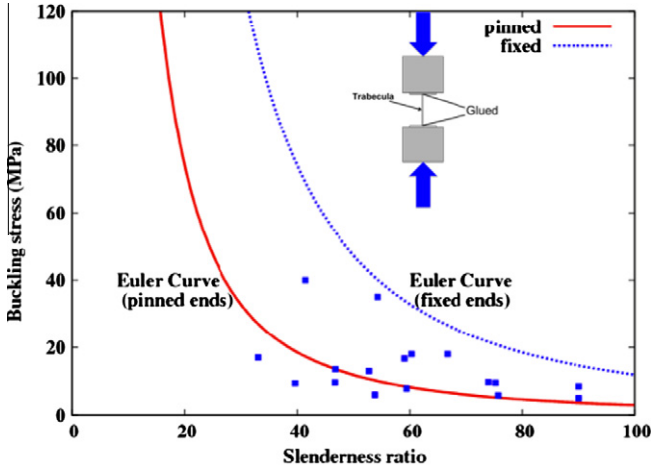


Fig. 151. Calculated Euler curves of toucan beak trabeculae with fixed ends (dashed curve) and pinned ends (continuous curve) and experimental compressive test results (squares). Taken from [74].

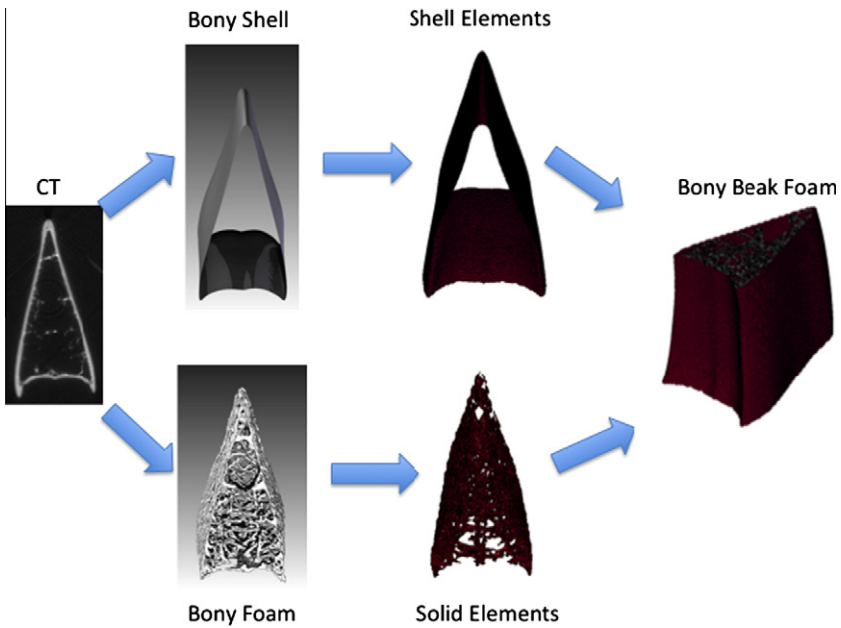


Fig. 152. Conversion from CT images to FE model of foam core: 150 CT images were used to create tridimensional models of bony foam and shell by DDV. The models were converted to FE models by ANSYS ICEM CFD. Both models were assembled to make the beak foam core. Taken from [74].

and shell part (cortical shell) of the beak foam were individually created. The tri-dimensional model of core was created and of the cortical shell were created. A piecewise linear plasticity model (material model 24) in LS-DYNA was used for the material model.

Fig. 153 shows two experimental stress–strain curves of the compressive behavior of the beak foam and a computationally predicted curve with three FE deformation models at different strains. The two experimental stress–strain curves of foam represent the different relative densities, 0.06 (with a lower

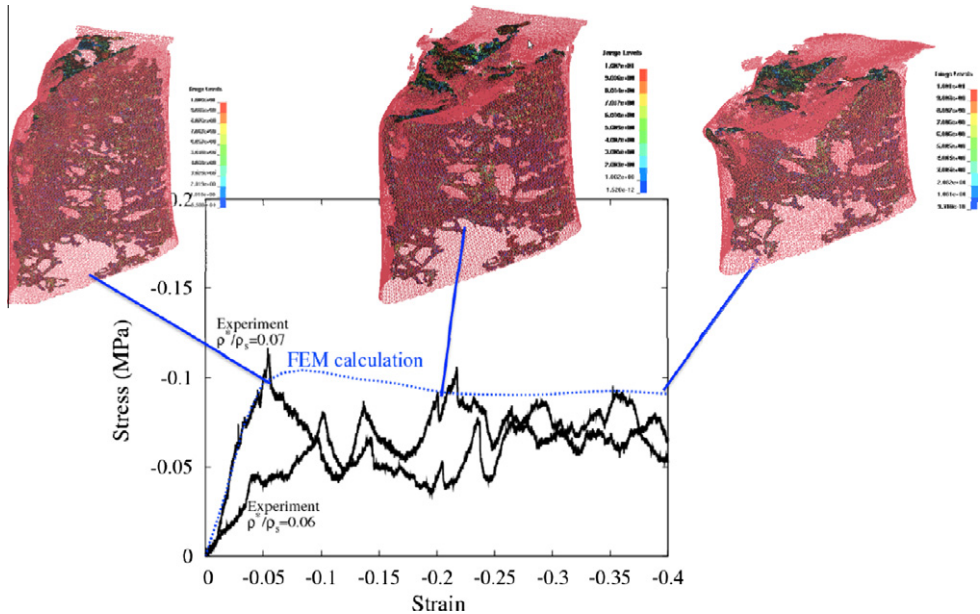


Fig. 153. Stress–strain curves of beak foam under compression, comparison between experiments and FE calculation. Foams in experiments have relative densities (ρ^*/ρ_s , density of foam core/density of foam material) of 0.06 and 0.07. Taken from [74].

modulus) and 0.07 (with higher modulus). The shell folding or buckling is visible at the culmen (upper ridge of a bird beak). At this stage, this deformation is at the end of the linear elastic region. At a strain of -0.20 , the trabeculae are compressed and the shell breakage is observed in simulation. The breakage of the shell becomes severe and the trabeculae undergo failure at a strain of -0.40 . The calculation shows the average stress at the plateau after the linear elastic region; there is $\sim 30\%$ difference in the plateau stress and a good agreement in stiffness, in comparison with the experimental stress–strain curve for 0.07 initial relative density.

The mechanical behavior of bird beaks is governed by both the ductile keratin integument and semi-brittle bony foam. Most of the mechanical loading on the beak is carried by the exterior keratin, whereas the foam increases the energy absorption and stabilizes the deformation of the beak to prevent catastrophic failure [72]. In the case of the toucan, the beak is mainly used for gathering food so that it is designed to resist bending moments. Indeed, the beak, having hollow core, exhibits a high bending resistance [72].

The stiffness of the beak keratin is mechanically isotropic in the transverse and longitudinal directions [72]. The IFs are assumed to be homogeneously distributed within the matrix proteins. The IF of beak keratin mechanically plays the same role as the fibers for fiber-reinforced composites materials. The branched structure of IF acts as an anchor in the keratin matrix and gives greater strength to the keratin composites. Indeed, the comparison between plain and branched fibers in composites theoretically proves that the branched fiber increases the strength of composites.

The study conducted by Seki and Meyers [456] demonstrates that the merging of characterization (μ CT and TEM), micromechanical testing, and finite element computation are converging to predict, in a realistic manner, the mechanical response of structures. This approach is being spearheaded by other groups and is currently applied to bones, teeth, and other biological materials.

5.3. Bird bones

Birds and other flying vertebrates (bats) have lightweight skeletons, which in part, makes flight possible. Birds range in mass from the 2 g hummingbird to the 100 kg ostrich, with over half of all

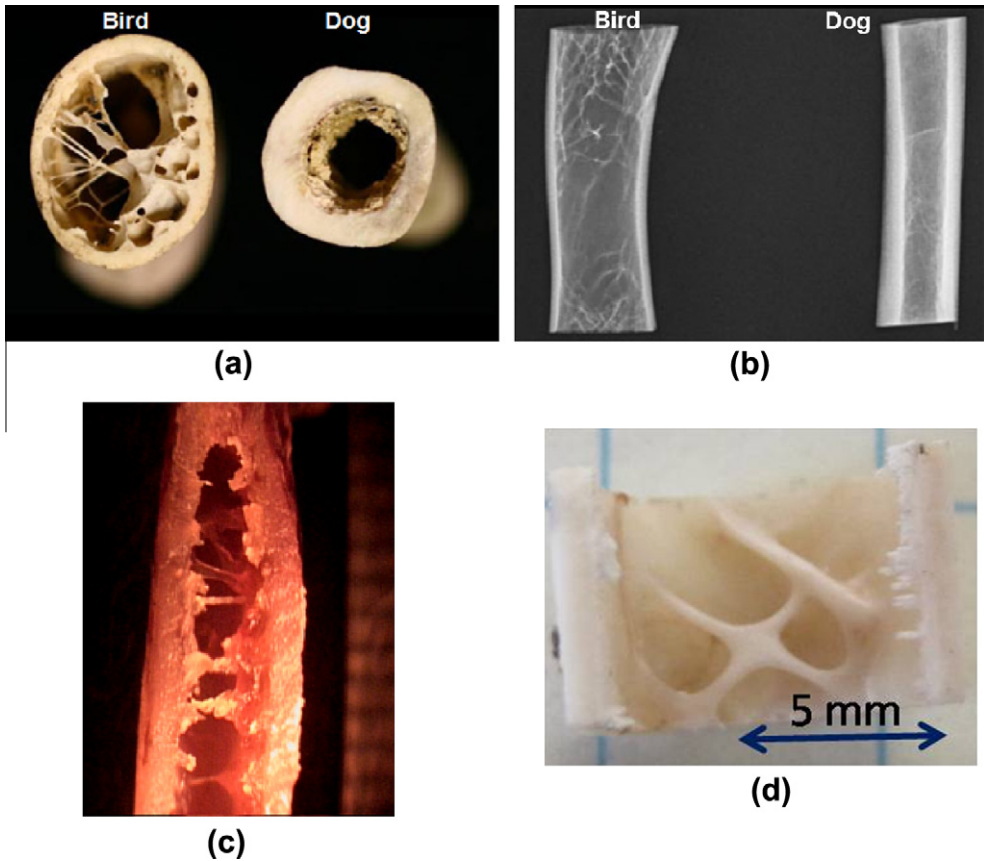


Fig. 154. Bird (left) compared with dog (right) bone: (a) photographic and (b) radiographic images. Bird bones are characterized by a much thinner cortical sheath. (c) Longitudinal section of distal end of Seagull humerus bone showing struts; (d) cross-section of vulture ulna showing reinforcement ribs at $\sim 600^\circ$ to bone axis. Taken from [462].

birds weighing less than 40 g. It has been reported that for bald eagles, the skeleton amounts to only 7% of the body mass, half of what the feathers represent [463]. For flight, other adaptations have evolved such as having a smaller number of bones than terrestrial vertebrates and the development of a lightweight beak, instead of a jaw with teeth. As early as Galileo's time, bird skeletons were reported to possess hollow bones. Fig. 154 illustrates the difference between bird and mammalian limb bones. The bird bones are characterized by a much thinner sheath of cortical bone, relative to the diameter of the bone. Additionally, for the bird, thin rods of bone are seen to extend across the medullary cavity. The internal structure of the bones varies between species. Flying birds have more hollow bones (not marrow filled) than flightless birds (e.g. ostrich, penguin). Diving birds and humming birds have few hollow bones. The diving birds need to have a higher density skeleton to propel themselves through water and for humming birds, the weight savings involved by having hollow bones would be minimal. The hollow bones have struts for reinforcement, similar to the wings on a biplane. Fig. 154c shows the internal structure of wing bones of seagulls. Internal reinforcement elements in the form of struts can be seen in vulture ulna (Fig. 154d). They ensure a high flexure strength/weight capability. Fig. 155a shows a cut-away of a hollow bone from a red hawk. Trabecular bone is observed at the end, which transitions to the struts, connecting the surrounding cortical bone. In Fig. 155b, the cross-section of a bird bone is shown. As with mammalian bone, there is a periosteal and endosteal sheath surrounding the cortical bone and a medullary core that is filled with less dense bone. The

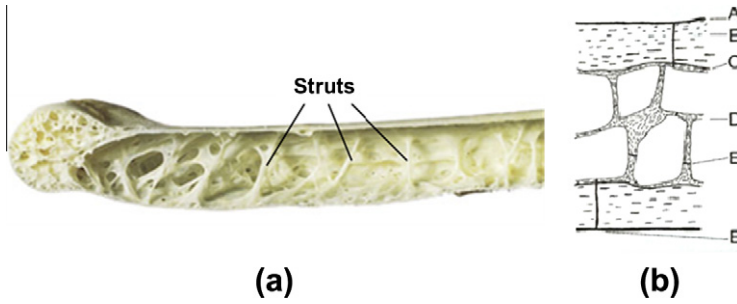


Fig. 155. (a) Photograph of the interior of a red hawk bone, showing trabecular bone at the head and the struts in the hollow interior. Adapted from [464]. (b) Cross-sectional schematic diagram of a bird bone. A – periosteal surface, B – lamellar cortical bone, C – endosteal surface, D – trabecular layer, E – pores/pneumatic or blood vessel openings. Taken from <http://platospond.com/WatsonsBlog/?p=22>.

hollow bones are also classified as pneumatic, because air is forced into them, thereby increasing buoyancy. However, for the flying birds, bones need to be strong and stiff enough to withstand forces during take off and landing, which necessitates some reinforcement in the bone interior.

One focus on study of the mechanical properties of bird bones has been on pneumatized (hollow) vs. marrow-filled bones. Currey and Alexander [465] found the ratio of the internal to external diameter was lower for pneumatized bone. The mean bending strength and flexural modulus were significantly higher for marrow-filled than pneumatic bones [466]. However, torsional resistance during flight has been proposed to be more significant than bending resistance [467]. Torsional resistance is maximized in thin-walled hollow bones at the expense of bending resistance. Fig. 154c and d show the wing bones of seagull and vulture, two soaring birds, respectively. The struts are present in the extremities of the tarsus for the seagull; for the vulture, internal ribs are seen (arrows). The latter provide torsional resistance. The internal ribs have an angle of $\sim 45^\circ$ with the longitudinal axis of the bone.

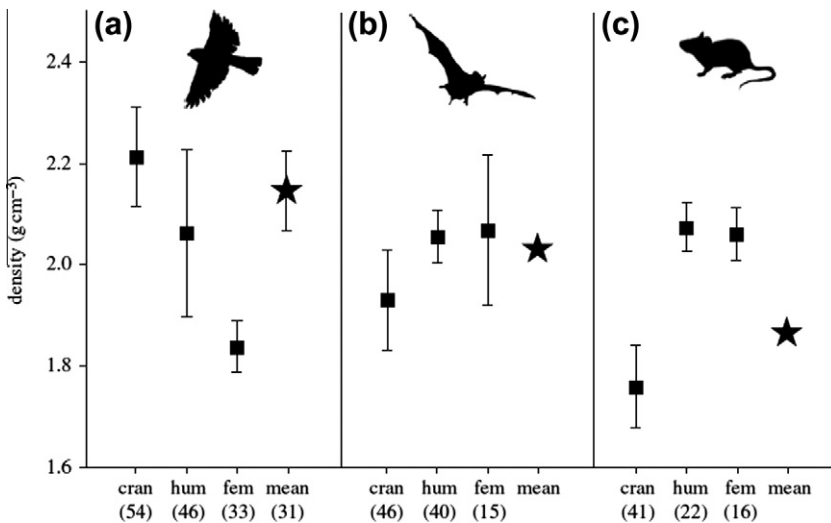


Fig. 156. Means and 95% confidence intervals for cranial (cran), humeral (hum) and femoral (fem) density in (a) birds, (b) bats and (c) rodents. Sample sizes in parentheses. Stars for bats and rodents indicate weighted means of bone density for each group. The mean of bone density for birds is based on 31 specimens for which density was available for all three skeletal elements, and is accompanied by 95% confidence intervals. Taken from [468].

Despite bird skeletons being described as ‘lightweight,’ bones are found to be a larger fraction of the body mass than mammals of similar size. Dumont [468] measured the bone fraction from the cranium, humerus and femur of song birds, bats and rats and found that, on average, the bird bone fraction was higher than the other two (Fig. 156). As an example, this means that the skeleton of a 100 g bird weights more than the skeleton of a 100 g rodent. It was proposed that additional strength and stiffness (provided by a higher mineral content) are required for bird bones for flight purposes. Thus bone density as well as its morphology form the basis for the stiffness and strength.

The skulls of birds can take on several configurations. Fig. 157a and b shows cross-sections of the skull of a pigeon and long eared owl (*Asio otus*), respectively. In the pigeon, the trabecular bone is randomly oriented and is thickest at the base of the head. For the larger owl, a layered sandwich structure is observed with an oriented cell structure. The high density of the cranium of birds, relative to bats and rats is associated with feeding habits [468].

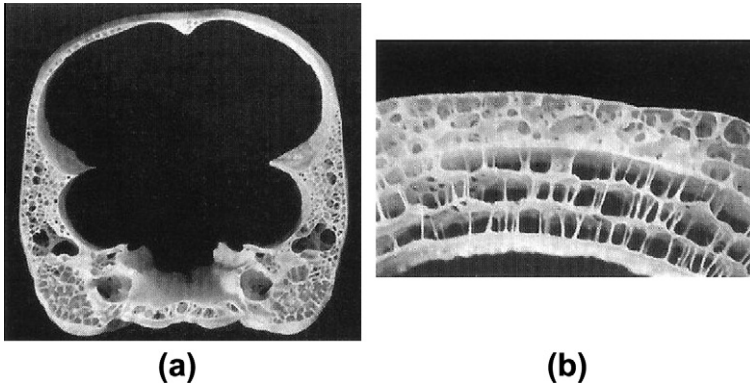


Fig. 157. Bird skull cross-sections. (a) Random foam core in a house pigeon and (b) oriented and multiple cellular structure of a long-eared owl (*Asio otus*). Adapted from [469].

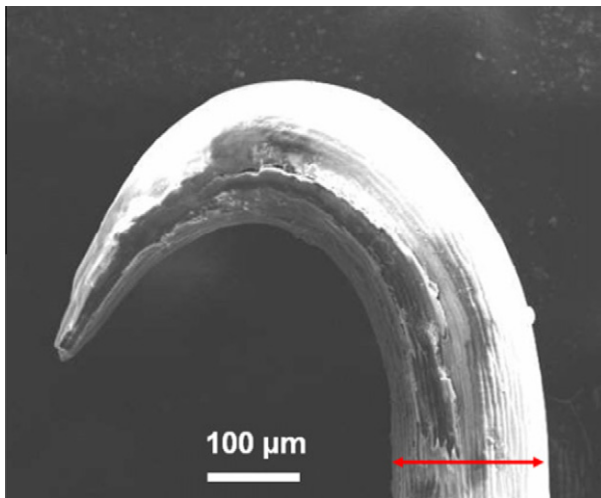


Fig. 158. Burr hook which inspired George de Mistral to create VELCRO.

6. Attachment

6.1. Sticking

A fascinating and challenging functionality of biological systems is the ability developed by some species to attach to surfaces under varying conditions. Barnacles [470–472] and mussels [473–476] attach in a permanent manner through intricate chemical processes, while a number of animals have evolved reusable attachment devices: insects, lizards, tree frogs, mammals, fish, and mollusks. Barnes [477] classifies attachment mechanisms found in animals into following categories:

- **Interlocking:** The mechanism by which mammals (e.g. felines and bears) climb trees. This is a strictly mechanical process and can be accomplished by penetrating the surface with sharp claws. A very simple mechanical attachment device are the hooks on burrs which attach themselves to hikers. This was the inspiration for the best known biomimicking application VELCRO. Fig. 158 shows one of these hooks. Each burr has thousands of these hooks that ensure attachment to wool loops in clothing and fur in animals. Thus, the seeds are carried away from their origin through attachment to a temporary host.
- **Friction:** It consists of the micro-scale interlocking of the surfaces due to their roughness and inter-molecular forces between materials and requires an angle which is below 90°.
- **Bonding:** Involves the formation of bonds between the animal and the surface and has three possible mechanisms acting separately or together: wet adhesion (capillarity), dry adhesion (van der Waals), and suction (through reduced internal pressure). Bonding can also happen through hydrogen bonding [478,479] or metal complexation between metallic ions or oxides and certain side-chain residues [480].

Here, we will illustrate these attachment mechanisms through five examples: the gecko, beetle, and ladybug, that use primarily van der Waals forces through setae having diameters that decrease with increasing body mass; the tree frog (*Scynax perereca*), and the abalone foot, that use a combination of mechanisms .

6.1.1. Gecko foot

The gecko foot is one of the most fascinating examples of how animals that can apparently defy gravity by using a unique structure in the foot pad. It has been intensively studied by several groups [481–484]. Fig. 159 shows the hierarchical structure of the gecko foot. At the macro-meter scale, the foot consists of “V” shaped patterns. At higher magnification, the setae arranged into approximately square bundles with 10 μm side in a regular pattern with channels between them. At the distal ends, the setae terminate into large numbers of nanosized fibrils, called spatulae, with diameters of ~100 nm. The setae and spatulae are keratinous.

Arzt et al. [482] and Huber et al. [484] calculated the stress required to pull off a contact and explained the scale effect. This calculation is based on the van der Waals forces combined with Hertzian contact stresses. For simplicity, spatulae are assumed to have semi-spherical extremities, as a first approximation. The contact radius, a , for a spherical cap of radius R in contact with a flat surface and subjected to a compressive force F is, according to Hertzian elasticity [485]:

$$a = 0.88 \left(\frac{2RF}{E^*} \right)^{1/3} \quad (6.1)$$

where E^* is an effective modulus. The astute reader will eventually discover the exact form of E^* . Johnson et al. [486] inserted the attractive force between the two bodies and obtained the expression (as quoted by [44]):

$$F = \frac{4}{3} E^* \frac{a^3}{R} - (4\pi E^* \gamma a)^{1/2} \quad (6.2)$$

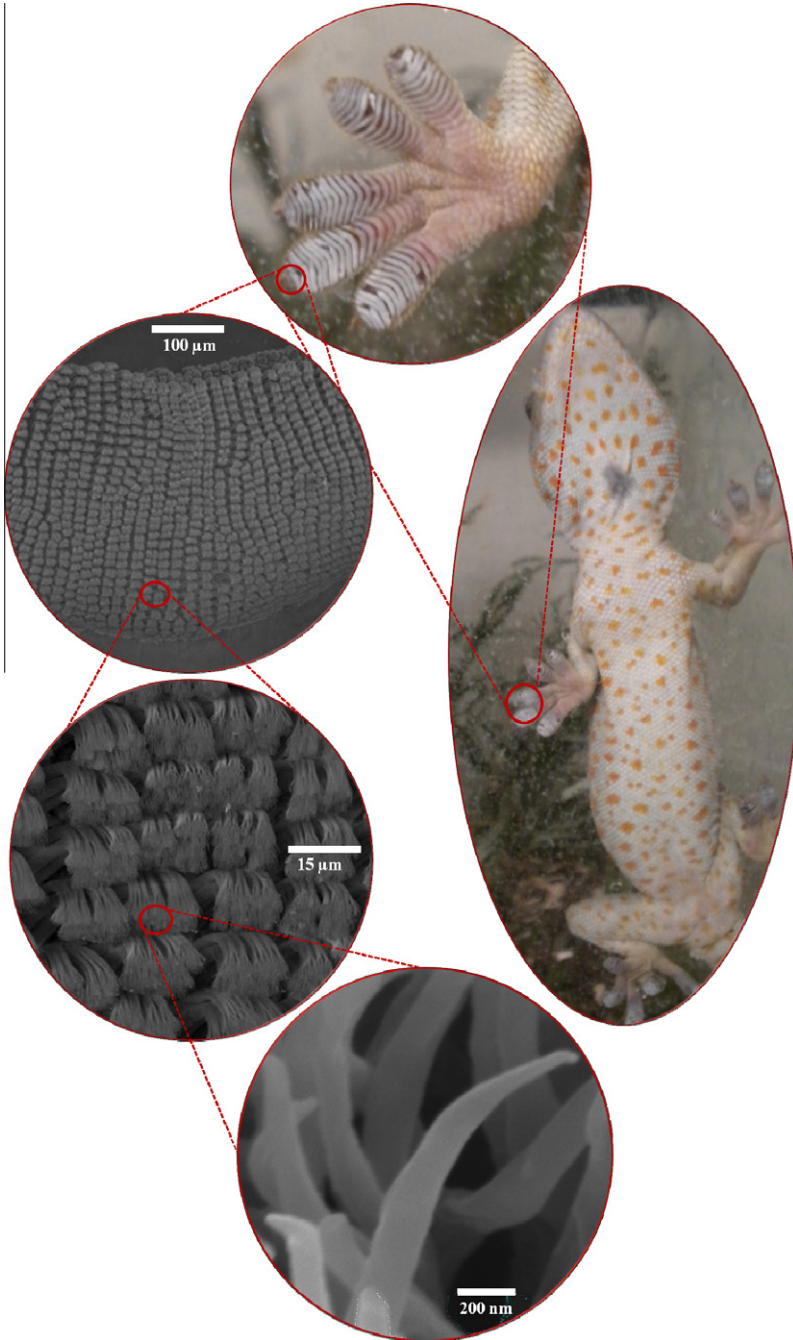


Fig. 159. Hierarchical structure of gecko foot shown at increasing magnifications, starting with setae in rectangular arrays terminating in spatulae with diameters of approximately 100–200 nm. Taken from [24].

where γ is the work of adhesion of the two surfaces that produces the van der Waals force. The critical radius of contact a_c is obtained by taking:

$$\frac{\partial F}{\partial a} = 0 \tag{6.3}$$

This leads to

$$F_c = \frac{3}{2} \pi R \gamma \tag{6.4}$$

This result is, surprisingly, independent of E (or E^*). More complex analyses incorporate the elastic constants. In the case of attachments, only a fraction of the surface, f_s , is covered by spatulae, since there is an average distance between them, $d > R$. The adhesion stress can be computed from F_c considering the area of contact of each spatula to be equal to πR^2 . The stress required to pull off a spatula is the force F divided by the apparent area.

$$\sigma_{app} = \frac{3}{2} \frac{f_s \gamma}{R} \tag{6.5}$$

where f_s , the fraction of the area covered by setae, is:

$$f_s = \frac{\pi R^2}{A_{app}} \tag{6.6}$$

A_{app} is equal to d^2 . It can be seen that the pull-off stress in Eq. (6.5) is inversely proportional to R . Thus, the larger the mass of the biological system, the smaller R has to be. For geckos, that have a mass of approximately 100 g, it is equal to 10 setae per μm^2 . Arzt et al. [44,482] arrived at a quantitative relationship. Considering a spherical body, the surface, S , varies with mass, m , as:

$$S \propto m^{2/3} \tag{6.7}$$

Assuming geometrical similarity, the area covered by setae, A_s is a constant fraction of the total body surface:

$$A_s = kS \tag{6.8}$$

The force required for attachment, F_A , is related to the mass, m , by:

$$F_A = mg \tag{6.9}$$

This force is the product of σ_{App} by A_s . Thus:

$$\frac{3}{2} \frac{f_s \gamma}{R} km^{2/3} \propto mg \tag{6.10}$$

This results in the proportionality between R , the spatula radius, and $m^{-1/3}$, the mass. This is obeyed, to a first approximation. However, there are other aspects that come into play, as will be seen in the next Section.

6.1.2. Beetles

The relationship developed by Arzt [44] predicts a spatular diameter that decreases with the body mass to the $-1/3$ power. This is obeyed in an approximate fashion, but there are significant differences between species. Often, in a species the spatular diameter is constant in spite of significant changes in diameter. Two examples are provided in Figs. 160 and 161, for the common beetle and the ladybug, respectively. The rain beetle (*Pleocoma puncticollis*) feet have hooks at the ends; the spatulae have a diameter $\sim 11 \mu\text{m}$. The Lady bug (*Coccinellidae*) is much smaller, with a mass of $\sim 0.2 \text{ g}$ and a density of 0.05–0.2 setae per μm^2 . The spatulae have a diameter of $\sim 3 \mu\text{m}$. These two examples go against the Arzt equation. Indeed, attachment is a complex biological process involving a number of mechanisms and different species exhibit different plateaus of response. Fig. 162 shows spatular radii as a function of body mass for several species [487]. The Arzt equation is superimposed and its generality and elegance are indeed striking. Qian and Gao [488] discuss the

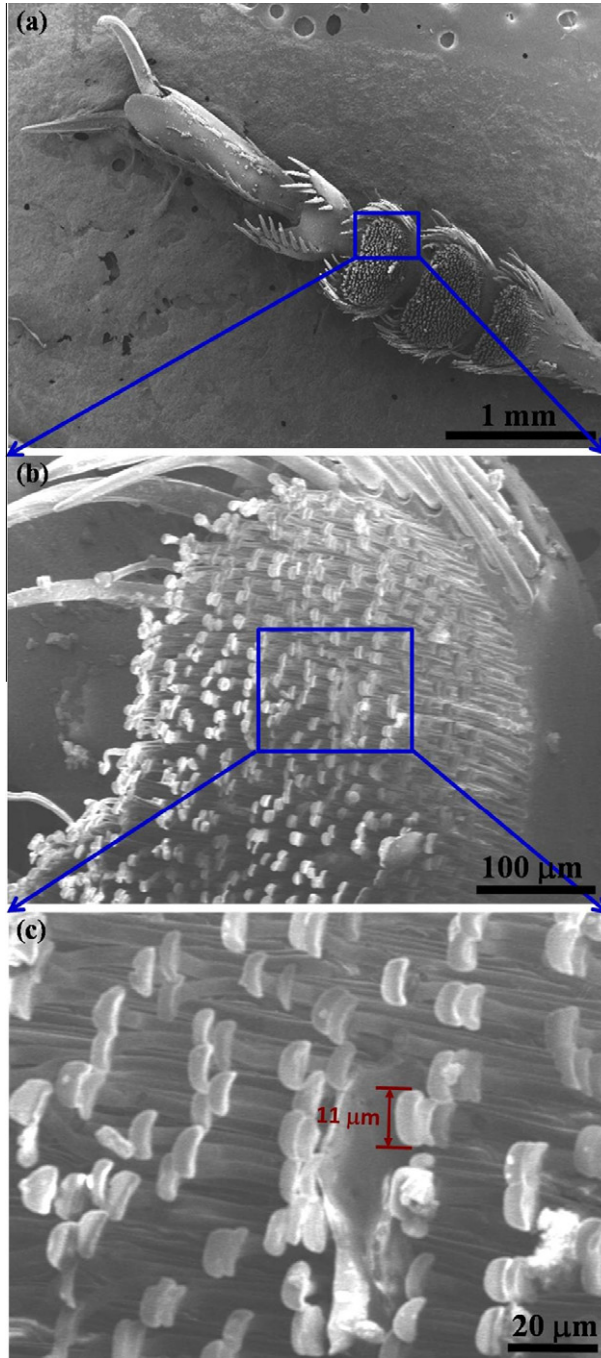


Fig. 160. (a) Rain beetle (*Pleocoma puncticollis*) foot with hooks at end. (b and c) Views at increasing magnification of setae terminating in spatulae with diameter $\sim 11 \mu\text{m}$. (Courtesy of W. Yang).

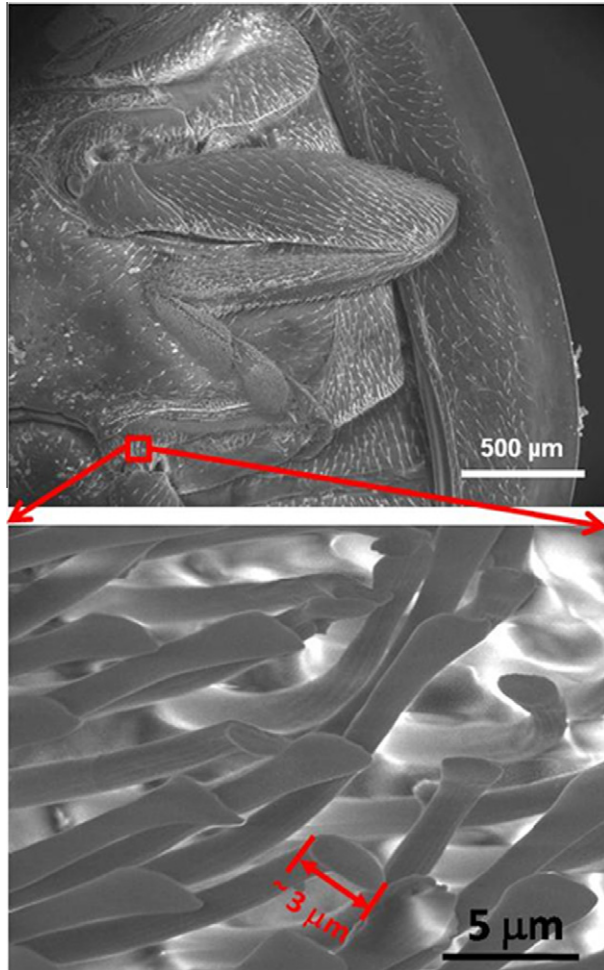


Fig. 161. Ladybug attachment device: top: retracted leg; bottom setae terminating in spatulae. Diameter $\sim 3 \mu\text{m}$ (Courtesy of W. Yang).

complexities of attachment: the effect of contributions beyond van der Waals forces, different geometrical relationships between species, differences in spatulae construction and geometry, contributions of capillarity to adhesion, and others.

6.1.3. Tree frog toe pad

The toe pad of the Brazilian tree frog (*Scynax perereca*) provides a splendid example of functional adhesion in nature. This animal, which lives in the moist environment of the subtropical rain forest, is able to jump from surface to surface, and attach itself effectively through a variety of electro/mechanical/chemical actions employed by the materials at the surface of its toe. Its movements are much more dynamic than the gecko. We observed that the toe pad of the Brazilian tree frog is also composed of aligned nanoscale fibrils. The fibrils are sectioned into highly ordered hexagonal bundles [25]. These bundles, described first in by Ernst [489], Welsh et al. [490] and studied later by others [491–493] are separated by canal-like grooves. More recent studies have been carried out by Hanna and Barnes [494] and Barnes et al. [495,496].

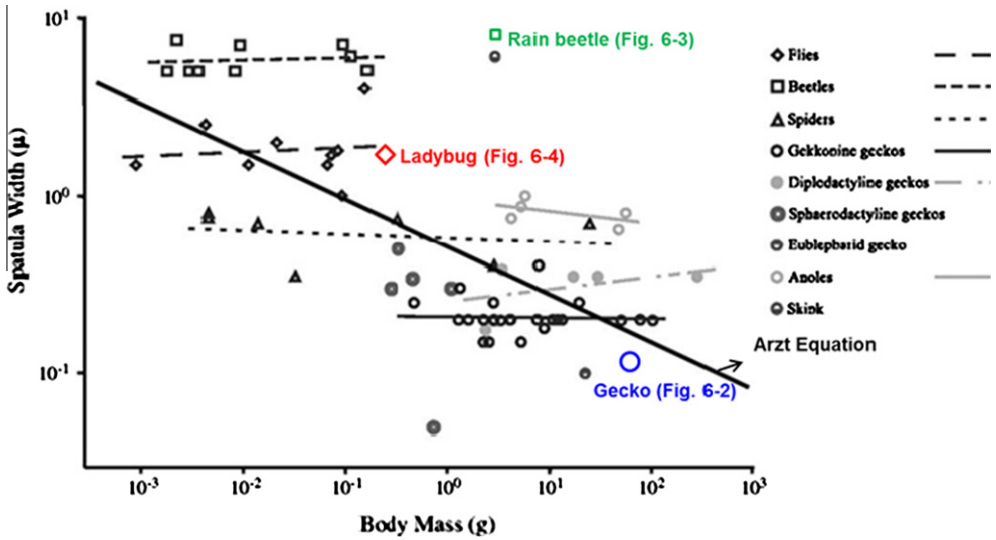


Fig. 162. Spatula width as a function of body mass for several species. The straight line with slope equal to $-1/3$ is the Arzt equation. It tracks the overall dependence well; however, within each species there is a much lower dependency on mass, as shown by the different lines. Adapted from [487].

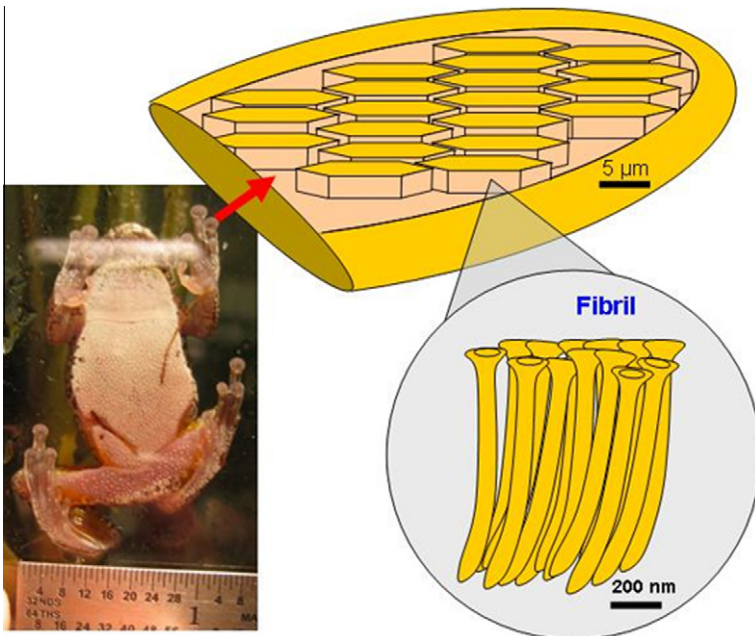


Fig. 163. Schematic diagram of the structural hierarchy found in the toe pad of a Brazilian tree frog (*Scynax perereca*).

The structure of the toe pad is depicted in the schematic diagram presented in Fig. 163. The diagram shows a tree frog attached to a glass substrate, with an illustration of the hexagonal subdivisions approximately $10\ \mu\text{m}$ in diameter. These subdivisions are comprised of closely packed fibers approximately $100\ \text{nm}$ in diameter. Each fiber terminates in a cup of approximately $200\ \text{nm}$ in diameter [24].

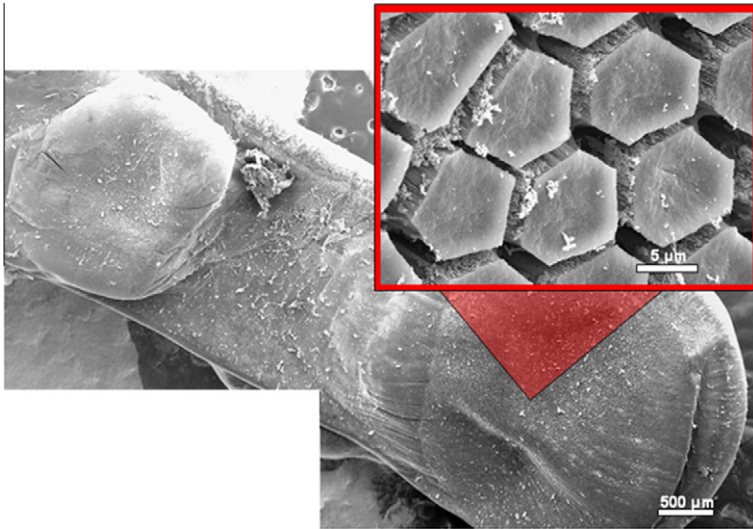


Fig. 164. Scanning electron micrograph of the toe pad of a Brazilian tree frog; (a) low magnification view of single toe, (b) hexagonal subsections found on the contact surface of the toe pad.

Each one of these cups is aligned with its neighbors forming a flat surface. Fig. 164 provides a scanning electron micrograph of a single toe at low magnification with an expanded view of the surface of the toe pad showing hexagonal subdivisions. A well defined circular pad of roughly 2.5 mm in diameter can be seen in the center of the toe. Fig. 165 provides (a) a top view, and (b) a cross sectional view of an individual bundle. The tightly packed, well aligned fibers which comprise these bundles are shown in greater detail in Fig. 165c. The terminating cups on neighboring fibers are aligned closely against each other to create a smooth and consistent surface.

Barnes [477] reported that the mucous glands excrete a viscous fluid which can be transported through the canals that exist between the hexagonal subsections. It had been suggested that the fluid plays an essential role in adhesion, indicating a domination of wet adhesion mechanism. It is proposed here that the contribution of molecular adhesion through van der Waals interactions between the nanofibril ends and a surface may have a place in the discussion of tree frog toe pad adhesion.

6.1.4. Abalone foot – underwater adhesion

Our group has extended the study of the structure of abalone to the attachment forces required to separate it from a surface [87]. The detachment stresses were measured on live and healthy abalone and found to be on the order of 115 kPa. The pedal foot of red abalone (*Haliotis rufescens*) is shown in Fig. 166a. The dark pedal folds, spaced approximately 0.5 mm apart, are the source of locomotion waves used in transportation [497,498]. These locomotion waves have an analog in Materials Science – the dislocation. The fold in the pedal propagates along the foot, generating, after its passage, a displacement equal to the length of surface at fold. Fig. 166b shows an abalone supporting its own weight via a single contact point (a human finger). Fig. 167 shows a large magnification SEM image of the cross-section of the soft tissue. Folds can be seen in greater detail as a mechanism in which the surface area of the foot can expand and contract allowing an increase or decrease in contact surface area and providing the mechanism for the propagation of waves on the ventral surface of the pedal muscle.

At higher magnification, Fig. 168a shows setae lining the outer surface of the tissue with a thickness of 1–2 μm . At their extremities, (Fig. 168b) the setae separate into nanoscale probes with hemispherical ends (c), averaging 150 nm in diameter and uniaxially aligned perpendicular to the plane of the foot tissue. It is proposed that, as in the case of the gecko, these nanofibrils create intimate contacts at the molecular level to form van der Waals interactions which can accumulate into a formidable macro-scale effect.

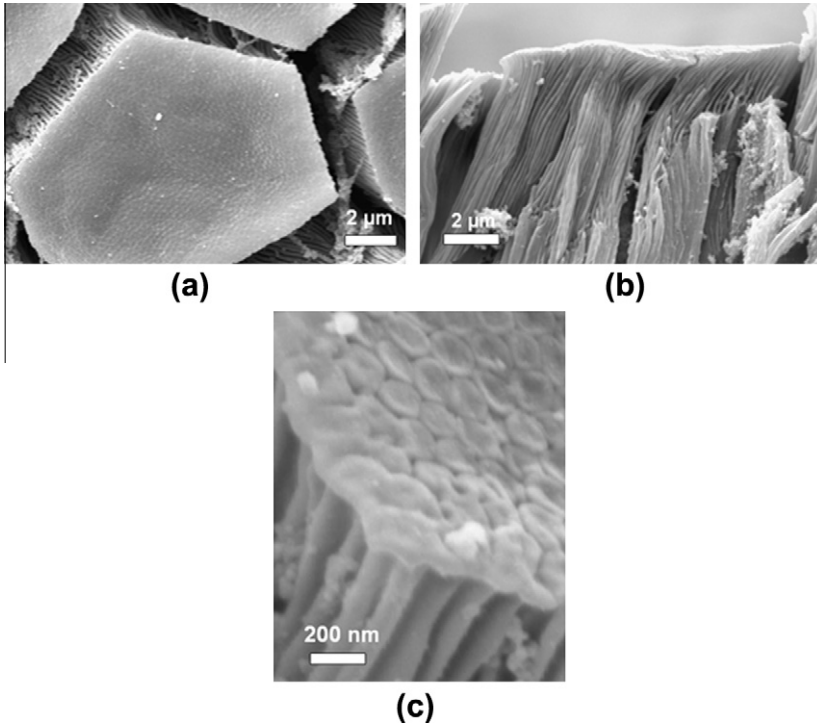


Fig. 165. Scanning electron micrographs of hexagonal subdivisions in toe pad of Brazilian tree frog (*Scynax perereca*): (a) top down view; (b) side view; (c) high magnification showing individual fibers ~ 100 nm in diameter. Adapted from [24].

The influence of a meniscus fluid between a fiber and a substrate is increasingly significant with decreased liquid-surface contact angle, i.e. a hydrophilic substrate would have more capillary interactions than a hydrophobic one. This is clearly seen in Fig. 169. In the case of the hydrophobic material (a carbon coated substrate) the average pull-off force was determined to be 294 nN, remaining constant under varying humidity. If one assumes that 60 nanofibrils on a single seta are in contact with the surface, this would correspond to an adhesion force of approximately 5 nN per nanofibril. This estimate is in exact agreement with the theoretical results of 5 nN calculated using the Johnson–Kendall–Roberts equation (hemispherical end, diameter ~ 150 nm). When the seta was tested on a hydrophilic substrate (SiO_2), at a relative humidity of 10%, the pull-off force was observed to be 424 nN before detachment. This represents an increased force of 130 nN relative to test on the hydrophobic substrate, which can be partially explained by the variation in surface energies for the two substrates (20 mJ/m^2 and 55.5 mJ/m^2 for the carbon-coated disk and silicon oxide, respectively). However, raising the relative humidity to 67% resulted in an additional increase in pull-off force to 558 nN. Similar to predictions by Autumn et al. [481] and work by Huber et al. [484] for the gecko foot, this shows evidence of capillary interactions. The characterization of the abalone foot pedal and the mechanical tests suggest that the three mechanisms proposed by Barnes [477] act cooperatively (and perhaps synergistically). Suction can generate attachment forces as explained schematically in Fig. 170a. It can be shown that the detachment force F_d is equal to:

$$F_d = PA \quad (6.11)$$

where P is the pressure and A is the projected area of the abalone foot on the plane of the surface of attachment. Assuming that the effect of the water column is negligible, i.e., $P = P_{atm}$, we obtain the mean attachment stress as,

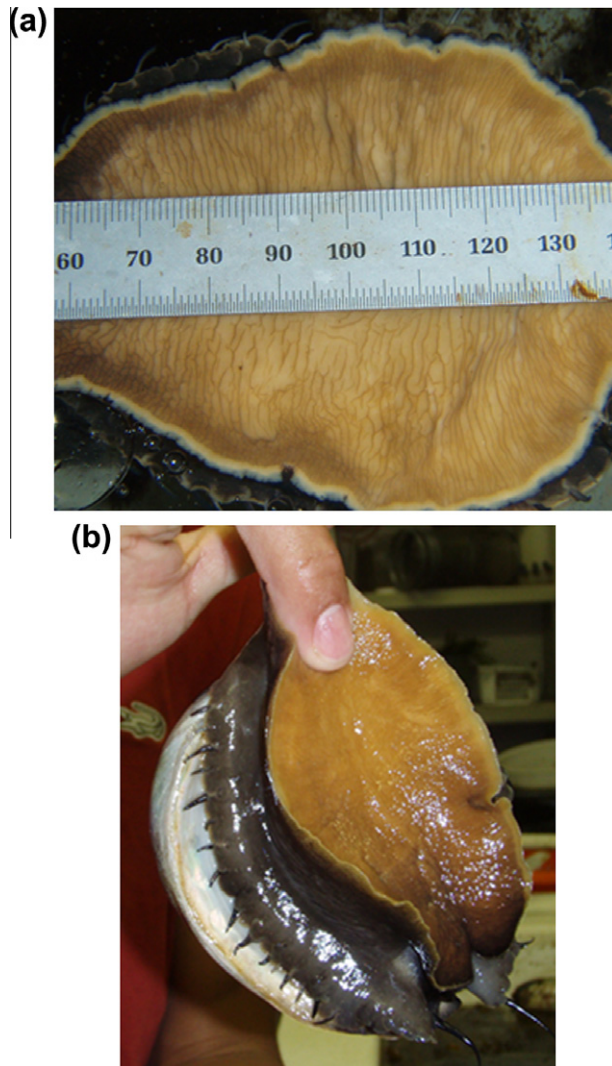


Fig. 166. The pedal foot of abalone: (a) optical image of bottom surface of foot; (b) abalone supporting its own hanging weight through single contact point. Adapted from [87].

$$\sigma_d = P_{atm} = 101 \text{ kPa} \quad (6.12)$$

Fig. 170b and c show schematically how the three mechanisms can operate cooperatively to create the attachment stress on the same order of magnitude as the theoretical suction stress. The setae and nanofibrils maintain intimate contact with any irregular surface, closing possible channels and impeding water penetration. The pressure at the interface, P_0 , is equal to P_{atm} when no external detachment force is applied. As F_d increases, P_0 decreases. Once it becomes zero, detachment occurs. Fig. 170c shows the situation for a non-conforming material: A continuous fluid path to the interface region ensures pressure equilibration around the animal and effectively eliminates suction. It is proposed that capillarity and van der Waals forces can maintain the intimate contact between the ventral

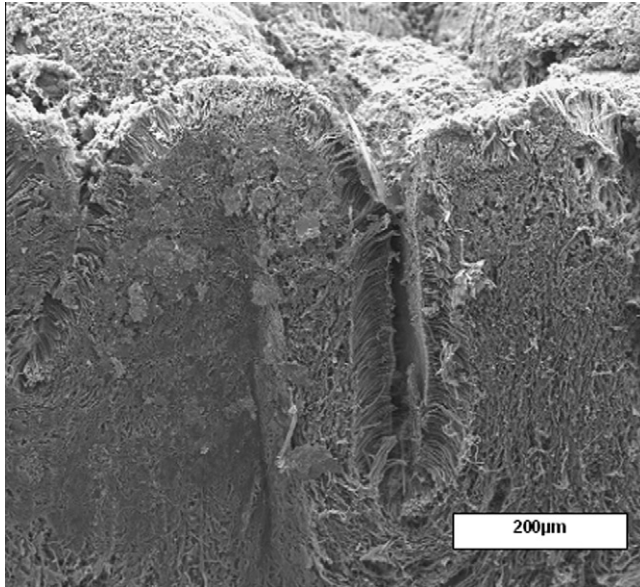


Fig. 167. Scanning electron microscopy of foot tissue of abalone cross-section, the top of the image represents the contact surface of the foot. Adapted from [87].

side of the foot pedal and the attachment surface; in this manner the suction force can reach and even exceed P_{atm} .

6.1.5. Spider web

There have been many studies on the microstructure and mechanical properties of spider silks [6,102,499–503] which has been reviewed in our earlier Prog. Mater. Sci. paper [21]. However, it is not until recently that the mechanical design of the adhesive coating on the webs has been revealed by Sahni et al. [504,505]. Orb-weaving spiders have evolved to produce adhesive droplets on their webs to capture prey. The adhesive droplets consist mainly of glycoprotein, along with other viscous small molecules and salts. Fig 171a shows the components of the capture thread of the spider *Larinioides cornutus*: (1) viscous coat of salts, (2) glycoprotein granule, and (3) axial silk fiber. Silk threads are immobilized on a glass surface and a conical glass probe 10 μm in diameter was brought into contact with single glue droplet (Fig. 171b) and then retracted at constant speeds (Fig. 171c). The critical pull-off forces at varying stretching rates were measured. The force–extension responses showed high pull-off rate dependency (Fig. 171d). Critical pull-off forces increase from 60 μN at a rate of 1 $\mu\text{m/s}$ to ~ 400 μN at 100 $\mu\text{m/s}$. Glycoprotein behaves as a viscoelastic solid, a property that is important in enhancing the adhesion of these almost invisible capture silk threads. At high extension rates, corresponding to the impact of fast-flying insects, the adhesive forces of the glue droplets are dramatically enhanced due to the high strain-rate effect, providing maximum adhesion to effectively capture preys. At low extension rates, similar to the movements of trapped insects, the glue droplets behave like an elastic rubber band, retaining the preys from escaping. The multifunctional design observed in the spider web adhesive droplets provides inspiration of novel synthetic adhesives. Buehler's group [135,506] modeled this on different scales using the physical mechanisms of chain extension.

6.1.6. Mussel byssal attachment

Mussels attach themselves to rocks through byssal threads. These threads have special mechanical properties that are discussed in detail elsewhere (e.g., [21]). They have two regions, the proximal, stiffer, and the distal, adjacent to the attachment site. The proximal region has a much lower stiffness.

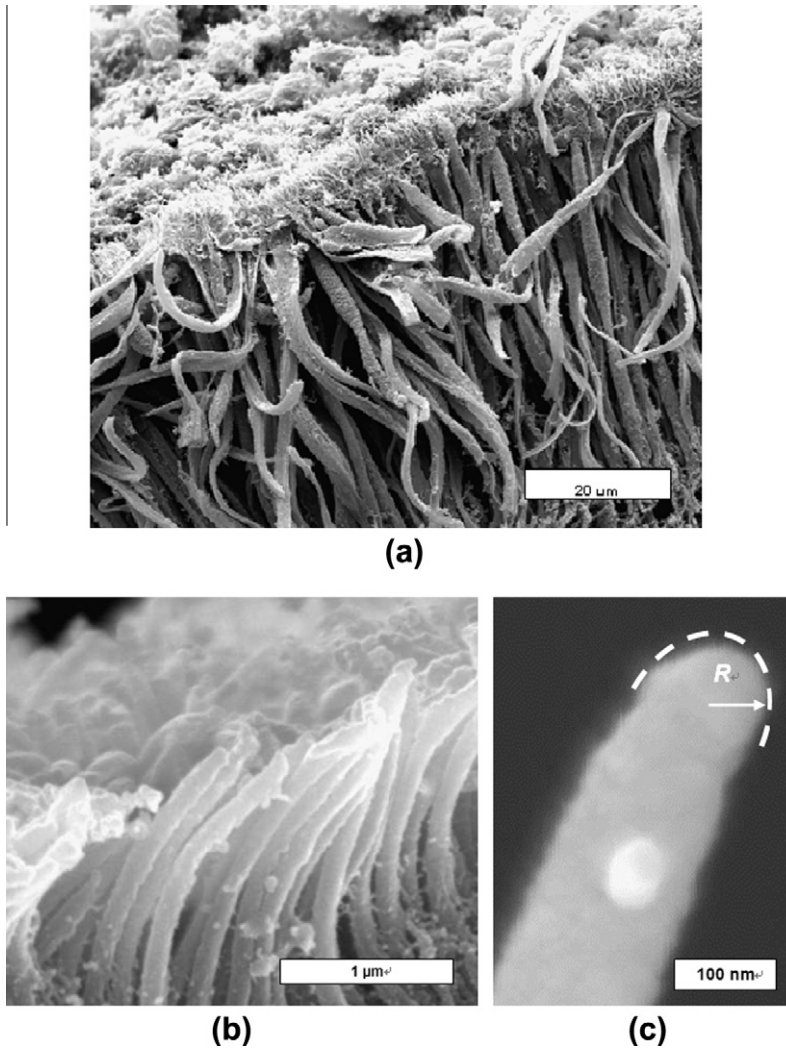


Fig. 168. SEM characterization of abalone foot tissue: (a) seta lining the outer surface of the foot; (b) nanofibers uniaxially aligned on seta; (c) single nanofiber with hemispherical tip. Adapted from [87].

Fig. 172a shows a California mussel (*Mytilus californianus*) attached to Plexiglas. The elongated pads (marked by arrows) constitute the attachment plaques. The attachment of the byssal threads to rock constitutes a fascinating and still only partially understood phenomenon.

For most glue, water is an impediment. They use a combination of mechanical interlocking with non-covalent interactions: salt bridges, hydrogen bonding, and van der Waals bonding. The attachment of the mussel byssus to rocks occurs underwater. A freeze-fractured section of the attachment plaque is shown in Fig. 172b. The core is porous, and this porous region acts as a shock absorber, distributing the stresses evenly over the interface. Waite et al. [507] identified the principal factors in the attachment of the mussel. The formation of this plaque proceeds by the squirting of adhesive from a gland near the tip of the mussel foot. This squirt is in the form of granules with 1–2 μm that coalesce at the surface, forming the adhesive and creating the foaming plaque. It is also believed that a plunger-

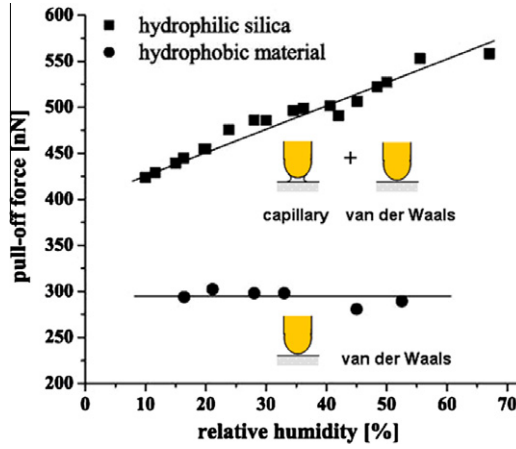


Fig. 169. Pull-off force as a function of relative humidity of a single seta on a hydrophobic (a carbon coated substrate) and a hydrophilic (SiO_2) substrate. Adapted from [87].

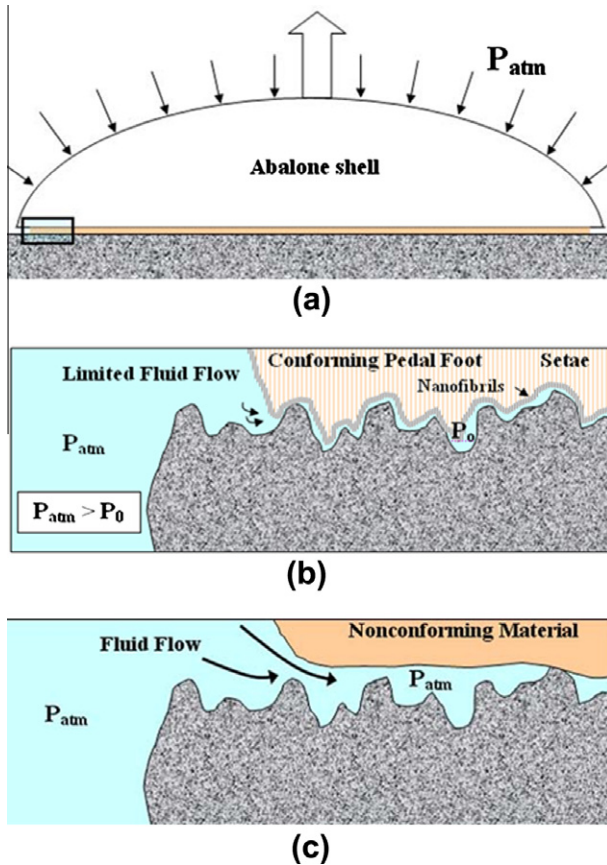


Fig. 170. Schematic representation of how suction might generate attachment forces. Adapted from [87].

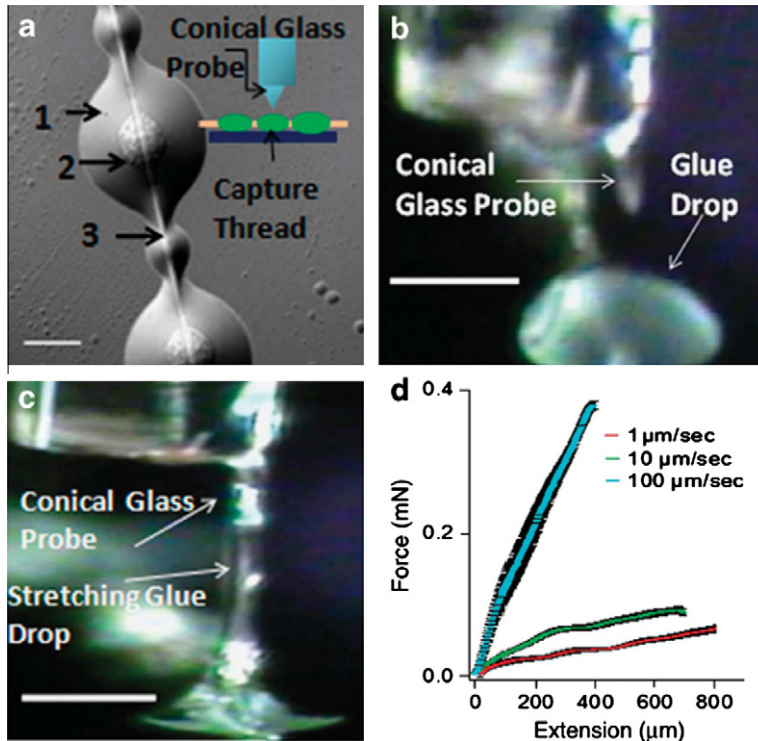


Fig. 171. (a) The components of the capture thread of the spider *L. cornutus*: (1) viscous coat, (2) glycoprotein granule and (3) axial thread. Scale bar is 20 μm . Inset shows a schematic of the single drop pulling experiments, wherein single glue drops (green) of a capture thread were stretched using a conical glass probe (blue) while force responses were recorded. (b) The conical glass probe approaching a single glue drop. Scale bar is 50 μm . (c) Stretching of a single glue drop using the conical glass probe. Scale bar is 60 μm . (d) Force responses when single glue drops were stretched at different rates until separation from the glass probe. Adapted from [504].

like action squeezes the water away from the interface. This still does not explain the high strength of the bond.

The answer seems to lie in the presence (30 mol%) of 3,4-dihydroxyl phenylalanine (DOPA) in the plaque. Underwater adhesion has been shown to be strongly correlated to the presence of a high DOPA content in the adhesive plaques of the mussels [507–509]. The critical role of DOPA on molecular-scale adhesion was demonstrated by Lee et al. [480] who performed single-molecule force type experiments with an AFM tip functionalized with DOPA. These data were complemented by Guvendiren et al. [510] who conducted AFM experiments using DOPA in the cantilever tip and found that the attachment energy to TiO_2 is very high: 130 kJ/mole. Such a high energy exceeds considerably non-covalent interactions and suggests that some type of charge transfer mechanism occurs at the surface. Following these studies, the main adhesive proteins responsible for the adhesion were identified by Zeng et al. [511] and Hwang et al. [512] by combining biochemical with biophysical techniques. More recently, it was also discovered that strong adhesion is made possible through redox-coupling interactions between the adhesive proteins. One protein is rich in DOPA and can form cooperative H-bonding. However, DOPA easily oxidizes into quinone above neutral pH, and quinone residues do not lead to strong adhesion [478]. But a second protein, which is rich in cysteine “rescues” DOPA by forming di-sulfide bonds, hence reducing back the quinone into DOPA. In other words, the cys-rich protein plays an anti-oxidant role that maintains strong adhesion through redox coupling with DOPA residues [479].

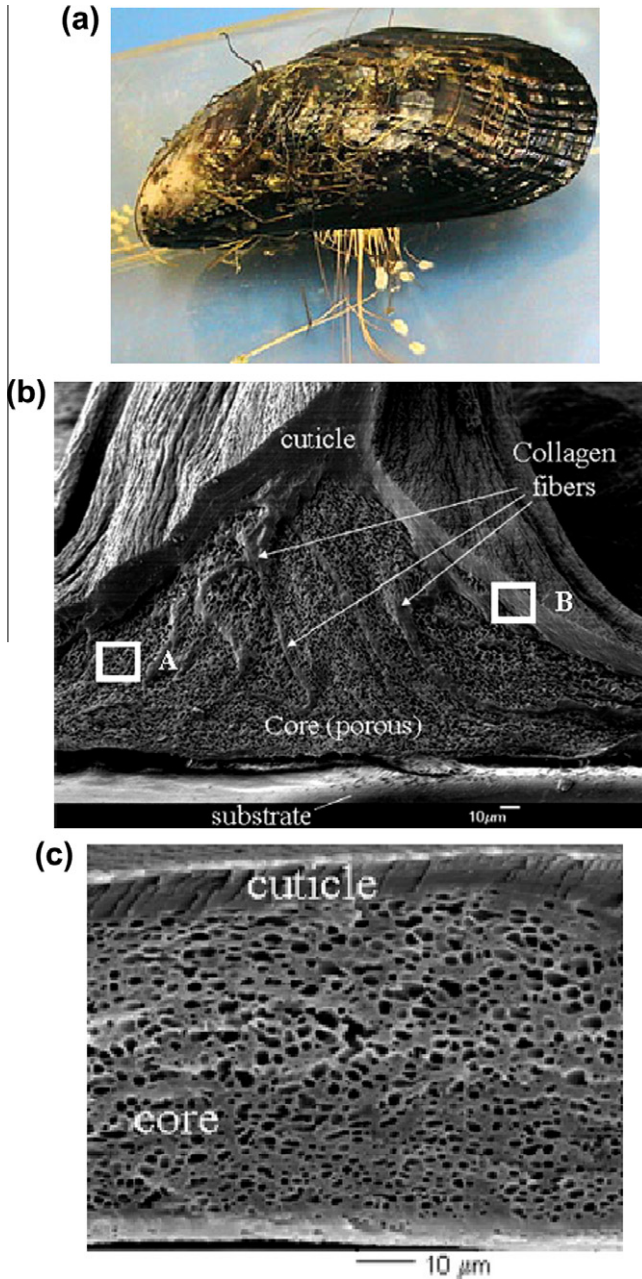


Fig. 172. (a) California mussel (*Mytilus californianus*) attached to Plexiglas; (b) attachment plaques and byssus shown by boxes A and B, respectively; (c) cross section of attachment plaque showing the porous core (Detail A). Adapted from [507].

6.2. Superhydrophobic surfaces

6.2.1. Lotus leaf

This lotus leaf was studied by Barthlott and co-workers [513–515] and recently reviewed by Koch et al. [516]. Fig. 173a shows a lotus leaf floating in the water. The water at its top does not wet it, but

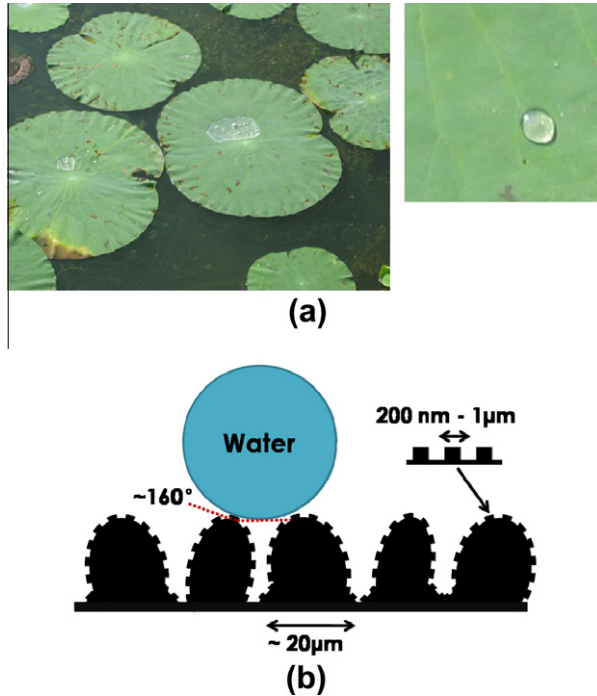


Fig. 173. The Lotus leaf effect: (a) lotus leaf upon which water does not wet; (b) schematic of the surface showing two scales of protrusions which lead to the angle greater than 90° . Taken from [24].

concentrates into small areas by virtue of the hydrophobicity of the surface. This is necessary to clean the lotus leaf and ensure its flotation. Drops of water will just roll off the leaf (shown in the right photograph of figure).

The surface of the lotus leaf has small pillars of a few micrometers height and spaced $\sim 20 \mu\text{m}$ (Fig. 173b). These are, in turn, covered by a smaller scale protrusions, with dimensions of $\sim 0.2\text{--}1 \mu\text{m}$. These are, on their turn, covered with wax. The net result is that the angle of contact between water droplets and the surface is dramatically increased. Hydrophilic surfaces have contact angles below 90° , whereas hydrophobic surfaces have angles above 90° . For the lotus, this angle can be as high as 160° , and it is therefore called super-hydrophobic. This hydrophobicity has an important effect: water droplets, almost perfect spheres, can roll over the surface. When they do this, they pick up dust particles which decrease their surface energy by being absorbed into the water droplets. Thus, the surface cleans itself. In 1999, a commercial and very successful product was launched: the facade paint *Lotusan* has been applied on more than 500,000 buildings worldwide so far. Other applications are self-cleaning glasses installed in the sensors of traffic control units on German highways and coatings applied to microwave antenna which help to keep them dust free and decrease the buildup of ice and snow.

7. Biomimetic and bioinspired materials

7.1. Introduction

The design of materials involves consideration of a wide number of structural elements which, on their turn, determine the resulting properties. The most important structural components are [58]:

- Atomic/molecular design.
- Nanostructures and boundaries.

- Dislocation and other defect structures.
- Cells and other substructures (size, morphology, structure, orientation).
- Grain size, orientation, morphology and structure.
- Particle and precipitate coherence, shape and distribution.
- Orientation distributions.
- Phase relationships and morphologies.
- Design of interfaces at all length scales.
- Phase transformations.

Materials design is a mature and highly developed field with massive investments globally. The approaches used range from fundamental thermodynamics and density-functional theory to Edisonian trial-and-error developments. Evolutionary and revolutionary changes have pushed the performance of synthetic materials (alloys, polymers, ceramics, and composites) to their limits. Hence, novel design concepts have to be implemented if we are to make progress. What seems to be effortless in a biological system that produces complex, multifunctional materials can, indeed, be translated to processing of synthetic materials. Layered structures, such as abalone nacre, exhibit high toughness values despite low fracture toughness constituents. For example, it has been shown that for metal/metal, polymer/polymer and glass/polymer laminates, thinner layers produce a tougher composite than do thicker layers [39,517–519]. This suggests that the scale and hierarchy are important considerations in materials design.

Challenges and opportunities for bioinspired materials development include [30,39,58,193,520,521]:

- Synthetic constituents to produce hierarchical materials with useful performance over a broad range of environmental conditions (e.g. temperature, pressure, humidity).
- Wear-resistant materials with low friction coefficients for joints and bearings (e.g. knee joints).
- Synthetic adhesives that recreate the sturdiness and toughness of biological adhesives (e.g. gecko feet).
- Composites with high volume fractions of the reinforcement (e.g. nacre).
- Multifunctional materials.
- Electro-optical devices.
- Manufacturing and synthesis techniques under ambient conditions.
- Self-assembled materials.
- Self-healing, environment-adaptable materials.

Additionally, a systems approach must be taken to put theory into practice. Biological systems adapt to changing ambient conditions, continually refining and adjusting shape, chemical and mechanical signaling. Some of the challenges include [58]:

- Strong, durable interfaces between the hard and soft constituents.
- Tribological joints with low friction coefficients and remarkable durability.
- Mechanistic understanding and analysis methods for deformation and failure of complex systems.
- Energy-absorbing mechanisms of rigid biological composites.
- Platelet and surrounded plate analytical concepts; and
- Moisture friendly synthetic systems.

It is clear that the design of materials and structures inspired in nature involves special challenges not encountered earlier. Traditional design has followed disciplinary lines, but bioinspired design will require multidisciplinary teams of engineers (design and structure) and life scientists (biochemistry, biology, physiology, anatomy molecular biology) to develop materials with complex, hierarchical structures. In this chapter, we present some biologically inspired materials and designs being investigated and classify them along the lines of this article: fracture and impact resistance; armor and defense; cutting edges; attachment; sensors and optical devices; medical applications. We also present

other interesting biomimetic applications that do not fall into this classification. We point out that we exclude the applications discussed in our earlier review [21].

7.2. Bioinspiration: fracture and impact resistance

7.2.1. Self-healing composites

Self-healing is a property of bone and most vascularized tissues. New research is directed at developing composite materials that can repair cracks after they have formed. The basic concept is to embed two different liquid precursors that will polymerize when in contact. If a crack propagates through both agents, they will leak out into the crack, mix, and polymerize thereby closing the fissure. This concept has been used with glass tubes filled with the healing agent and small pockets of catalyst and with microcapsules housing the healing agent with the pockets of catalyst [522]. Fig. 174a shows the biological mechanism of self-healing in bone. Osteoclasts remove bone, forming resorption cavities while at the same time, osteoblasts deposit new bone which is most effective under an applied load. This continuous remodeling of bone allows for self-healing of breaks and cracks in bone. Fig. 174b shows the microcapsule concept illustrating how the healing agent leaks out into the crack

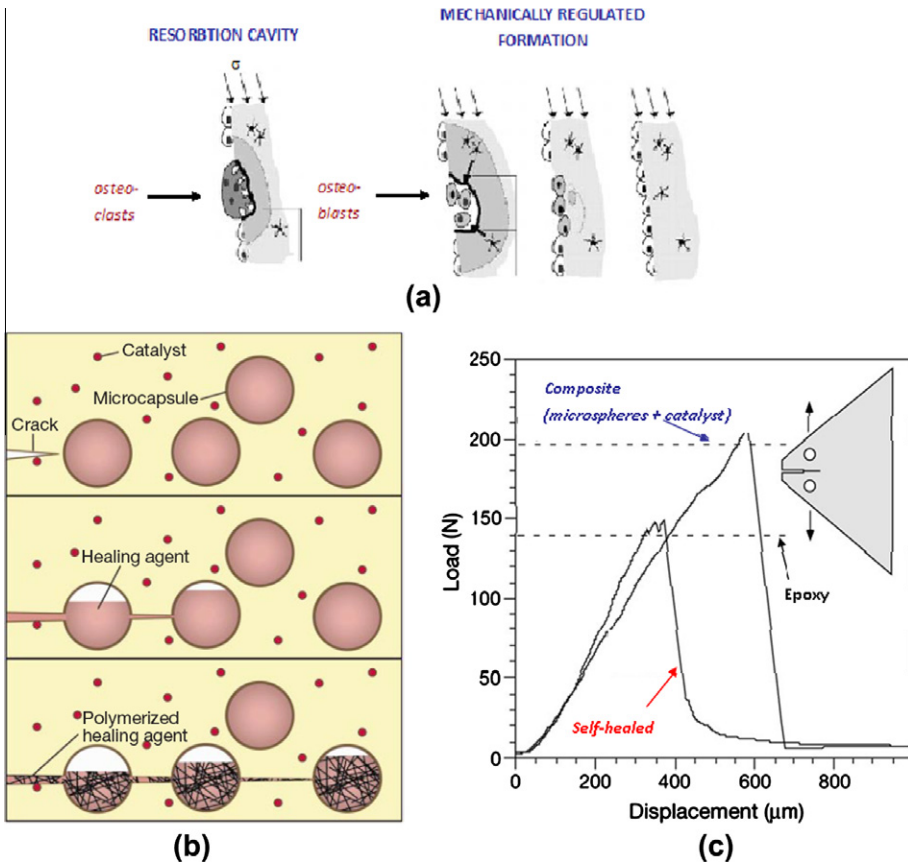


Fig. 174. (a) Biological mechanism of self-healing in bone. Osteoclasts break down bone creating resorption cavities while osteoblasts deposit new bone. Stress is needed for the efficient operation. (b) Design of a self-healing composite. Microcapsules of a healing agent are embedded in an epoxy matrix along with a catalyst. The crack ruptures the microcapsules and releases the healing agent. Polymerization occurs when the catalyst is contacted thereby bonding the crack faces. (c) Mechanical integrity of the self-healed composite. (b and c) Taken from [522].

but polymerizes to a hard polymer when the catalyst is impinged upon by the crack front. Fig. 174b demonstrates evidence of self-healing. The epoxy resin with the microcapsules and catalyst has a higher strength than the resin alone. After a crack has been introduced and allowed to propagate, the self-healed composite does not immediately break in half; rather, it retains significant structural integrity to have a strength over that of the pure epoxy resin.

A composite with microvascular channels that can self-heal has been developed by Toohey et al. [523]. This assembly behaves as skin, since surface cracks that develop can repair, in a process similar to what has been developed for bone-inspired self-healing composites. Fig. 175a shows a schematic diagram of the dermis, illustrating the vascular network at the surface. Fig. 175b shows the skin-

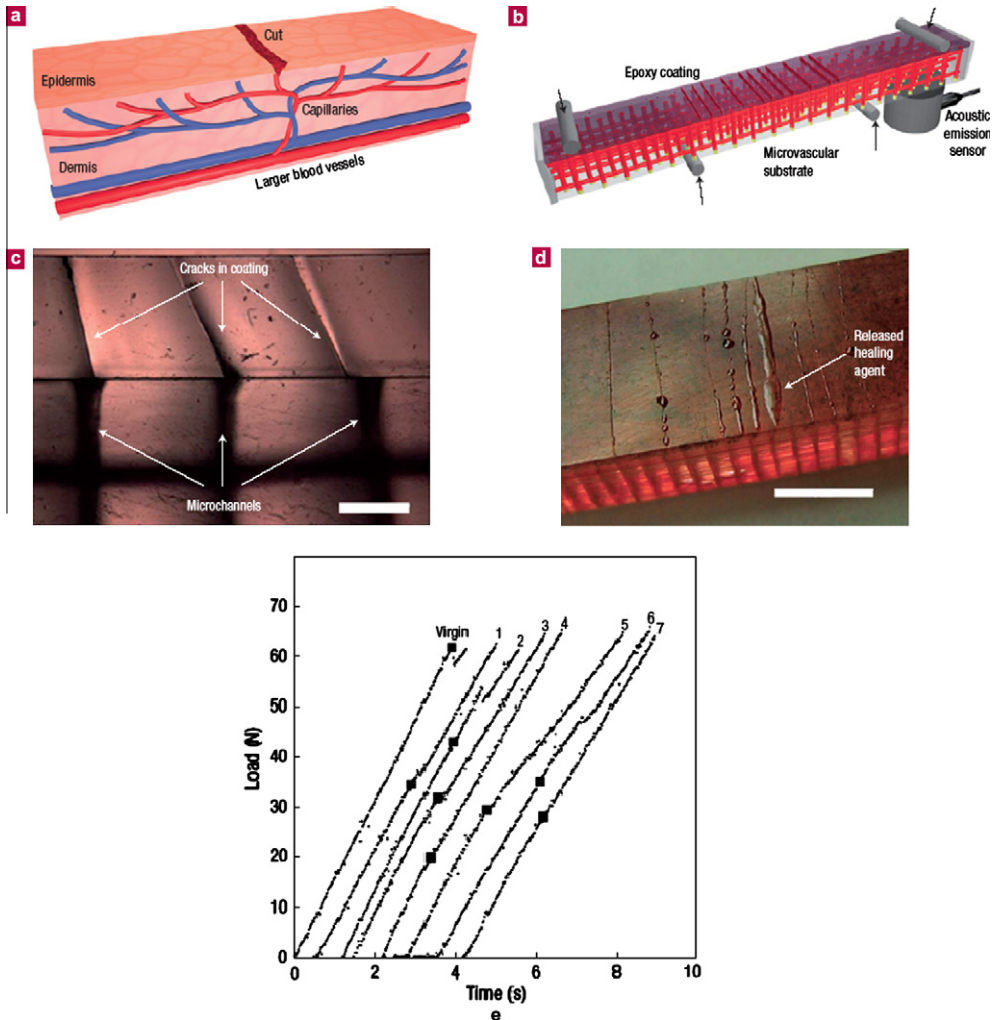


Fig. 175. Self-healing skin-like composites. (a) Schematic diagram of the skin dermal layer, illustrating the vascularity. (b) Bioinspired skin-like composite consisting of an epoxy layer with the catalyst embedded in it on top of an array of microchannels that contain the healing agent. (c and d) When cracks develop and impinge into the microchannel array, the healing agent and catalyst combine and polymerize to close the crack. (e) Stress–strain curves (off set for clarity) of the virgin epoxy and the self healed composites that demonstrate that the strength and stiffness can be retained in the self-healed material. Taken from [523].

mimicked structure consisting of a hard epoxy layer that is embedded with the catalyst on top of an array of channels that contain the healing agent. Cracks of sufficient length that form on the surface layer and impinge on the channel array are healed (Fig. 175c and d) through the polymerization of the healing agent with the catalyst. The stress–strain curves are shown in Fig. 175e, demonstrating that the initial strength and stiffness of the original composite can be retained, even after crack development.

7.2.2. Sheep horn composites

The sheep horn has keratin filaments that are embedded not only parallel to the growth direction but also extend from one layer to the next (Section 2.3). These cross-ply fibers aid in decreasing delamination by strongly holding together the layers. Composite materials companies recognize that delamination is the most common failure mode for layered composite materials and have fabricated composites that are cross-stitched together. However, although this improves the delamination strength, the presence of the holes from stitching decreases the overall fracture strength. The traditional $0^\circ/90^\circ/0^\circ$ unidirectional fibrous composite structure is shown in Fig. 176. A novel composite that has similarity to the structure of animal horns is shown in Fig. 177 [524]. A ‘forest’ of carbon nanotubes is grown on the surface of the laminate, which then holds the plies together. This resulted in enhanced mechanical properties: the fracture toughness was increased by $\sim 350\%$, the flexural modulus increased by $\sim 100\%$ and the flexural toughness increased by $\sim 525\%$ over the base composite.

7.2.3. Shock absorbers based on the woodpecker’s head

Bioinspired designs based on the woodpecker’s skull could lead to the development of new shock absorbers for airplane black boxes, helmets and other safety equipment. Yoon and Park [297] fabricated a shock absorbing system that consisted of:

- A high strength external layer that acts like the beak.
- A viscoelastic layer that evenly distributes mechanical vibration that acts like the hyoid.
- A porous structure that suppresses transmission of vibrations.
- Another high strength layer that has the porous structure of the skull bone.

In Fig. 178, the ‘beak’ is fabricated from steel, the ‘hyoid’ from an elastomer, ‘spongy bone’ from glass microspheres, the ‘skull bone and cerebral fluid’ from aluminum and the ‘brain’ from

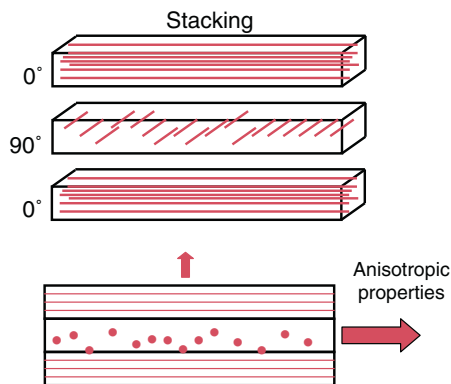


Fig. 176. Traditional stacking sequence of $0^\circ/90^\circ/0^\circ$ unidirectional fibrous composites. The properties are highly anisotropic, with strength and stiffness optimized in one direction.

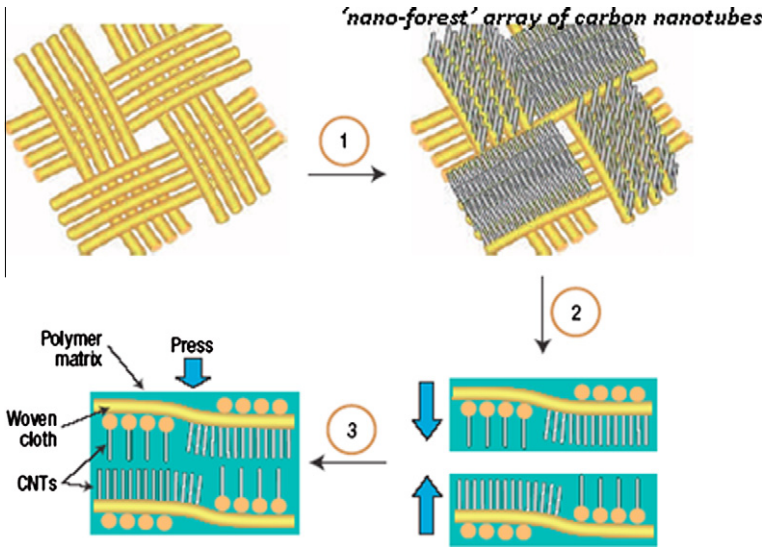


Fig. 177. Using a carbon nanotube forest, the laminates in this composite are stitched together to form a stronger, stiffer composite. Adapted from [524].

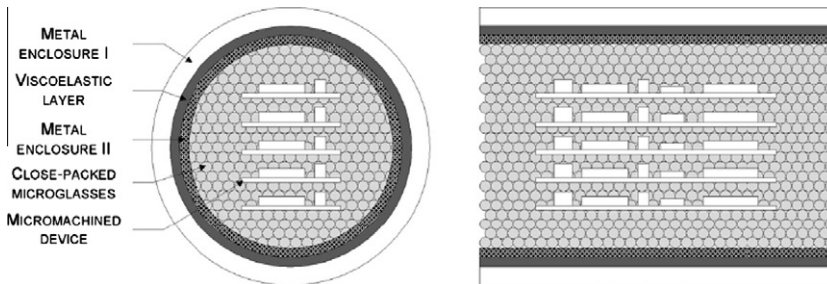


Fig. 178. Bioinspired shock absorption system based on the head of the woodpecker. A metal sheath encloses a viscoelastic layer and another layer. The cylinder is filled with microglass spheres. Taken from [297].

micromachined devices. The system was fired from a gas gun and survived up to 60,000 g's, indicating that a superior shock-absorbing device was fabricated.

7.2.4. Natural graded and sandwich structures (osteoderms)

The hexagonal tile configuration has many structural themes in history. One early example is the testudo formation of Roman armies (Fig. 179a). The soldiers formed small groups that marched together but held shields over the top and on the sides and front, thereby sacrificing mobility for protection, a configuration that looks similar to the armadillo armor. Ancient Japanese armor had hexagonal shaped leather tiles that formed a jacket (Fig. 179b), and finally LAST[®] tiles on an army tactical vehicles have shown to have excellent ballistic protection (Fig. 180). Other biomimetic applications have been proposed such as tents in which people could curl up and cover themselves from fire or other extreme environments. Fig. 181 illustrates the crocodile osteoderm, which is a bulletproof natural armor.

Many plant stems are cylinders with graded densities. These structures use an ingenious method of increasing the flexural strength/weight ratio. The design principle is similar to the one of beams with

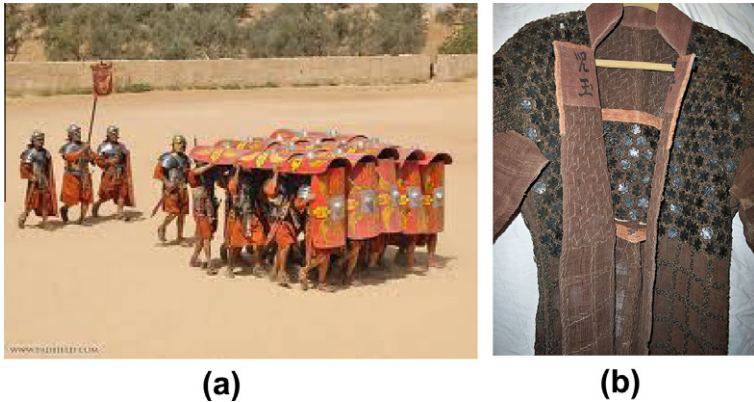


Fig. 179. (a) Testudo formation in Roman armies. Shields protect front, sides and top. Taken from (Padfield.com). (b) Japanese kikko armor composed of hexagonal leather or iron plates.



Fig. 180. LAST army tiles on an army tactical vehicle. These LAST[®] tiles have a ceramic interior and are coated with a polymer (picture taken from (<http://www.foster-miller.com/literature/documents/LASTGround.pdf#LASTGround>)).

an added complexity. In beams, the moment of inertia is increased by moving matter as far away from the neutral axis as possible. In biological structures, the density is varied using cellular materials that are graded, the density increasing with distance from the neutral axis. One extreme of lightness is the absence of matter, and many structures have a hollow core, such as bamboo. In some cases, there is a clear outside shell that sandwiches an inner cellular core, such as the toucan beak, the human skull, porcupine quills and hedgehog spines.

The introduction of sandwich and graded structures has been a major development in structural design and their use in numerous applications can be attributed to bioinspiration. The English long-bow, for instance, uses both the inside (dark) and outside of the yew, which confer different properties: strength and flexibility. The WW2 Mosquito airplane used wood in a sandwich arrangement. Light-weight balsa wood was sandwiched between denser wood veneer faces. The ubiquitous corrugated cardboard is another example of a sandwich structure.

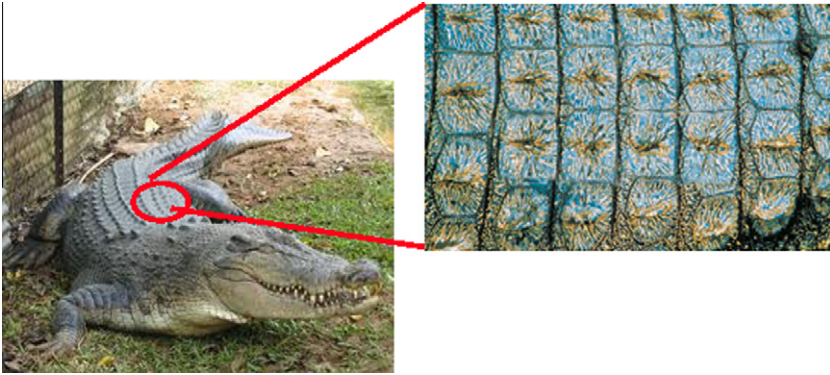


Fig. 181. Photographs showing a crocodile and detailed view of its osteoderms.

We present below three bioinspired concepts. Milwich et al. [525] copied the structure of the horsetail and giant reed stem using textile weaving techniques: a fiber pultrusion process using a braiding machine. He used these stems as models, suggesting that the methodology could be applied to a wide range of cylindrical designs. Fig. 182 shows the cross-sections of a (a) horsetail stem, (b) a

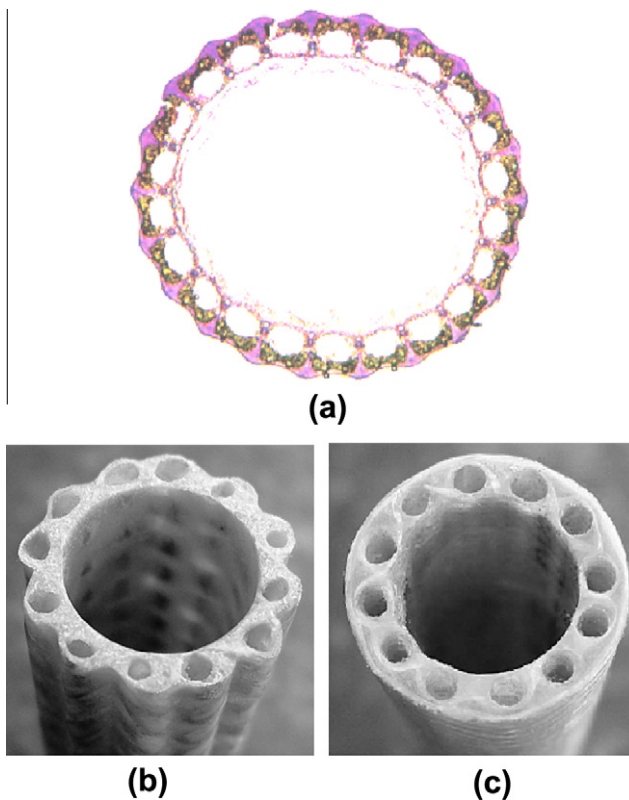


Fig. 182. Cross-sections of a (a) horsetail stem and (b and c) bioinspired woven composite using (b) polymeric (polyurethane) foam and (c) double-braided composite construction. Taken from [525].

bioinspired polyurethane foam, and (c) a bioinspired woven composite. The hollow external rim of the hollow cylinder contains, on its turn, holes. The horsetail stem can be reproduced at different scales.

The lotus root, characterized by a geometrical pattern of holes, has been mimicked by Utsunomiya et al. [526]. This was done by co-extruding copper and aluminum and by leaching out the aluminum; in such a manner a cylindrical copper beam was created with a hole pattern mimicking the lotus root.

An ingenious biomimicking method is described by Zampieri et al. [527] and Zollfrank et al. [528]. It was applied to rattan. It consists of pyrolyzing wood in an inert atmosphere at around 800 °C. This preserved the cellular structure with characteristic size of ~0.5 mm. Silicon gas was subsequently infiltrated into the structure, generating, through reaction, SiC. Similar process can be used to produce other carbides, such as TiC and ZrC. This process has also been applied to other woods [529]. The porous structure can also be infiltrated with a metal, such as aluminum, creating a fully dense composite.

7.3. Bioinspiration: armor and defense

7.3.1. Abalone shell nacre

Given the widespread interest in the structure and mechanical properties of abalone shell, there have been attempts to fabricate nacre-like structures. Various *potential* methods have been outlined to fabricate bioinspired materials based on the structure of nacre [25,38,36,50,324], Arias [530] and Mayer [362] and numerous research projects report on the results from successful techniques. Unfortunately, the term 'nacre-like' or 'mimic nacre' has been so generously applied that nearly all papers that claim a bioinspired nacre design are simply reports on the fabrication of a few-layer CaCO₃/organic structure. These formations are not unexpected considering that this has been the topic of research in the older ceramics literature on ceramic/organic materials. Other papers report on layered nanocomposites of SiO₂/organic, where a three-dimensional structure is obtained. Because of the particularities of SiO₂ gels, and the easy chemical linkages to other molecules and substances, it is not surprising that uniform, layered structures are obtained. Some papers actually produce a nacre-like arrangement, from nacre itself (demineralization of shell, then synthetic remineralization of the protein).

Heuer et al. [50] proposed to cast successive layers of polymer plus mineral precursor and initiate mineral precipitation through the use an external field. Other suggestions involve sputtering or physical vapor deposition of ceramic films but the incorporation of the inorganic phase was not discussed. Arias and Fernández proposed an elaborate method to fabricate the structure of a mollusk shell. First, an inorganic is chosen so that nucleation of calcium carbonate occurs on well-defined sites. Nucleation sites are formed by proteins (aspartate-, or glutamate-rich) and a gel is formed from other proteins, which will serve as the calcium carbonate nucleation matrix. The growth is stopped by the deposition of an inert layer. This process is complex and cumbersome. Mann et al. [26] have outlined a procedure that layered structures may grow from two dimensions to three dimensions with the inclusion of lipids that have an inorganic coating to self-assemble on the inorganic surface. Laser sintering of ceramic particles stacked between polymers has also been suggested [40,51].

Jackson et al. [356] were the first to fabricate synthetic a nacre-like structure. Glass slides were glued together in a staggered assembly. They used analytical techniques to calculate Young's modulus using a modified rule of mixtures and found a good fit. Tensile failure occurred by tile pull-out. Meldrum and Ludwigs [531] formed three-dimensional structures using a template directed growth of biominerals that resulted in sea sponge structures. To produce these, a sea urchin skeleton plate was first infused with a polymer. The skeleton was dissolved leaving a porous polymer template. Solutions containing Ca ions were filled into the mold, which nucleated and formed CaCO₃. They also demonstrated the formation of well-defined CaCO₃ crystals deposited on various substrates. Almqvist et al. [532] fabricated several talc/polymer mixtures that were processed to form a laminated structure with 10 wt.% polymer in the end product. Talc has a platy morphology and it was speculated that alignment of the plates could mimic nacre. The mixtures were treated by centrifuge, spinning cylinder, spinning plate, shearing plate and also dip coated by a glass slide. A maximum orientation factor ~50% was obtained. However, these composites were weak and were not pursued further. Mayer [39] fabricated a staggered, layered structure of Al₂O₃ with a polymer glue. Interestingly, decreasing the volume fraction of the organic to 11% from 18% significantly increased the toughness (Fig. 183). Mayer concluded

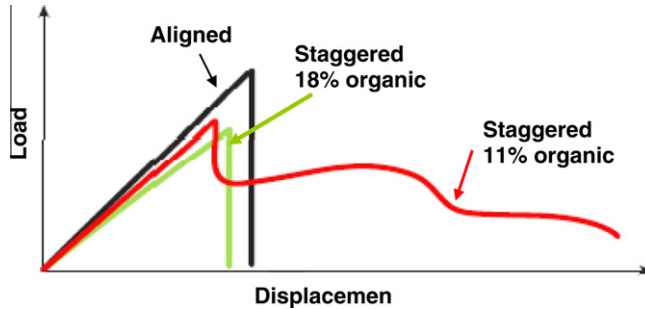


Fig. 183. Schematic diagram of three-point bend tests on an aligned, stacked laminate of Al_2O_3 and polymer glue, and staggered laminates with different amounts of the glue. Adapted from [39].

that even in this simple structure, multiple modes of energy absorption were present. Zhao et al. [533] prepared Al_2O_3 /epoxy laminates with thin plates (0.6 mm) that were dipped into epoxy vinyl ester resin then stacked to produce a laminate 5 layers thick. The work of fracture was found to be $6\times$ greater for the laminates than for pure Al_2O_3 , as observed by Mayer [39], the shear strength improved with additions of filler to the epoxy resin. Tang et al. [534] prepared a laminate that most closely resembles nacre. Using a sequential deposition method, they prepared a laminate of layers of oriented clay platelets (0.9 nm thick) and alternate layers with absorbed poly-(diallyldimethylammonium) chloride polycation (MW = 200,000). Building 200 layers resulted in a film 5 μm thick, which could be tested in a modified load frame. Fig. 184 shows a picture of the film along with SEM micrographs of the cross-section. The volume fraction of polymer was stated to be high, but no values were given. If a 0.9 nm clay layer thickness is assumed and there are 200 layers, this results in a total clay layer thickness of 180 nm, which is 36 vol.% clay. It appears that this material is more of a platelet-reinforced

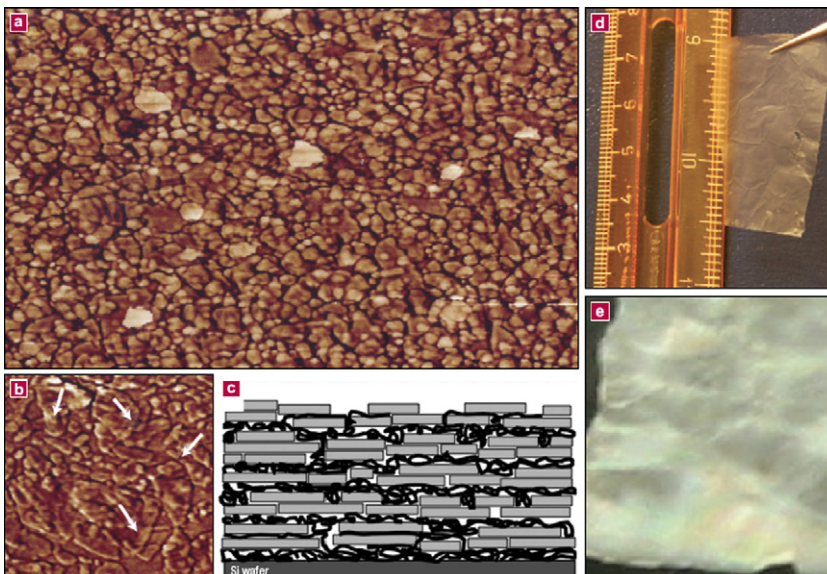


Fig. 184. Microscopic and macroscopic description of $(P/C)_n$ multilayers. (a) Phase-contrast AFM image of a $(P/C)_1$ film on Si substrate, (b) enlarged portion of the film in (a) showing overlapping clay platelets marked by arrows, (c) The $(P/C)_n$ film structure. The thickness of each clay platelet is 0.9 nm, (d) photograph of free-standing $(P/C)_{50}$ film after delamination, (e) close up photograph of the film in (d) under side illumination. Taken from [534].

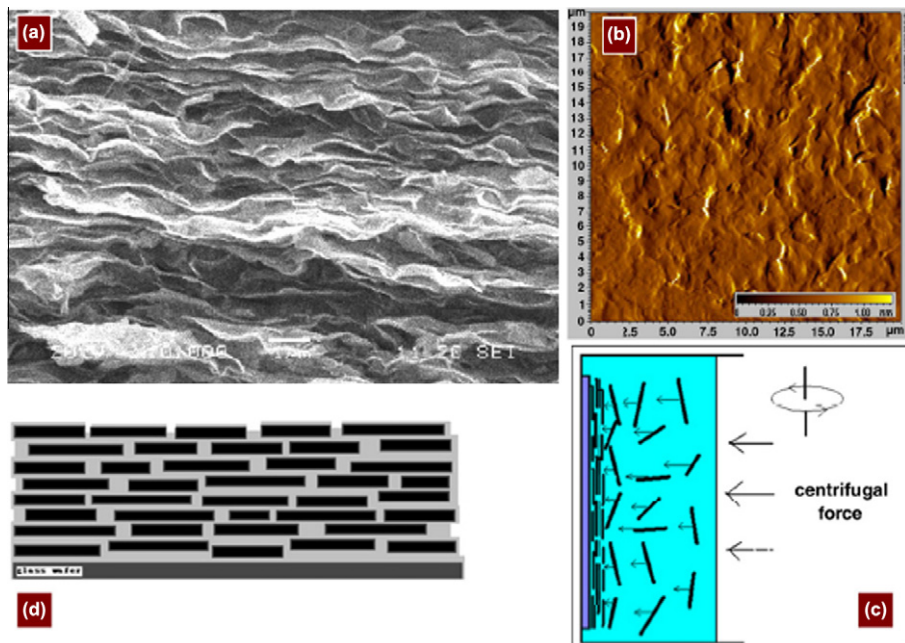


Fig. 185. Nacre bioinspired layered clay/polyimide composites fabricated from centrifugal force. (a) Cross-section of the clay platelets in the composite, (b) organic platelets inset in polymer, (c) the automatic alignment of clay platelets under the centrifugal force, (d) schematic representation of the ordered nanostructure. Taken from [535].

polymer, than a nacre-like composite. Another approach with aligned clay particles in polyimide was reported by Chen et al. [535]. Aligned layers of mineral separated by the polymer were fabricated by a centrifugal deposition process, which resulted in a composite with an organic fraction of 20 wt.% polymer, higher than nacre (5 wt.%). Fig. 185 shows an SEM micrograph of a cross-sectional area along with illustrations outlining the synthesis process. Films of thicknesses of up to 200 μm could be fabricated. The resulting mechanical properties (from nanoindentation) were comparable to the results of Tang et al. [534]. None of these designs incorporate the most important features that contribute to the toughness of nacre: the nanostructural features at the organic/inorganic interface, namely the mineral bridges and surface asperities on the ceramic tile.

By far the most successful method has been adopted by Tomsia and co-workers [536,537]. They have fabricated an interesting laminate structure by suspending ceramic particles in water and then freezing the system in a controlled thermal gradient. The freeze casting method has been developed in 1980 by Mahler and Bechtold [538] who applied for making silica-fibers and later used by Fukasawa et al. [539] and Qu et al. [540] for synthesizing porous ceramic scaffolds. A laminated structure resulted, including ‘mineral bridges’ that formed from dendrites that grew perpendicular to the main growth direction. After the water was sublimated, the scaffold was filled with epoxy or metals. Fig. 186 shows a schematic diagram of the ice-templating process, a comparison of the microstructure of nacre with the artificial layered composite (PMMA and alumina) and stress–strain curves that compare nacre with the layered composite. Increased strength and fracture toughness were obtained. The sintered laminate is shown in Fig. 187a with high magnification micrographs of the bridge area in Fig. 187b and c. Filling the empty spaces with PMMA resulted in a final product of a solid ceramic-based laminate composite with a high yield strength and fracture toughness. For a 80% Al_2O_3 – 20% PMMA laminate, a tensile strength of 200 MPa and fracture toughness of 30 $\text{MPa m}^{1/2}$ were obtained (Fig. 188a). These values represent specific properties comparable to those of aluminum alloys. It should be noted that this is accomplished with the majority being alumina. The resistance to crack

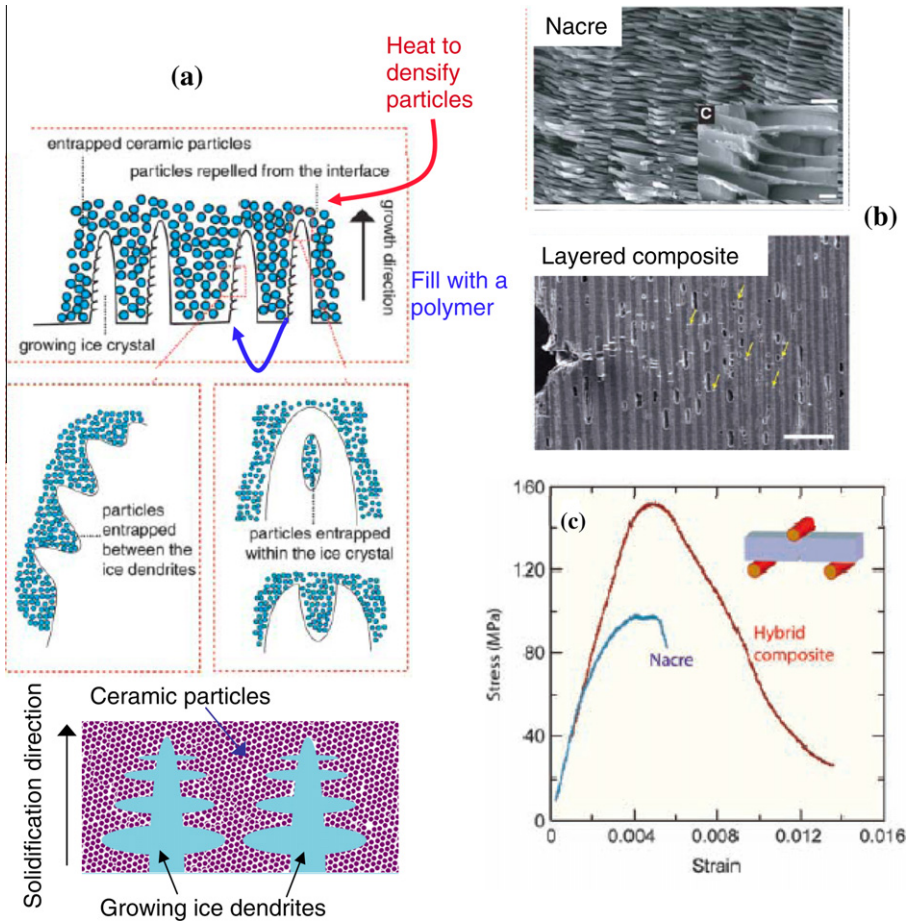


Fig. 186. Ice templating procedure and results. (a) Directional solidification of an aqueous ceramic (Al_2O_3) slurry results in ice dendrites that expel the particles. After solidification, the ice is removed and filled with a polymer (PMMA), (b) SEM micrographs comparing nacre with the synthetic layered structure and (c) stress–strain curves for nacre and the layered composite material. Adapted from [536,537].

propagation (R curve behavior) is shown in Fig. 188b. The increase in toughness with crack propagation is obvious. The curve rises to $K_{Ic} = 30 \text{ MPa m}^{1/2}$. This is in stark contrast with monolithic alumina, which has a flat curve with $K_{Ic} = 1 \text{ MPa m}^{1/2}$. One unique aspect of the architecture of this bioinspired material is that when it has the abalone brick-and-mortar structure with bridges between the tiles, the toughness is increased over the purely lamellar structure ($\sim 15 \text{ MPa m}^{1/2}$). The more conventional simple laminate structure is definitely less tough than the new material. This example illustrates the potential of (a) understanding and (b) mimicking biological materials. Barthelat and Zhu [365] proposed a synthetic material using the ‘wedge’ mechanism of toughening identified in their earlier studies [363,364].

7.4. Bioinspiration: cutting edges

Fig. 189 shows schematic representations of some successful and possible biomimetic approaches to devices inspired from the sharp objects described in Section 4. Fig. 189a represents a hypodermic needle inspired by the proboscis of a mosquito, which was developed by Oka et al. [442]. The

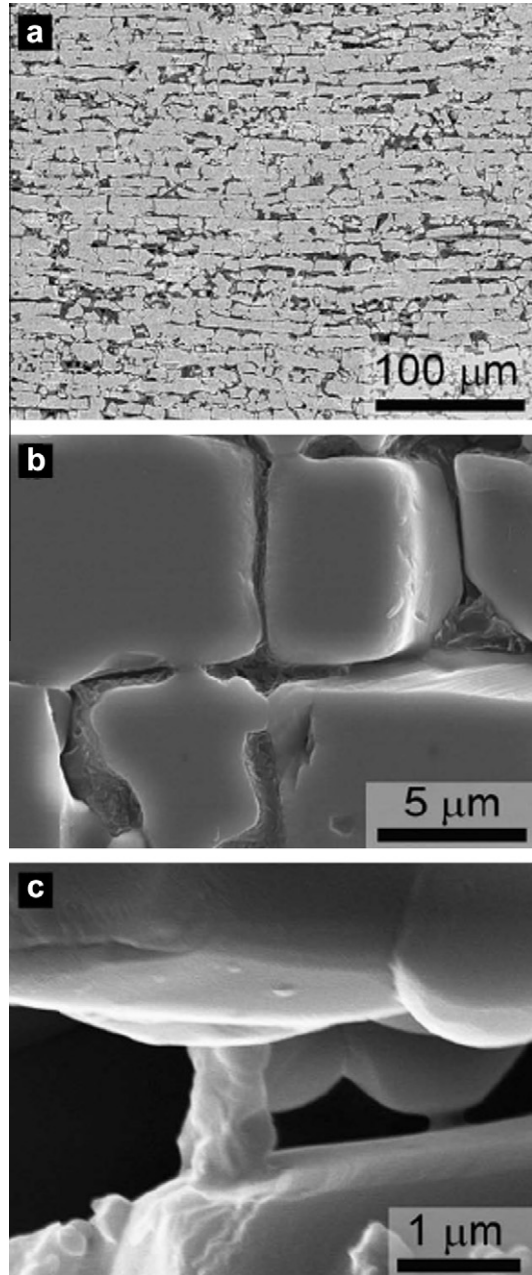


Fig. 187. Microstructure of abalone nacre-inspired $\text{Al}_2\text{O}_3/\text{PMMA}$ composites in (a) lamellar and (b) brick-and-mortar forms produced by freeze casting techniques; (c) bridge between two tile layers. Adapted from [541].

serrations in the needle help it to slice through the epidermis in a painless fashion. This mimicks the action of the mosquito, whose proboscis enters the body virtually unsuspecting to the host. This hypodermic needle has dimensions comparable with the mosquito proboscis but, more importantly, uses the serrated edges (on both sides) to slice through the tissue. The syringe manufactured by Oka et al.

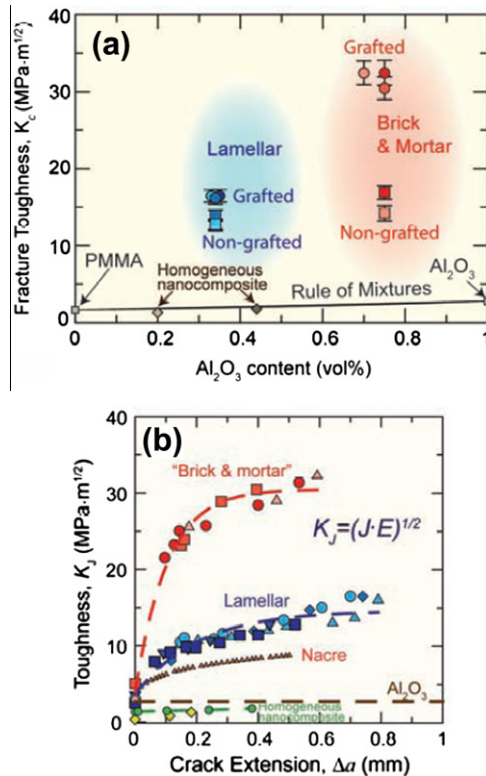


Fig. 188. (a) Fracture toughness for lamellar and brick-and-mortar composites compared with that for Al_2O_3 and PMMA. Both types of composites are significantly tougher than their constituents. (b) The composites show significant rising R-curve behavior due to micro- and nano-scale toughening mechanisms. Adapted from [537].

[442] has a built-in reservoir and is equipped with jagged edges that mimic the mosquito stylet. It is made from SiO_2 using a silicon micromachining technology.

Fig. 189b is a schematic drawing of a cutting tool which was designed to self-sharpen using the same mechanisms as the rodent teeth. The outside is a high hardness ceramic composite, whereas the inside is a high strength alloy. This equipment, inspired on the rat and rabbit incisors, was successfully manufactured in Germany [542]. It uses a hard titanium nitride ceramic reinforced with nanoparticles as the hard 'enamel' portion of the cutting blade. The soft 'dentine' part of the knife is made by a tungsten carbide-cobalt alloy. The titanium nitride layer is twice as hard as the alloy. In Fig. 189b the inner regions of the three blades of the shredder rub against the materials to be cut and wear out, keeping the outer layer, (the hard titanium nitride) exposed and sharp.

The coordination complex between imidazole and Zn ions, as observed in polychaete jaws, has been demonstrated in poly-imidazole based polymer cross-linked with Zn ions, which have improved mechanical properties for various potential applications [543].

7.4.1. Ovipositor drill

The mechanism of wood wasp ovipositor drilling (Section 4.7) has been applied to several designs. One is for a planetary probe and the other is for a surgical cranial drill. In both designs, no forces (impact or normal) are applied thereby minimizing damage to the surrounding material. For planetary probes (e.g. Mars exploration), they must operate in vacuum and excessive pressures cannot be applied, as is done with a conventional rotary drill. The ovipositor biomimetic drill is ideal, since holes can be drilled with a minimal amount of damage.

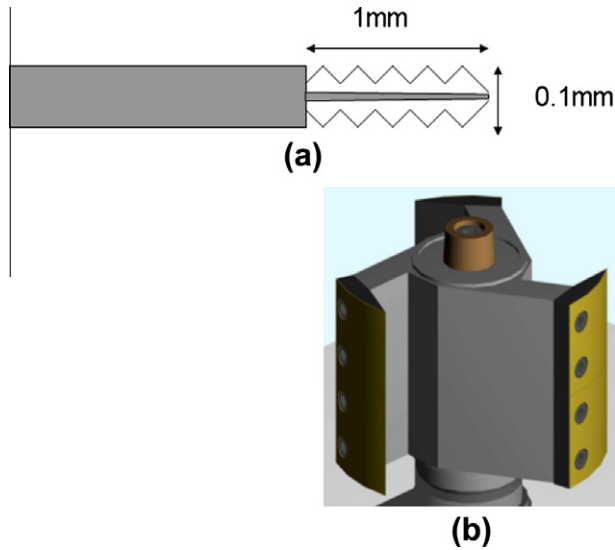


Fig. 189. Possible biomimetic devices: (a) syringe inspired by mosquito proboscis; (b) cutting blade inspired by rabbit incisors. Adapted from [85].

Fig. 190a shows a diagram of a planetary probe along with details of the drill bit [444]. Fig. 190b shows a diagram of the probe tip for a surgical drill. The successful development of a flexible, steerable probe for neurosurgery is shown in Fig. 190c. Since there is no net force in the ovipositor-inspired assembly, there are no stability problems.

7.5. Bioinspiration: aero and fluid dynamics

7.5.1. Birds

The 500 Series Shinkansen bullet train has a maximum speed of ~ 200 mph. It takes inspiration from birds in two places. The train's nose is patterned after the kingfisher's beak. The kingfisher's beak shape allows it to dive into water with a minimum amount of resistance. In the case of the bullet train, the shock waves are emitted when it exits a tunnel. This sonic boom is eliminated by this efficient design. The Shinkansen nose and kingfisher's beak are shown in Fig. 191a and b respectively.

Owls are predators that move silently through the air. The leading edge of the wings have feathers that are comb shaped, which breaks up streams of air in flight. Additionally, the flight feathers are covered with a downy barbules, which absorbs the sound of the moving wing. This stealthy property is used in components that connect the train to the electrical power supply. Serrations similar to the ones in the owl's feathers were introduced to reduce the noise and vibration. The architect, Andreas Harris, designed several structures based on the bird skull that have double layered shells. These open atria allow for uninterrupted flow of air across the top, while maintaining a light weight materials design (Fig. 192). A striking building in Abu Dhabi is the Zayed National Museum shown in Fig. 193. This energy efficient feather inspired design uses 'thermal chimneys' that draw cooling air currents through the building, thereby forcing the heat out to keep the building ventilated.

7.5.2. Fish

Bartol et al. [544,545] studied the fluid dynamics of the bony carapace of boxfish using digital particle image velocimetry (DPIV), pressure distribution and force balance measurements. The results showed that the boxfish carapace effectively generates self-correcting forces for pitching and yawing motions that contribute to the hydrodynamic stability of swimming. Mercedes Benz introduced a new car design at the Shanghai and New York auto shows in 2011 based on the body design of the boxfish.

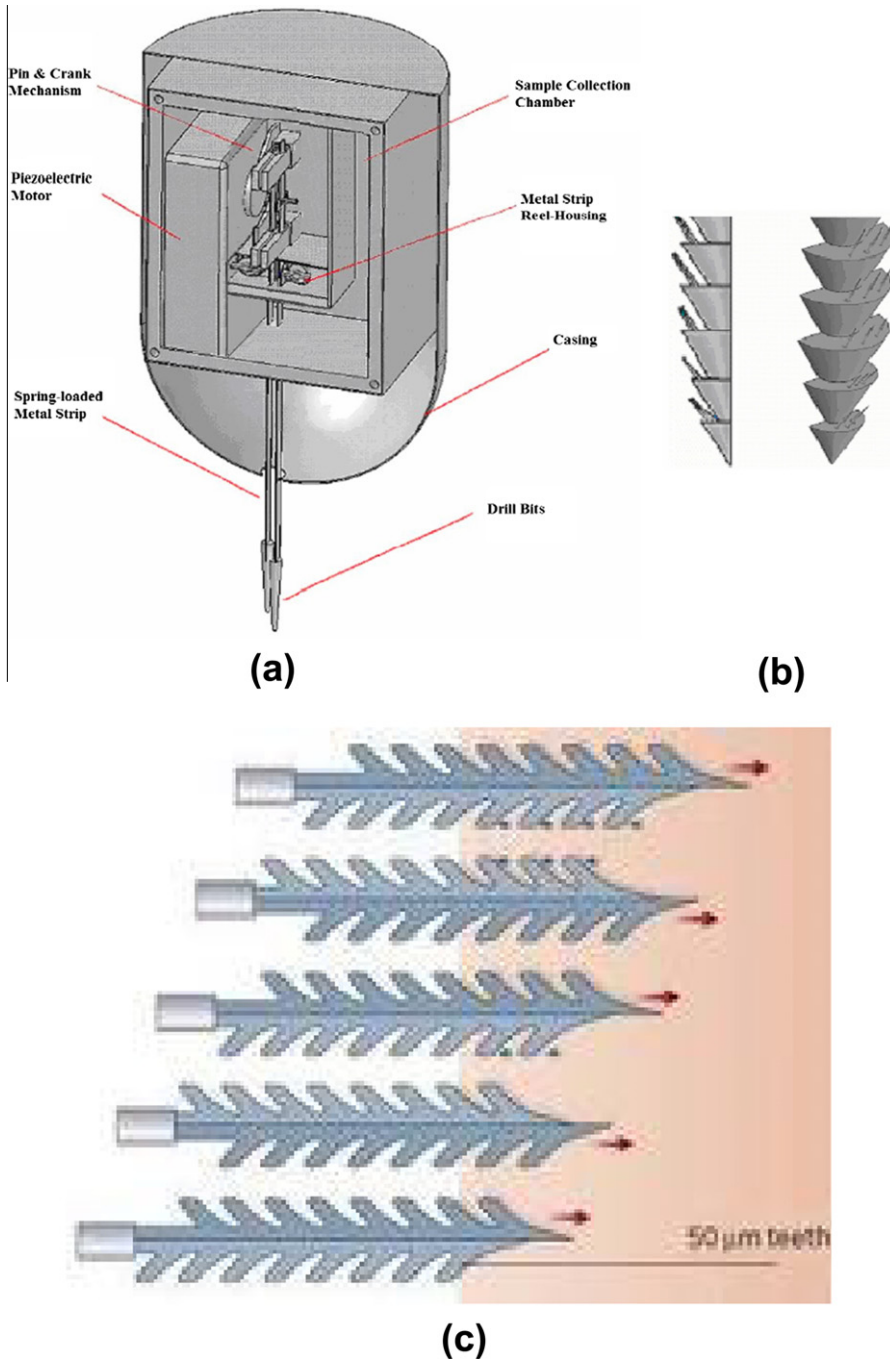


Fig. 190. Bioinspired drill: (a) schematic diagram and (b) close up of the drill bit configuration. Taken from [444]. (c) Mechanism of movement of the two valve drill from a cranial drill (Imperial College, London, Research in Mechatronics in Medicine).



(a) **(b)**

Fig. 191. (a) Shinkansen train nose and (b) kingfisher's beak.

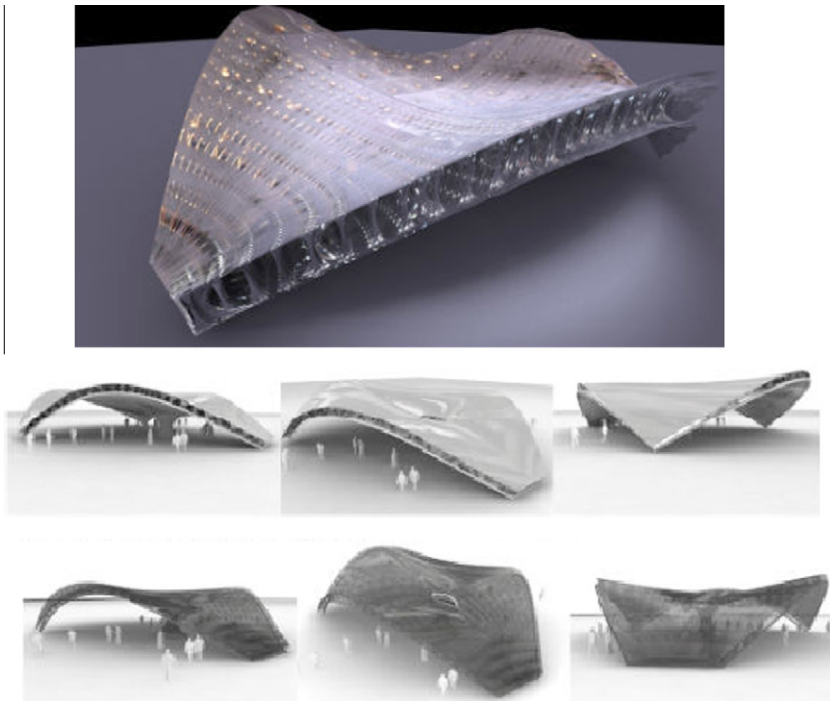


Fig. 192. Bioinspired architectural shells based on bird skulls. Architect Andreas Harris.

Fig. 194 shows the boxfish and a morphological shape, which has provided the design model for the car. It should be noticed that this shape does not optimize the aerodynamics but is a compromise between internal space and aerodynamic stability.

7.6. Bioinspiration: attachment

7.6.1. Gecko foot

The design principle of the gecko foot has given rise to extensive research in the hopes of creating structures that have reusable and effective attachment properties. Arzt and co-workers



Fig. 193. Feather inspired architecture of the Zayed National Museum, Abu Dhabi that is energy saving by drawing cooling air currents through the building.

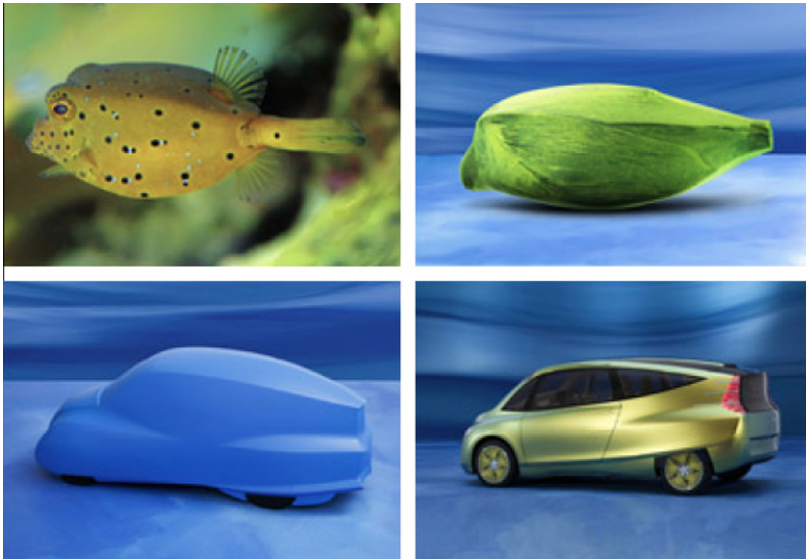


Fig. 194. Bioinspired Mercedes Benz, a class car based on the shape of the boxfish. Taken from <http://www.lukew.com/ff/content/blowfish.jpg>.

[482,484,546,547] have made significant progress in mimicking the structure of the gecko foot by producing polydimethylsiloxane (PDMS) surfaces, patterned with fibrils having different termination shapes, including flat and mushroom, as shown in Fig. 195a. The mushroom shape had a pull-off force approximately 20 times that for surfaces patterned with fibrils having simple semi-spherical cap geometry. For mushroom-shaped fibrils, exceptionally high adhesion strength values, approaching and exceeding that of the natural attachment of the gecko, were found. The sizes of the pillars were also changed and it was found that the pull-off stress increased with the decrease in radius according to $R^{-1/2}$, as shown in Fig. 195b. It should be noted that the Johnson-Kendall-Roberts [486] equation

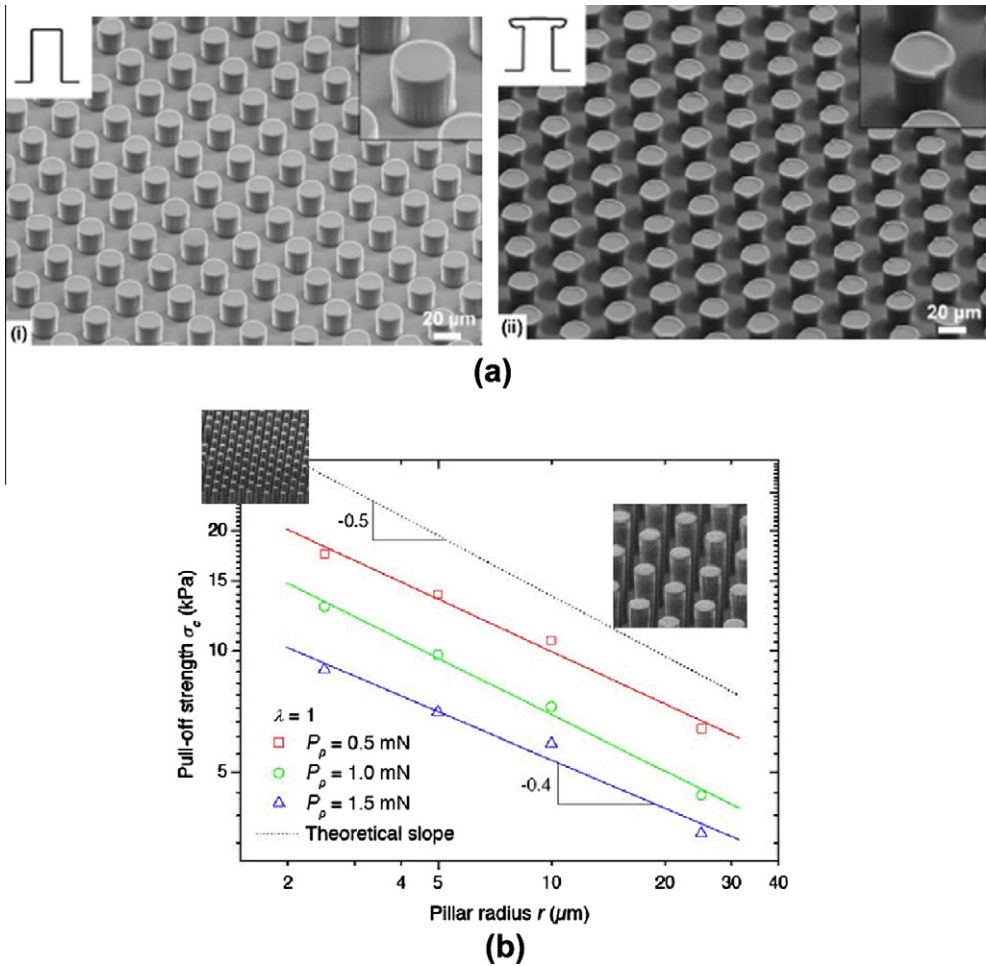


Fig. 195. SEM micrographs showing polydimethylsiloxane (PDMS) micro-pillar arrays with cylindrical and mushroom-like geometries. Pull-off strength increases with decreasing pillar radius. Taken from [484].

(Section 6.1.1, Eq. (6.5)) predicts a stress proportional to R^{-1} for semi-spherical terminations. The dependence on the radius is a function of the shape of the spatula. The dependence obtained experimentally is much closer to R^{-1} [88].

Mahdavi et al. [548] have recently developed a gecko-inspired adhesive for biomedical application. They demonstrated that gecko-inspired arrays of sub-micrometer pillars of PGSA (polyglycerol sebacate acrylate) (Fig. 196) provide attachment under water. This tape is proposed as a biocompatible and biodegradable polymer adhesive to tissue. The adhesion was tested *in vitro* to porcine intestine and *in vivo* to rat abdominal muscle. Carbon nanotube arrays are also being proposed to form fibrillar arrays and have self-cleaning properties due to an extreme hydrophobicity [549]. The effects of angled fibrillar attachments have also been investigated and it was demonstrated to have an important bearing.

7.6.2. Mussel byssal attachment

There have been an increasing number of DOPA-based polymers in recent years, which have been employed in various applications, especially in the biomedical field. These include, among others,

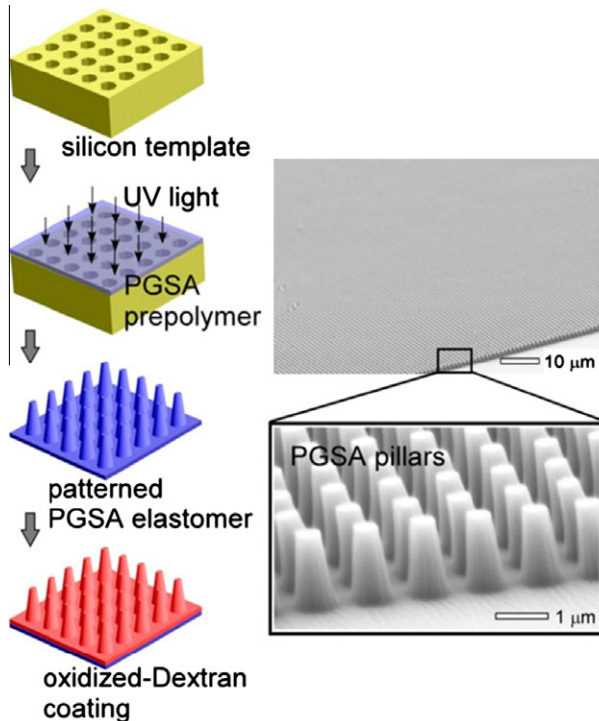


Fig. 196. The fabrication procedure of biodegradable gecko-inspired adhesives. SEM micrographs showing PGSA pillar arrays with tip pillar diameter ~ 500 nm and height ~ 1 μm . Taken from [548].

applications such as non-fouling coating [550], islet transplantation platform [551], orthopedic glues [552,553], electro-less deposition [554], or polymer agents for magnetic imaging agents [555]. Recently, Collaborative launched a product containing DOPA secreted from *Mytilus edulis* under the trade name BD Cell-Tak. This product is used to attach cells or tissue sections to many types of surfaces: glass, metals, and polymers.

Lee et al. [556] further synthesized a reversible wet/dry adhesive inspired by mussels and geckos by coating DOPA-like polymer onto nanofabricated polymer pillar arrays, as shown in Fig. 197. Underwater adhesive strength increased nearly 15-fold when coated with mussel-mimetic polymer. The system maintains its adhesive performance after over a thousand contact cycles in both dry and wet environments. This hybrid adhesive, which combines the design elements of both gecko nanostructure and mussel adhesives, may lead to applications in biomedical, construction, robotics, and marine engineering.

So in fact, far from having limited success, one could argue that DOPA-based chemistry has been a success story of biomimetic research, and this has been triggered by a mechanistic understanding at the biochemical level.

7.7. Bioinspiration: Sensors and optical devices

7.7.1. Structures from diatoms

In the diatom group, there are approximately 100,000 shapes of frustules. Each has a unique structure, with ridges, pores, and features on the order of ~ 100 nm. They are commonly used as filters for water. These cells reproduce several times per day and can be considered as biofactories of three-dimensional structures with nanoscale features. Sandhage et al. [557] developed a method to react

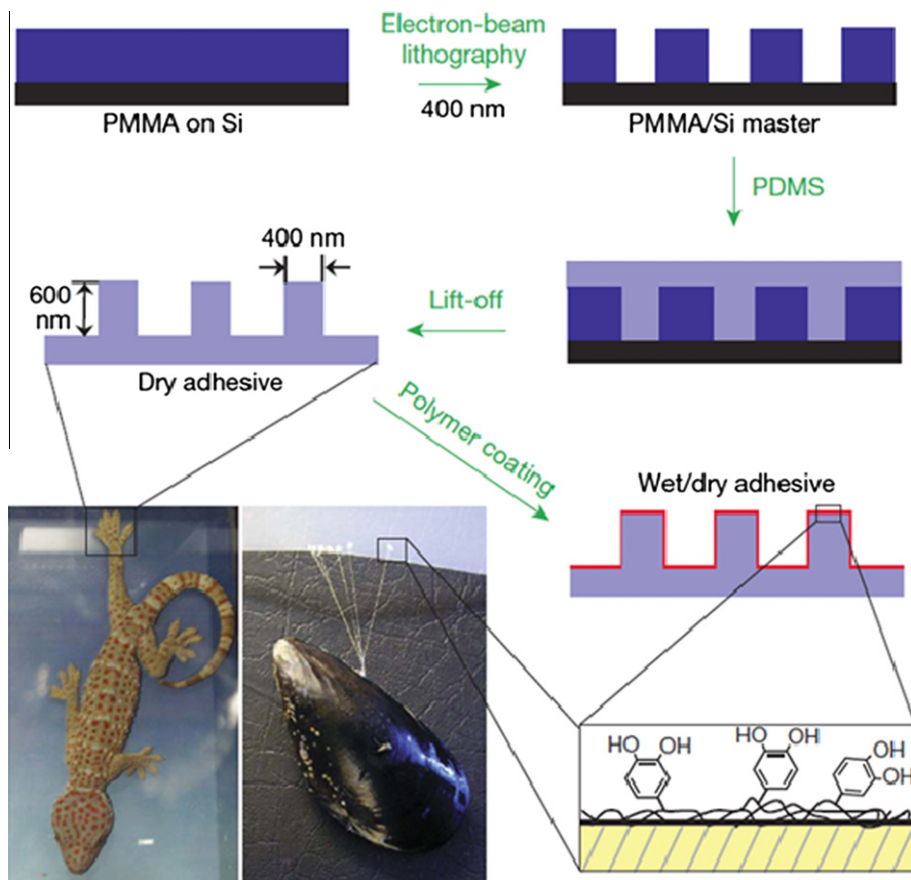


Fig. 197. Design and fabrication of wet/dry hybrid nanoadhesive. Electron-beam lithography was used to create an array of holes in a PMMA thin film supported on Si (PMMA/Si master). PDMS casting onto the master is followed by curing, and lift-off resulted in gecko-foot-mimetic nanopillar arrays. Finally, a mussel adhesive protein-mimetic polymer is coated onto the fabricated nanopillars. The topmost organic layer contains catechols, a key component of wet adhesive proteins found in mussels [556].

the diatoms with metals to displace the Si, creating thereby ceramic structures where the shape and features of the frustules are retained. Here are two reactions used:

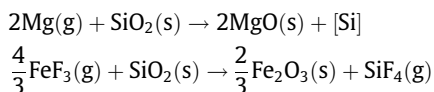


Fig. 198a and b show *Aulacoseira* frustules before and after reaction with Mg(g) for 4 h at 900 °C. Several well-preserved surface features are identified. It can be seen that they are retained by the reaction. There are other possible reactions with Ca, Li, Nb, Sr, Ta, Ti, and Zr. It is envisaged that, in the future, this approach can be used to produce genetically engineered devices such as sensors, optical gratings, catalysts, and actuators.

7.7.2. Structures based on echinoderms

Both the brittle sea star and sea urchin are echinoderms. They are composed of the calcite form of calcium carbonate. There are two unique aspects of these echinoderms that are inspiring researchers.

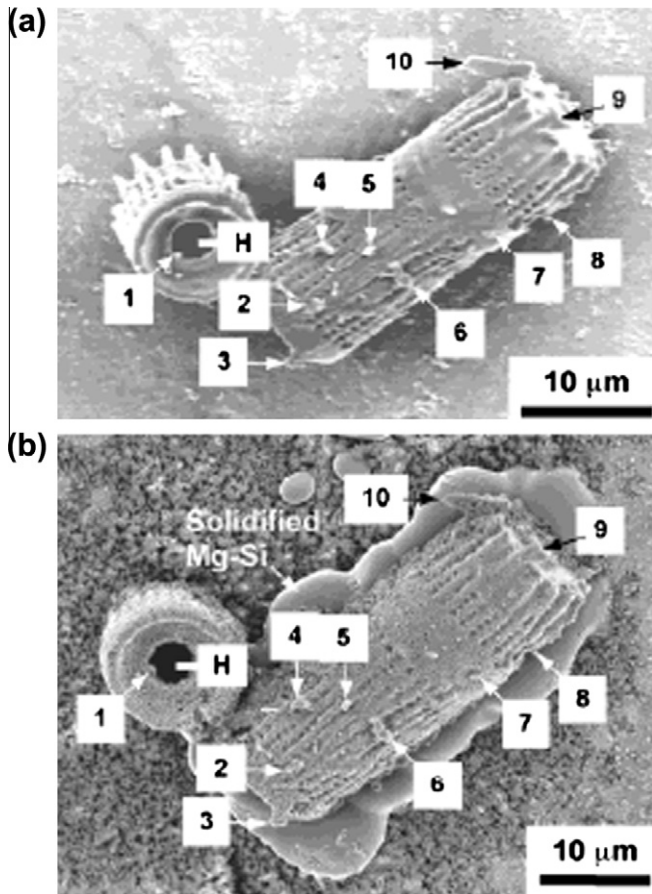


Fig. 198. SEM images of the same diatom frustules: (a) before and (b) after reaction with Mg(g) for 4 h at 900 °C. Ten features that are retained after reaction are marked as well as larger hole (H) and finer pores and ridges on the surfaces of the frustules. Taken from [557].

The brittlestar surface contains protuberances that act as lenses. Fig. 199a shows the wavy surface. The brittle star possesses an internal skeleton of calcite plates and a complex vascular system. It has five arms. The surface is parallel to the rhombohedral *c*-axis. For this orientation there is perfect refraction. These lenses, which have dimensions of ~10–40 μm, are perfectly designed and there is no aberration. The parallel light rays penetrate the surface and converge to the focal point to the lenses, where neural bundles capture the energy. The valleys have holes, whose function is to release the pigment that coats the brittle star during the day, making it black. At night, the brittle star is white. Aizenberg [521] mimicked this structure by combining microlenses and a fluidic network. She used three-beam interference lithography to create synthetic polymeric (non-calcitic) lenses surrounded by a porous network. One such structure is shown in Fig. 199b.

The sea urchin is covered with calcite spines that can pivot around their attachments, as shown in Fig. 200. Under these spines is a network of microflorets that is thought to protect the surface from parasites by continuously moving. One can envisage bioinspired mechanisms to move spines and Aizenberg [521] has created such a device, shown in Fig. 201a. The spines are made of silicon by a photo-etch method and have a diameter of ~200 nm. These nanoscale spines have one extremity embedded in a hydrogel. This hydrogel swells in the presence of water and the swelling causes the spines to stand up. When it shrinks, the spines ‘lay down.’ The actuation time is very small, around

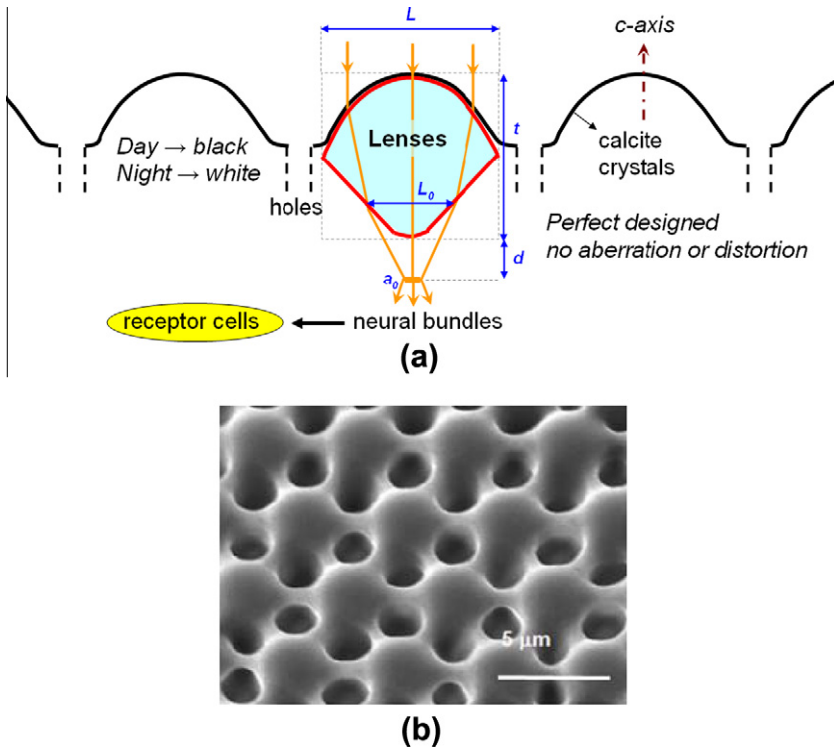


Fig. 199. (a) Surface of brittle star surface showing lenses and holes through which pigment is released; (b) bioinspired structure with protuberances and holes. Taken from [521].

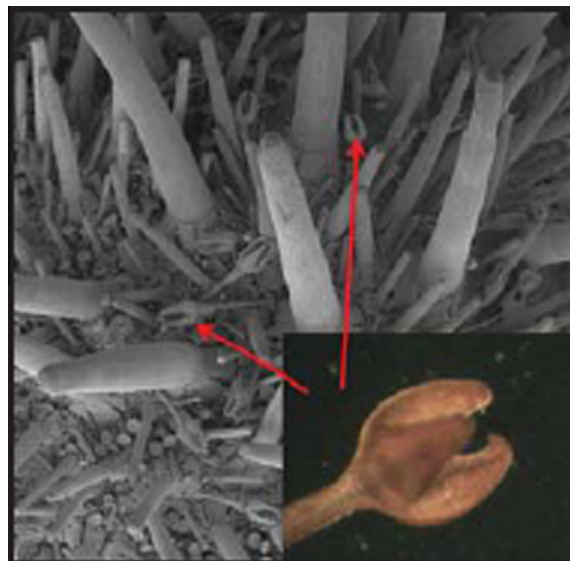


Fig. 200. Sea urchin surface consisting of spines and microflorets (pedicellariae); note larger spines. Taken from [521].

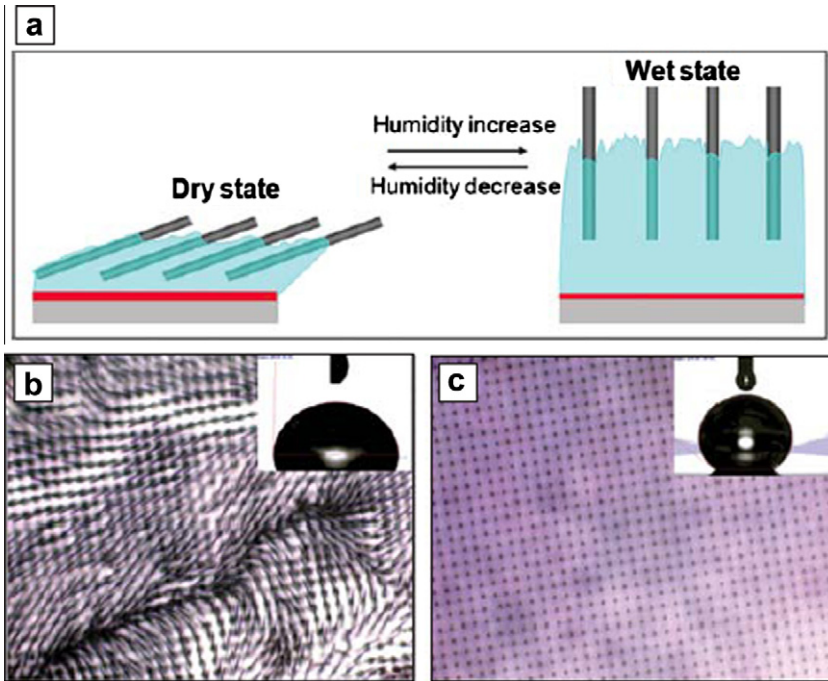


Fig. 201. (a) Schematic showing how nanospines can move in controlled and predictable manner when embedded in a hydrogel that swells in the presence of water: (b) hydrophobic surface created when hydrogel is dry; (c) hydrophilic surface created when surface is wet. Taken from [521].

60 ms. The surface with the spines upright is hydrophobic, i.e., water droplets do not ‘stick’ to it (Fig. 201b). When the spines are down, the surface is hydrophilic (Fig. 201c). Aizenberg [521] suggested that this and similar structures can be used for a variety of actuators.

Another inspiration from echinoderms comes from their mutable dermis, whose stiffness can be increased by an order of magnitude through a mechanism triggered by the nervous system [558,559]. This has been exploited by Capadona et al. [560] who prepared stimuli-responsive polymers using cellulose whiskers reinforcement.

7.7.3. Sonar-enabled cane inspired by bats

It is well established that bats use a sonar-like system in the dark for navigation and to prevent collisions. A similar approach has been used in the design of a cane for visually-impaired people (the Ultracane). It is a regular cane supplemented by an echolocation device. The person receives the information into vibrating buttons in the handle and can establish the location and distance of obstacles.

7.7.4. Butterfly wings

The beautiful, iridescent wings of butterflies have fascinated nature lovers and more recently materials scientists. The genus *Morpho* has over 80 species of butterflies that are found mainly in South and Latin America. The blue color arises from an intricate, periodic nanostructure on the surface of the wing, not from pigmentation. Fig. 202a shows a TEM cross-sectional micrograph of *Morpho* butterfly wing [561]. The dorsal surface has longitudinal ridges (R) that have cross-ribs (cr) that create air pockets. The ridges are $\sim 0.1 \mu\text{m}$ thick and spaced apart by $0.7 \mu\text{m}$, forming a lamellar structure. The ridges combined with the cross-ribs have a structure similar to that of a tree – the cross-rib length increases from the top to the base. Fig. 202b shows a SEM micrograph of a fracture surface of the wing that points out the various micro- and nanostructural features.

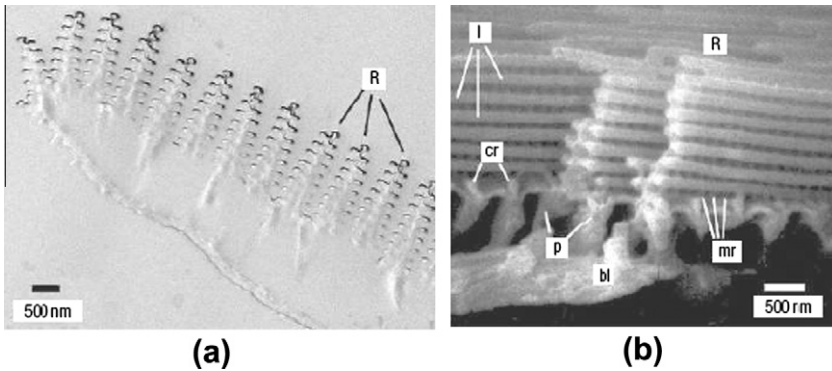


Fig. 202. *Morpho* butterfly wing structure: (a) TEM showing (R) and associated lamellae. (b) longitudinal SEM view of fractured surface showing the ridges (R), lamellae (l) and microribs (mr), pillars (p) and cross-ribs (cr). Taken from [561].

The surface morphology of the wings has been investigated for chemical sensing properties and for use as templates for photonic crystal growth due to their large surface area. General Electric is developing sensors based on the *Morpho* butterfly wing. Fig. 203a shows a schematic diagram of the wing scales. The wings were exposed to various chemicals with different concentrations and the differential reflectance spectra were obtained. In Fig. 203b, the spectral response to water, methanol and ethanol vapors were obtained, indicating that this structural morphology is very sensitive to chemical species. Several groups have attempted to mimic the structure of butterfly wings. Fig. 204 shows the structure produced by focused-ion beam etching combined with chemical vapor deposition [562,563] and Fig. 205 shows a ZnO network structure produced by dip coating *Ideopsis similis* butterfly wings in an aqueous precursor solution [564]. Other methods include alternate TiO₂ and SiO₂ (different indices of refraction) thin films from electron beam deposition [565]. Al₂O₃ nanostructures were fabricated by coating wings through a low temperature atomic layer deposition (ALD). Changing the thickness resulted in changing the reflection spectrum and thus the color observed [566]. Al₂O₃/TiO₂ multilayers on polymer films were also produced by ALD that had monodispersed micron-sized pores formed from a templated assembly [567]. This resulted in reflections of blue and yellow light that, when mixed, produced the green color observed on the wing of the *Papilio palinurus* butterfly. The color mixing effect was also found by Kolle et al. [568] who combined layer deposition methods (colloidal self-assembly, sputtering and ALD) that created photonic structures that mimicked the color mixing effect found on the wings of the *Papilio blumei*. Kustandi et al. [569] used nanoimprint lithography and shear patterning to stamp out tilted, multilayered nanostructures on a polymer film. The nanostructural features are shown in Fig. 206a–c at different magnifications, demonstrating that this more cost-effective approach can replicate the wing nanostructure. The periodic ridge structure creates a diffraction grating while the multilayers create interference and scattering. This results in tunable reflectance properties, as shown in Fig. 206d–f.

The reflective properties of the wings has been used for Qualcomm's mirasol[®] display, a MEMS based technology is using the reflective properties of materials, similar to butterfly wings. The display is a low power, sunlight readable device.

7.8. Bioinspiration: medical applications

7.8.1. Bioglass

Bioglass was developed by Hench and co-workers [570,571] during the Vietnam War as a result of the need to replace parts of bone destroyed in combat. This special glass was designed by adding CaO and P₂O₅ to SiO₂ to better simulate the composition of hydroxyapatite. Wide ranges of bioglass compositions are currently available, and their compositions depend on the function. Some of them bond to soft tissue and bone, some to bone, and some (with more than 65 mol.% SiO₂) do not bond at all and

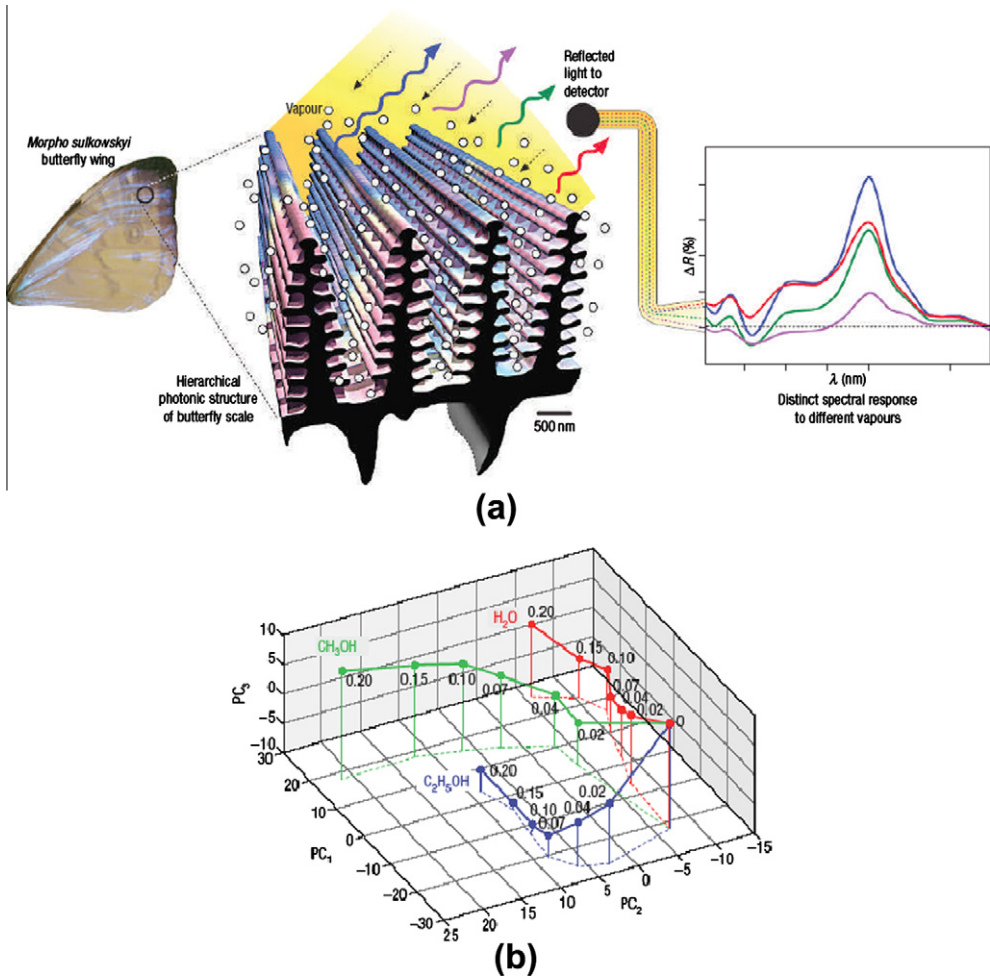


Fig. 203. (a) Highly selective vapor response based on hierarchical photonic structure of the wings of the *Morpho sulkovskiy* butterfly. Differential reflectance spectra was used to measure the response to different vapors and concentration of vapors. (b) Spectral response of water, methanol and ethanol vapors using principal components (PCs) analysis of reflectivity spectra. Numbers represent partial pressures. Taken from [561].

get encapsulated by fibrous tissue. Bioglass 45S5, one of the most important bioglasses, has 45 mol.% SiO_2 and has a $\text{CaO}/\text{P}_2\text{O}_5$ ratio of 5/1. Its Young's modulus is 30–35 GPa, close to that of cortical bone (~ 20 GPa). The flexural strength is 40–60 MPa, is quite low and therefore it is not a good structural material.

7.8.2. Tissue engineering scaffolds

One of the most active research areas in biomedical sciences is tissue scaffold engineering. Biological structures can be envisaged as comprised of cells and extracellular matrix (ECM). These scaffolds are, for the most part, porous. These scaffolds provide the environment that mimics the body's extracellular matrix and enable cells to attach themselves, multiply, differentiate, and exercise their functions. One of the important functions is to generate the extracellular matrix. The porosity must be sufficiently high to enable the cells to migrate. The scaffold must also be biodegradable, i.e., it must dissolve in the body when its function is gone. This process must occur at a prescribed rate to allow

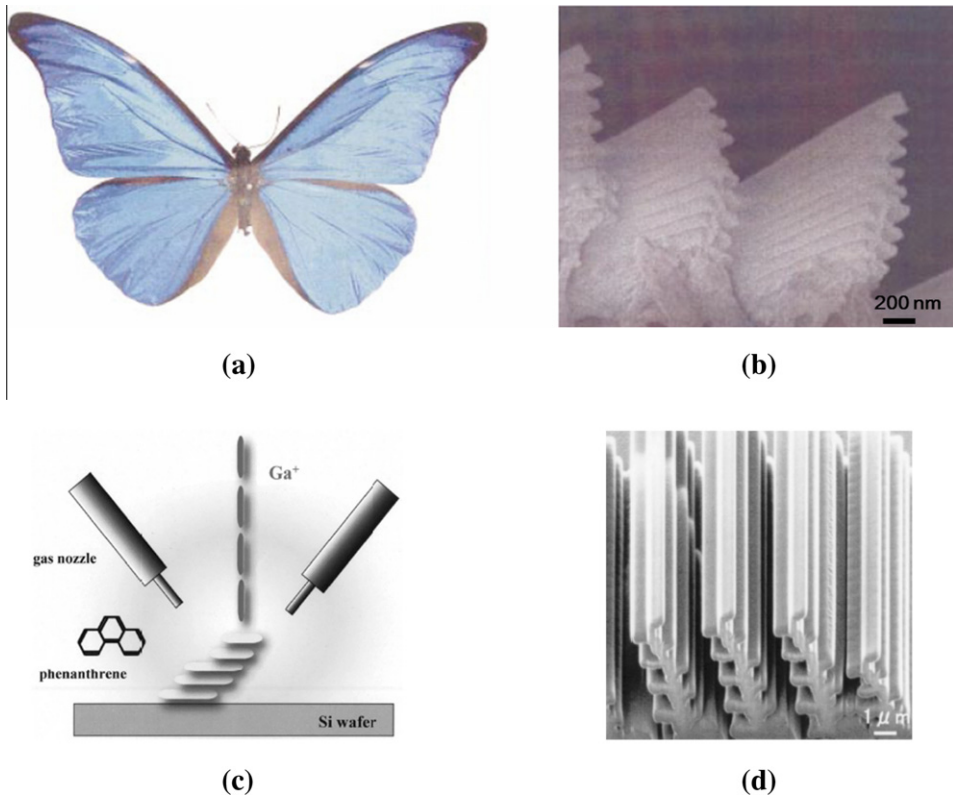


Fig. 204. (a) Optical micrograph of the *Morpho* butterfly wing. (b) Cross-sectional SEM image of the wing scales. (c) Schematic diagram of the FIB-CVD process to fabricate biomimetic wing scales. (d) Inclined SEM micrograph of the nanostructure. Taken from [563].

the new ECM generated by the cells to take on the mechanical functions. Typical values of pore sizes are: skin = 20–125 μm , bone = 100–500 μm .

A broad range of materials has been investigated for scaffolds. The most important are:

- Denatured native ECM where all cells have been removed.
- Biopolymers: collagen, glycosaminoglycans (GAG), alginate, chitosan, collagen-glycosaminoglycans.
- Synthetic polymers: polyglycolic acid (PGA), polylactic acid (PLA), PLGA.
- Hydrogels: polyethylene glycol (PEG), polyvinyl alcohol (PVA).
- Ceramics: calcium phosphate, hydroxyapatite, tricalcium phosphate (TCP).
- Metals: titanium, tantalum.

A broad variety of fabrication methods are used, including freeze casting, fiber bonding, foaming, and rapid prototyping. For skin scaffolds, collagen-based scaffolds are very successful.

A recent development that has considerable promise and is indeed already commercialized (Orthomimetics) is an osteochondral scaffold that has two sides and regenerates the bone-cartilage interface. It consists of a tape with a thickness of ~ 5 mm. Some of the aspects are described by Pek et al. [572]. This scaffold was developed as a collaborative work involving MIT (L. Gibson), Cambridge U. (W. Bonfield), and the Addenbrooke's Hospital (N. Rushton). One side enables bone growth (type I collagen and mineral) while the other cartilage growth (Type II collagen + glycosaminogly-

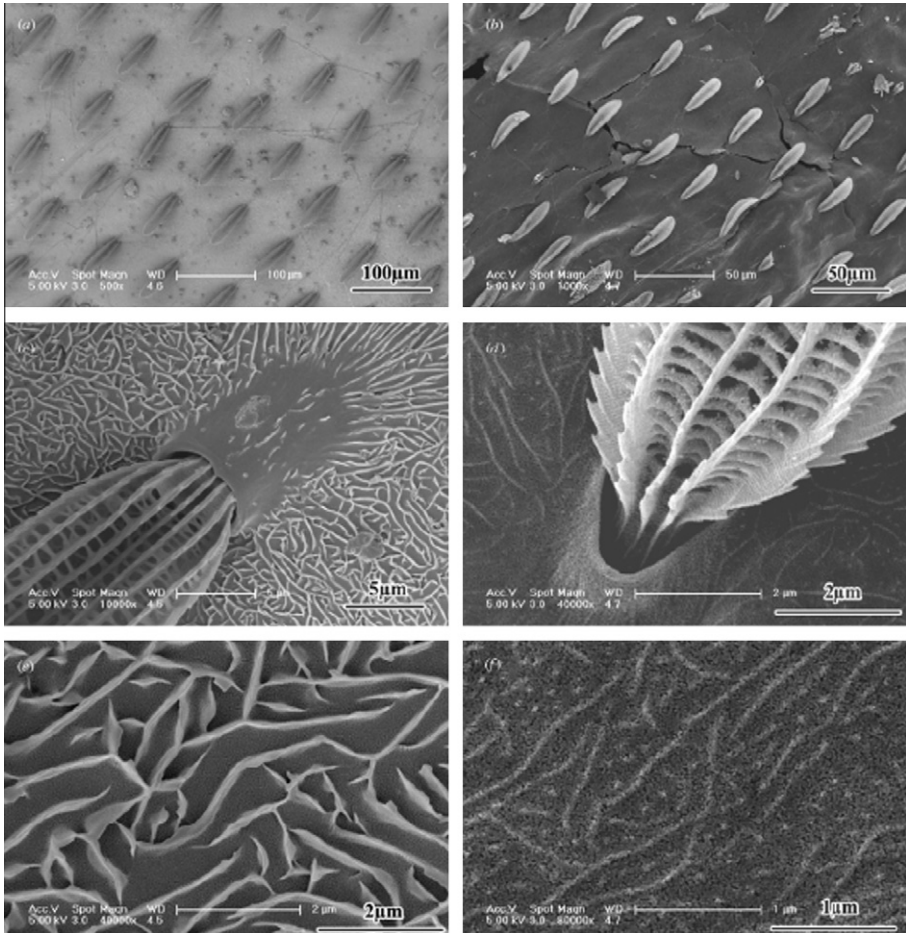


Fig. 205. SEM images of *Ideopsis similis* butterfly wings (left) and ZnO replica (right) at increasing magnification. Taken from [564].

cans-GAG). The chondrocytes penetrate the cartilage side whereas osteoblasts and osteoclasts penetrate the other side.

7.8.3. Vesicles for drug delivery

The cell boundaries are made of a lipid membrane forming a bilayer. This lipid membrane has one side that is hydrophobic and the other that is hydrophilic. The lipid bilayer is formed by the connection between the hydrophobic sides of the lipid membranes, as shown in Fig. 207. In the march toward creating life by synthetic means, the formation of vesicles, that are effectively ‘empty’ cells, has already been accomplished. They are called liposomes. Novel uses for these vesicles are being found, and an important one is to deliver drugs to targeted places in the body.

7.8.4. The blue blood of the horseshoe crab

The horseshoe crab (*Limulus polyphemus*) is a living fossil existing for over 200 million years; it has been reviewed by Walls et al. [573]. Unlike common crabs, its shell is not mineralized [24]. Its blood is not red, but blue, by virtue of copper ions, and not iron ions, that are associated with the metalloprotein in the blood cells in most animals. It lives in shallow waters infested with microbes.

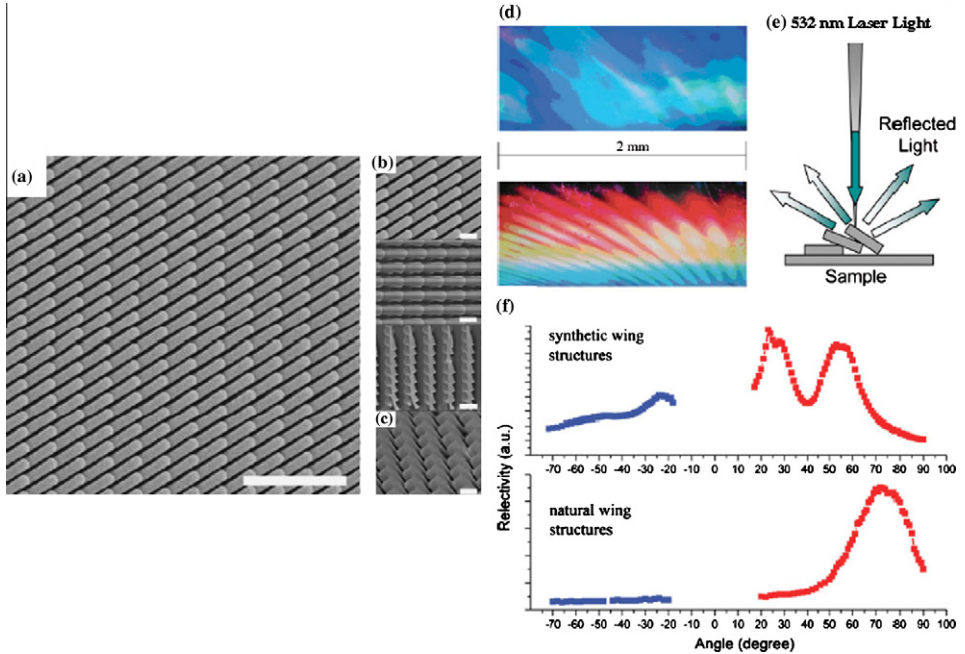


Fig. 206. Synthetic butterfly wing nanostructures produced by nanoimprint lithography and shear patterning. (a) Stacked polycarbonate nanostructures oriented by a horizontal force during the demolding process. Scale bar: 1 mm. (b) Higher magnification SEM images of the overlapping nanostructures (top view). Scale bar: 200 nm. (c) Cross sectional view of tilted multilayered structures comprising 50-nm-thick air gaps. Scale bar: 200 nm. Tunable iridescent effects of synthetic butterfly wing nanostructures. (d) Strong single and rainbow-type color patterns when the incident collimated white light beam is turned 360° around the vertical axis. (e) Schematic diagram of the measurement system to obtain a reflectivity spectrum of the natural and synthetic butterfly wings. (f) Reflection intensity distribution vs. angle along the ridge direction. Taken from [569].

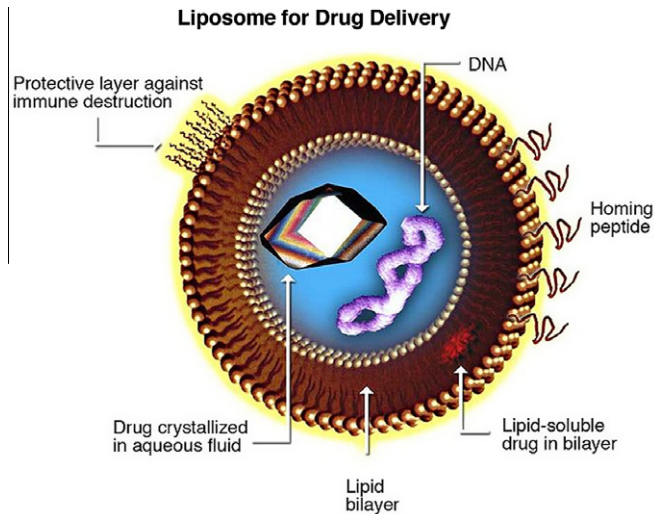


Fig. 207. Biologically-inspired vesicle (liposome) consisting of lipid bilayer for drug or DNA delivery; peptides are designed to hone in on targeted sites where drug/DNA is released. Taken from Wikipedia, Liposomes.

Not having an immune system like the one of mammals, producing antibodies that ‘attack’ invading bacteria that can cause disease (pathogens), it uses another system. This was discovered by Dr. Frederick Bang, when he injected marine bacteria into the horseshoe crab blood stream. The blood clotted extensively. The clotting source in the blood stream was identified as the amebocytes. This component was isolated by a lisate process and it is widely used currently for testing injectable drugs. If they contain bacteria or their toxins, the clotting reaction takes place. The product is called LAL (Lymulus Amebocyte Lisate). If an injectable drug contains bacteria, they can reproduce in the blood, leading to sepsis and finally, to death. Thus, this product is of great importance. The blue blood is extracted after the horseshoe crab is fished in shallow waters of the Cape Cod area; the animals are subsequently released without harm and their system replenishes the blood supply.

7.9. Other interesting bioinspired applications

7.9.1. Shark skin

The skin of shark has some unique characteristics: its surface is optimized for minimizing resistance to flow and it is singularly devoid of parasites and bacteria. Fig. 208a shows the shape of the skin, with micrometer-sized ridges. These ridges serve prevent the creation of eddies in the boundary layer thereby reducing drag. The skin has served as inspiration for the famous swimsuits that have caused havoc in the Olympic races. Speedo claims that its Fastkin FSII swimsuit can reduce friction in water by up to 4%. Additionally, the diamond-shaped bumps have an important role in keeping colonies of microbes from forming. The US Navy was interested in finding antifouling paints for submarine hulls to reduce algae coating the surfaces. This resulted in the development of Sharklet[®], a film that replicates the shark skin ridges. Fig. 208b shows a synthetic surface inspired by the shark skin. It has proven effective in reducing algae settlement by 85% and preventing the formation of *Escherichia coli* and *Staphylococcus A* colonies in a hospital. Bacteria attach singly or in small groups to establish large colonies. The Sharklet[®] surface keeps these films from forming because the patterned surface produces an energy barrier for colony formation.

7.9.2. Genetically derived materials

Resilin is a unique elastomer that exhibits extremely long fatigue life and high resilience. It is exclusively found in the wings of insects; thus it is impractical to try to harvest a sufficient quantity to employ as an engineering material. Researchers have isolated the genome for resilin and have inserted it into *E. coli* to proliferate [130]. Fig. 209a shows the conformation of both natural and synthetic resilin. The high elasticity of synthetic resilin is demonstrated by the ability to be tied into a knot with a small diameter (Fig. 209b); the synthetic resilin is similar to the natural elastomer. Fig. 209c shows normalized resilience of two common rubbers and artificial resilin. Although there

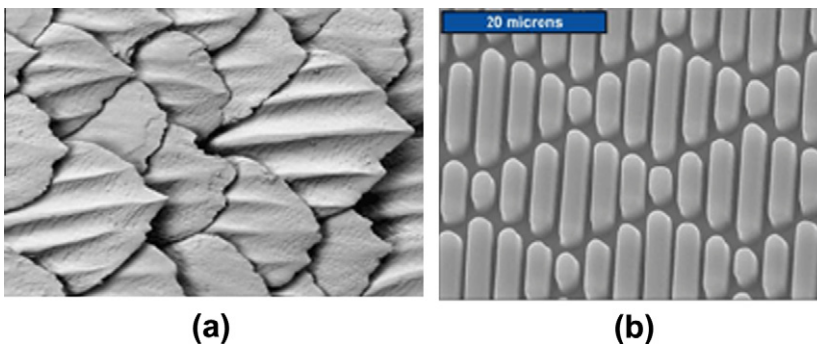


Fig. 208. (a) Microscopic morphology of shark skin and (b) Sharklet[®] Technologies surface for use in hospitals Taken from the Biomimicry Institute.

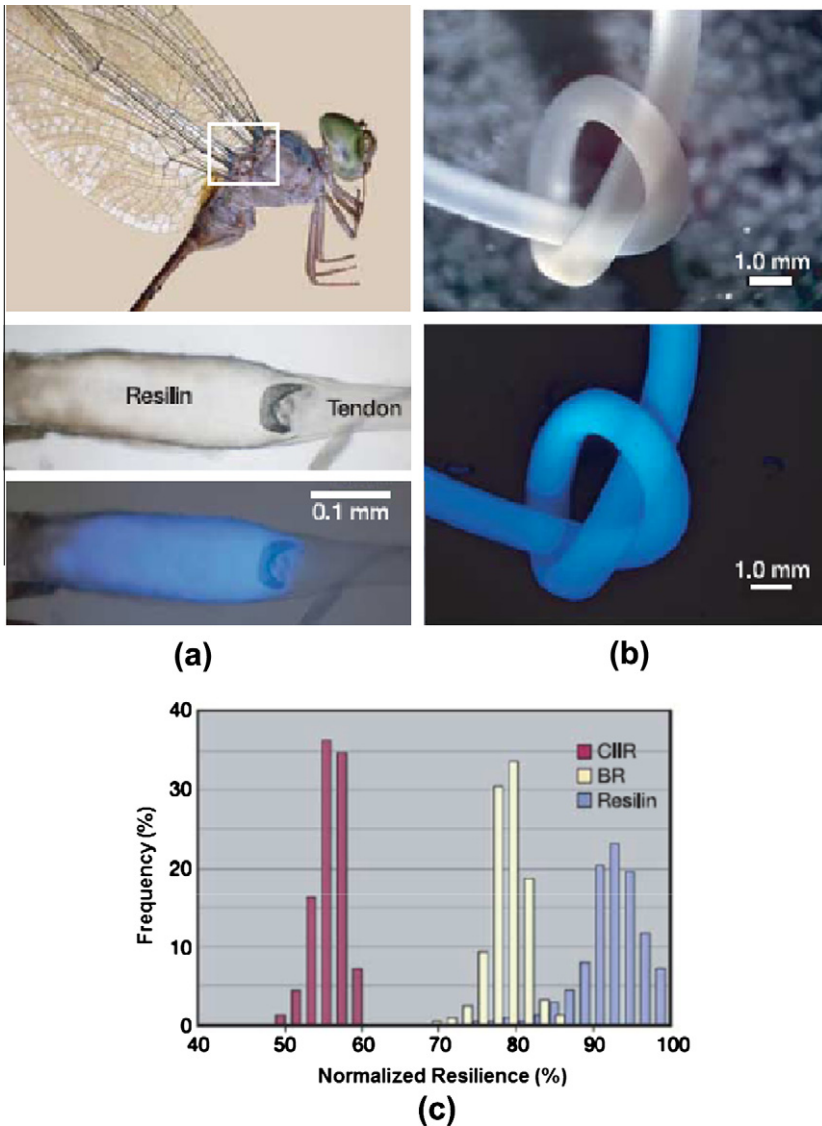


Fig. 209. Genomic DNA from the fruit fly, *Drosophila melanogaster* was used as a template for PCR and inserted into *E. coli* for growth. (a) The resilin tendon extracted from the wing and under ambient and ultraviolet light. (b) Synthetic resilin under ambient and ultraviolet light. (c) Resilience of the two common rubbers (chlorobutyl rubber, red and polybutadiene rubber, white) and artificial resilin (blue). Adapted from [129].

is significant variation from specimen to specimen, the resilience of resilin is higher than that of chlorobutyl and polybutadiene.

Silk, given its high strength-to-weight ratio, has attracted considerable attention because of the interest in synthesizing by recombinant techniques [574,575]. In one interesting example, genetically-modified goats were employed to produce silks from the goat milk. This has drawn much media attention, given the eccentric way of synthesizing it. Mammalian cells have also been employed successfully to produce silks through recombinant technology [576].

Lithium-ion batteries are an important component in the electric car as well as in numerous applications in consumer electronics and aerospace. In a lithium-ion battery, lithium ions flow between a negatively charged anode, usually graphite, and the positively charged cathode, usually cobalt oxide or lithium iron phosphate. It was demonstrated by Belcher and coworkers that viruses can be engineered to build both the negatively [577] and positively [578] charged ends of a lithium-ion battery. The new virus-produced batteries have the same energy capacity and power performance as state-of-the-art rechargeable batteries being considered to power plug-in hybrid cars, and they could also be used to power a range of personal electronic devices. The new batteries can potentially be manufactured with a cheap and environmentally benign process, inspired on nature.

Fig. 210 shows how M13 virus can assemble nanowires that are incorporated into the negative electrode (anode) materials. Materials-specific peptides identified by biopanning (phage display) were

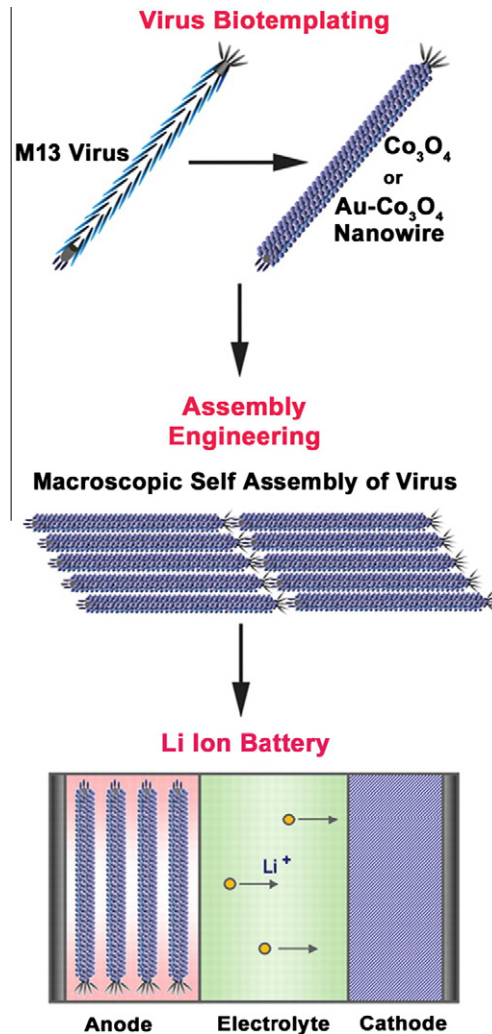


Fig. 210. M13 virus-enabled synthesis and assembly of nanowires as negative electrode materials for Li ion batteries. Materials-specific peptides identified by biopanning (phage display) were expressed on the major coat p8 proteins of viruses to grow Co_3O_4 and $\text{Au-Co}_3\text{O}_4$ nanowires. Macroscopic ordering of the engineered viruses was used to fabricate an assembled monolayer of Co_3O_4 nanowires for flexible, lightweight Li ion batteries. Taken from [577].

expressed on the major coat p8 proteins of viruses to grow Co_3O_4 and $\text{Au-Co}_3\text{O}_4$ nanowires. Macroscopic ordering of the engineered viruses was used to fabricate an assembled monolayer of Co_3O_4 nanowires. This can facilitate the manufacture of flexible, lightweight Li ion batteries.

Further development was reached when it was demonstrated that viruses recognize and bind specifically to carbon nanotubes. Fig. 211 shows dramatically how a M13 virus can grab a single wall carbon nanotube. In this case, each iron phosphate nanowire can be electrically “wired” to conducting carbon nanotube networks. Electrons can travel along the carbon nanotube networks, percolating throughout the electrodes to the iron phosphate and transferring energy in a very short time. By incorporating carbon nanotubes, these arrays can be added to the cathode. This increases the cathode’s conductivity without adding too much weight to the battery. In lab tests, batteries with the new cathode material could be charged and discharged at least 100 times without losing any capacitance. That is fewer charge cycles than currently available lithium-ion batteries, but the Belcher group expects them to be able to go much longer. Fig. 212 shows this design and assembly [578]. The prototype is packaged as a typical coin cell battery, but the technology allows for the assembly of very lightweight, flexible and conformable batteries that can take the shape of their container.

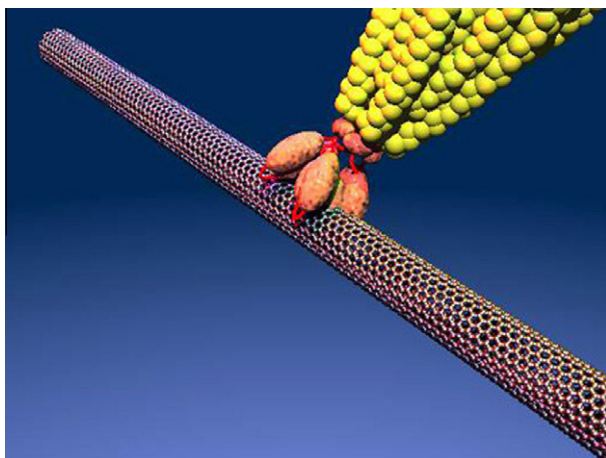


Fig. 211. M13 virus ‘grabbing a single wall a carbon nanotube. Source: <http://news.sciencemag.org/sciencenow/2009/04/03-01.html>.

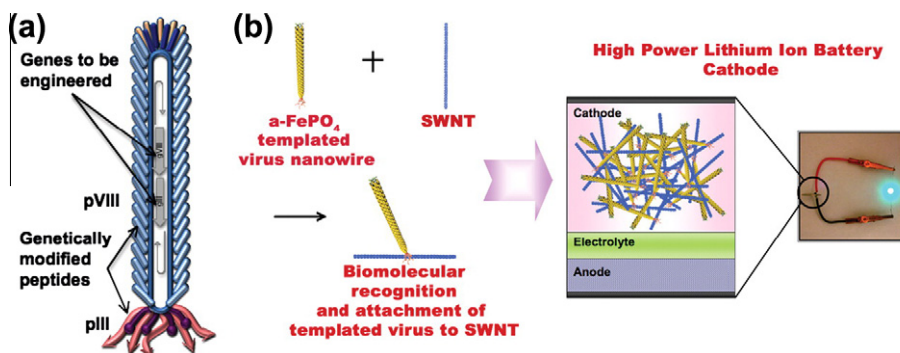


Fig. 212. M13 virus with peptides which attach to nanocrystalline $\alpha\text{-FePO}_4$, and the gene III protein (pIII) that is engineered to have a binding affinity for Single Wall Nano-Tubes (SWNTs); this leads to lithium ion battery cathode that has nanostructure and therefore enables greater current density. Taken from [578].

7.9.3. Origami structures

The leaves in the chestnut tree in the spring come out of the cocoon and unfold in a wonderful manner. Similarly, the wings of beetles unfold as their carapace (elytron) is lifted. These wings fold back when the beetle returns to its ambulatory configuration. This process of folding and unfolding of leaves is known as Ha-ori in Japanese and has inspired researchers. Biruta Kriesling was inspired by the chestnut trees in Paris and teamed up with Koryo Miura. This has led to the development of deployable solar panels in space vehicles based on Miura's origami pattern. The collapse of cans enabled by a pattern of pseudo cylindrical concave polyhedrons is well known in Japan. These cans are commercially used and fold easily after opened in an accordion-like fashion.

7.10. Bioinspiration from the molecular level: the bottom-up approach

Biological structures have molecular recognition. This molecular recognition enables them to self assemble, which leads to templating of atomic and molecular assemblages. This is the principle of the bottom-top approach, in contrast with many synthetic processes that use a top-bottom approach. The simplest example is how DNA strands will pair and form a double helix. Some of the concepts were discussed earlier [21] and are expanded here with emphasis on recent developments.

As illustrations, two examples from Seeman and Belcher [579] are described. Synthetic molecules with 'sticky ends' can be designed to build motifs in 1, 2, or 3 dimensions. A junction of four molecules with 'sticky ends' is shown in Fig. 213a. These 'sticky ends' will, on their turn, attach to each other, forming the regular pattern shown in the right-hand side of Fig. 213a. These arrays can serve as:

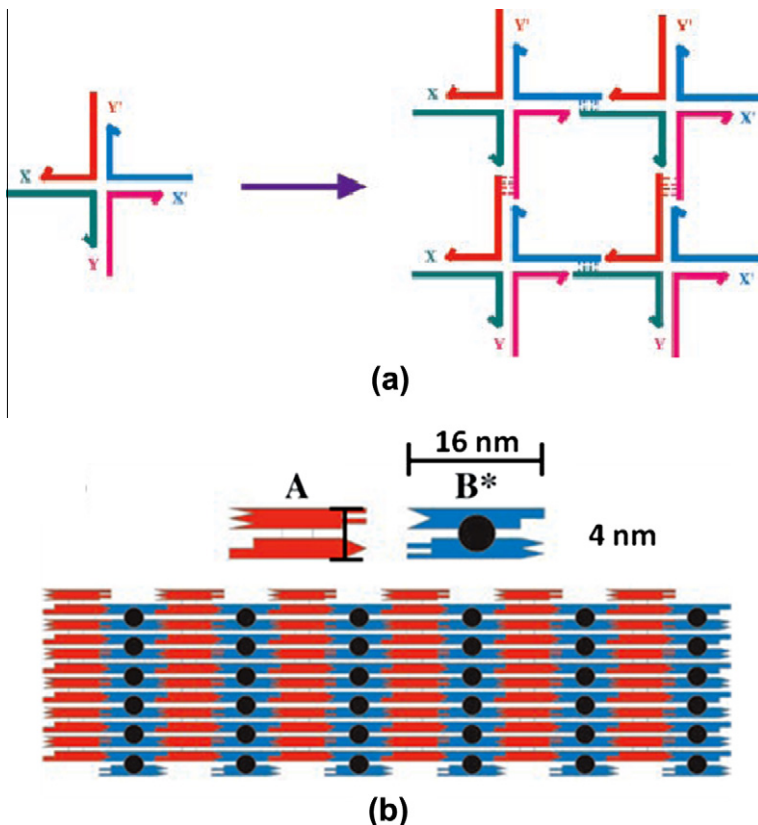


Fig. 213. (a) DNA pairs with 'sticky ends' forming a regular two-dimensional pattern; (b) more complex patterns of DNA. Taken from [579].

- Scaffold to crystallize biological macromolecules.
- Organization of compounds in nanoelectronics.
- Quantum dots (bioinspired nanocomponent chips).

A slightly more complex system is shown in Fig. 213b. Two DX (double crossover) DNA molecules are shown. The two helices are represented as rectangles. The complementary sticky ends are represented as shapes that fit into each other. A and B* are not identical. The repeat unit in the assembly is 32 nm, twice the width of each DX molecule. They build a two dimensional array that has been demonstrated to construct calculators. It was envisaged [579] that these DNA systems, created by self-assembly, can be used in combination with inorganic nanoparticles such as carbon nanotubes, to generate different functionalities.

7.10.1. Phage display

The process of mimicking nature can also be pursued through the use of viruses. Viruses do not have their own reproductive systems and are therefore the most primitive form of life. They inject their DNA into cells or bacteria and use their reproductive machinery that takes charge of carrying out viral replication. They can enter cells in a number of ways. Bacterial viruses, also known as bacteriophages or, in short, phages. The dimensions of a T4 phage are approximately 70 nm diameter and 200 nm length (including tail). The head is an icosahedron consisting of 20 equilateral triangles. It resembles a Mars Lander and enters the *E. coli* bacterium through an ingenious process of contraction of the tail sheath which forces the tail core to penetrate the *E. coli* wall prior to injecting the DNA [21]. Phages are commonly used in biochemistry and pharmaceutical fields since the momentous discovery of a new technique [580] for the study of protein–protein, protein–peptide, and protein–DNA interactions. Phages infect bacteria but are harmless to humans.

Common types of phages used are M13, T4, T7 and λ . Smith demonstrated in 1985 [580] the display of peptides on a filamentous phage by fusing the peptide of interest onto the gene of filamentous phage. In phage display technology, a variety of peptides, small antibodies, or proteins can be obtained from a large library and we select from them the variants, which attach to a phage.

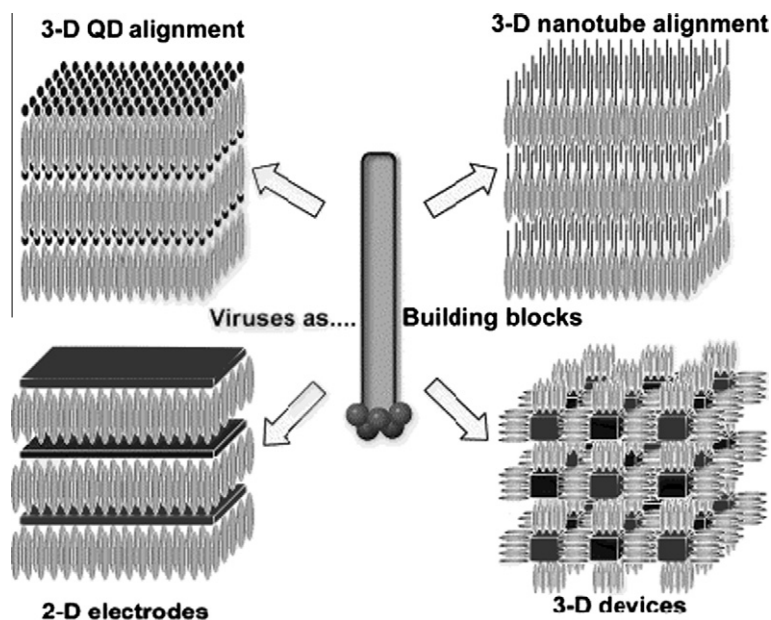


Fig. 214. Self-assembled structures using one-dimensional viruses with zero-dimensional quantum dots (top left), one dimensional nanowires/nanotubes (top right), two dimensional plate-shaped devices (bottom left) and three-dimensional components (bottom right). Taken from [581].

The technique has many variants, but in principle we start with a large library of proteins or DNA. Some of them will bind to the phages. The ones that do not bind are removed by washing. Those that remain are eluted. The repeated cycling is called ‘panning’ from the mining method of gold panning. Thus, the eluted phages can be injected into bacteria, which reproduces them.

Sarikaya et al. [582] and Tamerler and Sarikaya [583,584] used phage display methodology for obtaining genetically engineered polypeptides for inorganics. They were able to select specific peptides that adhered to desired surfaces. By this manner, they developed a procedure to assemble nanostructures from the bottom up.

Viruses can also be used directly as building blocks for nanostructures assembled from the bottom, as demonstrated by Flynn et al. [581]. The ability of phages to bind to nanoparticles (quantum dots), single wall carbon nanotubes, and tridimensional components was used to create structures illustrated in Fig. 214. These arrays have a number of potential applications, such as nanowires, semiconductors, and magnetic materials.

8. Conclusions and perspectives

Given below are some broad conclusions, which show the principal attributes of the emerging field of biological and bioinspired materials in Materials Science and Engineering. Researchers from around the world are making rapid progress in the understanding of the structure–property relations in biological materials, from the nanoscale to the structural level. The connections between the different hierarchical levels and the assembly processes used by organisms to develop their structures are being investigated using the powerful analytical, experimental, and computational tools that have been the hallmark of Materials Science and Engineering. We illustrated a number of essential concepts with the results of our research and important recent discoveries. Thus, this overview is limited in scope and only captures a small fraction of the work being carried out. It complements the broad overview in this journal by our group [21] and expands on it, focusing on the following functional aspects of biological materials:

- Fracture and impact resistance;
- Defense and armor;
- Cutting edges;
- Aero/fluid dynamics;
- Attachment.

In this review, we restrict ourselves to the extracellular matrix (ECM), which has the primary importance in determining the mechanical performance of the biological systems. Cells (immensely complex) are embedded in the ECM and perform functions that are essential for life. We purposely stay away from them and restrict ourself to the components of biological systems akin to synthetic materials. This review examines biological materials for their primary functional purpose, although many are multifunctional. An extremely important aspect that should always be emphasized is that hydration is important and is often overlooked.

Biological materials fall, for the most part, into the following: biopolymers and polymer composites, biological ceramics and ceramic-based composites, and cellular biological materials (foams). Ceramics are characterized by high compressive strength and low resistance to crack propagation. Biopolymers, primarily in the form of fibrils, that organize themselves hierarchically, have excellent tensile properties but poor compressive resistance. Thus, many ceramic composites exploit the advantages of these two classes of materials in a synergetic manner. In this fashion, biological materials have characteristics that can be broadly summarized as:

- Many biopolymers have J-shaped stress strain curves (especially, collagen-based) characterized by an increase in slope with increasing strain ($d^2\sigma/d\varepsilon^2 > 0$; $d^2\sigma/d\lambda^2 > 0$). The maximum strain depends on the initial configuration of the fibers. If they are aligned, it is smaller; if they are curved and loosely arranged, it is larger. The J shape decreases the amount of energy needed for elongation, compared to a Hookean solid, if one compares a final state with the same stress and strain for both.

- Biopolymers undergoing phase transitions exhibit an inflection in the stress strain curves ($d^2\sigma/d\varepsilon^2 = 0$; $d^2\sigma/d\lambda^2 = 0$), that have been observed for egg whelk [180], spider dragline [6], Merino wool [181,182], and hagfish thread [183]. The phase change produces a decrease in the slope of tensile stress–strain curve which is similar to the shape-memory effect in metallic alloys. The product phase, creating an extension, decreases the stored elastic energy of the sample, resulting in a decrease in the rate of loading. The α -coiled-coils to β -sheets transition is known to occur in egg whelk and wool.
- Collagen and keratin have some similarities – twisted helical molecules resulting in strong fibrous elements, with a comparable elastic modulus. They are the basic building blocks for most of the structural biological systems (except cellulose and lignin in plants and chitin in arthropods). The importance of collagen as a structural component (not its strength) has led Fung [19] to call it ‘the steel of biological materials.’
- Keratin differs from collagen in that keratin is grown from epidermal cells and always extracellular. In keratin the crystalline fibers (intermediate filaments, IFs) are embedded in an amorphous matrix. Keratin is a composite of short polymer fiber (crystalline IFs) reinforced elastomer (highly cross-linked amorphous protein).
- The effect of hydration is an important consideration in the mechanical response of biological materials. Water acts as a plasticizer; elastic modulus and strength commonly decrease while strain-to-failure and toughness increase with increasing water content.
- Dermal armor is a defense strategy for many species, whether on land or in water. However, there are a weight and flexibility penalties and mobility is restricted. Depending on animal, armor can be flexible or rigid. Birds, for which weight reduction is of primary import, are virtually devoid of armor. In some fishes, there is a graded structure in the scales, with highly a mineralized layer covering a lamellar and cross-plyed collagenous foundation. Other fish species have bony scales covered by ganoine, which has a hardness comparable with enamel. In shells, the protection layer is calcium carbonate which organizes itself, with the addition of organic macromolecules, into a number of different structures that provide toughness much beyond that of the monolithic mineral. Arthropods have exoskeletons consisting of chitin (land species) and chitin with mineral additions (aquatic species).
- Fracture resistance is highly dependent on the presence of interfaces, which deflect and stop cracks from propagation and causing catastrophic failure.
- In bones, teeth, and antlers, intrinsic and extrinsic toughening mechanisms equally important; R -curve fracture toughness values are more realistic than single value K_{IC} . This is due to the formation of a process zone during the opening of the crack which shields the tip from the high stresses and effectively increases the toughness from its original value. Age plays an important and degrades this capability.
- For flexure and torsion resistance, a compact outer sheath and a more porous, compliant core are optimal (horn, bird beak, antler, bone, plant stems).
- The cutting efficiency of biological materials depends on morphology and scale-microscopic sharp edges. Biological materials (even the hardest ones, such as enamel) are much less tough and hard than metals and a sharp cutting edge is obtained at much larger enclosed angles ($\sim 30^\circ$) than the cutting edges of knives ($\sim 15^\circ$). For teeth, the cutting ability is in many cases enhanced by the presence of serrations which effectively enhance the local stresses on muscle and dermal fibers of the prey. In insects, the scale is much lower and the stylet of mosquitoes relies on an ingenious serrated edges to penetrate the dermis and epidermis with minimal injury to the nerves.
- The reversible attachment of insects and some reptiles (geckos) depends on van der Waals forces, capillarity or suction forces that are spread out over millions of setae. van der Waals forces are the most important for terrestrial animals (e.g. gecko) – capillarity and suction are more important for marine animals (e.g. abalone). In order to obtain sufficiently large van der Waals forces, the spatulae have decreasing diameters for increasing animal mass.
- Lightweight structures are important for the flight capability. Birds exemplify design principles (e.g. beaks, feathers, bone structure). Feathers and beaks are sandwich structures where buckling is restrained by a cellular core, but strength and stiffness provided by outer sheath. Bird bones

are designed with internal struts and ribs that impede compressive collapse and improve torsional strength. The hierarchy is such that the stiffness/weight ratio is maximized.

- Bioinspired materials encompass a large and growing area that includes the functional groups discussed here along with sensors and medical applications: One major challenge is the concurrent materials synthesis and structural assembly, a hallmark of biological materials.
- Biomimicking is evolving from purely synthetic processes using design concepts from nature (e.g. VELCRO) to molecular-based processing in which self assembly and other unique natural processes of nature are used. Contemporary methods of biomimicking explore molecular and cellular chemistry.
- Recognizing the limited supply of materials available in biological systems and the narrow range of temperatures in which synthesis and processing takes place, we are using the design principles of nature to amplify their effectiveness. Our current technological capabilities can expand the biological manufacturing principles to a broader range of temperatures, pressures, and compositions, while retaining the essential features.

We foresee continued and expanded activity in the field of biological and bioinspired materials as large numbers of investigators globally explore natural materials and discover new structural designs and concepts. This expansion in our understanding will be (and already is) paralleled by a whole array of novel synthesis and processing methods to produce bioinspired materials and structures which require fundamental inputs from both the Physical and Life Sciences.

Acknowledgements

This research is funded by the US National Science Foundation, Division of Materials Research (Grant 1006931) and the Taiwan National Science Council (NSC 100-2218-E-007-016-MY3). We gratefully acknowledge Prof. Ali Miserez (Nanyang Technological University, Singapore) and Prof. Rizhi Wang (University of British Columbia, Canada) for their insightful and thorough review, which made significant improvement to the manuscript. The members of our groups that contributed to the findings presented here are kindly recognized: Dr. A.Y.M. Lin, Dr. Y. Seki, Dr. W. Yang, Y.-S. Lin, M.I. Lopez, E.E. Novitskaya, M. Porter, V. Sherman, H. Walsh, S.G. Bodde, I.H. Chen, J. Kiang, S. Lee, L. Tombolato. The use of the facilities of CALIT² (SEM) and NCMIR (TEM) at UCSD is of great help. We thank Mr. Gapar Ritterm Kuryake Lodge (Araguaia River) for kindly providing the Arapaimas scales and Mr. Raul Aguiar, La Bellota Ranch, Baja California, for the specimens of vulture bone. The discussions with Prof. Eduard Arzt (INM, Universität des Saarlandes, Germany) and Prof. Robert Ritchie (UC Berkeley) were very helpful. The inspiration and support provided by Prof. Ted Massalski (Carnegie Mellon University), Prof. George Mayer (University of Washington), Prof. Gareth Thomas (UC Berkeley), and Prof. Jenq-Gong Duh (National Tsing Hua University, Taiwan) are deeply appreciated.

References

- [1] Thompson DW. On growth and form. Cambridge: Cambridge University Press; 1917.
- [2] Kessler MR, Sottos NR, White SR. Self-healing structural composite materials. *Composites: Part A* 2003;34:743–53.
- [3] Currey JD. Bones: structure and mechanics. New Jersey: Princeton University Press; 2002.
- [4] Gibson LJ, Ashby MF, Harley BA. Cellular materials in nature and medicine. Cambridge: Cambridge University Press; 2010.
- [5] Reis L, Weiner S, editors. Learning from nature how to design new implantable biomaterials: from biomineralization fundamentals to biomimetic materials and processing routes. NATO science series, vol. 171. Dordrecht: Kluwer Academic Press; 2003.
- [6] Elices M. Structural biological materials: design and structure–property relationships. Oxford: Pergamon; 2000.
- [7] Vincent JFV. Structural biomaterials. Revised ed. New Jersey: Princeton University Press; 1990.
- [8] Brown CH. Structural materials in animals. London: Pitman; 1975.
- [9] Wainwright SA, Biggs WD, Currey JD, Gosline JM. Mechanical design in organisms. Princeton: Princeton University Press; 1982.
- [10] Vincent JFV, Currey JD, editors. The mechanical properties of biological materials, symposia of the society for experimental biology, vol. 34. Cambridge: Cambridge University Press; 1980.
- [11] Yamada H. Strength of biological materials. Evans, FG editor. Baltimore: Williams and Wilkins Company; 1970.
- [12] Ehrlich H. Biological materials of marine origin. New York: Springer; 2010. p. 569.
- [13] Simkiss K, Wilbur KM. Biomineralization: cell biology and mineral deposition. San Diego: Academic Press; 1989.
- [14] Lowenstam HA, Weiner S. On biomineralization. New York: Oxford University Press; 1989.

- [15] Bäuerlein E, editor. *Biom mineralization, from biology to biotechnology and medical application*. Weinheim: Wiley-VCH; 2000.
- [16] Mann S. *Biom mineralization: principles and concepts in bioinorganic materials chemistry*. New York: Oxford University Press; 2001.
- [17] Fratzl P, editor. *Collagen: structure and mechanics*. New York: Springer; 2008.
- [18] Neville AC. *Biology of fibrous composites*. Cambridge: Cambridge University Press; 1993.
- [19] Fung YC. *Biomechanics: mechanical properties of living tissues*. 2nd ed. New York: Springer; 2004.
- [20] Vogel S. *Comparative biomechanics: life's physical world*. New Jersey: Princeton University Press; 2003. p. 582.
- [21] Meyers MA, Chen P-Y, Lin AYM, Seki Y. *Biological materials: structure and mechanical properties*. *Prog Mater Sci* 2008;13:1–206.
- [22] Espinosa HD, Rim JE, Barthelat F, Buehler MJ. Merger of structure and material in nacre and bone – perspectives on de novo biomimetic materials. *Prog Mater Sci* 2009;54:1059–100.
- [23] Chen P-Y, Lin AYM, Lin Y-S, Stokes AG, Peyras J, Olevsy EA, et al. Structure and mechanical properties of selected biological materials. *J Mech Behav Biomed Mater* 2008;1:208–26.
- [24] Meyers MA, Chen P-Y, Lopez MI, Seki Y, Line AYM. *Biological materials: a materials science approach*. *J Mech Behav Biomed Mater* 2011;4:626–57.
- [25] Mann S, Archibald DD, Didymus JM, Douglas T, Heywood BR, Meldrum FC, et al. Crystallization at inorganic-organic interfaces: biominerals and biomimetic synthesis. *Science* 1993;261:1286–92.
- [26] Weiner S, Addadi L. Design strategies in mineralized biological materials. *J Mater Chem* 1997;7:689–702.
- [27] Ehrlich H. Chitin and collagen as universal and alternative templates in biomineralization. *Int Geol Rev* 2010;52:661–99.
- [28] Meyers MA, Lin AYM, Seki Y, Chen P-Y, Kad BK, Bodde S. Structural biological composites: an overview. *JOM* 2006;58:35–41.
- [29] Fratzl P, Weinkamer R. Nature's hierarchical materials. *Prog Mater Sci* 2007;52:1263–334.
- [30] Buehler MJ, Keten S, Ackbarow T. Theoretical and computational hierarchical nanomechanics of protein materials: deformation and fracture. *Prog Mater Sci* 2008;53:1101–241.
- [31] Buehler MJ. Hierarchical nanomechanics of collagen fibrils: atomistic and molecular modeling. In: Fratzl P, editor. *Collagen: structure and mechanics*. New York: Springer; 2008.
- [32] McKittrick J, Chen P-Y, Tombolato L, Novitskaya EE, Trim W, Lin YS, et al. Energy absorbent natural materials and bio-inspired design strategies: a review. *Mater Sci Eng C* 2010;30:331–42.
- [33] Dunlop JWC, Fratzl P. Biological composites. *Ann Rev Mater Res* 2010;40:1–24.
- [34] Wang R, Gupta HS. Deformation and fracture mechanisms of bone and nacre. *Annu Rev Mater Res* 2011;41:41–73.
- [35] Srinivasan AV, Haritos GK, Hedberg FL. Biomimetics: advancing man-made materials through guidance from nature. *Appl Mech Rev* 1991;44:463–82.
- [36] Heywood B, Mann S. Template directed nucleation and growth of inorganic materials. *Adv Mater* 1994;6:9–19.
- [37] Sarikaya M. An introduction to biomimetics: a structural viewpoint. *Microsc Res Technol* 1994;27:360–75.
- [38] Calvert P. Strategies for biomimetic mineralization. *Scripta Met* 1994;31:977–82.
- [39] Mayer G. Rigid biological systems as models for synthetic composites. *Science* 2005;310:1144–7.
- [40] Vincent JFV, Bogatyreva OA, Bogatyrev NR, Bowyer A, Pahl AK. Biomimetics: its practice and theory. *J R Soc Interface* 2006;3:471–82.
- [41] Kushner AM, Guan Z. Modular design in natural and biomimetic soft materials. *Angew Chem Int Ed Engl* 2011;50:9026–57.
- [42] Wegst UGK, Ashby MF. The mechanical efficiency of natural materials. *Philos Mag* 2004;84:2167–81.
- [43] Ashby MF. On the engineering properties of materials. *Acta Metal* 1989;37:1273–93.
- [44] Arzt E. Biological and artificial attachment devices: lessons for materials scientists from flies and geckos. *Mater Sci Eng C* 2006;26:1245–50.
- [45] Wang C, Zhang Y. Protein micropatterning via self-assembly of nanoparticles. *Adv Mater* 2005;17:150.
- [46] Huang M, Wang R. Bioinspired design of dental multilayers. *J Mater Sci Mater Med* 2007;18:57–64.
- [47] Gatto E, Stella L. Engineering bioinspired luminescent probes: antimicrobial peptides chelating lanthanide ions. *J Pept Sci* 2006;12(Suppl. 5):229.
- [48] Percec V. Bioinspired supramolecular liquid crystals. *Philos Trans R Soc A* 2006;364:2709–19.
- [49] Jin Y, Tai H, Hiltner A, Baer E, Shirk JS. New class of bioinspired lenses with a gradient refractive index. *J Appl Polymer Sci* 2007;103:1834–41.
- [50] Heuer AH, Kink DJ, Laraia VJ, Arias JL, Calvert PD, Kendall K, et al. Innovative materials processing strategies: a biomimetic approach. *Science* 1992;255:1098–105.
- [51] Kaplan DL. Mollusc shell structures: novel design strategies for synthetic materials. *Curr Opin Solid State Mater Sci* 1998;3:232–8.
- [52] Currey JD. The design of mineralized hard tissues for their mechanical functions. *J Exp Biol* 1999;202:3285–94.
- [53] Mayer G, Sarikaya M. Rigid biological composite materials: structural examples for biomimetic design. *Exp Mech* 2002;42:395–403.
- [54] Oaki Y, Imaai H. The hierarchical architecture of nacre and its mimetic material. *Angew Chem Int Ed* 2005;44:6571–5.
- [55] Jackson AP, Vincent JFV, Turner RM. The mechanical design of nacre. *Proc R Soc Lond B* 1988;234:415–40.
- [56] Zarella C, Belcher AM, Fritz M, Li Y, Mann S, Hansma PK, et al. Critical transitions in the biofabrication of abalone shells and flat pearls. *Chem Mater* 1996;8:679–90.
- [57] Fratzl P, Weiner S. Bio-inspired materials – mining the old literature for new ideas. *Adv Mater* 2010;22:4547–750.
- [58] Tirrell M, editor. *Hierarchical structures in biology as a guide for new materials*, committee on synthetic hierarchical structures, commission on engineering and technical systems, National Research Council. Washington (DC): The National Academies Press; 1994 [NMAB-464].
- [59] Currey JD. Differences in the tensile strength of bone of different histological types. *J Anat* 1959;93:87–95.
- [60] Currey JD. Strength of bone. *Nature* 1962;195:513–4.
- [61] Currey JD, Taylor JD. The mechanical behavior of some molluscan hard tissue. *J Zool* 1974;173:395–406.

- [62] Currey JD. Mechanical properties of mother-of-pearl in tension. Proc R Soc Lond B 1977;196:443–83.
- [63] Brear K, Currey JD. Structure of a sea-urchin tooth. J Mater Sci 1976;11:1977–8.
- [64] Brear K, Currey JD, Kingsley MCS. The mechanical design of the tusk of the narwhal (*Monodon monoceros, cetacea*). J Zool Part III 1993;230:411–23.
- [65] Zioupos P, Currey JD, Sedman AJ. An examination of the micromechanics of failure of bone and antler by acoustic emission tests and laser scanning confocal microscopy. Med Eng Phys 1994;16:203–12.
- [66] Zioupos P, Currey JD, Casinos A, DeBuffrenil V. Mechanical properties of the rostrum of the whale *Mesopoldon densirostris*, a remarkably dense bony tissue. J Zool 1997;241:725–37.
- [67] Menig R, Meyers MH, Meyers MA, Vecchio KS. Quasi-static and dynamic mechanical response of *Haliotis rufescens* (abalone) shells. Acta Mater 2000;48:2383–98.
- [68] Lin AYM, Meyers MA, Vecchio KS. Mechanical properties and structure of *Strombus gigas*, *Tridacna gigas* and *Haliotis rufescens* sea shells: a comparative study. Mater Sci Eng C 2006;26:1380–9.
- [69] Meyers MA, Lin AYM, Chen P-Y, Muyco J. Mechanical strength of abalone nacre: role of the soft organic layer. J Mech Behav Biomed Mater 2008;1:76–85.
- [70] Lopez MI, Chen P-Y, McKittrick J, Meyers MA. Growth of nacre in abalone: seasonal and feeding effects. Mater Sci Eng C 2011;31:238–45.
- [71] Chen P-Y, Lin AYM, McKittrick J, Meyers MA. Structure and mechanical properties of crab exoskeleton. Acta Biomater 2008;4:587–96.
- [72] Seki Y, Schneider MS, Meyers MA. Structure and mechanical behavior of a toucan beak. Acta Mater 2005;52:5281–96.
- [73] Seki Y, Kad B, Benson D, Meyers MA. The toucan beak: structure and mechanical response. Mater Sci Eng C 2006;26:1412–20.
- [74] Seki Y, Bodde SG, Meyers MA. Toucan and hornbill beaks: comparative study. Acta Biomater 2010;6:331–43.
- [75] Chen I, Chen P-Y, Meyers MA, McKittrick J. Armadillo armor: mechanical testing and microstructural evaluation. J Mech Behav Biomed Mater 2011;4:713–22.
- [76] Bodde SG, Meyers MA, McKittrick J. Correlation of the mechanical and structural properties of cortical rachis keratin of rectrices of the Toco Toucan (*Ramphastos toco*). J Mech Behav Biomed Mater 2011;4:723–32.
- [77] Chen P-Y, Stokes AG, McKittrick J. Comparison of the structure and mechanical properties of bovine femur bone and antler of the North American elk (*Cervus elaphus canadensis*). Acta Biomater 2009;5:693–706.
- [78] Launey ME, Chen P-Y, McKittrick J, Ritchie RO. Mechanistic aspects of the fracture toughness of elk antler bone. Acta Biomater 2010;6:1505–14.
- [79] Kulin RM, Chen P-Y, Jiang F, McKittrick J, Vecchio KS. Dynamic fracture resilience of elk antler: biomimetic inspiration for improved crashworthiness. JOM 2010;62:41–6.
- [80] Chen P-Y, Toroian D, Price PA, McKittrick J. Mineral forms a continuum phase in mature cancellous bone. Calcif Tissue Int 2011;88:351–61.
- [81] Chen P-Y, McKittrick J. Compressive mechanical properties of demineralized and deproteinized cancellous bone. J Mech Behav Biomed Mater 2011;4:961–73.
- [82] Castro-Ceseña AB, Novitskaya EE, Chen P-Y, Hirata GA, McKittrick J. Kinetic studies of bone demineralization at different HCl concentrations and temperatures. Mater Sci Eng C 2011;31:523–30.
- [83] Tombolato L, Novitskaya EE, Chen P-Y, Sheppard FA, McKittrick J. Microstructure and elastic and fracture properties of horn keratin. Acta Biomater 2010;6:319–30.
- [84] Trim W, Horstemeyer MF, Rhee H, Park S-J, El Kadiri H, Williams L, et al. Parametric study of the structure-property relations of bighorn sheep (*Ovis canadensis*) horn. Acta Biomater 2011;7:1228–40.
- [85] Meyers MA, Lin AYM, Lin YS, Olevsky EA, Georgalis S. The cutting edge: sharp biological materials. JOM 2008;60:21–6.
- [86] Lawn BR, Lee JJ-W, Chai H. Teeth: among nature's most durable biocomposites. Annu Rev Mater Res 2010;40:55–75.
- [87] Lin AYM, Brunner R, Chen P-Y, Talke FE, Meyers MA. Underwater adhesion of abalone: the role of van der Waals and capillary forces. Acta Mater 2009;57:4178–85.
- [88] Lin YS, Wei CT, Olevsky EA, Meyers MA. Mechanical properties and laminate structure of *Arapaima gigas* scale. J Mech Behav Biomed Mater 2011;4:1145–56.
- [89] Yang W, Chao C, Novitskaya EE, McKittrick J. Investigation of mechanical behavior of porcupine quills subjected to compressive loading. Unpublished work.
- [90] Saunders M, Kong C, Shaw JA, Macey DJ, Clode PL. Characterization of biominerals in the radula teeth of the chiton, *Acanthopleura hirtosa*. J Struct Biol 2009;167:55–61.
- [91] Harrington MJ, Waite JH. Holdfast heroics: comparing the molecular and mechanical properties of *Mytilus californianus* byssal threads. J Exp Biol 2007;210:4307–18.
- [92] Harrington MJ, Masic A, Holten-Andersen N, Waite JH, Fratzl P. Iron-clad fibers: a metal-based biological strategy for hard flexible coatings. Science 2010;328:216–20.
- [93] Broomell CC, Waite JH, Zok FW. Role of transition metals in sclerotization of biological tissue. Acta Biomater 2008;4:2045–51.
- [94] Marshall C, Gillespie JM. The keratin proteins of wool, horn and hoof from sheep. Aust J Bio Sci 1977;30:389–400.
- [95] Franzblau C. Elastin. In: Florkin M, Stotz EH, editors. Comparative biochemistry, 26C. Amsterdam: Elsevier; 1971. p. 659–712.
- [96] Kelly RE, Rice RV. Abductin: a rubber-like protein from the internal triangular hinge ligament of pecten. Science 1967;155:208–10.
- [97] Kahler GA, Fisher FM, Sass RL. The chemical composition and mechanical properties of the hinge ligament in bivalve mollusks. Biol Bull 1976;151:161–81.
- [98] Alexander RM. Rubber-like properties of the inner hingeligament of Pectinidae. J Exp Biol 1966;44:119–30.
- [99] Meyers MA, Chawla KC. Mechanical behavior of materials. 2nd ed. Cambridge: Cambridge University Press; 2009.
- [100] Koenders MMJF, Yang L, Wisman RG, van der Werf KO, Reinhardt DP, Daamen W, et al. Microscale mechanical properties of single elastic fibers: the role of fibrillin-microfibrils. Biomaterials 2009;30:2425–32.
- [101] Omenetto FG, Kaplan DL. New opportunities for an ancient material. Science 2010;329:528–31.

- [102] Gosline JM, Guerette PA, Ortlepp CS, Savage KN. The mechanical design of spider silks. *J Exp Biol* 1999;202:3295–303.
- [103] Agrawal S, Patidar D, Dixit M, Sharma K, Saxena NS. Investigation of thermo-mechanical properties of PMMA. *AIP Conf Proc* 2010;1249:79–82.
- [104] Weis-Fogh T. A rubber-like protein in insect cuticle. *J Exp Biol* 1960;37:889–907.
- [105] Sasaki N, Odajima S. Stress-strain curve and young's modulus of a collagen molecule as determined by the X-ray diffraction technique. *J Biomech* 1996;29:655–8.
- [106] Weaver JC, Wang Q, Miserez A, Tantuccio A, Stronberg R, Bozhilov KN, et al. Analysis of an ultra hard magnetic biomineral in chiton radular teeth. *Mater Today* 2010;13:42–52.
- [107] Imbeni V, Kruzic JJ, Marshall GW, Marshall SJ, Ritchie RO. The dentin–enamel junction and the fracture of human teeth. *Nat Mater* 2005;4:229–32.
- [108] de With G, Vandijk HJA, Hattu N, Prijs K. Preparation, microstructure and mechanical properties of dense polycrystalline hydroxyapatite. *J Mater Sci* 1981;16:1592–98.
- [109] Osorio AG, dos Santos LA, Bergmann CP. Evaluation of the mechanical properties and microstructure of hydroxyapatite reinforced with carbon nanotubes. *Rev Adv Mater Sci* 2011;27:58–63.
- [110] Marshall GW, Balooch M, Gallagher RR, Gansky SA, Marshall SJ. Mechanical properties of the dentinoenamel junction: AFM studies of nanohardness, elastic modulus, and fracture. *J Biomed Mater Res* 2001;54:87–95.
- [111] Habelitz S, Marshall GW, Balooch M, Marshall SJ. Nanoindentation and storage of teeth. *J Biomech* 2002;35:995–8.
- [112] Subhash G, Yao S, Bellinger B, Gretz MR. Investigation of mechanical properties of diatom frustules using nanoindentation. *J Nanosci Nanotech* 2005;5:50–6.
- [113] Giraud-Guille MM. Twisted plywood architecture of collagen fibrils in human compact bone osteons. *Calcif Tissue Int* 1988;42:167–80.
- [114] Giraud-Guille MM. Plywood structures in nature. *Curr Opin Solid State Mater Sci* 1998;3:221–8.
- [115] Fraser RD, MacRae TP, Parry DA, Suzuki E. Intermediate filaments in alpha keratins. *Proc Natl Acad Sci USA* 1986;83:1179–83.
- [116] Parry DAD, North ACT. Hard a-keratin intermediate filament chains: substructure of the N- and C-terminal domains and the predicted structure and function of the C-terminal domains of type I and type II chains. *J Struct Biol* 1998;122:67–75.
- [117] Fraser RD, MacRae TP. Molecular structure and mechanical properties of keratin. In: Vincent JFV, Currey JD, editors. The mechanical properties of biological materials, symposium of the society of experimental biology. Cambridge: Cambridge University Press; 1980. p. 211–46.
- [118] Chapman BM. A review of mechanical properties of keratin fibres. *J Text Inst* 1969;60:181.
- [119] Voet D, Voet JG, Pratt CW. *Biochemistry: life at the molecular level*. 3rd ed. New York: John Wiley & Sons; 2008.
- [120] Prosser IW, Mecham RP. Regulation of extracellular matrix accumulation: a short review of elastin biosynthesis. In: Varner JE, editor. *Self-assembling architecture*. New York: Wiley-Liss; 1988. p. 1–23.
- [121] Pasquali-Ronchetti I, Baccarani-Contri M. Elastic fiber during development and aging. *Microsc Res Technol* 1997;38:428–35.
- [122] Williams D. "Sows' ears, silk purses and goats' milk: new production methods and medical applications for silk. *Med Device Technol* 2003;14:9–11.
- [123] Jones J, Rothfuss H, Steinkraus H, Lewis R. Transgenic goats producing spider silk protein in their milk; behavior, protein purification and obstacles. *Transgenic Res* 2010;19:135.
- [124] Cao Q, Wang Y, Beyley H. Sequence of abduktion, the molluscan rubber protein. *Curr Biol* 1997;7:R677–8.
- [125] Denny MW, Miller L. Jet propulsion in the cold: mechanics of swimming in the Antarctic scallop *Adamussium colbecki*. *J Exp Biol* 2006;209:4503–14.
- [126] Gray WR, Sandberg LB, Forster JA. Molecular model for elastin structure and function. *Nature* 1973;246:461–6.
- [127] Aaron BB, Gosline JM. Elastin as a random-network elastomer: a mechanical and optical analysis of single elastin fibers. *Biopolymers* 1981;20:1247–60.
- [128] Urry DW, Harris RD, Long MM, Prasad KU. Polytetrapeptide of elastin: temperature-correlated elastomeric force and structure development. *Int J Peptide Protein Res* 1986;28:649–60.
- [129] Elvin CM, Carr AG, Huson MG, Maxwell JM, Pearson RD, Vuocolo T, et al. Synthesis and properties of crosslinked recombinant pro-resilin. *Nature* 2005;437:999–1002.
- [130] Weis-Fogh T. Thermodynamic properties of resilin. *J Mol Biol* 1961;3:520–31.
- [131] Weis-Fogh T. Molecular interpretation of the elasticity of resilin, a rubber-like protein. *J Mol Biol* 1961;3:648–67.
- [132] Fonseca PJ, Bennett-Clark HC. Asymmetry of tymbal action and structure in a cicada: a possible role in the production of complex songs. *J Exp Biol* 1998;201:717–30.
- [133] Bennet-Clark HC. Tymbal mechanics and the control of song frequency in the cicada *Cyclochila australasiae*. *J Exp Biol* 1997;200:1681–94.
- [134] Alberts B, Bray D, Hopkin K, Johnson A, Lewis J, Raff M, et al. *Essential cell biology*. 2nd ed. New York: Garland Science; 2004.
- [135] Keten S, Buehler MJ. Atomistic model of the spider silk nanostructure. *Appl Phys Lett* 2010;96:15.
- [136] Denny M. The physical properties of spider's silk and their role in the design of orb-webs. *J Exp Biol* 1976;65:483–506.
- [137] Kohr E. *Chitin: fulfilling a biomaterials promise*. Oxford: Elsevier Science; 2001.
- [138] Hamm CE, Merkel R, Springer O, Jurkojc P, Maier C, Prechtel K, et al. Architecture and material properties of diatom shells provide effective mechanical protection. *Nature* 2003;421:841–3.
- [139] Runnegar B, Bengtson S. Origin of hard parts: early skeletal fossils. In: Briggs DEG, Crowther PR, editors. *Palaeobiology: a synthesis*. Oxford: Wiley-Blackwell; 1992. p. 24–9.
- [140] Mann S. Molecular recognition in biomineralization. *Nature* 1988;332:119–24.
- [141] Hildebrand M. *personal communication*; 2010.
- [142] Addadi L, Raz S, Weiner S. Taking advantage of disorder: amorphous calcium carbonate and its roles in biomineralization. *Adv Mater* 2003;15:959–70.
- [143] Sass RL, Vidale R. Interatomic distances and thermal anisotropy in sodium nitrate and calcite. *Acta Crystall* 1957;10:567–70.

- [144] De Villiers JPR. Crystal structures of aragonite, strontianite, and witherite. *Am Mineral* 1971;56:758–67.
- [145] Kay MI, Young RA, Posner AS. Crystal structure of hydroxyapatite. *Nature* 1964;204:1050–2.
- [146] Jackson SA, Cartwright AG, Lewis D. The morphology of bone mineral crystals. *Calcif Tissue Res* 1978;25:217–22.
- [147] Weiner S, Price PA. Disaggregation of bone into crystals. *Calcif Tissue Int* 1986;39:365–75.
- [148] Ziv V, Weiner S. Bone crystal sizes: a comparison of transmission electron microscopic and X-ray diffraction width broadening techniques. *Connect Tissue Res* 1994;30:165–75.
- [149] Boskey A. Bone mineral crystal size. *Osteoporos Int* 2003;14:16–21.
- [150] Fratzl P, Groschner M, Vogl G, Plenk H, Eschberger J, Fratzl-Zelman N. Mineral crystals in calcified tissues: a comparative study by SAXS. *J Bone Mineral Res* 1992;7:329–34.
- [151] Watchtel E, Weiner S. Small-angle X-ray scattering study of dispersed crystals from bone and tendon. *J Bone Mineral Res* 1994;9:1651–5.
- [152] Ertz D, Gathercole LJ, Atkins EDT. Scanning probe microscopy of intrafibrillar crystallites in calcified collagen. *J Mater Sci Mater Med* 1994;5:200–6.
- [153] Tong W, Glimcher MJ, Katz JL, Kuhn L, Eppell SJ. Size and shape of mineralites in young bovine bone measured by atomic force microscopy. *Calcif Tissue Int* 2003;72:592–8.
- [154] Hassenkarm T, Fantner GE, Cutroni JA, Weaver JC, Morse DE, Hansma PK. High-resolution AFM imaging of intact and fracture trabecular bone. *Bone* 2004;35:4–10.
- [155] Warén A, Bengtson S, Goffredi SK, Van Dover CL. A hot-vent gastropod with iron sulfide dermal sclerites. *Science* 2003;302:1007.
- [156] Lichtenegger HC, Schöberl T, Bartl MH, Waite H, Stucky GD. High abrasion resistance with sparse mineralization: copper biomineral in worm jaws. *Science* 2002;298:389–92.
- [157] Pontin MG, Moses DN, Waite JH, Zok FW. A nonmineralized approach to abrasion-resistant biomaterials. *Proc Natl Acad Sci USA* 2007;104:13559–64.
- [158] Goffredi SK, Warén A, Orphan VJ, Van Dover CL, Vrijenhoek RC. Novel forms of structural integration between microbes and a hydrothermal vent gastropod from the Indian Ocean. *Appl Environ Microbiol* 2004;70:3082–90.
- [159] Yao H, Dao M, Imholt T, Huang J, Wheeler K, Bonilla A, et al. Protection mechanisms of the iron-plated armor of a deep-sea hydrothermal vent gastropod. *Proc Natl Acad Sci USA* 2010;107:987–92.
- [160] Hildebrand M, York E, Kelz JI, Davis AK, Frigeri LG, Allison DP, et al. Nanaoscale control of silica morphology and three-dimensional structure during diatom cell wall formation. *J Mater Res* 2006;21:2689–98.
- [161] Weiner S, Wagner HD. The material bone: structure–mechanical function relations. *Annu Rev Mater Sci* 1998;28:271–98.
- [162] Fantner GE, Hassenkarm T, Kindt JH, Weaver JC, Birkedal H, Pechenik L, et al. Sacrificial bonds and hidden length dissipate energy as mineralized fibrils separate during bone fracture. *Nat Mater* 2005;4:612–6.
- [163] Ji B, Gao H. Mechanical properties of biological composites. *Annu Rev Mater Sci* 2010;40:77–100.
- [164] Yao H, Gao HJ. Multi-scale cohesive laws in hierarchical materials. *Int J Solids Struct* 2007;44:8177–93.
- [165] Bechtle S, Ang SF, Schneider GA. On the mechanical properties of hierarchically structured biological materials. *Biomater* 2010;31:6378–85.
- [166] Morgan EF, Bayraktar HH, Keaveny TM. Trabecular bone modulus-density relationships depend on anatomic site. *J Biomech* 2003;36:897–904.
- [167] Gibson LJ, Ashby MF. Cellular solids: structure and properties. 2nd ed. Cambridge: Cambridge University Press; 1997.
- [168] Gibson LJ. Biomechanics of cellular solids. *J Biomech* 2005;38:377–99.
- [169] Hodgkinson R, Currey JD, Evans GP. Hardness, an indicator of the mechanical competence of cancellous bone. *J Orthop Res* 1989;7:754–8.
- [170] Ashman RB, Corin JD, Turner CH. Elastic properties of cancellous bone: measurement by an ultrasonic technique. *J Biomech* 1987;20:979–86.
- [171] Callister WD. Materials science and engineering, an introduction. 7th ed. New York: John Wiley and Sons; 2007.
- [172] Karam GN, Gibson LJ. Elastic buckling of cylindrical shells with elastic cores I: analysis. *Int J Solids Struct* 1995;32:1259–83.
- [173] Hubbard RP. Flexure of layered cranial bone. *J Biomech* 1971;4:251–63.
- [174] Treloar LRG. The physics of rubber elasticity. 3rd ed. Oxford: Oxford University Press; 1975.
- [175] Mooney M. A theory of large elastic deformation. *J Appl Phys* 1940;11:582–92.
- [176] Rivlin RS, Saunders DW. Large elastic deformations of isotropic materials. VII. Experiments on the deformation of rubber. *Philos Trans R Soc Lond A* 1951;243:251–88.
- [177] Ogden RW. Large deformation isotropic elasticity – on the correlation of theory and experiment for incompressible rubberlike solids. *Proc R Soc Lond A* 1972;326:565–84.
- [178] Arruda EM, Boyce MC. A three-dimensional model for the large stretch behavior of rubber elastic materials. *J Mech Phys Solids* 1993;41:389–412.
- [179] Liao J, Yang L, Grashow J, Sacks M. Molecular orientation of collagen in intact planar connective tissues under biaxial stretch. *Acta Biomater* 2005;1:45–54.
- [180] Fratzl P, Misof K, Zizak I, Rapp G, Amenitsch H, Bernstorff S. Fibrillar structure and mechanical properties of collagen. *J Struct Biol* 1997;122:119–22.
- [181] Miserez A, Wasko SS, Carpenter CF, Waite JH. Non-entropic and reversible long-range deformation of an encapsulating bioelastomer. *Nat Mater* 2009;8:910–6.
- [182] Feughelman M. Mechanical properties and structure of α -keratin fibres: wool, human hair and related fibres. Sydney: University of New South Wales Press; 1997.
- [183] Feughelman M. Mechanical properties and structure of alpha-keratin fibres: wool, human hair and related fibres. Sydney: University of New South Wales Press; 1997.
- [184] Fudge DS, Gosline JM. Molecular design of the alpha-keratin composite: insights from a matrix-free model, hagfish slime threads. *Proc R Soc Lond B* 2004;271:291–9.
- [185] Flory PJ. Principles of polymer chemistry. New York: Cornell University Press; 1964.
- [186] Fung YC. Elasticity of soft tissues in simple elongation. *Am J Physiol* 1967;213:1532–44.

- [187] Weinberg K. Lecture notes, Chapter 4, Constitutive equations; 2011. <<http://mech2.pi.tu-berlin.de/weinberg>>.
- [188] Onck PR, Koeman T, Van Dillen T, Van Der Giessen E. Alternative explanation of stiffening in cross-Linked semiflexible networks. *Phys Rev Lett* 2005;95:178101–4.
- [189] Storm C, Pastore JJ, MacKintosh FC, Lubensky TC, Janmey PA. Nonlinear elasticity in biological gels. *Nature* 2005;45:191–4.
- [190] Dao M, Li J, Suresh S. Molecularly based analysis of deformation of spectrin network and human erythrocyte. *Mater Sci Eng C* 2006;26:1232–44.
- [191] Dobrynin AV, Carillon J-MY. Universality in nonlinear elasticity of biological and polymeric networks and gels. *Macromolecules* 2011;44:140–6.
- [192] Cook J, Gordon JE, Evans CC, Marsh DM. A mechanism for the control of crack propagation in all-brittle systems. *Proc R Soc Lond A* 1964;282:508–20.
- [193] Gordon JE. The science of structures and materials. New York: W.H. Freeman and Company; 1988. p. 98.
- [194] Gao HJ, Ji BH, Jäger IL, Arzt E, Fratzl P. Materials become insensitive to flaws at nanoscale: lessons from nature. *Proc Natl Acad Sci USA* 2003;100:5597–600.
- [195] Ji B, Gao H, Hsia KJ. How do slender mineral crystals resist buckling in biological materials? *Philos Mag Lett* 2004;84:631–41.
- [196] Bazant ZP. Size effect on structural strength: a review. *Arch Appl Mech* 1999;69:703–25.
- [197] Olsza MJ, Cheng X, Jee SS, Kumar R, Kim Y-Y, Kaufman MJ, et al. Bone structure and formation: a new perspective. *Mater Sci Eng R* 2007;58:77–116.
- [198] Weiner S, Traub W, Wagner HD. Lamellar bone: structure–function relations. *J Struct Biol* 1986;126:241–55.
- [199] Rho JY, Kuhn-Spearing L, Zioupos P. Mechanical properties and the hierarchical structure of bone. *Med Eng Phys* 1998;20:92–103.
- [200] Ritchie RO, Buehler MJ, Hansma PK. Plasticity and toughness in bone. *Phys Today* 2009;62:41–7.
- [201] Curry JD. Mechanical properties and adaptations of some less familiar bony tissues. *J Mech Behav Biomed Mater* 2010;3:357–72.
- [202] Krauss S, Monsonego-Orman E, Zelzer E, Fratzl P, Shahar R. Mechanical function of a complex three-dimensional suture joining the bony elements in the shell of the red-eared slider turtle. *Adv Mater* 2009;21:407–12.
- [203] Krauss S, Fratzl P, Seto J, Currey JD, Estevez JA, Funari SS, et al. Inhomogeneous fibril stretching in antler starts after macroscopic yielding: indication for a nanoscale toughening mechanisms. *Bone* 2009;44:1105–10.
- [204] Rhee H, Horstemeyer MF, Hwang Y, Lim H, El Kadiri H, Trim W. A study on the structure and mechanical behavior of the Terrapene carolina carapace. A pathway to design bio-inspired synthetic composites. *Mater Sci Eng C* 2009;29:2333–9.
- [205] Rhee H, Horstemeyer MF, Ramsay A. A study on the structure and mechanical behavior of the *Dasyus novemcinctus* shell. *Mater Sci Eng C* 2011;31:363–9.
- [206] Currey JD. Mechanical properties of bone tissues with greatly differing functions. *J Biomech* 1979;12:313–9.
- [207] Nalla RK, Kinney JH, Ritchie RO. Mechanistic fracture criteria for the failure of human cortical bone. *Nat Mater* 2003;2:164–8.
- [208] Nalla RK, Kruzic JJ, Kinney JH, Ritchie RO. Mechanistic aspects of fracture and *R*-curve behavior of human cortical bone. *Biomaterials* 2005;26:217–31.
- [209] Ritchie RO, Kinney JH, Kruzic JJ, Nalla RK. Cortical bone fracture. In: Akay M, editor. *Wiley encyclopedia of biomedical engineering*. New Jersey: John Wiley & Sons Inc.; 2006. p. 1–18.
- [210] ASTM E399 – 09e2 Standard test method for linear elastic plane strain fracture toughness K_{Ic} of metallic materials.
- [211] Wright TM, Hayes WC. Fracture mechanics parameters for compact bone – the effects of density and specimen thickness. *J Biomech* 1977;10:419–30.
- [212] Currey JD, Brear K, Zioupos P. The effects of aging and changes in mineral content in degrading the toughness of human femora. *J Biomech* 1996;29:257–60.
- [213] Yeni YN, Brown CU, Norman TL. Influence of bone composition and apparent density on fracture toughness of the human femur and tibia. *Bone* 1998;22:79–84.
- [214] Yeni YN, Norman TL. Calculation of porosity and osteonal cement line effects on the effective fracture toughness of cortical bone in longitudinal crack growth. *J Biomed Mater Res* 2000;51:504–9.
- [215] Yeni YN, Brown CU, Wang Z, Norman TL. The influence of bone morphology on fracture toughness of the human femur and tibia. *Bone* 1997;21:453–9.
- [216] Zioupos P, Currey JD. Changes in the stiffness, strength, and toughness of human cortical bone with age. *Bone* 1998;22:57–66.
- [217] Wang X, Bank R, Tekoppele J, Agrawal C. The role of collagen in determining bone mechanical properties. *J Orthop Res* 2001;19:1021–6.
- [218] Wang RZ, Suo Z, Evans AG, Yao N, Aksay IA. Deformation mechanisms in nacre. *J Mater Res* 2001;16:2485–93.
- [219] Wang X, Shen X, Li X, Agrawal C. Age-related changes in the collagen network and toughness of bone. *Bone* 2002;31:1–7.
- [220] Martin RB, Burr DB. A hypothetical mechanism for the stimulation of osteonal remodeling by fatigue damage. *J Biomech* 1982;15:137–9.
- [221] Burr DB, Schaffler MB, Frederickson RG. Composition of the cement line and its possible mechanical role as a local interface in human compact bone. *J Biomech* 1988;21:939–45.
- [222] Vashishth D, Behiri JC, Bonfield W. Crack growth resistance in cortical bone: concept of microcrack toughening. *J Biomech* 1997;10:763–9.
- [223] Vashishth D, Tanner KE, Bonfield W. Contribution, development and morphology of microcracking in cortical bone during crack propagation. *J Biomech* 2000;33:1169–74.
- [224] Vashishth D, Tanner KE, Bonfield W. Experimental validation of a microcracking-based toughening mechanism for cortical bone. *J Biomech* 2003;36:121–4.
- [225] Vashishth D. Rising crack-growth-resistance behavior in cortical bone: implication for toughness measurements. *J Biomech* 2004;37:943–6.

- [226] Malik CL, Gibeling JC, Martin RB, Stover SM. Equine cortical bone exhibits rising *R*-curve fracture mechanics. *J Biomech* 2003;36:194.
- [227] Nalla RK, Kruzic JJ, Kinney JH, Ritchie RO. On the origin of the toughness of mineralized tissue: microcracking or crack bridging? *Bone* 2004;34:790–8.
- [228] Gao H. Application of fracture mechanics concepts to hierarchical biomechanics of bone and bone-like materials. *Int J Fract* 2006;138:101–37.
- [229] Yang QD, Cox BN, Nalla RK, Ritchie RO. Re-evaluating the toughness of human cortical bone. *Bone* 2006;38:878.
- [230] Launey ME, Buehler MJ, Ritchie RO. On the mechanistic origins of toughness in bone. *Annu Rev Mater Res* 2010;40:25–53.
- [231] Ritchie RO. Mechanisms of fatigue crack propagation in metals, ceramics and composites: role of crack tip shielding. *Mater Sci Eng A* 1988;103:15–28.
- [232] Ritchie RO. Mechanisms of fatigue-crack propagation in ductile and brittle solids. *Int J Fract* 1999;100:55–83.
- [233] Thompson JB, Kindt JH, Drake B, Hansma HG, Morse DE, Hansma PK. Bone indentation recovery time correlates with bone reforming time. *Nature* 2001;414:773–5.
- [234] Li VC, Stang H, Krenchel H. Micromechanics of crack bridging in fibre-reinforced concrete. *Mater Struct* 1993;26:486–94.
- [235] Nalla RK, Kruzic JJ, Kinney JH, Balooch M, Ager JW, Ritchie RO. Role of microstructure in the aging-related deterioration of the toughness of human cortical bone. *Mater Sci Eng C* 2006;26:1251–60.
- [236] Koester KJ, Ager III JW, Ritchie RO. The true toughness of human cortical bone measured with realistic short cracks. *Nat. Mater* 2008;7:672–6.
- [237] Buehler MJ, Wong SY. Entropic elasticity controls nanomechanics of single tropocollagen molecules. *Biophys J* 2007;93:37–43.
- [238] Hansma PK, Fantner GE, Kindt JH, Thurner PJ, Schitter G, Turner PJ, et al. Sacrificial bonds in the interfibrillar matrix of bone. *J Musculoskelet Neuronal Interact* 2005;5:313–5.
- [239] Henshaw J. Antlers – the unbrittle bones of contention. *Nature* 1971;231:469.
- [240] Lincoln GA. The role of antlers in the behaviour of red deer. *J Exp Zool* 1972;182:233–49.
- [241] Lincoln GA. Biology of antlers. *J Zool Lond* 1992;226:517–28.
- [242] Clutton-Brock TH. The function of antlers. *Behavior* 1982;79:108–24.
- [243] Skedros JG, Durand P, Bloebaum RD. Hypermineralized peripheral lamellae in primary osteons of deer antler: potential functional analogues of cement lines in mammalian secondary bone. *J Bone Mineral Res* 1995;10(Suppl. 1):441.
- [244] Martin RB, Boardman DL. The effects of collagen fiber orientation, porosity, density and mineralization on bovine cortical bone bending properties. *J Biomech* 1993;26:1047–54.
- [245] Kim JH, Niinomi M, Akahori T. Influence of bone structure on mechanical properties of bovine and swine compact bones. *Mater Sci Forum* 2005;475–479:2407–10.
- [246] Bonfield W, Datta PK. Young's modulus of compact bone. *J Biomech* 1974;7:147–9.
- [247] Reilly DT, Burstein AH, Frankel VH. The elastic modulus for bone. *J Biomech* 1974;7:271–5.
- [248] Carter DR, Hayes WC. The compressive behavior of bone as a two-phase porous structure. *J Bone Joint Surg Am* 1977;59:954–62.
- [249] Skedros JG, Holmes JI, Vajda EG, Bloebaum RD. Cement lines of secondary osteons in human bone are not mineral-deficient: new data in a historical perspective. *Anat Rec A* 2006;286:781–803.
- [250] Lakes RS, Saha S. Cement line motion in bone. *Science* 1979;204:501–3.
- [251] Frasca P, Harper R, Katz JL. Strain and frequency dependence of shear storage modulus for human single osteons and cortical bone microsamples: size and hydration effects. *J Biomech* 1981;14:679–90.
- [252] Schaffler MB, Burr DB, Frederickson RG. Morphology of the osteonal cement line in human bone. *Anat Rec* 1987;217:223–8.
- [253] Currey JD. The mechanical consequences of variation in the mineral content of bone. *J Biomech* 1969;2:1–11.
- [254] Currey JD. Effects of differences in mineralization on the mechanical properties of bone. *Philos Trans R Soc Lond B* 1984;304:509–18.
- [255] Currey JD. The effect of porosity and mineral content on the Young's modulus of elasticity of compact bone. *J Biomech* 1988;21:131–9.
- [256] Currey JD. Strain rate dependence of the mechanical properties of reindeer antler and the cumulative damage model of bone fracture. *J Biomech* 1989;22:469–75.
- [257] Currey JD. Physical characteristics affecting the tensile failure properties of compact bone. *J Biomech* 1990;23:837–44.
- [258] Currey JD, Brear K. Fractal analysis of compact bone and antler fracture surfaces. *Biomimetics* 1992;1:103–18.
- [259] Zioupos P, Wang XT, Currey JD. Experimental and theoretical quantification of the development of damage in fatigue tests of bone and antler. *J Biomech* 1996;29:989–1002.
- [260] Gupta HS, Seto J, Wagermaier W, Zaslansky P, Beosecke P, Fratzl P. Cooperative deformation of mineral and collagen in bone at the nano-scale. *Proc Natl Acad Sci USA* 2006;103:17741–6.
- [261] Kulin RM, Chen P-Y, Jiang F, Vecchio KS. A study of the dynamic compressive behavior of Elk antler. *Mater Sci Eng C* 2011;31:1030–41.
- [262] McElhaney JH. Dynamic response of bone and muscle tissue. *J Appl Physiol* 1966;21:123.
- [263] Adharapurapu RR, Jiang F, Vecchio KS. Dynamic fracture of bovine bone. *Mater Sci Eng C* 2006;26:1325–32.
- [264] Skalak RJ, Farrow DA, Hoger AJ. Kinematics of surface growth. *J Math Biol* 1997;35:869–907.
- [265] Kitchener A. Fracture toughness of horns and a reinterpretation of the horning behaviour of bovids. *J Zool* 1987;213:621–39.
- [266] Kitchener A. Effect of water on the linear viscoelasticity of horn sheath keratin. *J Mater Sci Lett* 1987;6:321–2.
- [267] Kitchener A, Vincent JFV. Composite theory and the effect of water on the stiffness of horn keratin. *J Mater Sci* 1987;22:1385–9.
- [268] Kitchener A. An analysis of the forces of fighting of the blackbuck (*Antelope cervicapra*) and the bighorn sheep (*Ovis canadensis*) and the mechanical design of horns of bovids. *J Zool* 1988;214:1–20.
- [269] Kitchener AC. The evolution and mechanical design of horns and antlers. In: Rayner JMV, Wootton RJ, editors. *Biomechanics and evolution*. Cambridge: Cambridge University Press; 1991.

- [270] Kitchener AC. Fighting and the mechanical design of horns and antlers. In: Domenici P, Blake RW, editors. Biomechanics in animal behavior. Oxford: BIOS Scientific Publishers; 2000.
- [271] Warburton FL. Determination of the elastic properties of horn keratin. J Text Inst 1948;39:297–307.
- [272] Ryder ML. Structure of the rhinoceros horn. Nature 1962;193:1199–201.
- [273] Hieronymus TL, Witmer LM, Ridgely RC. Structure of white rhinoceros (*Ceratotherium simum*) horn Investigated by X-ray computed tomography and histology with implications for growth and external form. J Morphol 2006;267:1172–6.
- [274] Lee S, Reyante B, Tsukasa T, Wooley E, Tombolato L, Chen P-Y, et al. Impact testing of structural biological materials. Mater Sci Eng C 2011;31:730–9.
- [275] Kasapi MA, Gosline JM. Design complexity and fracture control in the equine hoof wall. J Exp Biol 1997;200:1639–59.
- [276] Kasapi MA, Gosline JM. Micromechanics of the equine hoof wall: optimizing crack control and material stiffness through modulation of the properties of keratin. J Exp Biol 1999;202:377–91.
- [277] Bertram JEA, Gosline JM. Fracture toughness design in horse hoof keratin. J Exp Biol 1986;125:29–47.
- [278] Bertram JEA, Gosline JM. Functional design of horse hoof keratin: the modulation of mechanical properties through hydration effects. J Exp Biol 1987;130:121–36.
- [279] Kasapi MA, Gosline JM. Exploring the possible functions of equine hoof wall tubules. Equine Vet J 1998;26:10–4.
- [280] Franck A, Cocquyt G, Simoens P, De Belie N. Biomechanical properties of bovine claw horn. Biosyst Eng 2006;93:459–67.
- [281] Clark C, Petrie L. Fracture toughness of bovine claw horn cattle with and without vertical fissures. Vet J 2007;173:541–7.
- [282] Baillie C, Fitford R. The three-dimensional composite structure of cow hoof wall. Biomimetics 1996;4:1–22.
- [283] Patek SN, Korff WL, Caldwell RL. Biomechanics: deadly strike mechanism of a mantis shrimp. Nature 2004;428:819–20.
- [284] Currey JD, Nash A, Bonfield W. Calcified cuticle in the stomatopod smashing limb. J Mater Sci 1982;17:1939–44.
- [285] Taylor AM, Bonser RHC, Farrent JW. The influence of hydration on the tensile and compressive properties of avian keratinous tissue. J Mater Sci 2004;39:939–42.
- [286] Baden HP, Maderson PF. Morphological and biophysical identification of fibrous proteins in the amniote epidermis. J Exp Zool 1970;174:225–32.
- [287] Wagner IP, Hood DM, Hogan HA. Comparison of bending modulus and yield strength between outer stratum medium and stratum medium zone alba in equine hooves. Am J Vet Res 2001;62:745–51.
- [288] Farran L, Ennos AR, Starkie M, Eichhorn SJ. Tensile and shear properties of fingernails as a function of a changing humidity environment. J Biomech 2009;42:1230–5.
- [289] Bendit EG. Properties of the matrix in keratins: Part II: The “Hookean” region in the stress-strain curve of keratins. Textile Res J 1978;48:717–22.
- [290] Chou SF, Overfelt RA. Tensile deformation and failure of North American porcupine quills. Mater Sci Eng C 2011;31:1729–36.
- [291] Vincent JFV, Owers P. Mechanical design of hedgehog spines and porcupine quills. J Zool 1986;210:55–75.
- [292] Papir Y, Hsu K, Wildnauer R. The mechanical properties of stratum corneum I. The effect of water and ambient temperature on the tensile properties of newborn rat stratum corneum. Biochimica et Biophysica Acta 1975;399:170–80.
- [293] Meredith R, editor. The Mechanical properties of textile fibers. Amsterdam, Netherlands: North Holland Publishing Co; 1956.
- [294] Taylor JRA, Patek SN. Ritualized fighting and biological armor: the impact mechanics of the mantis shrimp's telson. J Exp Biol 2010;213:3496–504.
- [295] May PRA, Newman P, Fuster JM, Hirschman A. Woodpeckers and head injury. Lancet 1976;28:454–5.
- [296] May PRA, Fuster JM, Jaber J. Woodpecker drilling behavior – endorsement of the rotational theory of impact brain damage. Arch Neurol 1979;36:370–3.
- [297] Yoon S-H, Park S. A mechanical analysis of woodpecker drumming and its application to shock-absorbing systems. Bioinsp Biomim 2011;6:1–12.
- [298] Oda J, Sakamoto J, Sakamoto K. Mechanical evaluation of the skeletal structure and tissue of the woodpecker and its shock absorbing system. JSME Int A 2006;49:390–6.
- [299] Kobayashi I, Samata T. Bivalve shell structure and organic matrix. Mater Sci Eng C 2006;26:692–8.
- [300] Menig R, Meyers MH, Meyers MA, Vecchio KS. Quasi-static and dynamic mechanical response of *Strombus gigas* (conch) shells. Mater Sci Eng A 2001;297:203.
- [301] Taylor JD, Layman M. The mechanical properties of bivalve (Mollusca) shell structures. Palaeontology 1972;15:73–87.
- [302] Shepherd SA, Avalos-Borja M, Ortiz Quintanilla M. Towards a chronology of *Haliotis fulgens*, with a review of abalone shell microstructure. Mar Freshwater Res 1995;46:607–15.
- [303] Wada K. Nucleation and growth of aragonite crystals in the nacre of some bivalve molluscs. Biomineralisation 1972;6:141–59.
- [304] Watanabe N, Wilber KM. Influence of the organic matrix on crystal type in molluscs. Nature 1960;188:334.
- [305] Wada K. Studies on the mineralization of calcified tissues in molluscs – VIII. Behavior of eosinophil granules and of organic crystals in the process of mineralization of secreted organic matrices in glass coverslip preparations. Bull Nat Pear Res Lab 1964;9:1087–98.
- [306] Towe KM, Hamilton GH. Ultrastructure and inferred calcification of the mature and developing nacre in bivalve molluscs. Calcif Tissue Res 1968;1:306–18.
- [307] Bevelander G, Nakahara H. An electron microscope study of the formation of the nacreous layer in the shell of certain bivalve molluscs. Calcif Tissue Int 1969;3:84–92.
- [308] Bevelander G, Nakahara H. An electron microscope study of the formation and structure of the periostracum of a gastropod, *Littorina littorca*. Calcif Tissue Res 1970;5:1–12.
- [309] Wise SW. Microarchitecture and deposition of gastropod nacre. Science 1970;167:1486–8.
- [310] Erben HK. On the structure and growth of the nacreous tablets in gastropods. Biomineralization 1972;7:14–27.
- [311] Erasmus J, Cook PA, Sweijnd N. Internal shell structure and growth lines in the shell of the abalone *Haliotis midae*. J Shellfish Res 1994;13:493–501.
- [312] Fritz M, Belcher AM, Radmacher M, Walters DA, Hansma PK, Stucky GD, et al. Flat pearls from biofabrication of organized composites on inorganic substrates. Nature 1994;371:49–51.

- [313] Manne S, Zaremba CM, Giles R, Huggins L, Walters DA, Belcher A, et al. Atomic force microscopy of the nacreous layer in mollusc shells. *Proc R Soc Lond B* 1994;236:17–23.
- [314] Belcher AM, Wui XH, Christensen RJ, Hansma PK, Stucky GD, Morse DE. Control of crystal phase switching and orientation by soluble mollusk-shell proteins. *Nature* 1996;381:56–8.
- [315] Falini G, Albeck S, Weiner S, Addadi L. Control of aragonite or calcite polymorphism by mollusk shell macromolecules. *Science* 1996;271:67–9.
- [316] Schäffer TE, Zanetti CI, Proksch R, Fritz M, Walters DA, Almqvist N, et al. Does abalone nacre form by heteroepitaxial nucleation or by growth through mineral bridges? *Chem Mater* 1997;9:1731–40.
- [317] Walters DA, Smith BL, Belcher AM, Paloczi GT, Stucky GD, Morse DE, et al. Modification of calcite crystal growth by abalone shell proteins: an atomic force microscope study. *Biophys J* 1997;72:1425–33.
- [318] Graham T, Sarikaya M. Growth dynamics of red abalone shell: a biomimetic model. *Mater Sci Eng C* 2000;11:145–53.
- [319] Lin A, Meyers MA. Growth and structure in abalone shell. *Mater Sci Eng A* 2005;290:27–41.
- [320] Addadi L, Joester D, Nudelman F, Weiner S. Mollusk shell formation: a source of new concepts for understanding biomineralization process. *Chem Eur J* 2006;12:980–7.
- [321] Lin AYM, Chen P-Y, Meyers MA. The growth of nacre in the abalone shell. *Acta Biomater* 2008;4:131–8.
- [322] Heiland BB, Schneider AS, Arzt E, Weiss IM. Skalenübergreifende Strukturanalyse an Anschliffen und Dünnschliffen von Seeohr – Schalen, report, INM – Leibniz Institut für Neue Materialien, Saarbrücken; 2011.
- [323] Heiland BB, Schneider AS, Arzt E, Weiss IM. Skalenübergreifende Strukturanalyse an Anschliffen und Dünnschliffen von Seeohr – Schalen, Report, INM – Leibniz Institut für Neue Materialien, Saarbrücken, 2011.
- [324] Sarikaya M, Aksay IA. Nacre of abalone shell: a natural multifunctional nanolaminated ceramic-polymer composite material. In: Case ST, editor. *Results and problems in cell differentiation – biopolymers*. Berlin: Springer-Verlag; 1992. p. 1–26.
- [325] Meyers MA, Lim CT, Li A, Hairul Nizam BR, Tan EPS, Seki Y, et al. The role of organic layer in abalone nacre. *Mater Sci Eng C* 2010;29:2398–410.
- [326] Checa AG, Cartwright JH, Willinger MG. The key role of the surface membrane in why gastropod nacre grows in towers. *Proc Natl Acad Sci USA* 2009;106:38–43.
- [327] Nakahara H. Nacre formation in bivalve and gastropod mollusks. In: Suga S, Nakahara H, editors. *Mechanisms and phylogeny of mineralization in biological systems*. New York: Springer; 1991. p. 343–50.
- [328] Grégoire C, Duchateau G, Florkin M. La trame protidique des nacres. *Experientia* 1954;10:37–40.
- [329] Grégoire C. Topography of the organic components in mother-of-pearl. *J Biophys Biochem Cytol* 1957;3:797–808.
- [330] Grégoire C. Structure of the conchiolin cases of the prisms in *Mytilus edulis* linne. *J Biophys Biochem Cytol* 1961;9:395–400.
- [331] Brictieux-Grégoire S, Florkin M, Grégoire CH. Prism conchiolin of modern or fossil molluscan shells: an example of protein paleization. *Comp Biochem Physiol* 1968;24:567–72.
- [332] Weiner S, Hood L. Soluble protein of the organic matrix of mollusk shells: a potential template for shell formation. *Science* 1975;190:987–9.
- [333] Weiner S. Aspartic acid-rich proteins: major components of the soluble organic matrix of mollusk shells. *FEBS Lett* 1980;111:311–6.
- [334] Weiner S, Talmon Y, Traub W. Electron diffraction of mollusc shell organic matrices and their relationship to the mineral phase. *Int J Biol Macromol* 1983;5:325–8.
- [335] Weiner S, Traub W, Parker SB. Macromolecules in mollusc shells and their functions in biomineralization. *Philos Trans R Soc Lond B* 1984;304:425–34.
- [336] Nudelman F, Gotliv BA, Addadi L, Weiner S. Mollusk shell formation: mapping the distribution of organic matrix components underlying a single aragonitic tablet in nacre. *J Struct Biol* 2006;153:176–87.
- [337] Shen X, Belcher AM, Hansma PK, Stucky GD, Morse DE. Molecular cloning and characterization of Lustrin A, a matrix protein from shell and pearl nacre of *Haliotis rufescens*. *J Biol Chem* 1997;272:32472–81.
- [338] Fu G, Valiyaveetil S, Wopenka B, Morse DE. CaCO₃ biomineralization: acidic 8-kDa proteins isolated from aragonitic abalone shell nacre can specifically modify calcite crystal morphology. *Biomacromolecules* 2005;6:1289–98.
- [339] Bruet BJF, Qi HJ, Boyce MC, Panas R, Tai K, Frick L, et al. Nanoscale morphology and indentation of individual nacre tablets from the gastropod mollusc *Trochus niloticus*. *J Mater Res* 2006;20:2400–19.
- [340] Marin F, Luquet G. Molluscan biomineralization: the proteinaceous shell constituents of *Pinna nobilis* L. *Mater Sci Eng C* 2005;25:105–11.
- [341] Blank S, Arnoldi M, Khoshnavaz S, Treccani L, Kuntz M, Mann K, et al. The nacre protein perlucin nucleates growth of calcium carbonate crystals. *J Microsc* 2003;212:280–91.
- [342] Kim IW, DiMasi E, Evans JS. Identification of mineral modulation sequences within the nacre-associated oyster shell protein, n16. *Cryst Growth Design* 2004;4:113–8.
- [343] Wustman BA, Morse DE, Evans JS. Structural characterization of the N-terminal mineral modification domains from the molluscan crystal-modulating biomineralization proteins, AP7 and AP24. *Biopolymers* 2004;74:262–76.
- [344] Heinemann F, Treccani L, Fritz M. Abalone nacre insoluble matrix induces growth of flat and oriented aragonite crystals. *Biochem Biophys Res Comm* 2006;344:45–9.
- [345] Suzuki M, Saruwatari K, Kogure T, Yamamoto Y, Nishimura T, Kato T, et al. An acidic matrix protein, Pif, is a key macromolecule for nacre formation. *Science* 2009;325:1388–90.
- [346] Song F, Bai XH, Bai YL. Microstructure and characteristics in the organic matrix layers of nacre. *J Mater Res* 2002;17:1567–70.
- [347] Barthelat F, Li CM, Comi C, Espinosa HD. Mechanical properties of nacre constituents and their impact on mechanical performance. *J Mater Res* 2006;21:1977–86.
- [348] Lin AYM, Meyers MA. Interfacial shear strength in abalone nacre. *J Mech Behav Biomed Mater* 2009;2:607–12.
- [349] Song F, Soh AK, Bai YL. Structural and mechanical properties of the organic matrix of nacre. *Biomaterials* 2003;24:3623–31.

- [350] Evans AG, Suo Z, Wang RZ, Aksay IA, He MY, Hutchinson JW. Model for the robust mechanical behavior of nacre. *J Mater Res* 2001;16:2475–93.
- [351] Li X, Chang WC, Chao YJ, Wang R, Chang M. Nanoscale structural and mechanical characterization of a natural nanocomposite material: the shell of red abalone. *Nano Lett* 2004;4:613–7.
- [352] Currey JD. Further studies on mechanical properties of mollusk shell material. *J Zool* 1976;180:445–53.
- [353] Currey JD. Mechanical properties of mollusk shell. In: Vincent JFV, Currey JD, editors. *The mechanical properties of biological materials* (Symp. Soc. Exp. Biol. 34). Cambridge: Cambridge University Press; 1980. p. 73–87.
- [354] Currey JD, Brear K. Fatigue fracture of mother-of-pearl and its significance for predatory techniques. *J Zool* 1984;204:541–8.
- [355] Currey JD, Zioupos P, Davis A, Casinos A. Mechanical properties of nacre and highly mineralized bone. *Proc R Soc Lond B* 2001;268:107–11.
- [356] Jackson AP, Vincent JFV, Turner RM. A physical model of nacre. *Compos Sci Technol* 1989;36:225–66.
- [357] Jackson AP, Vincent JFV, Turner RM. Comparison of nacre with other ceramic composites. *J Mater Sci* 1990;25:3173–8.
- [358] Laraiá VJ, Heuer AH. Novel composite microstructure and mechanical behavior of mollusk shell. *J Am Ceram Soc* 1989;72:2177–9.
- [359] Sarikaya M, Gunnison KE, Aksay IA. Seashells as a natural model to study ceramic-polymer composites. In: Bailey GW, editor. *Proc 47th ann meeting EMSA*. San Francisco: San Francisco Press; 1989. p. 558–9.
- [360] Sarikaya M, Gunnison KE, Yasrebi M, Aksay IA. Mechanical property-microstructural relationships in abalone shell. In: Rieke PC, Calvert PD, Alper M, editors. *Materials synthesis utilizing biological processes*. MRS symp proc, vol. 174. Pittsburgh: Materials Research Society; 1990. p. 109–16.
- [361] Sarikaya M, Liu J, Aksay IA. Nacre properties, crystallography, morphology, and formation. In: Sarikaya M, Aksay IA, editors. *Biomimetics: design and processing of materials*. New York: American Institute of Physics; 1995. p. 35–90.
- [362] Mayer G. New classes of tough composite materials – lessons from natural rigid biological systems. *Mater Sci Eng C* 2006;26:1261–8.
- [363] Tang H, Barthelat F, Espinosa HD. An elasto-viscoplastic interface model for investigating the constitutive behavior of nacre. *J Mech Phys Solids* 2007;7:1410–38.
- [364] Barthelat F, Espinosa HD. An experimental investigation of deformation and fracture of nacre – mother of pearl. *Exp Mech* 2007;47:311–24.
- [365] Barthelat F, Zhu D. A novel biomimetic material duplicating the structure and mechanics of natural nacre. *J Mater Res* 2011;26:1203–15.
- [366] Yang W, Zhang GP, Zhu XF, Li XW, Meyers MA. Structure and mechanical properties of *Saxidomus purpuratus* bivalve shells. *J Mech Behav Biomed Mater* 2011;4:1514–30.
- [367] Yang W, Kashani N, Li XW, Zhang GP, Meyers MA. Structural characterization and mechanical behavior of a bivalve shell (*Saxidomus purpuratus*). *Mater Sci Eng C* 2011;31:724–9.
- [368] Schultz H. Sea urchins. Hemdingen: Heinke & Peter Schutz Partner; 2006.
- [369] Magdans U, Gies H. Single crystal structure analysis of sea urchin spine calcites: systematic investigations of the Ca/Mg distribution as a function of habitat of the sea urchin and the sample location in the spine. *Eur J Mineral* 2004;16:261–8.
- [370] Presser V, Schultheiß S, Berthold C, Nickel KG. Sea urchin spines as a model-system for permeable, light-weight ceramics with graceful failure behavior. Part I. Mechanical behavior of sea urchin spines under compression. *J Bionic Eng* 2009;6:203–13.
- [371] Ma Y, Cohen SR, Addadi L, Weiner S. Sea urchin tooth design: An “all-calcite” polycrystalline reinforced fiber composite for grinding rocks. *Adv Mater* 2008;20:1555–9.
- [372] Ma Y, Aichmayer B, Paris O, Fratzl P, Meibomc A, Metzler RA, et al. The grinding tip of the sea urchin tooth exhibits exquisite control over calcite crystal orientation and Mg distribution. *Proc Natl Acad Sci USA* 2009;106:6048–53.
- [373] Sethman I, Hinrichs R, Wörheide G, Putnis A. Nano-cluster composite structure of calcitic sponge spicules – a case study of basic characteristics of biominerals. *J Inorg Biochem* 2006;100:88–96.
- [374] Woesz A, Weaver JC, Kazanci M, Dauphin Y, Aizenberg J, Morse DE, et al. Micromechanical properties of biological silica in skeletons of deep-sea sponges. *J Mater Res* 2006;21:2068–78.
- [375] Aizenberg J, Weaver JC, Thanawala MS, Sundar VC, Morse DE, Fratzl P. Skeleton of *Euplectella sp*: structural hierarchy from the nanoscale to the macroscale. *Science* 2005;309:275–8.
- [376] Cha JN, Shimizu K, Zhou Y, Christiansen SC, Chmelka BF, Stucky GD, et al. Silicatein filaments and subunits from a marine sponge direct the polymerization of silica and silicones in vitro. *Proc Natl Acad Sci USA* 1999;96:361–5.
- [377] Cha JN, Stucky GD, Morse DE, Deming TJ. Biomimetic synthesis of ordered silica structures mediated by block copolypeptides. *Nature* 2000;403:289–92.
- [378] Miserez A, Schneberk T, Sun C, Zok FW, Waite JH. The transition from stiff to compliant materials in squid beaks. *Science* 2008;319:1816–9.
- [379] Aizenberg J, Hendlar G. Designing efficient microlens arrays: lessons from nature. *J Mater Chem* 2004;14:2066–72.
- [380] Poulsen N, Sumper M, Kröger N. Biosilica formation diatoms: characterization of native silaffin-2 and its role in silica morphogenesis. *Proc Natl Acad Sci* 2003;100:12075–80.
- [381] Armbrust EV, Berges JA, Bowler C, Green BR, Martinez D, Putnam NH, et al. The genome of the diatom *Thalassiosira pseudonana*: ecology, evolution, and metabolism. *Science* 2004;306:79–86.
- [382] Hildebrand M. Prospects of manipulating diatom silica nanostructure. *J Nanosci Nanotechnol* 2005;5:146–57.
- [383] Hildebrand M. Diatoms, biomineralization processes, and genomics. *Chem Rev* 2008;108:4855–74.
- [384] Kulchin YN, Bezverby AV, Bukin OA, Voznesensky SS, Galkina AN, Drozdov AL, et al. Optical and nonlinear optical properties of sea glass sponge spicules. *Prog Mol Subcell Biol* 2009;47:315–40.
- [385] Shergold EA, Norman A, Fleck NA, Radford D. The uniaxial stress versus strain response of pig skin and silicone rubber at low and high strain rates. *Int J Impact Eng* 2006;32:1384–402.
- [386] Zhou B, Xu F, Chen CQ, Lu TJ. Strain rate sensitivity of skin tissue under thermomechanical loading. *Philos Trans R Soc A* 2010;368:679–90.
- [387] Olson P, Watabe N. Studies on formation and resorption of fish scales. *Cell Tissue Res* 1980;211:303–16.

- [388] Zylberberg L, Nicolas G. Ultrastructure of scales in a teleost (*Carassius auratus* L.) after use of rapid freeze-fixation and freeze-substitution. *Cell Tissue Res* 1982;223:349–67.
- [389] Zylberberg L, Bereiter-Hahn J, Sire JY. Cytoskeletal organization and collagen orientation in the fish scales. *Cell Tissue Res* 1988;253:597–607.
- [390] Bruet BJF, Song J, Boyce MC, Ortiz C. Materials design principles of ancient fish armor. *Nat Mater* 2008;7:748–56.
- [391] Vernerey FJ, Barthelat F. On the mechanics of fish scale structures. *Int J Sol Struct* 2011;47:2268–75.
- [392] Ikoma T, Kobayashi H, Tanaka J, Wals D, Mann S. Microstructure, mechanical, and biomimetic properties of fish scales from *Pagrus major*. *J Struct Biol* 2003;142:327–33.
- [393] Scheyer TM, Sander PM. Histology of ankylosaur osteoderms: implications for systematics and function. *J Vert Paleontol* 2004;24:874–93.
- [394] Farlow JO, Hayashi S, Tattersall GJ. Internal vascularity of the dermal plates of *Stegosaurus* (Ornithischia, Thyreophora). *Swiss J Geosci* 2010;103:173–85.
- [395] Song J, Ortiz C, Boyce MC. Threat-protection mechanics of an armored fish. *J Mech Behav Biomed Mater* 2011;4:699–712.
- [396] Onozato H, Watabe N. Studies on fish scale formation and resorption. *Cell Tissue Res* 1979;201:409–22.
- [397] Zylberberg L, Bonaventure J, Cohen-Solal L, Hartmann DJ, Bereiter-Hahn J. Organization and characterization of fibrillar collagens in fish scales in situ and in vitro. *J Cell Sci* 1992;103:273–85.
- [398] Meyers MA, Lin YS, Olvesky EA, Chen P-Y. Battle in the Amazon: Arapaima (Pirarucu) vs. Serrasalminae (Piranha). *Adv Biomater* 2012;14:B1–10. <http://dx.doi.org/10.1002/adem.20118002>.
- [399] Torres FG, Troncoso OP, Nakamatsu J, Grande CJ, Gomez CM. Characterization of the nanocomposite laminate structure occurring in fish scales from *Arapaima gigas*. *Mater Sci Eng C* 2008;28:1276–83.
- [400] Hight TK, Brandeau JF. Mathematical modeling of the stress strain-strain rate behavior of bone using the Ramberg-Osgood equation. *J Biomech* 1983;16:445–50.
- [401] Bouligand Y. Twisted fibrous arrangements in biological materials and cholesteric mesophases. *Tissue Cell* 1972;4:189–217.
- [402] Dai Z, Yang Z. Macro-/micro-structures of elytra, mechanical properties of the biomaterial and the coupling strength between elytra in beetles. *J Bionic Eng* 2010;7:6–12.
- [403] Mahoney E, Holt A, Swain M, Kilpatrick N. The hardness and modulus of elasticity of primary molar teeth: an ultra-micro-indentation study. *J Dent* 2000;28:589–94.
- [404] Hughes PM. Insect cuticular growth layers seen under the scanning electron microscope: a new display method. *Tiss Cell* 1987;19:705–12.
- [405] Lichtenegger HC, Schöberl T, Ruokolainen JT, Cross JO, Heald SM, Birkedal H, et al. Zinc and mechanical prowess in the jaws of *Nereis*, a marine worm. *Proc Natl Acad Sci USA* 2003;100:9144–9.
- [406] Broomell CC, Mattoni MA, Zok FW, Waite JH. Critical role of zinc in hardening of *Nereis* jaw. *J Exp Biol* 2006;209:3219–25.
- [407] Broomell CC, Khan RK, Moses DN, Miserez A, Pontin MG, Stucky GD, et al. Mineral minimization in nature's alternative teeth. *Proc Royal Soc Inter* 2007;4:19–31.
- [408] Nishino T, Matsui R, Nakame K. Elastic modulus of the crystalline regions of α -chitin and chitosan. *J Polym Sci Part B: Polym Phys* 1999;37:1191–6.
- [409] Vincent JFV, Wegst UGK. Design and mechanical properties of insect cuticle. *Arthropod Struct Dev* 2004;33:187–99.
- [410] Rebers JE, Willis JH. A conserved domain in arthropod cuticular proteins binds chitin. *Insect Biochem* 2001;31:1083–93.
- [411] Hamodrakas SJ, Willis JH, Iconomidou VA. A structural model of the chitin-binding domain of cuticle proteins. *Insect Biochem* 2002;32:1577–83.
- [412] Raabe D, Al-Sawalimih A, Yi SB, Fabritius H. Preferred crystallographic texture of alpha-chitin as a microscopic and macroscopic design principle of the exoskeleton of the lobster *Homarus americanus*. *Acta Biomater* 2007;3:882–95.
- [413] Sachs C, Fabritius H, Raabe D. Influence of the microstructure on deformation anisotropy of mineralized cuticle from the lobster *Homarus americanus*. *J Struct Biol* 2008;161:120–32.
- [414] Nikolov S, Raabe D. Hierarchical modeling of the elastic properties of bone at submicron scales: the role of extrafibrillar mineralization. *Biophys J* 2008;94:4220–32.
- [415] Nikolov S, Petrov M, Lymparakis L, Friák M, Sachs C, Fabritius H, et al. Revealing the design principles of high-performance biological composites using ab initio and multiscale simulations: the example of lobster cuticle. *Adv Mater* 2010;22:519–26.
- [416] Nikolov S, Fabritius H, Petrov M, Friák M, Lymparakis L, Sachs C, et al. Robustness and optimal use of design principles of arthropod exoskeletons studied by ab initio-based multiscale simulations. *J Mech Behav Biomed Mater* 2011;4:129–45.
- [417] Wu T-M, Fink DJ, Arias JL, Rodriguez JP, Heuer AH, Caplan AI. The molecular control of avian eggshell mineralization. In: Slavkin HC, Price P, editors. *Chemistry and biology of mineralized tissues*. New York: Elsevier; 1992. p. 133–41.
- [418] Silyn-Roberts H, Sharp RM. Crystal growth and the role of the organic network in eggshell biomineralization. *Proc R Soc Lond B* 1988;227:303–24.
- [419] Flory PJ. Theory of elastic mechanisms in fibrous proteins. *J Am Chem Soc* 1956;78:5222–35.
- [420] Vincent JFV. Survival of the cheapest. *Mater Today* 2002;5:24–41.
- [421] Karam GN, Gibson LJ. Biomimicking of animal quills and plant stems: natural cylindrical shells with foam cores. *Mater Sci Eng C* 1994;2:113–32.
- [422] Atkins AG. *The science and engineering of cutting*. Oxford: Butterworths-Heinemann; 2009.
- [423] Chen P-Y, Schirer J, Simpson A, Nay R, Lin Y-S, Yang W, et al. Predation vs. protection: fish teeth and scales evaluated by nanoindentation. *J Mater Res* 2012;27:100–12.
- [424] Diamond JM. How great white sharks, saber-toothed cats and soldiers kill. *Nature* 1986;322:773–4.
- [425] Frazzetta TH. The mechanics of cutting and the form of shark teeth (*Chondrichthyes, Elasmobranchii*). *Zoomorphology* 1988;108:93–107.
- [426] Johnson W, Soden PD, Trueman ER. A study in jet propulsion: an analysis of the motion of the squid, *Loligo vulgaris*. *Exp Biol* 1972;56:155–65.
- [427] Miserez A, Rubin D, Waite JH. Cross-linking chemistry of squid beak. *J Biol Chem* 2010;285:38115–24.

- [428] Miserez A, Weaver JC, Pedersen PB, Schneeberk T, Hanlon RT, Kisailus D, et al. Microstructural and biochemical characterization of the nanoporous sucker rings from *Dosidicus gigas*. *Adv Mater* 2009;21:401–6.
- [429] Moses DN, Harrelld JD, Stucky GD, Waite JH. Melanin and Glycera Jaws. Emerging dark side of a robust biocomposite structure. *J Biol Chem* 2006;281:34826–32.
- [430] Moses DN, Pontin MG, Waite JH, Zok FW. Effects of hydration on mechanical properties of a highly sclerotized tissue. *Biophys J* 2008;94:3266–72.
- [431] Rubin D, Miserez A, Waite JH. Antecedents of arthropod sclerotization. In: Casas J, editor. *Advances in insect physiology*, vol. 38. New York: Elsevier; 2010. p. 75–133.
- [432] Hillerton JE, Reynolds SE, Vincent JFV. On the indentation hardness of insect cuticle. *J Exp Biol* 1982;96:45–52.
- [433] Hillerton JE, Vincent JFV. The specific location of zinc in insect mandibles. *J Exp Biol* 1982;101:333–66.
- [434] Quicke DLJ, Wyeth P, Fawke JD, Basibuyuk HH, Vincent JFV. Manganese and zinc in the ovipositors and mandibles of hymenopterous insects. *Zool J Linn Soc* 1998;124:387–96.
- [435] Schofield RMS, Nesson MH, Richardson KA. Tooth hardness increases with zinc-content in mandibles of young adult leaf-cutter ants. *Naturwissenschaften* 2002;89:579–83.
- [436] Cribb BW, Stewart A, Huang H, Truss R, Noller B, Rasch R, et al. Insect mandibles – comparative mechanical properties and links with metal incorporation. *Naturwissenschaften* 2008;95:17–23.
- [437] Cribb BW, Lin C-L, Rintoul L, Rasch R, Hasenpusch J, Huang H. Hardness in arthropod exoskeletons in the absence of transition metals. *Acta Biomater* 2010;6:3152–6.
- [438] Hörschemeyer T, Beutel RG, Pasop F. Head structures of *Priacma serrata* Leconte (Coleoptera, Archostemata) inferred from X-ray tomography. *J Morphol* 2002;252:298–314.
- [439] Dickinson M. Mechanical properties of an arthropod exoskeleton – nanoindentation of the beetle *Scarites subterraneus*. *HysitronTM Nanoindentation Application Note*; 2008.
- [440] Patek SN, Baio JE, Fisher BL, Suarez AV. Multifunctionality and mechanical origins: ballistic jaw propulsion in trap-jaw ants. *Proc Natl Acad Sci* 2006;103:12787–92.
- [441] Ikeshoji T. The interface between mosquitoes and humans. Tokyo: University of Tokyo Press; 1999.
- [442] Oka K, Aoyagi S, Hashiguchi G, Isono Y, Fujita H. Fabrication of a micro needle for a trace blood test. *Proc Sensors and Actuators A* 2002;97–98:478–85.
- [443] Vincent JFV, King MJ. The mechanism of drilling by wood wasp ovipositors. *Biomimetics* 1995;3:187–201.
- [444] Gao Y, Ellery A, Jaddou M, Vincent J. Deployable wood wasp drill for planetary subsurface sampling. *IEEEAC paper #1591*, version 1. *IEEE*; 2006. p. 1–8.
- [445] Crenshaw DG. Design and materials of feather shafts: very light, rigid structures. *Symp Soc Exp Biol* 1980;34:485–6.
- [446] Chernova OF. Polymorphism of the architectonics of definitive contour feathers. *Doklady Akademii Nauk* 2005;404:280–5.
- [447] Lingham-Soliar T, Bonser RHC, Wesley-Smith J. Selective biodegradation of keratin matrix in feather rachis reveals classic bioengineering. *Proc R Soc B* 2009;277:1161–8.
- [448] Friedmann H, Davis M. Left-handedness in parrots. *The Auk* 1938;55:478.
- [449] Filshie BK, Rogers GE. An electron microscope study of the fine structure of feather keratin. *J Cell Biol* 1962;13:1–12.
- [450] Bonser RHC. Melanin and the abrasion resistance of feathers. *The Condor* 1995;95:590–1.
- [451] Bonser RHC, Purslow PP. The Young's modulus of feather keratin. *J Exp Biol* 1995;198:1029–33.
- [452] Prum RO. Development and evolutionary origin of feathers. *J Exp Zool* 1999;285:291–306.
- [453] Pabisch S, Puchegger S, Kirchner HOK, Weiss IM, Peterlik H. Keratin homogeneity in the tail feathers of *Pavo cristatus* and *Pavo cristatus* mut. *Alba*. *J Struct Biol* 2010;172:270–5.
- [454] Burgess SC, King A, Hyde R. An analysis of optimal structural feathers in the peacock tail feather. *Opt Laser Technol* 2006;38:329–34.
- [455] Weiss IM, Kirchner HOK. The peacock's train (*Pavo cristatus* and *Pavo cristatus* mut. *alba*) I. Structure, mechanics, and chemistry of the tail feather coverts. *J Exp Zool* 2010;313A:690–703.
- [456] Seki Y, Meyers MA. Unpublished result; 2011.
- [457] Fecchio RS, Seki Y, Bodde SG, Gomes MS, Kolosowski J, Rossi JL, et al. Mechanical behavior of prosthesis in Toucan beak (*Ramphastos toco*). *Mater Sci Eng C* 2010;30:460–4.
- [458] Ryan SD, Williams JL. Tensile testing of rodlike trabeculae excised from bovine femoral bone. *J Biomech* 1989;22:351–5.
- [459] Lucchinetti E, Thomann D, Danuser G. Review: micromechanical testing of bone trabeculae-potentials and limitations. *J Mater Sci* 2000;35:6057–64.
- [460] Bini F, Marinozzi A, Marinozzi F, Patane F. Microtensile measurement of single trabeculae stiffness in human femur. *J Biomech* 2002;35:1515–9.
- [461] Hernandez CJ, Tang SY, Baumbach BM, Hwu PB, Sakke AN, van der Ham F, et al. Trabecular microfracture and the influence of pyridinium and non-enzymatic glycation-mediated collagen cross-links. *Bone* 2005;37:825–32.
- [462] Kiang J, McKittrick J, Meyers MA. Wing bone design of soaring birds. Unpublished work.
- [463] Brodtkorb P. Number of feathers and weights of various systems in a bald eagle. *Wilson Bull* 1955;67:142.
- [464] Davis PG. The bioerosion of bird bones. *Int J Osteoarch* 1998;7:388–401.
- [465] Currey JD, Alexander RM. The thickness of the walls of tubular bones. *J Zool A* 1985;206:453–68.
- [466] Cubo J, Casinos A. Incidence and mechanical significance of pneumatization in the long bones of birds. *Zool J Linn Soc* 2000;130:499–510.
- [467] Swartz SM, Bennett ME, Carrier DR. Wing bone stresses in free flying bats and the evolution of skeletal design for flight. *Nature* 1992;359:726–9.
- [468] Dumont ER. Bone density and the lightweight skeletons of birds. *Proc R Soc B* 2010;277:2193–8.
- [469] Buhler P. Sandwich structures in the skull capsules of various birds: the principles of light-weight structures in organisms. In: *Information of the Institute for Lightweight Structures*, vol. 1L4, Stuttgart: University of Stuttgart; 1972.
- [470] Berglin M, Gatenholm P. The barnacle adhesive plaque: morphological and chemical differences as a response to substrate properties. *Colloids Surf* 2003;28:107–17.

- [471] Kamino K, Inoue K, Maruyama T, Takamatsu N, Harayama S, Shizuri Y. Barnacle cement proteins. Importance of disulfide bonds in their insolubility. *J Biol Chem* 2000;275:27360–5.
- [472] Kamino K. Underwater adhesive of marine organisms as the vital link between biological science and material science. *Marine Biotechnol* 2008;10:111–21.
- [473] Waite JH, Tanzer ML. Polyphenolic substance of *Mytilus edulis*—novel adhesive containing L-DOPA and hydroxyproline. *Science* 1981;212:1038.
- [474] Waite JH. Nature's underwater adhesive specialist. *Int J Adhes* 1987;7:9.
- [475] Bell EC, Gasoline JM. Mechanical design of mussel byssus: material yield enhances attachment strength. *J Exp Biol* 1996;199:1005–17.
- [476] Lee BP, Messersmith PB, Israelachvili JN, Waite JH. Mussel-inspired adhesives and coatings. *Annu Rev Mater Res* 2011;41:99–132.
- [477] Barnes WJP. Functional morphology and design constraints of smooth adhesive pads. *MRS Bull* 2007;32:479–85.
- [478] Yu J, Wei W, Danner E, Israelachvili JN, Waite JH. Effects of interfacial redox in mussel adhesive protein films on mica. *Adv Mater* 2011;23:2362–6.
- [479] Yu J, Wei W, Danner E, Ashley RK, Israelachvili JN, Waite JH. Mussel protein adhesion depends on interprotein thiol-mediated redox modulation. *Nat Chem Biol* 2011;7:588–90.
- [480] Lee H, Scherer NF, Messersmith PB. Single-molecule mechanics of mussel adhesion. *Proc Natl Acad Sci USA* 2006;103:12999–3003.
- [481] Autumn K, Sitti M, Liang YA, Peattie AM, Hansen WR, Sponberg S, et al. Evidence for van der Waals adhesion in gecko setae. *Proc Natl Acad Sci USA* 2002;99:12252–6.
- [482] Arzt E, Gorb S, Spolenek R. Evidence for van der Waals adhesion in gecko setae. *Proc Natl Acad Sci USA* 2003;100:10603–6.
- [483] Spolenek R, Gorb S, Gao H, Arzt E. Effects of contact shape on the scaling of biological attachments. *Proc R Soc A* 2005;461:305–19.
- [484] Huber G, Mantz H, Spolenek R, Mecke K, Jacobs K, Gorb SN, et al. *Proc Natl Acad Sci USA* 2005;102:16293–6.
- [485] Ugral AC, Fenster SK. Advanced strength and applied elasticity. New York: Elsevier; 1987.
- [486] Johnson KL, Kendall K, Roberts AD. Surface energy and the contact of elastic solids. *Proc R Soc Lond* 1971;324:301–13.
- [487] Peattie AM, Full RJ. Phylogenetic analysis of the scaling of wet and dry biological fibrillar adhesives. *Proc Natl Acad Sci USA* 2007;104:18595.
- [488] Qian J, Gao H. Scaling effects of wet adhesion in biological attachment systems. *Acta Biomater* 2006;2:51–8.
- [489] Ernst VV. The digital pads of the tree frog *Hyla cinerea*. I. The epidermis. *Tissue Cell* 1973;5:83–96.
- [490] Welsh U, Storch V, Fuchs W. The fine structure of the digital pads of rhacophorid tree frogs. *Cell Tissue Res* 1974;148:407–16.
- [491] Green DM. Tree frog toe pads: comparative surface morphology using scanning electron microscopy. *Can J Zool* 1979;57:2033–46.
- [492] Green DM, Simon P. Digital microstructure in ecologically diverse sympatric microhylid frogs, genera *Cophixalus* and *Sphenophryne* (Amphibia: Anura) Papua New Guinea. *Aust J Zool* 1986;34:135–45.
- [493] McAllister A, Channing L. Comparisons of toe pads of some Southern African climbing frogs. *S Afr J Zool* 1983;18:110–4.
- [494] Hanna G, Barnes WJP. Adhesion and detachment of the toe pads of treefrogs. *J Exp Biol* 1991;155:103–25.
- [495] Barnes WJP, Perez-Goodwyn P, Gorb SN. Mechanical properties of the toe pads of the tree frog *Litoria caerulea*. *Comp Biochem Physiol A* 2005;141:S145.
- [496] Barnes WJP, Oines C, Smith JM. Whole animal measurements of shear and adhesive forces in adult tree frogs: insights into underlying mechanisms of adhesion obtained from studying the effects of size and shape. *J Comp Physiol A* 2006;192:1179–91.
- [497] Trueman ER, Hodgson AN. The fine structure and function of the foot of *Nassarius krausslanus*, a gastropod moving by ciliary locomotion. *J Moll Stud* 1990;56:221–8.
- [498] Donovan DA, Carefoot TH. Locomotion in the abalone *Haliotis kamschatkana*: pedal morphology and cost of transport. *J Exp Biol* 1997;200:1145–53.
- [499] Kaplan DL, Lombardi SJ, Muller WS, Fossey SA. In: Byrom D, editor. *Biomaterials: novel materials from biological sources*. New York: Stockton Press; 1991.
- [500] Kaplan D, Adams WW, Viney C, Farnen B. *Am Chem Soc Symp* 1994:S544.
- [501] Gosline JM, Denny MW, DeMont ME. Spider silk as rubber. *Nature* 1984;309:551–2.
- [502] Perez-Rigueiro J, Viney C, Llorca J, Elices M. Mechanical properties of silkworm silk in liquid media. *J Appl Polym Sci* 2000;75:1270–7.
- [503] Vollrath F. Strength and structure of spiders' silks. *Rev Mol Biotechnol* 2000;74:67–83.
- [504] Sahni V, Blackledge TA, Dhinojwala A. Viscoelastic solids explain spider web stickiness. *Nat Commun* 2010;1:19.
- [505] Lee H. Biomaterials: intelligent glue. *Nature* 2010;465:298–9.
- [506] Nova A, Ketten S, Pugno N, Redaelli A, Buehler MJ. Molecular and nanostructural mechanisms of deformation, strength and toughness of spider silk fibrils. *Nano Lett* 2010;10:2626–34.
- [507] Waite JH, Holten-Andersen N, Jewhurst S, Sun CJ. Mussel adhesion: finding tricks worth mimicking. *J Adhes* 2005;81:297–317.
- [508] Waite JH. Precursors of quinone tanning: dopa-containing proteins. *Methods Enzymol* 1995;258:1–20.
- [509] Lin Q, Gourdon D, Sun C, Holten-Andersen N, Anderson TH, Waite JH, et al. Adhesion mechanisms of the mussel foot proteins mfp-1 and mfp-3. *Proc Natl Acad Sci USA* 2007;104:3782–6.
- [510] Guvendiren M, Brass DA, Messersmith PB, Shull R. Adhesion of DOPA-functionalized model membranes to hard and soft surfaces. *J Adhes* 2009;9:631–45.
- [511] Zeng H, Hwang DS, Israelachvili JN, Waite JH. Strong reversible Fe³⁺ mediated bridging between dopa-containing protein films in water. *Proc Natl Acad Sci USA* 2010;107:12850–3.
- [512] Hwang DS, Zeng H, Masic A, Harrington MJ, Israelachvili JN, Waite JH. Protein- and metal-dependent interactions of a prominent protein in mussel adhesive plaques. *J Biol Chem* 2010;285(33):25850–8.

- [513] Barthlott W, Ehler N. Raster-Elektronenmikroskopie der Epidermis-Oberflächen von Spermatophyten. *Trop subtrop Pflanzenwelt (Akad Wiss Lit Mainz)* 1977;19:110.
- [514] Barthlott W. Scanning electron microscopy of the epidermal surface in plants. In: Claugher D, editor. *Application of the scanning EM in taxonomy and functional morphology*. Systematics Association's Special Volume. Oxford: Clarendon Press; 1990. p. 69–94.
- [515] Barthlott W, Neinhuis C. The purity of sacred lotus or escape from contamination in biological surfaces. *Planta* 1997;202:1–8.
- [516] Koch K, Bhushan B, Barthlott W. Multifunctional surface structures of plants: an inspiration for biomimetics. *Prog Mater Sci* 2009;54:137–78.
- [517] Ma M, Vijayan K, Hiltner A, Baer E, Im J. Thickness effects in microlayer composites of polycarbonate and poly-(styrene-acrylonitrile). *J Mater Sci* 1990;25:2039–46.
- [518] Ma M, Im J, Hiltner A, Baer E. Fatigue crack propagation of polycarbonate and poly-(styrene-acrylonitrile). *J Appl Poly Sci* 1990;40:669–84.
- [519] Syn CK, Lesuer DR, Wolfenstine J, Sherby OD. Layer thickness effect on ductile tensile fracture of ultrahigh carbon steel-brass laminates. *Mater Trans A* 1993;24:1647–53.
- [520] Ortiz C, Boyce MC. Bioinspired structural materials. *Science* 2008;319:1053–4.
- [521] Aizenberg J. New nanofabrication strategies: inspired by biomineralization. *MRS Bull* 2010;35:323–30.
- [522] White SR, Sottos NR, Geubelle PH, Moore JS, Kessler MR, Sviran SR, et al. Autonomic healing of polymer composites. *Nature* 2001;409:794–7.
- [523] Toohy KS, Sottos NR, Lewis JA, Moore JS, White SR. Self-healing materials with microvascular networks. *Nat Mater* 2007;6:581–5.
- [524] Veedu VP, Cao A, Li X, Ma K, Soldano C, Kar S, et al. Multifunctional composites using reinforced laminate with carbon-nanotube forests. *Nat Mater* 2006;5:457–62.
- [525] Milwich M, Speck T, Speck O, Stegmaier T, Planck H. Biomimetics and technical textiles: solving engineering problems with the help of nature's wisdom. *Am J Botany* 2006;93:1455–65.
- [526] Utsunomiya H, Koh H, Miyamoto J, Skai T. High strength porous copper by cold extrusion. *Adv Eng Mater* 2008;10:826–9.
- [527] Zampieri A, Sieber H, Selvam T, Mabande GTP, Schwiager W, Scheffler F, et al. Biomimetic SiSiC/zeolite ceramic composites: from rattan palm to bioinspired structured monoliths for catalysis and sorption. *Acta Mater* 2005;17:344–9.
- [528] Zollfrank C, Travitzky N, Sieber H, Selchert T, Greil P. Biomimetic SiSiC/Al–Si ceramic composites manufactured by squeeze casting: microstructure and mechanical properties. *Adv Eng Mater* 2005;7:743–6.
- [529] Griel P, Lifka T, Kaindl A. Biomimetic cellular silicon carbide ceramics from wood: I. *J Eur Ceram Soc* 1998;18:1961–73.
- [530] Arias JL, Fernandez MS. Biomimetic processes through the study of mineralized shells. *Mater Charact* 2005;50:189–95.
- [531] Meldrum FC, Ludwigs S. Template-directed control of crystal morphologies. *Macromol Biosci* 2007;7:152–62.
- [532] Almqvist N, Thomson NH, Smith BL, Stucky GD, Morse DE, Hansma PK. Methods for fabricating and characterizing a new generation of biomimetic materials. *Mater Sci Eng C* 1999;7:37–43.
- [533] Zhao S, Zhang J, Zhao S, Li W, Li H. Effect of inorganic-organic interface adhesion of mechanical properties of Al₂O₃/polymer laminate composites. *Compos Sci Technol* 2003;63:1009–14.
- [534] Tang Z, Kotov NA, Magonov S, Ozturk B. Nanostructured artificial nacre. *Nat Mater* 2003;2:413–9.
- [535] Chen R, Wang C, Huang Y, Le H. An efficient biomimetic process for fabrication of artificial nacre with ordered-nanostructure. *Mater Sci Eng C* 2008;28:218–22.
- [536] Deville S, Saiz E, Natta RK, Tomsia AP. Freezing as a path to build complex composites. *Science* 2006;311:515–8.
- [537] Munch E, Launey ME, Alsem DH, Saiz E, Tomsia AP, Ritchie RO. Tough, bio-inspired hybrid materials. *Science* 2008;322:1516–20.
- [538] Mahler W, Bechtold MF. Freeze-formed silica fibres. *Nature* 1980;285:27–8.
- [539] Fukasawa T, Ando M, Ohji T, Kanzaki S. Synthesis of porous ceramics with complex pore structure by freeze-dry processing. *J Am Ceram Soc* 2001;84:230–2.
- [540] Qu F, Rahaman MN, Dogan F, Bai BS. Freeze casting of porous hydroxyapatite scaffolds. I. Processing and general microstructure. *J Biomed Mater Res B – Appl Biomater* 2008;86:125–34.
- [541] Launey ME, Munch E, Alsem DH, Barth HD, Saiz E, Tomsia AP, et al. Designing highly toughened hybrid composites through nature-inspired hierarchical complexity. *Acta Mater* 2009;57:2919–32.
- [542] Berling J, Rechberger M. Knives as sharp as Rat's Teeth, research news 1 (Oberusel, Germany: Fraunhofer Institute for Environmental, Safety and Energy Technology, Topic3; 2007 www.fraunhofer.de/fhg/EN/press/pi/2005/01/Mediendienst012005Thema3.jsp).
- [543] Srivastava A, Holten-Andersen N, Stucky GD, Waite JH. Ragworm jaw-inspired metal ion cross-linking for improved mechanical properties of polymer blends. *Biomacromolecules* 2008;9:2873–80.
- [544] Bartol IK, Gharib M, Weihs D, Webb PW, Hove JR, Gordon MS. Hydrodynamic stability of swimming in ostraciid fishes: role of the carapace in the smooth trunkfish *Lactophrys triqueter* (Teleostei: Ostraciidae). *J Exp Biol* 2003;206:725–44.
- [545] Bartol IK, Gharib M, Webb PW, Weihs D, Gordon MS. Body-induced vortical flows: a common mechanism for self-corrective trimming control in boxfishes. *J Exp Biol* 2005;208:327–44.
- [546] Del Campo A, Greiner C, Alvarez I, Arzt E. Patterned surfaces with pillars with 3D tip geometry mimicking bioattachment devices. *Adv Mater* 2007;19:1973–7.
- [547] Greiner C, Arzt E, Del Campo A. Hierarchical gecko-like adhesives. *Adv Mater* 2009;21:479–82.
- [548] Mahdavi A, Ferreira L, Sundback C, Nichol J, Chan E, Carter D, et al. A biodegradable and biocompatible geckoinspired adhesive. *Proc Natl Acad Sci USA* 2008;105:2307–12.
- [549] Sethi S, Ge L, Ajayan PM, Dhinojwala A. Gecko-inspired carbon nanotube based self cleaning adhesives. *Nano Lett* 2008;8:822–5.
- [550] Dalsin JD, Hu B-H, Lee BP, Messersmith PB. Mussel adhesive protein mimetic polymers for the preparation of nonfouling surfaces. *J Am Chem Soc* 2003;125:4253–8.
- [551] Brubaker CE, Kissler H, Wang L-K, Kaufman DB, Messersmith PB. Biological performance of mussel-inspired adhesive in extrahepatic islet transplantation. *Biomaterials* 2010;31:420–7.

- [552] Shao H, Bachus KN, Stewart RJ. A water-borne adhesive modeled after the sandcastle glue of *P. californica*. *Macromol Biosci* 2009;9:464–71.
- [553] Shao H, Stewart RJ. Biomimetic underwater adhesives with environmentally triggered setting mechanisms. *Adv Mater* 2010;22:729–33.
- [554] Lee H, Dellatore SM, Mille WM, Messersmith PB. Mussel-inspired surface chemistry for multifunctional coatings. *Science* 2007;318:426–30.
- [555] Amstad E, Gillich T, Bilecka I, Textor M, Reimhult E. Ultrastable iron oxide nanoparticle colloidal suspensions using dispersants with catechol-derived anchor groups. *Nano Lett* 2009;9:4042–8.
- [556] Lee H, Lee BP, Messersmith PB. A reversible wet/dry adhesive inspired by mussels and geckos. *Nature* 2007;448:338–41.
- [557] Sandhage KH, Dickerson MB, Huseman PM, Caranna MA, Clifton JD, Bull TA, et al. Novel, bioclastic route to self-assembled, 3D, chemically tailored meso/nanostructures: shape-preserving reactive conversion of biosilica (diatom) microshells. *Adv Mater* 2002;14:429–33.
- [558] Trotter JA, Trotter JA, Tipper J, Lyons-Levy G, Chino K, Heuer AH, et al. Towards a fibrous composite with dynamically controlled stiffness: lessons from echinoderms. *Biochem Soc Trans* 2000;24:357–62.
- [559] Tamori M, Yamada A, Nishida N, Motobayashi Y, Oiwa K, Motokawa T. Tensilin-like stiffening protein from *Holothuria leucospilota* does not induce the stiffest state of catch connective tissue. *J Exp Biol* 2006;209:1594–602.
- [560] Capadona JR, Shanmuganathan KT, Tyler DJ, Rowan SJ, Weder C. Stimuli-responsive polymer nanocomposites inspired by the sea cucumber dermis. *Science* 2008;319:1370–4.
- [561] Potyrailo RA, Ghiradella H, Vertiatichikh A, Dovidenko K, Cournoyer JR, Olson E. Morpho butterfly wing scales demonstrate highly selective vapor response. *Nat Photonics* 2007;1:123–8.
- [562] Watanabe K, Hoshino T, Kanada K, Haruyama Y, Matsui S. Brilliant blue observation from a morpho-butterfly-scale quasi-structure. *Jpn J Appl Phys* 2005;44:L48–50.
- [563] Watanabe K, Hoshino T, Kanda K, Haruyama Y, Kaito T, Matsui S. Optical measurement and fabrication from a morpho-butterfly-scale quasi-structure by focused ion beam chemical vapor deposition. *J Vac Sci Technol B* 2005;23:570–4.
- [564] Zhang W, Zhang D, Fan T, Ding J, Gu J, Guo Q, et al. Biomimetic zinc oxide replica with structural color using butterfly (*Ideopsis similis*) wings as templates. *Bioinsp Biomim* 2006;1:89–95.
- [565] Saito A, Miyamura Y, Nakajima M, Ishikawa Y, Sogo K, Kuwahara Y, et al. Reproduction of the Morpho blue by nanocasting lithography. *J Vac Sci Technol B* 2006;24:3248–51.
- [566] Huang J, Wang X, Wang ZL. Controlled replication of butterfly wings for achieving tunable photonic properties. *Nano Lett* 2006;6:2325–31.
- [567] Crne M, Sharma V, Blair J, Park JO, Summers CJ, Srinivasarao M. Biomimicry of optical microstructures of *Papilio palinurus*. *EPL* 2011;93(14001):1–4.
- [568] Kolle M, Salgard-Cunha PM, Scherer MRJ, Huang F, Vukusic P, Mahajan S, et al. Mimicking the colourful wing scale structure of the *Papilio blumei* butterfly. *Nat Nanotechnol* 2010;5:511–5.
- [569] Kustandi TS, Low HY, Teng JH, Rodriguez I, Yin R. Mimicking domino-like photonic nanostructures on butterfly wings. *Small* 2009;5:574–8.
- [570] Hench LL. Bioactive glasses and glass-ceramics. *Bioceramics* 1999;293:37–63.
- [571] Hench LL. The story of Bioglass®. *J Mater Sci Mater Med* 2006;17:967–78.
- [572] Pek YS, Spector M, Yanna IV, Gibson LJ. Degradation of a collagen-chondroitin-6 sulfate matrix by collagenase and chondroitinase. *Biomater* 2004;25:472–82.
- [573] Walls EA, Berkson JM, Smith SA. The horseshoe crab, *Limulus polyphemus*: 200 million years of existence, 100 years of study. *Rev Fisheries Sci* 2002;10:39–73.
- [574] Scheibel TR. Protein fibers as performance proteins: new technologies and applications. *Curr Opin Biotechnol* 2005;16:427–33.
- [575] Porter D, Vollrath F. Silk as a biomimetic ideal for structural proteins. *Adv Mater* 2009;21:487–92.
- [576] Lazaris A, Arcidiacono S, Huang Y, Zhou JF, Duguay F, Chretien N, et al. Spider silk fibers spun from soluble recombinant silk produced in mammalian cells. *Science* 2002;295:472.
- [577] Nam KT, Kim DW, Yoo PJ, Chung-Yi, Chiang C-Y, Meethong N, et al. Virus-enabled synthesis and assembly of nanowires for lithium ion battery electrodes. *Science* 2006;312:886–8.
- [578] Lee YJ, Yi H, Kang K, Yun DS, Strano MS, Ceder G, et al. Fabricating genetically engineered high-power lithium-ion batteries using multiple virus genes. *Science* 2009;324:1051–5.
- [579] Seeman NC, Belcher AM. Emulating biology: building nanostructures from the bottom up. *Proc Natl Acad Sci USA* 2002;99:6451–5.
- [580] Smith GP. Filamentous fusion phage: novel expression vectors that display cloned antigens on the virion surface. *Science* 1985;228:1315–7.
- [581] Flynn CE, Lee S-W, Peelle BR, Belcher AM. Viruses as vehicles for growth, organization, and assembly of materials. *Acta Mater* 2003;51:5867–80.
- [582] Sarikaya M, Tamerler C, Jen AKY, Schulten K, Baneyx F. Molecular biomimetics: nanotechnology through biology. *Nat Mater* 2003;2:577–85.
- [583] Tamerler C, Sarikaya M. Molecular biomimetics: utilizing nature's molecular ways to practical engineering. *Acta Biomater* 2007;3:289–99.
- [584] Tamerler C, Sarikaya M. Molecular biomimetics: genetic synthesis, assembly, and formation of materials using peptides. *MRS Bull* 2008;33:504–10.